CHARACTERIZATION OF ZrO₂ REINFORCED Al-12.5Si ALLOY MATRIX COMPOSITE FABRICATED THROUGH SPRAY FORMING TECHNIQUE

Thesis
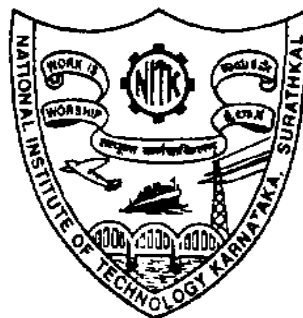
Submitted in partial fulfilment of the requirements for the degree of

DOCTOR OF PHILOSOPHY

By

ISHWARAGOUDA S PATIL.

(Registration No-155117ME15P02)

DEPARTMENT OF MECHANICAL ENGINEERING

NATIONAL INSTITUTE OF TECHNOLOGY KARNATAKA

SURATHKAL, MANGALORE-575025

July, 2022

`

`

Dedicated To My Mothers
Late Sharanavva S Patil
Late Nagavva R Patil
And
My father Shekaragowda Patil
Thanks for your great support
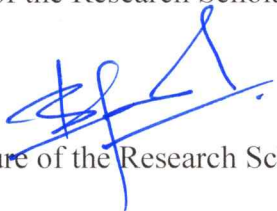*and continuous care*

`

DECLARATION
By the Ph.D. Research Scholar

I hereby declare that the Research Thesis entitled **"CHARACTERIZATION OF ZrO$_2$ REINFORCED Al-12.5Si ALLOY MATRIX COMPOSITE FABRICATED THROUGH SPRAY FORMING TECHNIQUE"** which is being submitted to the **National Institute of Technology Karnataka, Surathkal** in partial fulfilment of the requirements for the award of the degree of **Doctor of Philosophy** in **Mechanical Engineering** is a bonafide report of the research work carried out by me. The material contained in this Research Thesis has not been submitted to any other Universities or Institutes for the award of any degree.

Register Number: **155117ME15P02**

Name of the Research Scholar: **ISHWARAGOUDA S PATIL**

Signature of the Research Scholar: Department of Mechanical Engineering

Place: NITK-Surathkal

Date: 15.07.2022

CERTIFICATE

This is to certify that the Research Thesis entitled **"CHARACTERIZATION OF ZrO$_2$ REINFORCED Al-12.5Si ALLOY MATRIX COMPOSITE FABRICATED THROUGH SPRAY FORMING TECHNIQUE"** submitted by **MR. ISHWARAGOUDA S PATIL** (Register Number: ME15P02) as the record of the research work carried out by his is accepted as the Research Thesis submission in partial fulfillment of the requirements for the award of the degree of **Doctor of Philosophy**.

Research Guides

Prof. Shrikantha S. Rao

Professor

Department of Mechanical Engineering

Date: 15.07.2022

Dr. Mervin A. Herbert

Associate Professor

Department of Mechanical Engineering

Date: 15.07.2022

Chairman-DRPC

Date: 19.7.22

DEPARTMENT OF MECHANICAL ENGINEERING

NATIONAL INSTITUTE OF TECHNOLOGY KARNATAKA, SURATHKAL

MANGALORE - 575025

`

`

ACKNOWLEDGMENT

Undertaking this PhD has been a truly life-changing experience for me and it would not have been possible to do without the support and guidance that I received from many people.

The author, **Mr. Ishwaragouda Patil** wishes to express his deep sense of gratitude to his guide and supervisor, **Dr. Shrikantha S Rao**, Professor, and **Dr. Mervin A Herbert**, Associate Professor, Department of Mechanical Engineering, National Institute of Technology Karnataka (N.I.T.K), Surathkal for their invaluable guidance, motivation, untiring efforts and meticulous attention at all stages of this research work. Their constant encouragement, help and review of the entire work during the course of the investigation are invaluable. Without their guidance and constant feedback this PhD would not have been achievable.

I am immensely grateful to **Prof.Ravikiran kadolli**, Professor and Head, Department of Mechanical Engineering for extending the Departmental facilities, which ensured the satisfactory progress of my research work.

I would like to thank my co-researchers and friends for their kind help, encouragement for successful completion of this research work.

For this dissertation, I would like to thank my RPAC committee members: **Dr. Narayana Prabhu and Dr. Shivananda Nayak** for their time, interest, and helpful comments. I feel infinitely blessed for all the opportunities and good moments that I have had during these years of my Ph.D.

I would like to thank all the Teaching and non-Teaching staff members of the Department of Mechanical Engineering, of Tontadaraya college of Engineering for their continuous help and support throughout the research work.

I would also like to share the happiest moment with my wife **Mrs. Puspha I Patil** and my son **Mr. Rohit** and my Cousin s daughters **Vandana,Soujanya and Muktha** their support and endeavour kept my moral high throughout the research. I feel happy to express my sincere appreciation to all my family members including **my brother and cousin** for their understanding, care, support and encouragement. My friends outside of the programme have also been key. Thanks for checking in on me and cheering me on.

I fail in my duty if I fail to thank my younger friend **Anarghya A Murthy** for his constant encouragement, timely help and morale support

`

The list goes on and there are many others I should mention. There are people who have helped me all the way and provided me support when I didn't even realize I needed it, or needed it now, or needed it constantly. Listing all of them would fill a book itself, so I merely will have to limit myself to a few words: I THANK YOU ALL……!

<div align="right">

_____

(Ishwargouda S Patil)

</div>

`

ABSTRACT

Aluminium and its alloys possess high stiffness, lightweight and high strength. They can provide solutions to optimize strength-weight ratio in aerospace and automobile industries. Among several methods to fabricate Aluminium metal matrix composites, spray deposition method is used for large-scale production due to its high deposition efficiency.

In the first phase, stir cast processing route was employed to prepare the composite. Taguchi experimental plan with a set of parameters such as stir speed, stir time, ZrO_2 % reinforcement, and casting temperature were studied to know their influence on the composite properties. Super ranking concept was adopted to optimize the key process parameters of stir casting. It has resulted in 25.02% and 5.64% increase in ultimate tensile strength and hardness, respectively, whereas the reduction in wear loss of composites was 37.68% compared to initial stir casting conditions. The hot-pressing technique was applied to the composites prepared according to optimized stir casting conditions. The hot-pressing parameters (pressure, temperature, and dwell time) were analysed to know the process insights on composite properties. The pressure is the most dominating factor followed by temperature on all the properties of composites. The optimal hot-pressing conditions were again obtained by Super ranking concept. The usage of these optimal conditions showed a 39.3% reduction in wear loss, 11.54% and 4.88% increase in ultimate tensile strength and hardness values, respectively, compared to initial hot-pressing condition. The comparison of properties exhibited by samples fabricated by initial, and optimal conditions of stir casting and hot-pressing technique have resulted in excellent enhancement of properties which was strongly justified with the analysis of resulted microstructures and worn surface morphologies.

In second phase, the metal matrix composites were fabricated using 99.9 wt. % aluminium and silicon (the wt % 12.5Si) is reinforced with the (5wt%, 10 wt% and 15wt%) ZrO_2 powder particles by stir casting and spray deposition method. Mechanical properties, micro hardness and evolution of microstructure of AlSi alloy with three different wt. % of zirconium oxide as particulate reinforcement were studied. The microstructural results indicate that the rich interface among the metal matrix and AlSi-ZrO_2 particles and depicts the agglomeration of reinforced phase resulting to poor wettability of ZrO2 and observed decohesion. The mechanical testing results indicate that the tensile strength increases with the percentage of ZrO_2. Moreover, as cast composites exhibit reverse tendency in compressive and hardness values. The highest compressive values for as cast and hot-pressed composites

were 380 MPa and 337 MPa for the addition of 10% ZrO_2. The highest tensile strength of 191.83 MPa was obtained for 5% ZrO_2 as cast composite and 164 MPa for 15% ZrO_2 hot pressed composite. It is to note that as cast composite method represented more homogenous data compared to the hot-pressed composites. Hot pressed samples exhibited the reduction in the porosity compared to the as cast.

In the third phase, research aims to study the effect of flight distance as a potential key factor that changes the optimum percentage of AlSi-ZrO_2 in terms of mechanical and microstructural properties. The alloy is sprayed at varying the flight distance from 320 mm to 480 mm. The alloys were prepared by spray deposition technique and effects on microstructural properties were investigated. The AlSi-ZrO_2 alloy was subjected to hot isostatic pressing for reducing the porosity of the deposit from 14.4% to 8.2%. Series of experimental study were carried out in the laboratory by varying the flight distance from 320 mm to 480 mm for AlSi-ZrO_2 alloy to characteristic loading. In this paper, an optimized artificial neural network using genetic algorithm are developed to predict the mechanical behaviour for AlSi-ZrO_2 composites. Based on the experimental data, the ANN models were developed, trained and tested. The microstructure of the AlSi-ZrO_2 alloy consisted of finely divided globular shaped eutectic Si uniformly distributed in the Al matrix. With addition of ZrO_2 composition to AlSi alloy, the tensile strength and micro hardness increased from 123 MPa to 147 MPa and 48 HV to 72 HV. The preferred flight distance for the current study is found to be 420 mm. Microstructural images obtained at flight distance consist of co-existing primary Si phase and needle like eutectic Si. The physical properties, such as tensile strength, compressive strength, yield strength, micro hardness and porosity of sprayed AlSi-ZrO_2 can hence be adjusted by setting the optimized flight distance. The developed ANN-GA method proved to be accurate, reduced time and efficient to predict the numerous samples, and it will help materials designers to design their future experiments effectively.

In fourth phase, the wear behaviour and microstructural characterization of aluminium silicon alloy with a reinforced ZrO_2 composite material with respect to various flight distances are investigated. The amounts of ZrO_2 (5, 10 & 15 wt %) were added to Al-12.5Si alloy. The microstructural characterization of the developed composites was analysed using Scanning Electron Microscope (SEM) and Energy Dispersive Spectrum (EDS). The effect of flight distance (320 to 480 mm), applied load (30 to 50 N) and the influence of reinforced ZrO_2 (5, 10 and 15 wt %) were investigated using the design of experiment (5x3x5 mm). The findings of the study reveals that there is a remarkable improvement in wear behaviour when

`

surfactant functionalized MWCNT-in-oil is used. Finally, a wear map of the underlying wear mechanisms is also presented. This investigation showed that wear resistance of the developed Al-12.5Si alloy can be improved by the effect of optimized effect of flight distance and wt% of ZrO_2. In addition, ANN-GA model were developed to predict the wear behaviour of Al-12.5Si with reinforced material of ZrO_2, applied load and the effect of flight distance as inputs. The estimated values were compared with experimental tests and the results showed that a high degree of association (Correlation coefficient, R ranging from 0.91 to 0.96). Therefore, the develop model can be used to predict the behaviour of wear within the range of tests performed.

Another important outcome of this research is the development of prediction model using ANN and genetic algorithm (GA) to assist in validation. This method is a combination of two soft-computing methods of ANN and GA. GA logic helps in the transformation of the human knowledge and the ANN helps in the learning process and reduces the rate of errors in the determination of rules in ANN logic.

Keywords: Wear; Metal matrix composite; Friction; Spray deposition; ANN-GA; Hot-pressing; Stir casting; Zirconium di-oxide; Taguchi method; Super ranking concept

List of Publications based on Ph.D. Research Work

Sl. No.	Title of the paper	Authors (in the same order as in the paper. Underline the Research Scholar's name)	Name of the Journal/ Conference/ Symposium, Vol., No., Pages	Month, Year of Publication	Category *
1.	Effect of zirconium oxide particulate composites with Al-Si on the microstructural and mechanical properties of hot pressed, spray forming and stir casting methods	<u>Ishwargouda S Patil</u>, Anarghya A, Shrikantha S Rao, Mervin A Herbert, Rohit Kushwaha	Australian Journal of Mechanical Engineering/ https://doi.org/10.1080/14484846.2021.1913872	June 2021	1
2.	Experimental Investigation and Optimisation of Mechanical and Microstructure Behaviour of Stir Cast and Hot-Pressed Al-12.5%Si-ZrO2 Composites: Taguchi and Super Ranking Concept	<u>Ishwargouda S Patil</u>, Anarghya A, Shrikantha S Rao, Mervin A Herbert, Dayanand M Goudar	Advances in Materials and Processing Technologies / https://doi.org/10.1080/2374068X.2021.1927648	July 2021	1
3.	Mechanical and microstructural analysis of a AlSi-ZrO$_2$ metal matrix composite using optimized artificial neural network and experimental data	<u>Ishwargouda S Patil</u>, Anarghya A, Shrikantha S Rao, Mervin A Herbert, Dayanand M Goudar	Materials today Communications, 27, 102398 https://doi.org/10.1016/j.mtcomm.2021.102398	June 2021	1
4.	Comparison of wear behaviour of Al-Si alloy reinforced with ZrO2 composite using spray deposition and stir casting technique	<u>Ishwargouda S Patil</u>, Shrikantha S Rao, Mervin A Herbert	The International Conference on Advanced Production and Industrial Engineering (ICAPIE). Proceedings will be published in Sprinjer.	July 2021	3

5.	Experimental investigation of tensile fractography and wear properties of Al-12.5Si alloy reinforced with ZrO2 using spray deposition method	Ishwargouda S Patil, Anarghya A, Shrikantha S Rao, Mervin A Herbert	Materials today Communications, 30, 103217 https://doi.org/10.1016/j.mtcomm.2022.103217	April 2022	1
6.	Dataset on mechanical and microstructural properties assessment of eutectic Al-12.5Si with reinforcements of Zirconium-dioxide	Ishwargouda S Patil, Anarghya A, Shrikantha S Rao, Mervin A Herbert	Data in Brief	(Under Review)	1

*Category:
1: Journal paper, full paper reviewed 2: Journal paper, Abstract reviews 3: Conference/Symposium paper, full paper reviewed 4: Conference/Symposium paper, abstract reviewed 5: Others (including papers in Workshops, NITK Research Bulletins, Short notes etc.)

`

TABLE OF CONTENTS

`

`

LIST OF FIGURES

LIST OF TABLES

`

`

CHAPTER 1

INTRODUCTION

1.1 Rationale for Research

The growing demands in the automotive and aerospace industry for reduction in energy consumption and producing more fuel-efficient vehicles continues to be a big challenge. The aluminium-silicon alloys have gained increased market shares in the aerospace and automotive industry and have replaced competing ferrous materials. Aluminium-silicon alloys are widely used in the automotive industry due to the high strength-to-weight ratio, good corrosion resistance and good castability. However, the performance of aluminium-silicon alloys at elevated temperature are limited because of degradations in the mechanical properties. The effect of the elevated temperatures in aluminium-silicon alloys have been investigated by several researchers during the last decade (Stadler et al., 2011, 2012; Ceschini et al., 2015). However, the effect of zirconium oxide as a reinforcing material on the mechanical and microstructural properties of aluminium-silicon alloys at elevated temperatures has received limited attention. The aim of this thesis is to gain a deeper understanding of aluminium-silicon alloys elevated temperature applications. The work focuses on the effect of zirconium oxide as a reinforcing material on the mechanical properties, wear properties and microstructure in aluminium-silicon alloys at room and elevated temperatures.

1.2 Aim of research

The main subject of this PhD Thesis is the use of zirconium oxide in aluminium silicon matrix by means of two technologies: Stir casting and Spray deposition. Understanding the behaviour of the deposited material requires an understanding of the characteristics of each technique. Furthermore, process conditions have a significant impact on the functional response and operation of metal oxide layers in various application sectors. Figure 1.1 depicts the project's overall structure.

The aim of this research is fourfold:

• The scope of the PhD thesis consisted of developing aluminium-silicon alloys for elevated temperature applications. Taguchi experimental plan with a set of parameters such as stir speed, stir time, ZrO_2 % reinforcement and casting temperature were studied to know their

1

influence on the composite properties. ZrO_2 % reinforcement, followed by stir speed, is the most dominant factor influence on composite properties. Super ranking concept is employed to determine the optimal conditions for stir casting.

• The research also focuses on the effect of silicon on mechanical properties, thermal properties and microstructure in aluminium-silicon alloys by varying the percentage of zirconium oxide on the mechanical properties, wear properties and evolution on microstructure using stir casting and spray depositing methods.

• The research is also aimed at investigating the different flight distances with the objective to analyse the developed composite by spray deposition method. Series of experimental study were carried out in the laboratory by varying the flight distance from 320 mm to 480 mm for AlSi-ZrO_2 alloy.

• In addition, the wear behaviour and microstructural characterization of aluminium silicon alloy with a reinforced ZrO_2 composite material were also investigated.
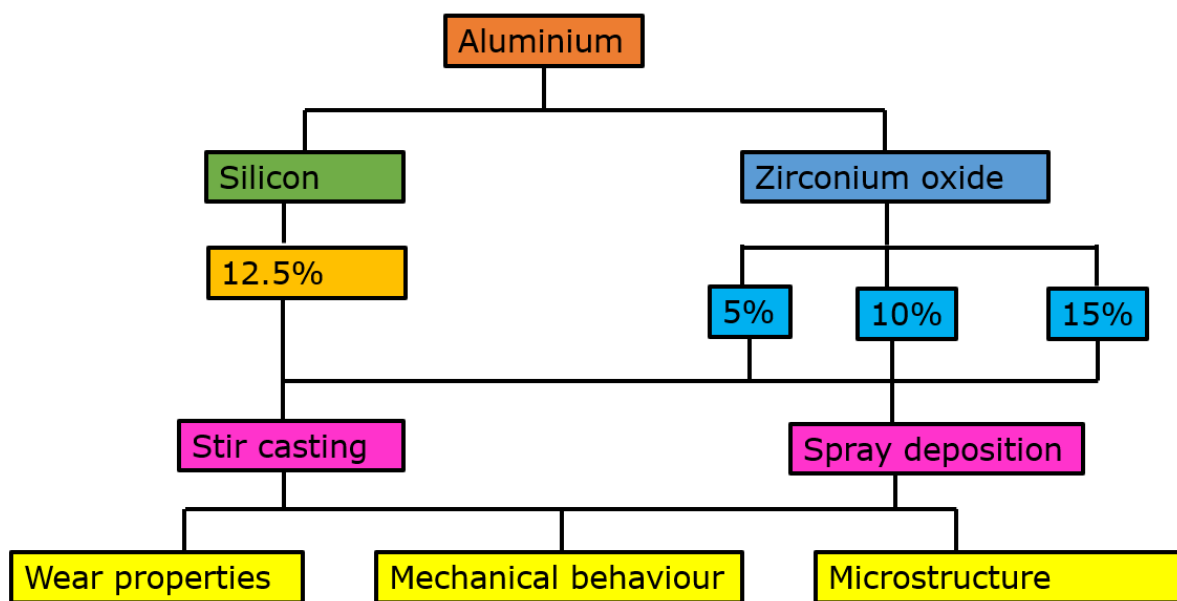
Figure 1.1: PhD thesis scheme

1.3 Thesis outline

The thesis is split into six chapters:

- Chapter 1 opens up the thesis with the introduction, consisting of mainly background information and the motivation of the project.

`

- It is then followed by Chapter 2 on a summary of relevant works reported in the open literature of the use of aluminum silicon eutectic alloy, as well as a description of stir casting and spray formation theory and implementations, as well as selected published findings. This indicates that reinforced particles have a favorable impact on the mechanical properties of cast aluminium alloys, with the vast majority of tensile testing findings indicating increased strength over permanent mold/gravity cast alloys. Spray forming increased elongation values in most cases, although there was more variability, with decreases in elongation being more common, but only in the minority of cases.

- Chapter 3 addresses the experimental spray and stir casting test rig's design, manufacture, and commissioning. A system configuration was chosen after reviewing the experimental designs. The experimental casting rig's final design is seen. The chapter ends with an examination of the equipment's operation and suggestions for future development.

- The experimental methods used in the development and study of the squeeze castings are detailed in Chapter 4. It covers the production of semi-automated quantitative metallography techniques used in the analysis of specimens developed by the spray forming and stir casting apparatus, as well as the Taguchi design of experiments method used in this study. The ANN-GA algorithm is developed to predict the wear and mechanical properties.

- The findings of the castings study are recorded and discussed in Chapter 5. It includes macro-porosity, macro-segregation, secondary dendrite arm spacing, and micro hardness checking of the eutectic and aluminum dendrites on cast specimens. A large number of micrographs are included, which are used to explain the discussions in this chapter.

The conclusions and recommendations arising from this experimental work are in Chapter 6.

`

CHAPTER 2

LITERATURE SURVEY

2.1.Background

Understanding and minimising the number of imperfections is a critical aspect of manufacturing durable high-strength aluminium castings. The automotive industry, in its quest to make vehicles lighter, has a strong desire for durable higher strength alloys. The automotive industry is the largest consumer of cast aluminium, and the global demand for automobiles is growing (world car sales 2004-2014 (OICAs, 2013)) and has produced an increasing demand for aluminium alloys. As a result, high-quality castings made from recycled aluminium are becoming increasingly important. However, each time scrap is remelted to make new alloys, the risk of imperfections increases. Recycled aluminium alloys, on the other hand, use far less energy than primary aluminium alloys made from mined bauxite; the European Aluminium Association (EAA) claims that recycled aluminium alloys save up to 95 percent of energy.

Imperfections in the castings are often linked to changes in mechanical properties (Polmear et al., 2005; Dai et al., 2003; Eisaabadi et al., 2012) or the melt itself (Liu et al., 1998; Tian et al., 2012). Recycled aluminium melts usually contain more imperfections than primary aluminium (Das et al., 2007). If not diluted with more pure aluminium, this results in a loss of mechanical properties and can also affect physical properties. Castings made with a gradient solidification process, in which imperfections are pushed ahead of the solidification front, have far less imperfections. As compared to samples cast using traditional casting methods, tensile test samples cast using this technique show increased strength and elongation (see Figure 2.1). This demonstrates that recycled aluminium castings have yet to achieve their full potential.

`
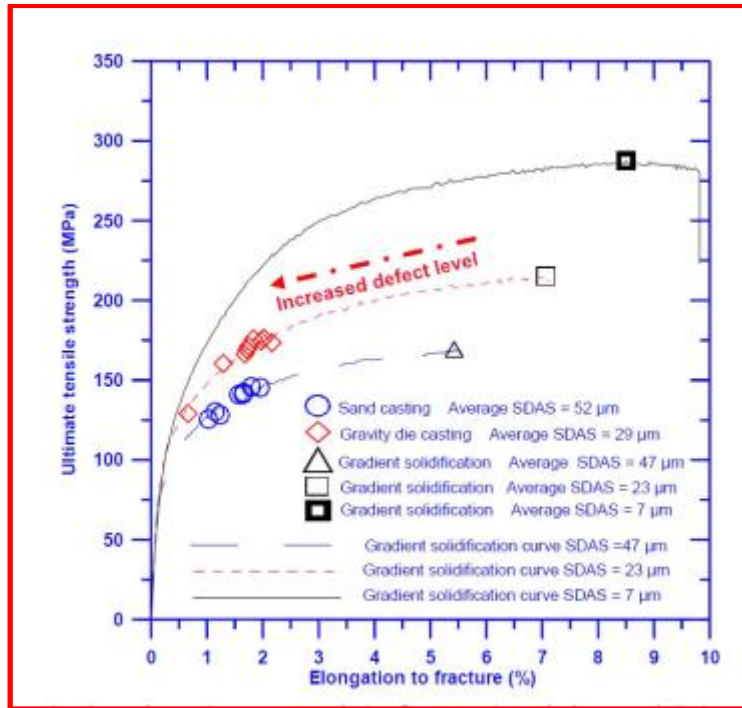
Figure 2.1. Graph showing the potential of cast aluminium with lower number of defects (Seifeddine et al., 2006)

Aside from increased strength and elongation to fracture (ef), mechanical property scattering is a problem. The tensile properties of a heat-treated alloy cast in a standardised permanent mould by a variety of different foundries are shown in a study from the Aluminum Association (AA), cited by Sigworth (Sigworth et al., 2011). The mould had five different areas with different section thicknesses, resulting in different solidification speeds; Table 2.1 shows the range of values recorded for ultimate tensile strength (UTS), yield strength (YS), and elastic modulus (ef). The assets had a lot of variety, as you can see in the graph.

Table 2.1. The range of values for the same alloy cast in the same mould by different foundries (Sigworth et al., 2011)

Area	UTS (MPa)	YS (MPa)	Elongation (%)
1	235-276	166-242	1.8-4
2	231-283	166-242	1.5-4.5
3	252-297	173-162	3-7.7
4	259-314	166-269	3.5-9.5
5	248-293	162-173	3-7.5

2.2 Aluminium

There are two main types of aluminium that are categorised based on non-heat treatable and heat treatable. They are wrought aluminium alloys and cast aluminium alloys.

2.2.1 Introduction to aluminium

Wrought aluminium – cast as billets or ingots and then hot or cold moulded into shape by rolling, extrusion, or forging, for example. Aluminum that has been specifically cast into form in a mould made mainly of sand or steel. The silicon (Si) content is the main chemical difference between the two forms of aluminium. Cast aluminium has a higher Si content to improve castability, or the ability to produce a sound casting with good mechanical properties. The Al-Si phase diagram with the most commonly used Si contents is shown in Figure 2.2. Hypereutectic compositions are those that are higher than 11.7 percent Si, whereas hypoeutectic compositions are those that are lower.
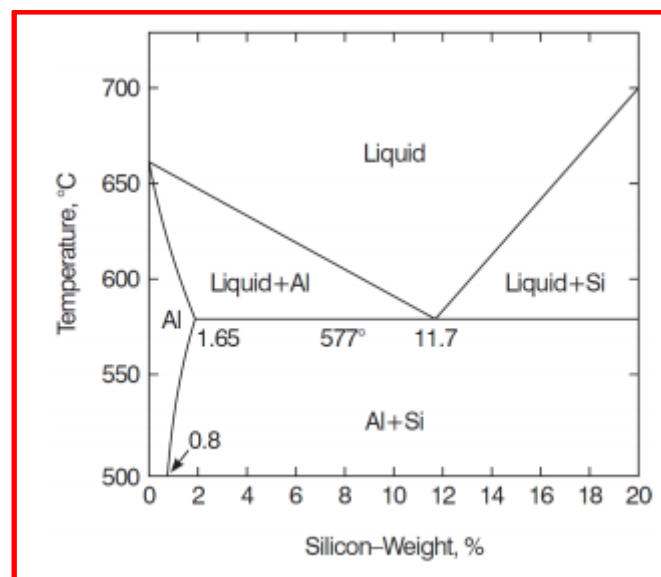
Figure 2.2. The Al-Si phase diagram, showing the most frequently used Si contents (Sigworth et al., 2011)

Aluminium is alloyed with copper, manganese, magnesium, zinc, nickel, and silicon as major alloying elements to satisfy different requirements. When these alloying additives are applied in desired percentages, they strengthen the properties of aluminium. The AAA (Aluminium Association of America) has a four-digit classification scheme for wrought aluminium alloys. The International Alloy Development System (IADS) and the majority of countries around the world use this designation. In the four-digit scheme, Table 2.2-2.3 shows the basis for

`

classification of wrought and cast aluminium alloys. The first digit indicates the alloy type, while the second indicates the alloy alteration. The last two digits show the unique aluminium alloy or, in the case of pure aluminium, the purity standard.

Table 2.2- Designation of Wrought Aluminium alloys (Sigworth et al., 2011)

Alloy Designation	Detail
1XXX	99% pure Aluminium
2XXX	Cu containing alloy
3XXX	Mn containing alloy
4XXX	Si containing alloy
5XXX	Mg containing alloy
6XXX	Mg and Si containing alloy
7XXX	Zn containing alloy
8XXX	Other alloys
9XXX	Unassigned

Table 2.3- Designation of Cast Aluminium alloys (Sigworth et al., 2011)

Alloy Designation	Detail
1XX.X	99% pure Aluminium
2XX.X	Cu containing alloy
3XX.X	Cu/Mg containing alloy
4XX.X	Si containing alloy
5XX.X	Mg containing alloy
7XX.X	Zn containing alloy
7XXX	Sn containing alloy
9XX.X	Other alloys
6XX.X	Unassigned

The condition of temper of Aluminium alloys is denoted by specific letters as shown below. Numeric additions indicate specific variations

2.2.1.1 Cast aluminium

Casting is a cost-effective way of manufacturing near-net formed products with complex geometries, since the as-cast product usually only needs minimal machining. Si increases the castability of aluminium alloys by increasing fluidity, resistance to hot cracking, and feeding (Brown et al., 1999). Aluminium alloys are cast using two distinct types of moulds: expandable moulds and permanent moulds. Patterns may be both expandable and permanent. The most common type of expandable mould is a sand mould with different types of binder materials, but other types of expandable moulds may also be used, such as plaster moulds.

`

Steel is commonly used for permanent moulds. They should be resistant to thermal fatigue, so high thermal conductivity, high strength at elevated temperatures, low thermal expansion, and low modulus of elasticity can be achieved (Wallace et al., 2001). Gravity casting in a permanent mould has the advantage of a faster solidification rate, which results in a finer structure and thus stronger mechanical properties.

Pressurized molten metal can be used to fill the mould cavity in permanent moulds, and with process automation, output rates can be high. Pressure die casting, on the other hand, necessitates a relatively high financial investment in the die, making it only suitable for large series (>20000 castings per year) (Svensson, 2003).

2.2.1.2 Main alloying elements

Al-Si alloy presents a great industrial potential in many applications due to its cast ability and the presence of Si that strengthens these alloys and improve their wear resistance. The most common applications of these alloys are in marine, electrical, automobile and aerospace industries. Aluminium-silicon alloys are most important amongst the various foundry alloys contributing 80% of the aluminium castings. This is because of their excellent casting characteristics, pressure tightness, and good mechanical properties, low co-efficient of thermal expansion, high thermal conductivity, high fluidity, good weld ability, easy brazing and high corrosion resistance. The outstanding mechanical, physical, and casting properties of Al-Si alloys make them attractive for use in cheaper and lighter engineering components. The most widely employed aluminium silicon alloys are often hypoeutectic and eutectic. The microstructure and alloy constituents are required to obtain good mechanical characteristics. Grain size, dendritic arm spacing, and silicon morphology in the eutectic process are all important microstructural characteristics. However, a major focus in the production of cast aluminium silicon alloys has been to use them to replace various steel and cast-iron moving parts, especially automotive castings. To enhance properties such as casting characteristics and strength, alloying elements are used. With a UTS value of about 70MPa and elongation of about 43 percent, commercially pure aluminium (99 percent Al) has a low tensile strength and strong elongation (Hunsicker et al., 1990). Silicon (Si)improves castability, or the ability to fill dies quickly and solidify without hot cracking as a part. Si leads to a higher degree of isothermal solidification in casting alloys, which increases fluidity. Si has a five-fold higher fusion heat than aluminium, which contributes to hypereutectic alloys' high fluidity. The eutectic liquid reduces the possibility of hot cracking in a well-fed casting (Sabatino et al., 2009). In both as-cast and heat-treated conditions, copper (Cu) increases strength and

8

hardness. Copper also increases machinability by increasing matrix hardness, making small cutting chips and a high surface finish easier to achieve. Cu, on the other hand, decreases corrosion resistance (Major et al., 2008). After heat treatment, magnesium (Mg) increases strength and hardness by forming Si2Mg precipitates, which effectively increase strength by precipitation hardening. Surface oxides called spinel, MgAl2O4, form in aluminium alloys with less than 2% magnesium, and spinel converts to MgO in alloys with more than 2% magnesium; if entrapped in the melt, these oxides will damage the final casting (Campbell, 2011). By increasing the high temperature pressure, iron (Fe) reduces the risk of die soldering or die sticking (Shankar et al., 2002) and improves resistance to hot tearing (Wang et al., 1995). Manganese (Mn) is used to change the morphology of dangerous Fe platelets into Al15(Fe,Mn,Cr)3Si2, which has a more compact form and may be less dangerous. In the industry, a maximum Fe:Mn ratio of 2:1 has been the agreed rule to prevent the formation of Al5FeSi (Crepeau et al., 1995). Chromium (Cr) promotes -Al15(Fe,Mn,Cr)3Si2 and increases the size of Fe-rich particles in AlSi9Cu3 alloys (Timelli et al., 2013). The aluminium silicon eutectic is modified by strontium (Sr), antimony (Sb), sodium (Na), and calcium (Ca). The eutectic silicon is changed from coarse continuous networks of thin platelets to finer fibrous or lamellar structures after modification (Major et al., 2008). Aluminium alloys account for a large percentage of lightweight metals used in manufacturing. Among the various foundry alloys, Aluminium-Silicon alloys are the most important, accounting for 80 percent of aluminium castings. This is due to their excellent casting properties, pressure tightness, good mechanical properties, low thermal expansion coefficient, high thermal conductivity, high fluidity, good weldability, fast brazing, and high corrosion resistance. Al-Si alloys are desirable for use in cheaper and lighter engineering components due to their excellent mechanical, physical, and casting properties. The consistency of an Al-Si alloy casting's microstructure (i.e., the fineness of the structure, the shapes and morphologies of the micro constituents present therein, as well as the amount of porosity contained in the casting) determines its strength and quality. The value and applications of aluminium and its alloys for machine parts are growing by the day. Many of the most commonly used aluminium silicon alloys are hypoeutectic and eutectic. To achieve optimal mechanical properties, the microstructure and alloy constituents are needed. Grain size, dendritic arm spacing, and silicon morphology in the eutectic process are all important microstructural characteristics.

`

2.2.1.3 Solidification

Thermal analysis (TA), which records the temperature of the metal over time, can be used to measure solidification. <u>Figure 2.3</u> depicts an example of an A380 alloy cooling curve. The molten alloy is cooled down from the peak temperature on the left to the nucleation temperature of the -Al dendrites; the curve depicts the undercooling needed to shape the -Al dendrites. As grain refiners are used, the amount of undercooling needed is reduced, and the cooling curve can be used to determine the grain size in the casting. The -Al dendrites develop and fill the casting in the next area, between -Al nucleation and eutectic nucleation. Growth can only occur laterally after the dendrites have filled the casting. As a result, this region is linked to the SDAS, which is a popular method for determining the local solidification period in a casting. When the SDAS is difficult to differentiate, particularly in high-pressure die castings, another measurement called cell size or cell count can be used. The number of rounded Al-phase features in a measured length is known as cell size or cell count. The second undercooling is linked to eutectic nucleation and can provide details on the Si particle modification level in the eutectic; a smaller undercooling suggests a higher level of modification. The temperature at which eutectic nucleation occurs is also reduced in a modified alloy. Intermetallics such as Al_2Cu and $Al_5Mg_8Si_2Cu_2$ are precipitated during the last reaction. The cooling curve does not demonstrate the nucleation of Fe-rich intermetallics. Depending on chemical composition and cooling rate, they nucleate at temperatures below -Al dendrites and up to eutectic nucleation temperatures.
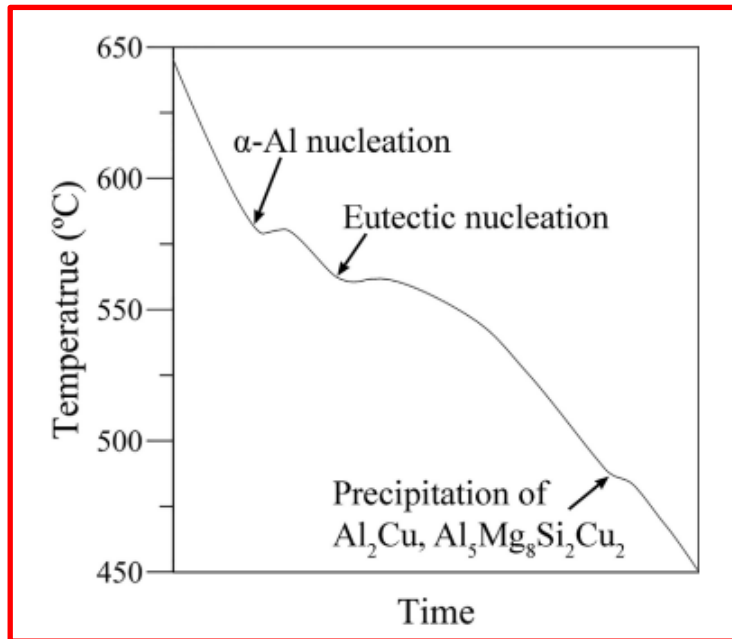
Figure 2.3. Cooling curve of an A380 alloy, temperature versus time, showing a cooling rate of 0.6°C/s (after solidification) (Backerud et al., 1990)
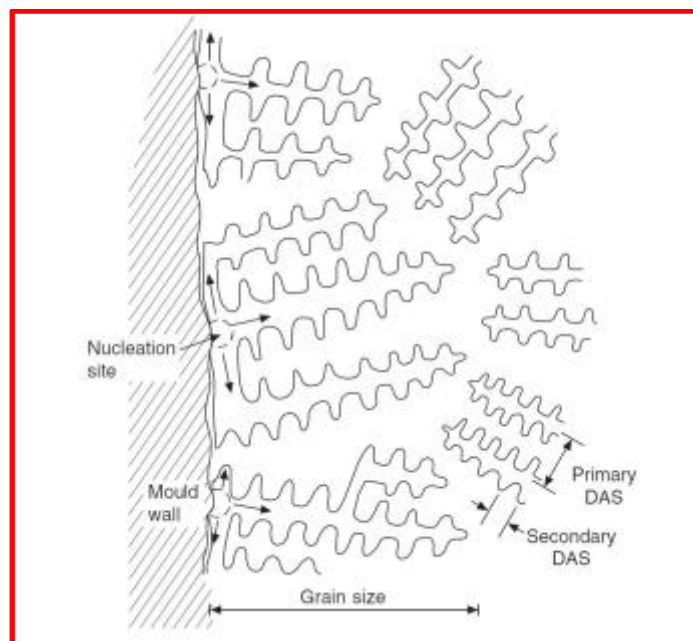
Figure 2.4 Grain size of an A380 alloy (after solidification) (Backerud et al., 1990)

Classification of Al-Si alloys

These alloys are classified into three groups depending on their composition (Gruzleski J. E. 1990). The phase diagram of Al-Si alloys is shown in Figure 2.5. These are:

- Hypoeutectic (Si<10%)

- Eutectic (10% to 13% Si) and

- Hypereutectic (Si>13%) alloys.

Good cast ability and corrosion resistance characterize the binary hypoeutectic and eutectic Al-Si alloys, while the hypereutectic alloys exhibit excellent wear resistance and low thermal expansion.
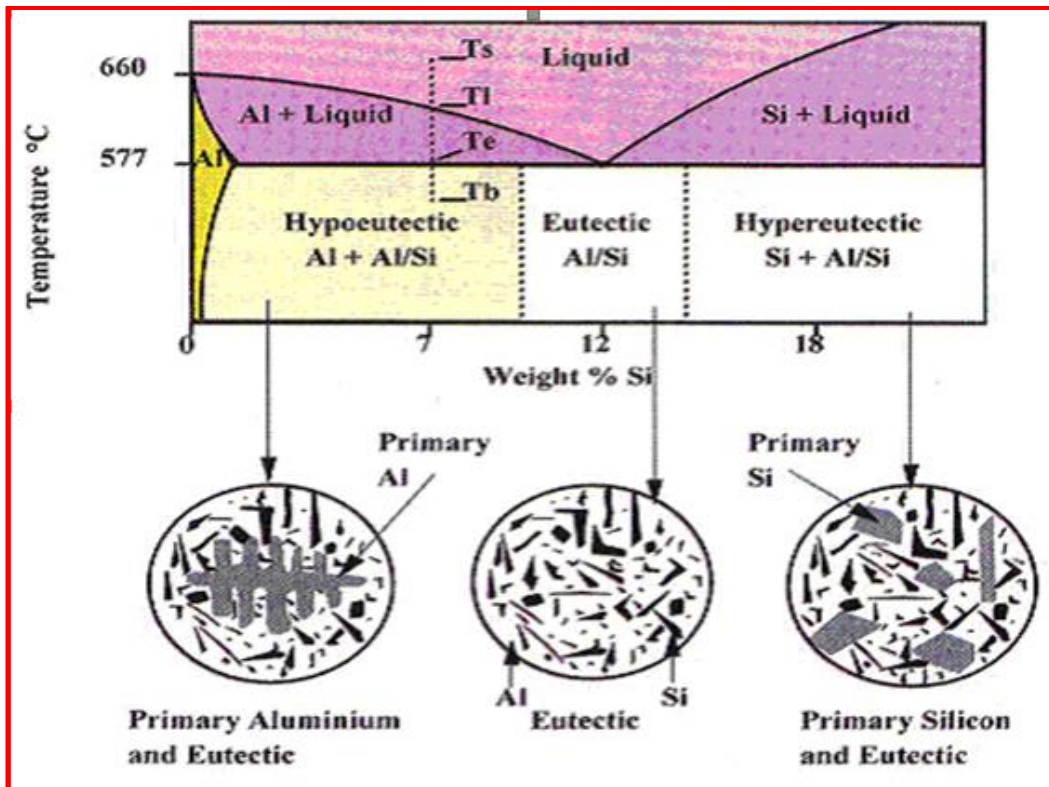
Figure 2.5: Phase Diagram of Al-Si alloys (Metallurg, 2003)

2.3 Zirconium oxide

It's a metal made from baddeleyite, an oxide mineral, and Zirconium silicate, a silicate mineral. More abundant than lead and copper, zirconium is the nineteenth most abundant element in the earth's crust. It has a strong proclivity for forming metallic salts of excellent electrical conductivity. It is used in different structural components of nuclear reactors because of these properties, Martin Heinrich Klaproth, a German chemist, discovered it in 1789. Jons J. Berzelius, a Swedish chemist, developed the metallic powder in 1824. J.H. de Boer and Anton E van Arkel, two Dutch chemists, invented a method to purify usable amounts of metal in 1925. They also developed a thermal iodide method to decompose Zirconium tetraiodide thermally. The amount of grinding time needed for its machining is about half that of any other element. The surface finish after grinding is significantly better than a comparable feature in any other material.

`

The process of manufacturing the zirconium oxide is given below

- Advanced synthesis methods for high purity Zirconia have been developed, and the mineral Zircon silicate is used as the raw material for manufacturing Zirconia. Melting coke and lime will produce ZrO2 on a large scale. Reactions in the gas phase, molten salt baths, hydrothermal powder synthesis, and sol-gel processes are among the processing methods used.

- Gas phase processing will produce Zirconia powder with particle sizes ranging from 0.01 to 0.10 µm. Green bodies are made by tape casting, dry pressing, and slip casting from the powder obtained by this process after it has been combined with additives.

- The sintering additives stay in the ceramic after that, although the auxiliary substances, which are volatile organic compounds, are separated from the moulding prior to the sintering process. The green body is sintered into a raw product, then polished and ground according to the application.

- During the sintering process, the mouldings are given their actual properties. By reducing to their basic form, the ceramic powder contracts. A temperature-dependent diffusion method is used to achieve this.

- Using the right sintering additives, the speed of solid body diffusion can be increased. Sintering can be achieved with a liquid phase or under particular pressure if solid body diffusion is too slow. The sintering process, which takes place at high temperatures and pressures, raises the cost of producing ceramic components.

2.3.1 Main features of zirconium oxide

Zirconium is a highly refractory material, exhibiting chemical and corrosion inertness.
The other features are

- High density.
- Chemical inertness.
- Low thermal conductivity.
- Ionic electrical conduction.
- Ability to withstand molten metals.
- Extremely tough.
- Resistance to wear.

`

- Ability to withstand temperatures of up to 2400 degrees Celsius.
- Extremely high fracture durability.

Zirconium dioxide (ZrO_2), also known as Zirconia, is a monoclinic crystalline metal that occurs naturally. It has the same properties and design as alumina, but when surface ground, it produces a better finish than alumina (Grant, 1991). In relation to alumina, zirconia is much easier to machine. When machining Zirconia, three basic principles should be followed: high feed rates, slow speeds, and a flood coolant system with a water-soluble oil lubricant.

d

- Wire and thread guides
- Powder compacting dies to compact powder.
- In the milling industry.
- Membranes for fuel cells.
- Seats and ball valves that requiring precision.
- Subsectors of high-temperature induction furnaces
- Metal tube shaped rollers and guides
- Seals and shaft guides for marine pumps.
- Valve seats for deep wells.

2.4 Survey of papers

Anand et al. (1997) produced a hypereutectic aluminium-silicon alloy using spray deposition and atomization method. Figure 2.6 depicts the spray atomization and deposition apparatus used in this analysis. The study found that the spray processed alloy has greater strength and ductility than a traditional ingot metallurgy processed alloy of the same chemical composition in tensile tests at ambient and elevated temperatures. Finally, the authors addressed the manufacturing and intrinsic microstructural effects of the spray-processed alloy's quasi-static fracture characteristics.
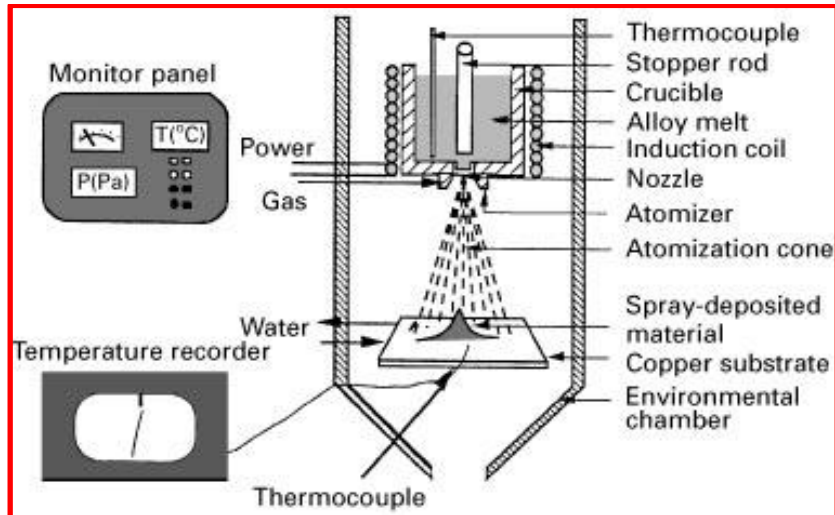
Figure 2.6: Experimental apparatus used for spray atomization and deposition processing (Anand et al., 1997)

A computational model for predicting grain size in inoculated castings was presented by A. Greer et al. (2000). This model improves on Maxwell and Hellawell's earlier model by considering grain appearance to be regulated for free growth rather than nucleation, and by considering a distribution of inoculant particle diameters. The model makes quantitatively accurate predictions for grain size and variance with refiner addition stage, cooling rate, and melt composition using calculated particle size distributions as input. The model optimizes the efficiency of the refiner to 100% by suggesting that the particle-diameter distribution be restricted to the shaded portion of the Figure 2.7. The authors conclude that the model can assist in optimizing the use of existing refiners and in developing improved refiners by optimizing the parameters which influence the development of the refiners.
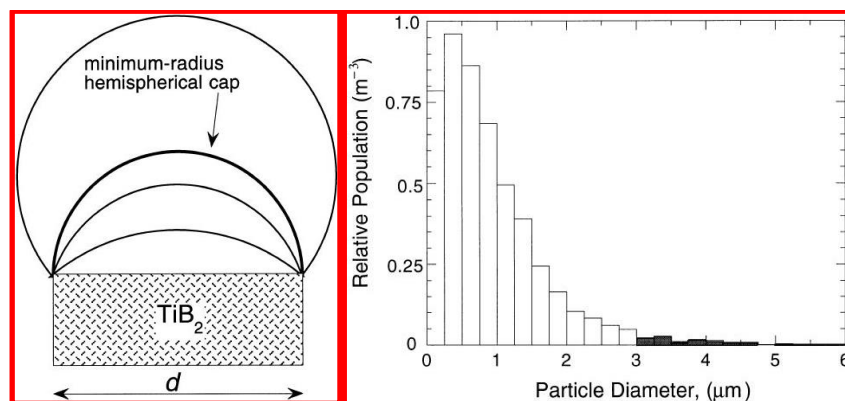
Figure 2.7 (a): Crystal growth following nucleation (b) The shape of the TiB2 particle distribution in Al-5Ti-1B (wt%) refinement (Greer et al., 2000)

Benzergaet et al. (2001), carried out tensile tests on the specimens made of an A356 alloy with 7% Si as the main alloying element. The microstructure within each grain is composed of pro-eutectic aluminium dendrites separated by a boundary eutectic area of segregated silicon particles of 2–3 μm diameter for both processing conditions. The rapid cooling rate causes a secondary dendrite arm spacing of approximately 20–30 μm, while the secondary dendrite arm spacing obtained with the slow cooling rate is about 80–100 μm. The cast aluminium alloy is modelled as having two "phases," each with different elastic and plastic properties. The matrix material (pro-eutectic aluminium dendrites) and the wall material (eutectic boundary region) are the two phases, respectively. The light microscopy of the deformed samples with coarse and fine microstructures are shown in the Figure 2.8. The matrix-wall interface is a critical domain, and Figure 2.8 shows the AFM topography at this site, which shows the accumulation of dislocations.
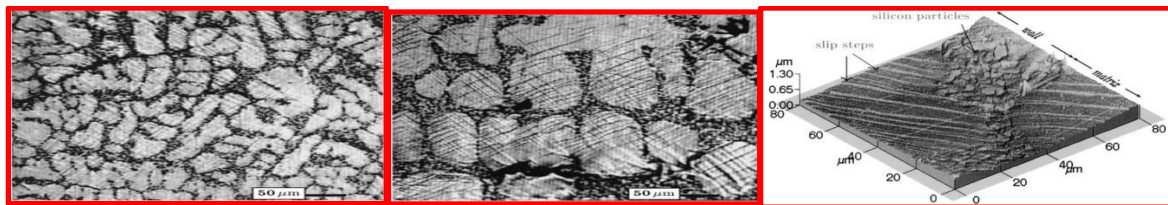
Figure 2.8: SEM image and the AFM topography (Benzergaet et al., 2001)

Srivastava et al. (2001), have analyzed the main characteristics of heat flow pattern and droplet dynamics. According to the authors, the size of the droplets and their relative velocity with the gas stream have a significant impact on the heat transfer coefficient at the droplet–gas interface. As a result, the microstructure evolution in the deposit will be governed by the droplet dynamics and thermal state during deposition. The authors looked at the solidification structure of spray deposits from the periphery to the core, using a spray atomization and deposition facility available at NPL in conical and flat disc shapes. The authors found that the the microstructure induced during spray deposition was a uniform fine grained, as can be seen from the Figure 2.9. The authors concluded by comparing and explaining the study of process parameters during atomization and deposition, as well as their effects on the scale of microstructure in atomized droplets and spray deposits, based on preliminary observations.
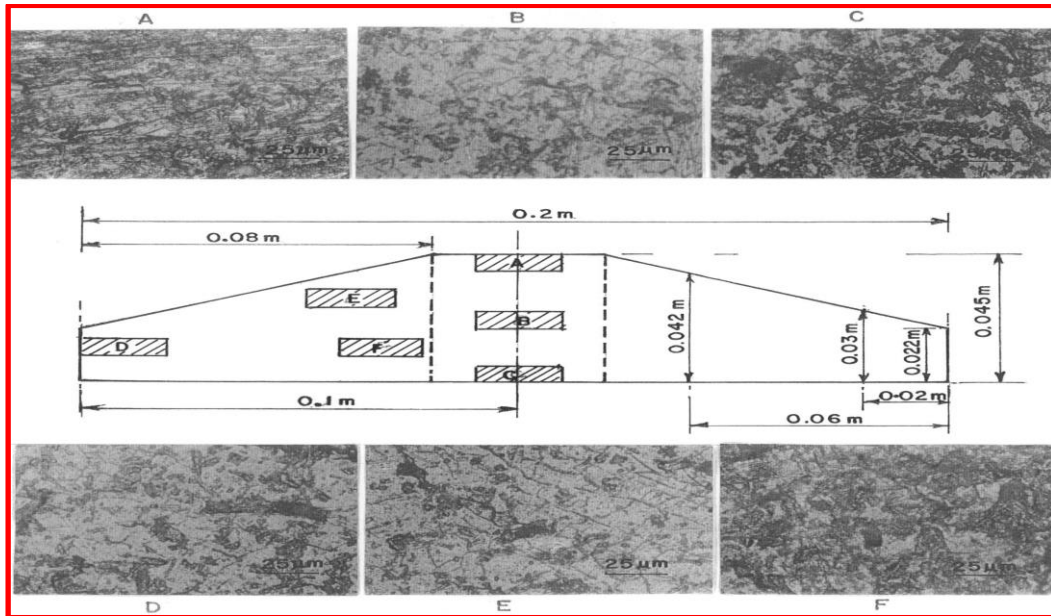
Figure 2.9: The evolution of microstructure in various regions of a spray-formed aluminium deposit. On micrographs and schematics, different regions are labelled A–F. (Srivastava et al., 2001)

The function of the tribo-layers that form on the contact surfaces during the sliding wear of graphitic cast aluminium matrix composites was investigated by (Riahi et al., 2001). The authors looked at three different wear regimes: ultra-mild, mild, and extreme wear. The tribo-layers were removed by extrusion process at the onset of severe wear as shown in Figure 2.10. Iron-rich layers made up the topmost portion of the tribo-layer. The remaining tribo-layer was made up of broken SiC and Al3Ni particles, as well as thin graphite films that were elongated over long distances in the sliding direction, minimising shear stresses transmitted to the subsurface. The authors observed that, the tribo-layers were eliminated in the extreme wear regime, and the stiffness of the worn surfaces was significantly reduced. Finally, the authors concluded that at load and sliding speed combinations, the graphitic composites showed a transformation from mild to extreme wear.

17

`
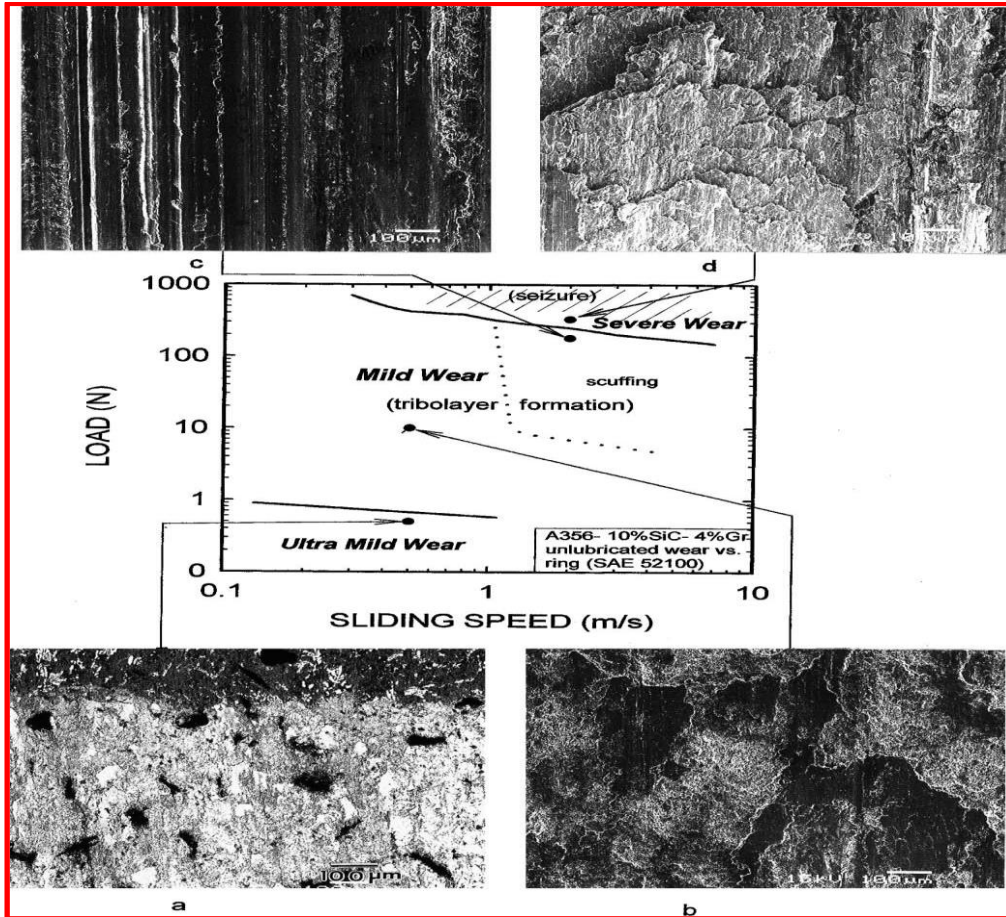
Figure 2.10: Surface morphologies of the A356 Al–10% SiC–4% Gr in three wear regimes marked on the wear map of the composite. (a) Ultra-mild wear regime (0.5 N, 0.5 m/s) back dispersed SEM micrograph. The unworn surface is visible in the upper portion. A continuous layer of iron oxide covers the worn surface (light coloured area). (b) Secondary electron SEM micrograph of the worn surface in the mild wear regime (10 N, 0.5 m/s) at low sliding speed and load. The tribo-layers are the darker areas of smooth surfaces. (c) Similar to (b), but with a higher load and faster sliding speed (150 N, 2 m/s). The tribo-layers fully cover the wear trail. (d) Secondary electron SEM micrograph of a highly worn surface in the extreme wear regime (300 N, 2 m/s) with no tribo-layer (Riahi et al., 2001)

The effect of the gas-to-meting metal (G/M ratio) in the spray forming process on the size of the primary Si phase in hypereutectic Al–Si alloy was investigated by (Baiqing et al., 2003). The authors contrasted the microstructure of different samples extruded at the same temperature but with different extrusion ratios, and they addressed the effects of the hot extrusion ratio on the refining of the primary Si phase distributed in the matrix of hypereutectic Al–Si alloys. The authors found that as the G/M ratio increased, the average

size of the primary Si process shrank. The authors demonstrated that a high extrusion ratio can refine the primary Si step while also allowing α-Al to re-fill microcracks during the extrusion process using various extrusion experiments, as can be seen in the Figure 2.11.
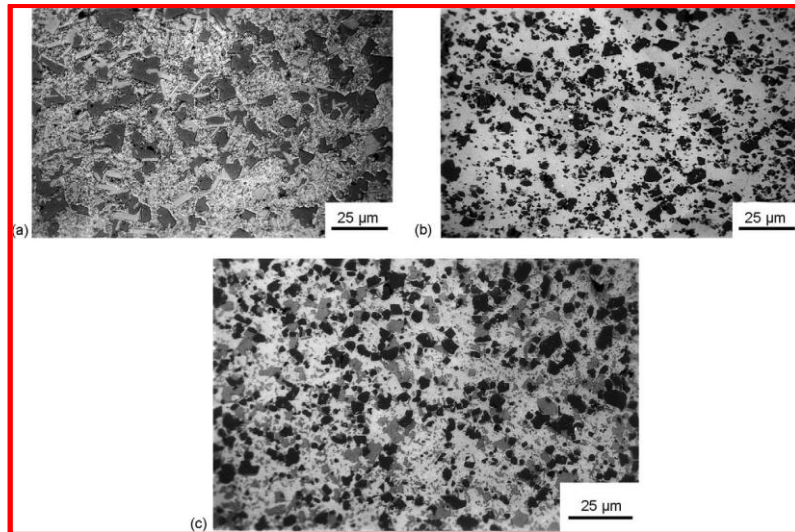
Figure 2.11 Micrographs of billets extruded at various extrusion ratios (Ø = 3.8 mm): (a) 10:1; (b) 14:1; (c) 28:1 (Baiqing et al., 2003)

Wang et al. (2004) produced a hypereutectic Al-20Si(wt%) alloy by combining two methods: spray deposition and traditional casting. In contrast to the traditional cast alloy, the spray-deposited alloy had better wear resistance across the entire range of applied load, according to the authors. The surfaces of the worn samples were studied under a scanning electron microscope (SEM) to investigate the wear mechanism. Figure 2.12 shows typical worn surfaces of the pins at a load of 35.6 N. From Figure 2.12 (a), the worn surface of the traditional cast alloy, several large dimples can be seen, indicating that block-like primary Si phases were fragmented and broken off during wear. Moreover, in the Figure 2.12 (b) only small dimples and grooves are visible. Figure 2.13 (a) depicts the wear debris of the conventional casting alloy, which is visually dark in colour and powder like in texture. Furthermore, the Figure 2.13 (b) shows the fine particles (average size = 10μm) obtained from the wear debris of spray deposited alloy. The authors concluded in the end that the oxidative mechanism was the dominant wear mechanism for the spray-deposited alloy, while delamination was the dominant wear mechanism for the cast alloy.
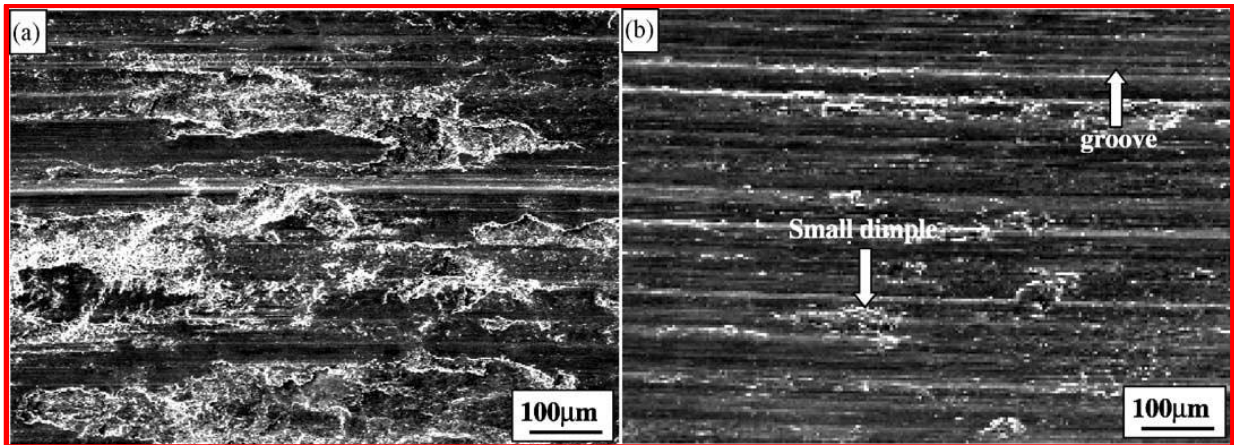
Figure 2.12. SEM morphologies of worn surfaces of as-cast and as-spray-deposited Al–20Si samples at the load of 35.6 N: (a) as-cast; (b) as-spray-deposited (Wang et al., 2004)
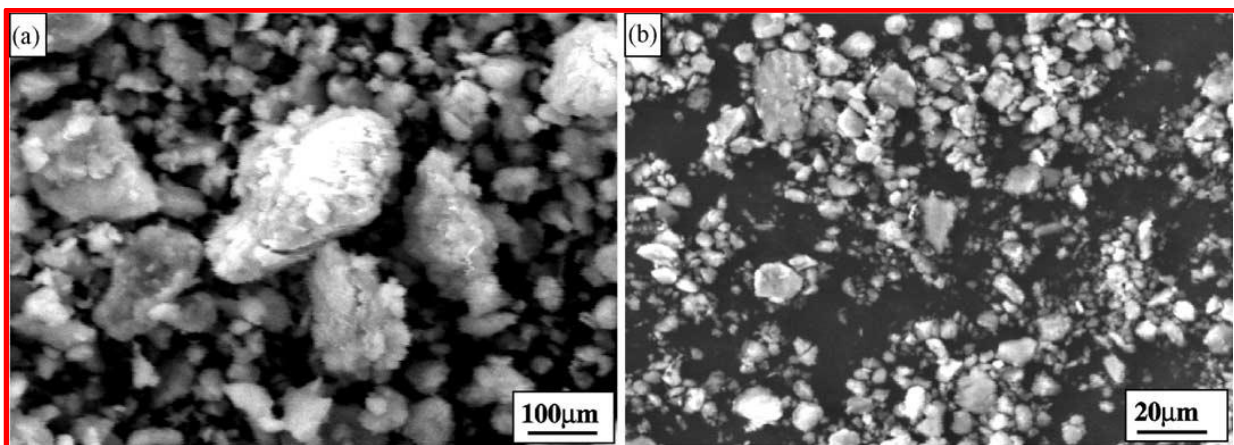
Figure 2.13 SEM micrographs showing wear debris generated at the load of 35.6 N: (a) as-cast; (b) as-spray-deposited Wang et al., 2004

Prasad et. al. (2004), investigated and presented a description of the tribological activity of Al MMCs reinforced with hard particles. Squeeze penetration of molten alloys into fibre, which can be used to manufacture near net-shape parts, is a common example of advanced manufacturing technology that the automotive industry is interested in. During a standard ball-on-disk friction test, aluminium is transferred to a steel ball is as shown in the Figure 2.14. Sliding will continue to move aluminium, and wear debris can form as a result of the asperities of the hard steel ploughing the soft aluminium surface, or patches from the transfer film flaking off. The hard-phase protrusions will fully shield the matrix from further abrasion within a certain critical volume fraction of the second phase—specifically, the interparticle spacing in relation to the size of the abrasive particles, as shown schematically in Figure 2.15. Typical microstructures of the pressure cast Al MMC reinforced with short carbon fibres and

`

SiC particulates are shown in Figure 2.16. Finally, the authors concluded that Al MMCs can withstand high mechanical and thermal loads while maintaining increased cylinder pressure, and thus minimise heat losses by forming a tighter fit, which is possible due to lower thermal coefficient of expansion of AL MMCs.
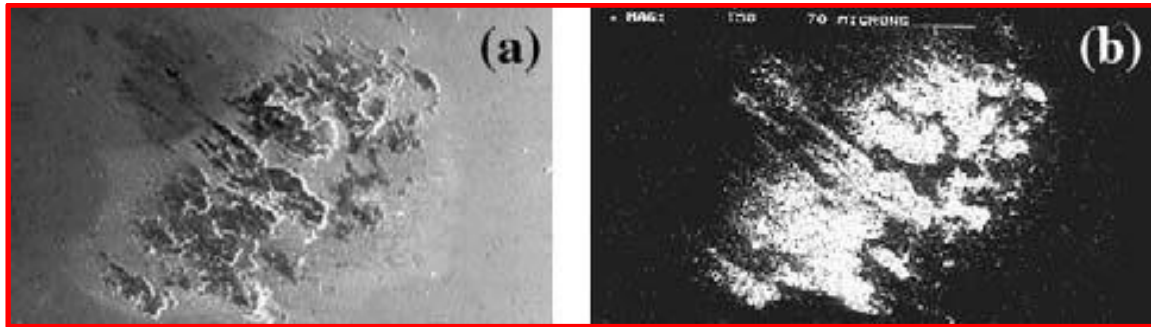
Figure 2.14: Smearing of Al on the steel ball during a ball-on-disk friction and wear test. (a) SEM image, and (b) Al X-ray map Prasad et al., 2004
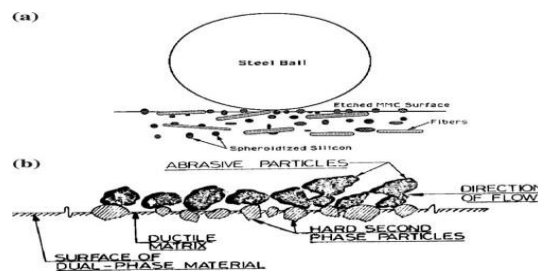
Figure 2.15: Schematic illustration of (a) a steel ball sliding on an etched surface of an Al–Si alloy fibre composite (Prasad et al., 2004)
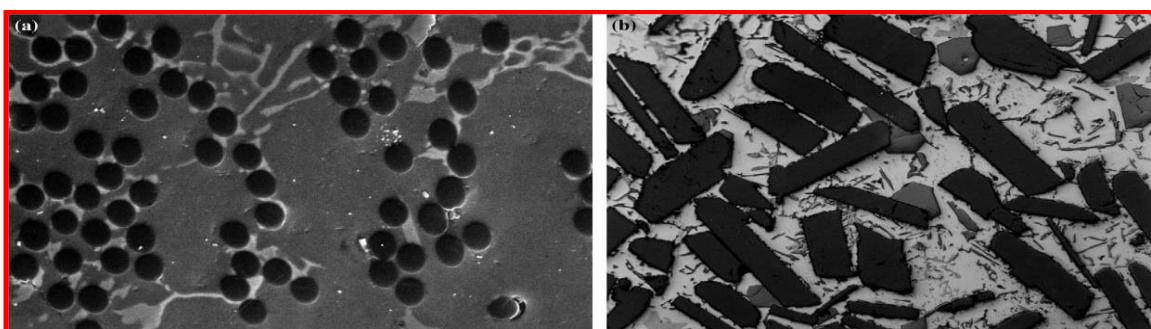
Figure 2.16: Microstructures of pressure-cast Al MMCs reinforced with (a) short carbon fibers (·1000), and (b) SiC particulates (·400) Prasad et al., 2004

The effect of Al grain size and -Al dendritic arm spacing (DAS) in Al–7Si alloy on wear behaviour of Al and Al–7Si alloy was investigated by (Rao et al., 2004). At a load of 50 N, a sliding distance of 1800 m, and a sliding velocity of 1 m/s under dry

sliding conditions, the wear rate decreases as the grain size and DAS of Al and Al–7Si alloys decrease, respectively. Figure 2.17(a) and (b) shows the microstructure of the Al–7Si alloy without grain refiner addition and with 1.0 wt. percent Al–1Ti–3B addition at a 120-minute holding period, respectively. It is evident from Figure 2.17(b) that the addition of grain refiner not only reduces DAS but also reduces the size of eutectic Si particles, despite no major changes in morphology. The authors concluded that the wear properties are determined by the grain size/DAS of the metal/alloy and the existence of a second step (eutectic Si in Al–Si alloy) rather than the type of grain refiner used.
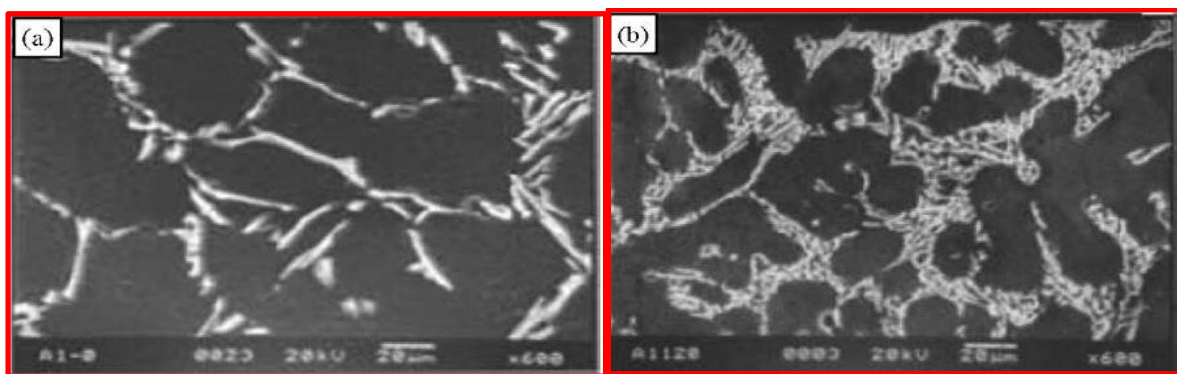
Figure 2.17: Photomicrographs of Al–7Si alloy (a) without addition of grain refiner and (b) with addition of 1.0 wt.% M13 grain refiner (120 min holding time) (Rao et al., 2004)

The effect of copper on the wear-friction behaviour of a hypereutectic Al–Si alloy (Al–18% Si–0.5% Mg) was investigated by (Dwivedi et al., 2004). The wear rate of sliding metal is a function of contact load, sliding speed, composition, and thermal softening characteristics, according to the authors. The wear properties of aluminium alloys against a hardened ground steel (En-31) disc with a hardness of RC60 and a surface roughness (Ra) of 0.5m was evaluated using a pin on disc form wear monitor (DUCOM, TL-20, Bangalore) with data acquisition system as observed in the Figure 2.18(a). SEM image of oblique section of Aluminium–18% Silicon–0.5% alloy (Figure 2.18(b)) shows the extent of the subsurface damage caused by the sliding process. The authors came to the conclusion that each alloy has a critical sliding speed (at a given load) at which transition from mild to extreme wear happens. The addition of copper to a hypereutectic alloy has no effect on the critical speed.
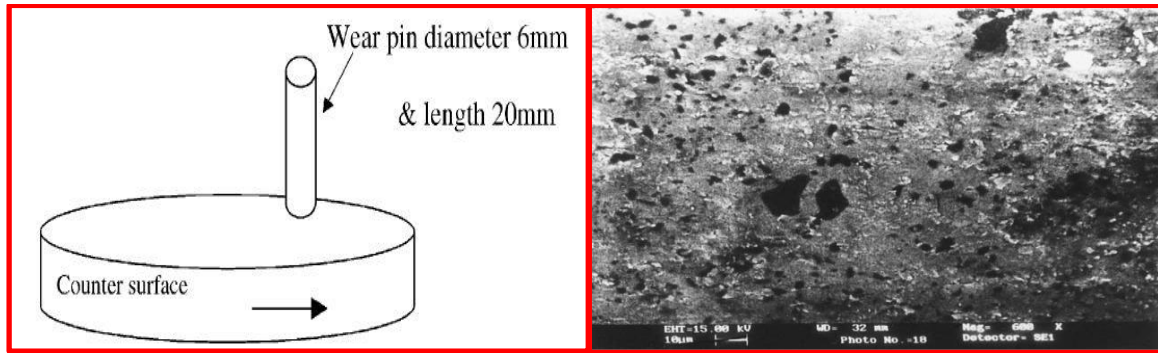
Figure 2.18: (a) Principle diagram of pin on disc wear and friction monitor. (b) SEM images of subsurface region of alloy with 2% copper after sliding at 50N load and 2.0 m/s sliding speed (Dwivedi et al., 2004

Yasmin et al. (2004), investigated wear properties of both the heat-treated and as-cast aluminium-silicon alloy. A weight loss technique was used to estimate the degree of wear injury. Pin-on-disk testing machines (Figure 2.19(a)) are commonly used to investigate wear properties and identify material rank. Figure 2.19(b) shows the microstructure of an aluminium-silicon eutectic alloy in its as-cast state. The matrix structure is made up of alpha aluminium dendrites, acicular eutectic silicon, and a few plates formed primary silicon crystals, as well as some intermetallic compounds. The authors concluded that both as-cast and heat-treated specimens showed an increase in wear as speed, input load, and sliding distance increased.
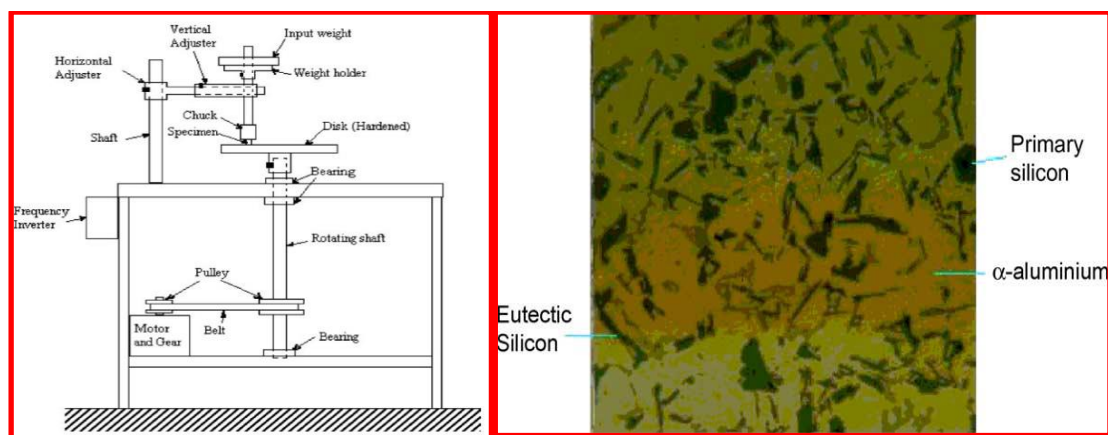
Figure 2.19 (a) Pin-on-disk type wear testing machine, (b) Microstructure of Al–Si eutectic base alloy (Yasmin et al., 2004)

Venclet et al. (2004), studied the tribological properties of Al-based metal matrix composites with respect to percentage of reinforcement material and dimension, variation of shape and manufacturing technologies. The most frequently used method of casting in the automotive

industry is the squeeze casting method. The schematic of the squeeze casting can be seen in the Figure 2.20(a). The schematic of the vortex method in stir casting is as seen in the Figure 2.20(b), which has many advantages such as enabling production of low-price casts, composites of complex configuration and thin walls. The authors finally concluded that the automotive sector has a huge scope in using the Al MMCs.
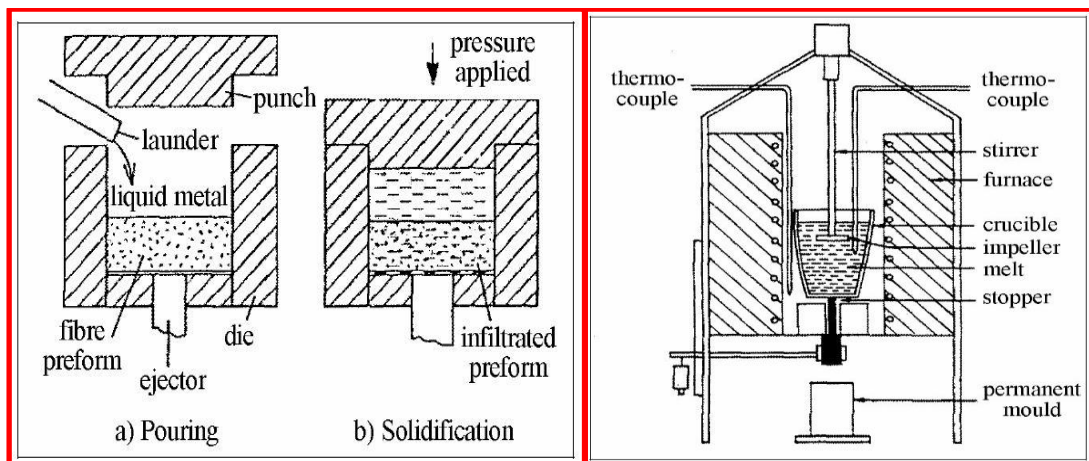
Figure 2.20: Scheme of the squeeze casting method (b) Scheme of vortex method (Venclet et al., 2004)

Rao et al. (2005), investigated mechanical and wear properties on Al–7Si alloy after various melt treatments like grain refinement and/or modification. The authors found that the combined modification and grain refinement improves the alloy's tensile strength and wear resistance, as well as its load bearing capability during dry sliding wear. Figure 2.21(a) and (b) show microstructure of as cast Al–7Si alloy without modification and grain refinement. These results indicate the presence of needle/plate like dendrites and eutectic Si proeutecticα-Al (secondary dendritic arm spacing (SDAS) = 60μm). Figure 2.22(a) and (b) show the combined effect of modification (by 0.02% Sr) and grain refinement (by 1% Al–1Ti-3B master alloy). The microstructure displays fine -Al dendrites (SDAS = 22m) and fine fibrous eutectic Si particles after 5 minutes of holding after adding the grain refiner and modifier.
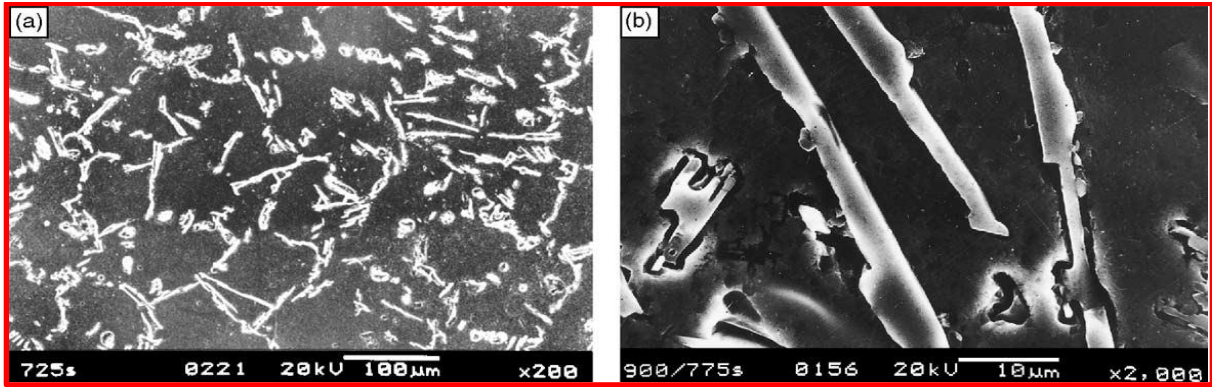
Figure 2.21: SEM photomicrographs of Al–7Si alloy without grain refinement/modification at (a) low magnification and (b) at high magnification (Rao et al., 2005)
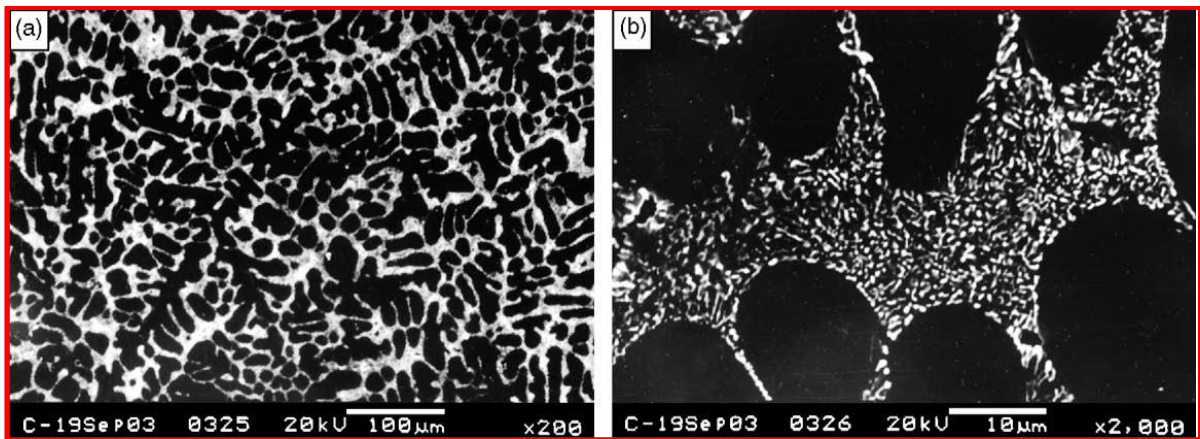
Figure 2.22: SEM photomicrographs of Al–7Si alloy grain refined and modified with 1% Al–1Ti-3B and 0.02% Sr at (a) low magnification and (b) at high magnification (Rao et al., 2005)

Dwivediet et al. (2006), reported the effect of alloying elements on the wear behaviour of cast hypereutectic aluminium alloys, both binary (Al–17 percent Si) and multi-component (Al–17Si–0.8Ni–0.6Mg–1.2Cu–0.6Fe). The wear behaviour of Al–17Si and Al–17Si–X alloys (X = Ni, Cu, Mg, Fe) was investigated using an ASTM G99 pin on disc friction and wear testing unit. The authors found that adding an alloying factor to a mild oxidative wear condition not only reduces the wear rate but also increases the transition load. The temperature of the wear pin near the sliding surface was measured and linked to the wear and friction behaviour of the experimental alloys. Scanning electron microscopy (Figure 2.23(a) and (b)) of wear surface of binary and multi-component alloys after sliding at constant normal 10 N shows oxidised surface, delamination, and scoring as key mechanisms responsible for material loss,

`

indicating the occurrence of mild oxidative wear, while in extreme wear area gross plastic deformation and surface damages can be seen on wear surface after sliding binary alloys at 30 N load and multi-component alloy at 40 N load, indicating the occurrence of severe oxidative wear (Figure 2.23(c), (d)). Alloying has resulted in an increase in hardness. The authors used SEM to analyse and infer the mode of wear and wear process from wear surface and wear debris.
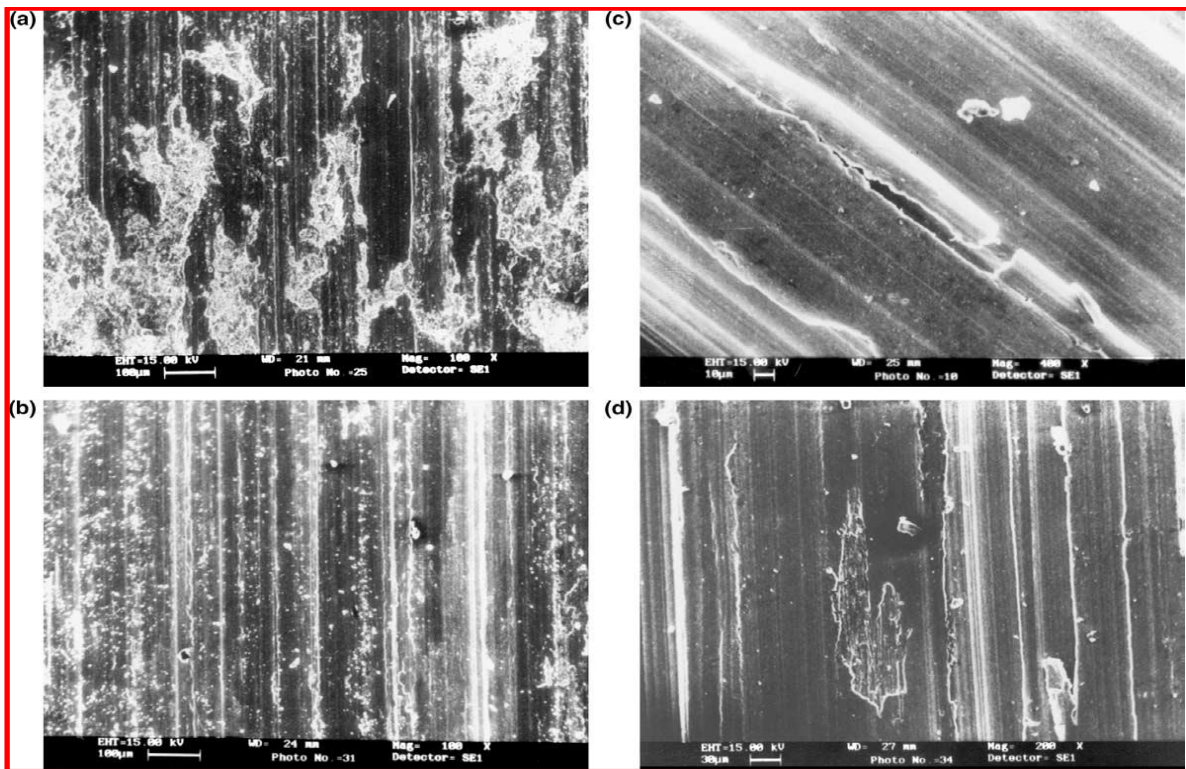
Figure 2.23: SEM images of worn out surface of alloy in (a) binary alloy (b) multi-component alloy at after sliding at 0.2 m/s speed and 30 N load and after sliding at 4.0 m/s speed of (c) binary alloy at 30 N load (d) multi-component alloys at 40 N load (Dwivediet et al., 2006)

Yang et al. (2008), aimed at improving the capability of the precision spray forming (PSF) rapid tooling process so that it can be extended to various applications. The authors were able to improve the insert size so that the diameter of the insert has been increased from around 200mm to 400mm, making the process more effective for making complex structures. The authors discovered that the twin atomiser system is more effective than the single atomiser system in spray forming small inserts with a diameter of about 200mm and a high level of complexity, as can be observed from the Figure 2.24. The impact of deposition temperature and substrate movement speed on the process, as well as technical methods to eliminate surface flaws while spray forming big inserts, were discussed by the authors. In their

research, they present a new method for spray shaping cooling channels into die inserts or other high-temperature components. The authors summarized that the improved cooling can not only extend the tool's life, but it may also boost efficiency by reducing part cycle time.
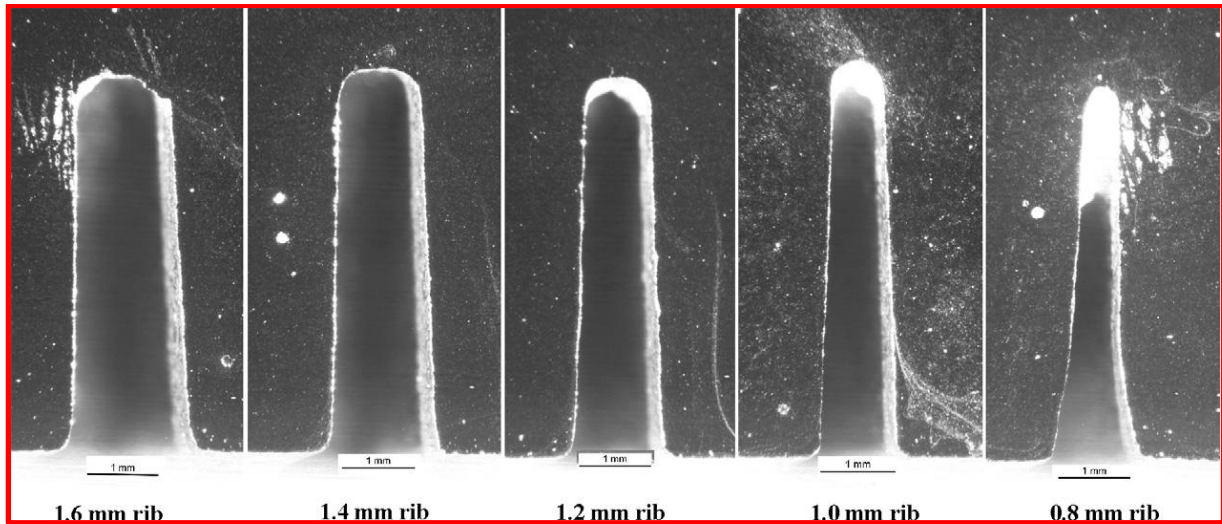
Figure 2.24: Stereomicroscope images of the polished rib sections, 10× (Yang et al., 2008)

Jung et al. (2009), investigated the control of the transition from the columnar to equiaxed growth upon the addition of the refiners in Al-based alloys. The authors found that the equiaxed grains nucleate preferentially on the refiners and can compete with columnar grains. Due to the Si poisoning effect, the measurements had the lowest efficiency of the same particles in the refined Al-7.0wt% Si. The differential scanning calorimetry technique resulted in comparing the refined alloy with the non-refined alloy as shown in the Figure 2.25. The authors concluded in the end, that for the quantitative prediction of equiaxed growth by the models, the nucleation undercooling measured can be used
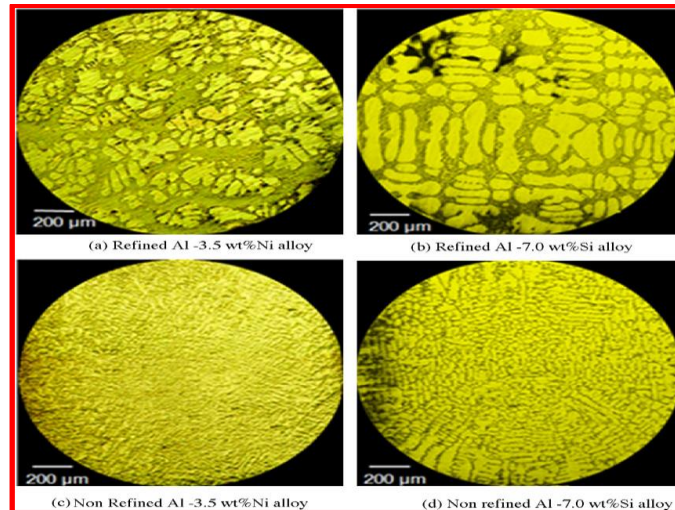
Figure 2.25: Microstructures obtained by classical metallography of the samples elaborated during the DSC experiments in Al-based alloys. (a) Refined Al–3.5 wt% Ni alloy. (b)Refined Al–7.0 wt% Si alloy. (c) Non-refined Al–3.5 wt% Ni alloy. (d) Non-refined Al–7.0 wt% Si alloy (Jung et al., 2009)

Feng et al. (2011), synthesized the Al-20Si-5Fe-3Mn-3Cu-1Mg alloy by the spray deposition and atomization methods. The authors investigated the mechanical and microstructural properties using scanning electron microscopy, tensile tests, x-ray diffraction and transmission electron microscopy (TEM). The SEM micrograph of the spray deposited Al-20Si-5Fe-3Mn-3Cu-1Mg alloy is shown in the Figure 2.26, which is composed of the Al matrix. The Si phase, which consists primarily of spherical particles, as well as some fine intermetallic phases. The intermetallic phases range in size from 1-3 μm. In the microstructure, the particle-like intermetallic phase is distributed at random. Finally, the authors concluded that after the aging treatment at 135 ^{0}C, two types of precipitates are formed (S-Al$_2$CuMg and r-Al$_5$Cu$_6$Mg$_2$) to improve the tensile strength of the devloped composite for both at the ambient temperature and higher tempetatures (above 300 ^{0}C).
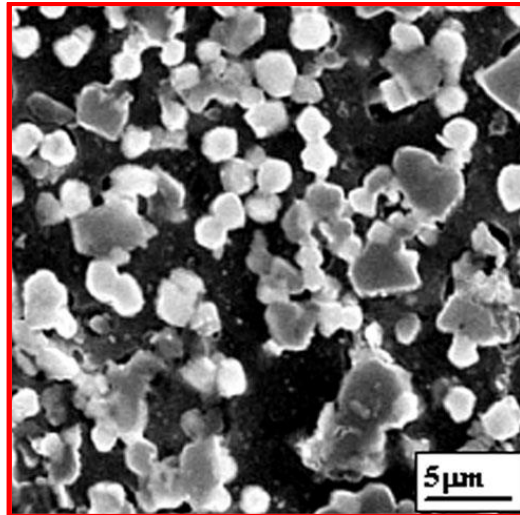
Figure 2.26: SEM micrograph of the spray-deposited Al-20Si-5Fe-3Mn-3Cu-1Mg alloy (Feng et al., 2011)

Rashmimittal et al. (2012), investigated the wear behavior of Al-12Si-Sn/ZrSiO$_4$ composite and Al-12Si alloy. The test specimens were prepared using spray deposition technique. The experiments were conducted at dry sliding conditions with different temperatures and loads. The authors found that the wear rate of spray deposit composite was very much lesser than that of as cast Al-12Si alloy. The wear rate increased rapidly with the increase in sliding distance, and then started to decrease gradually. However, beyond 300 m sliding distance, the wear rate becomes constant. The Figure 2.27 depicts the SEM micrographs of the worn surfaces of as cast alloy A at 80 ^{0}C for 4kg of wear load. As compared to larger particles in the same matrix, smaller ZrSiO$_4$ particles were able to reduce the wear rate to a greater degree. The authors concluded in the end, that with the increase in the amount of Sn, the wear rate decreases.
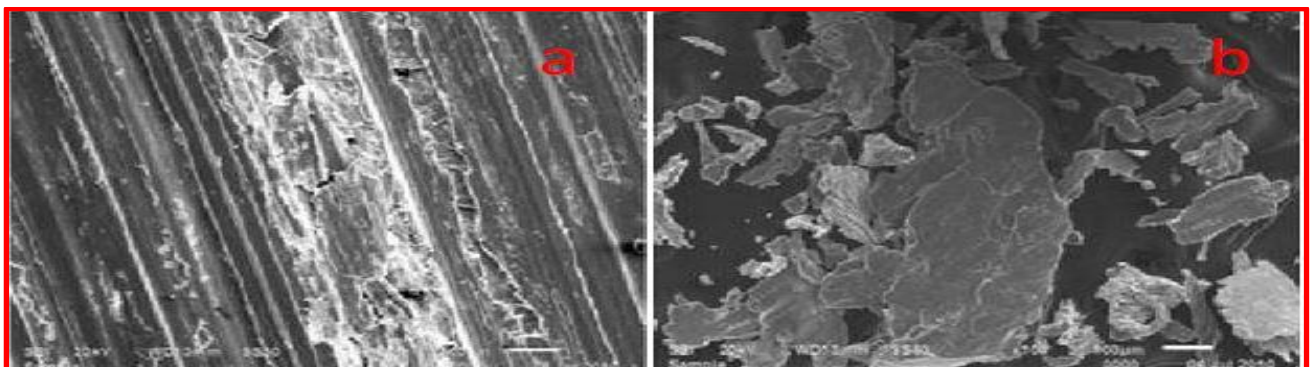
Figure 2.27(a): SEM micrograph of worn surface of as cast alloy A at 80 ^{0}C for 4 kg wear load and (b) debris of as cast alloy A at 80 ^{0}C for 4 kg wear load (Rashmimittal et al. (2012)

Bao et al. (2013), investigated the thermal-spray enamelling of aluminium, and found that it can be successfuly acheived by introducing a pre-heat step prior to spraying, so that the enamel will flow for a long time, allowing the residual stress to be relieved. It was observed that the magnesium segregated to the substrate–enamel interface in the Al–Mg alloy substrate under examination, affecting adhesion. As a result, the authors concluded that the preheating temperature should be optimised to provide adherence while avoiding unnecessary substrate softening and magnesium segregation. The Al–Mg alloy under investigation in this study is strong due to two main mechanisms: first, solid-solution strengthening, which occurs when room-temperature aluminium dissolves 1.8 wt% magnesium under equilibrium conditions, as shown in the phase diagram of Al–Mg in the Figure 2.28. Second, under equilibrium conditions, precipitation hardening as the intermetallic phase Al3Mg$_2$ forms below 230 °C (with its morphology depending upon the processing conditions). The authors summarized in the end that optimally flame-sprayed enamel increased the wear resistance of the Al–Mg alloy by a factor of ten, and discussed the thermal-spray enamelling of generic aluminium alloys.
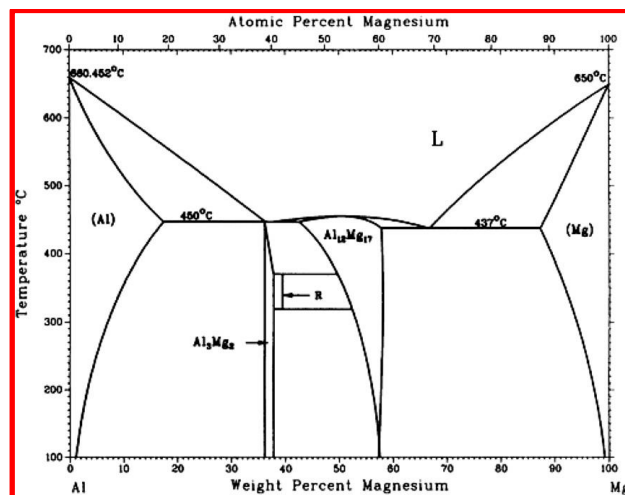
Figure 2.28: The aluminium–magnesium phase diagram (Bao et al., 2013)

The effect of copper (Cu) and iron (Fe) on the wear behaviour of spray-formed Al–28Si alloys was investigated by Goudar et al. (2013a). The authors found that the spray deposition is the most useful method in refining the microstructures of Al–28Si–5Cu–4Fe and Al–28Si alloys. Al–28Si–5Cu–4Fe alloy consisted of uniform and fine distribution of β-Al4FeSi2 and θ-Al2Cu phases along with primary silicon particles in aluminium matrix. It was found that the the porosity can be reduced by 50% in Al–28Si and 73% in Al–28Si–5Cu-4Fe alloys

`

using hot pressing technique. The worn surfaces of Al–28Si–5Cu–4Fe and Al–28Si alloys at an applied nominal load of 70 N are shown in the Figure 2.29. The authors found that the hot pressed and spray deposition Al–28Si–5Cu–4Fe alloy exhibhited a higher hardness value of 160 VHN, when compared to as-cast and spray formed alloys. The wear resistance of Al–28Si alloy can be improved the addition of Fe and Cu composition. The authors concluded that the coefficient of friction is lowest and the wear resistance is highest and for hot pressed and spray formed Al–28Si–5Cu– 4Fe alloy compared to as-cast as-spray formed alloys.
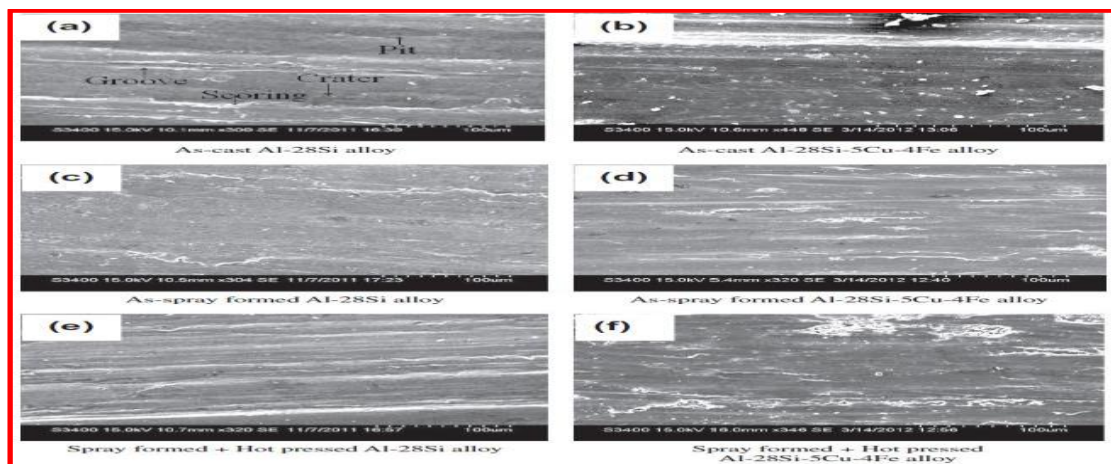
Figure 2.29: Worn surfaces of Al–28Si and Al–28Si–5Cu–4Fe alloys at a load of 70 N. (Goudar et al., 2013a)

Goudar et al. (2013b), evaluated individually the hardness, microstructure and wear properties of secondary processed and spray formed alloys. In comparison to as-cast alloy, spray shaped Al–30Mg2Si–2Cu alloy showed a refined and uniform distribution of primary Mg2Si phase, modified eutectic, and Al2Cu, Q-phases. Alloy surfaces that have been worn out is as shown in the Figures 2.30. The microstructural changes, especially the refinement, fragmentation, and redistribution of primary phase, resulted in improved wear resistance in the spray shaped Al–30Mg2Si–2Cu alloy compared to the as-cast alloy. The abrasive wear mechanism dominates in spray formed and secondary processed alloys, while delamination dominates in as-cast alloys. The authors finally concluded that The spray moulded and hot pressed Al–30Mg2Si–2Cu alloy exhibited high wear resistance after ageing, with a wear rate roughly one-third that of the as-cast alloy.
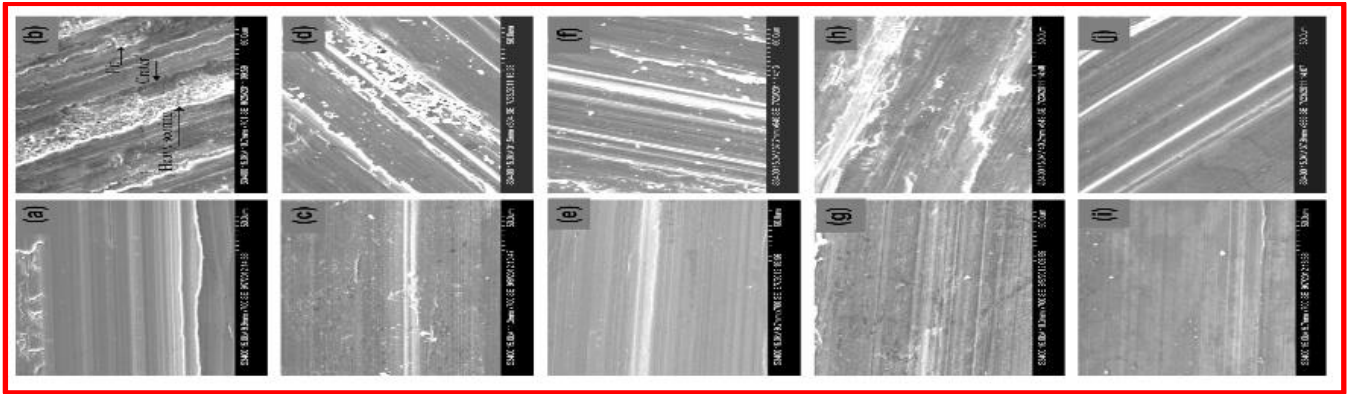
Figure 2.30: Worn surface of Al-30Mg₂Si-2Cu (Goudar et al., 2013b)

Goudar et al. (2015) investigated applied load as a function of sliding speed, the effect of Sn on the dry sliding wear behaviour of spray shaped and hot pressed Al–17Si alloy was investigated and compared to that of as-cast alloy. Spray developed Al–17Si alloys have fine and uniformly distributed Si particles, while Al–17Si–10Sn alloys have fine and uniform dispersion of Si particles as well as ultra-fine Sn particles in an a-Al matrix. Segregated and coarse microstructurial images were observed in as-cast alloys. The worn out surfaces of the various alloys ar shown in the Figure 2.31. The wear resistance of spray formed alloys is higher than that of as-cast alloys. As-cast Al–17Si–10Sn alloy has a higher wear resistance than as-cast Al–17Si alloy.
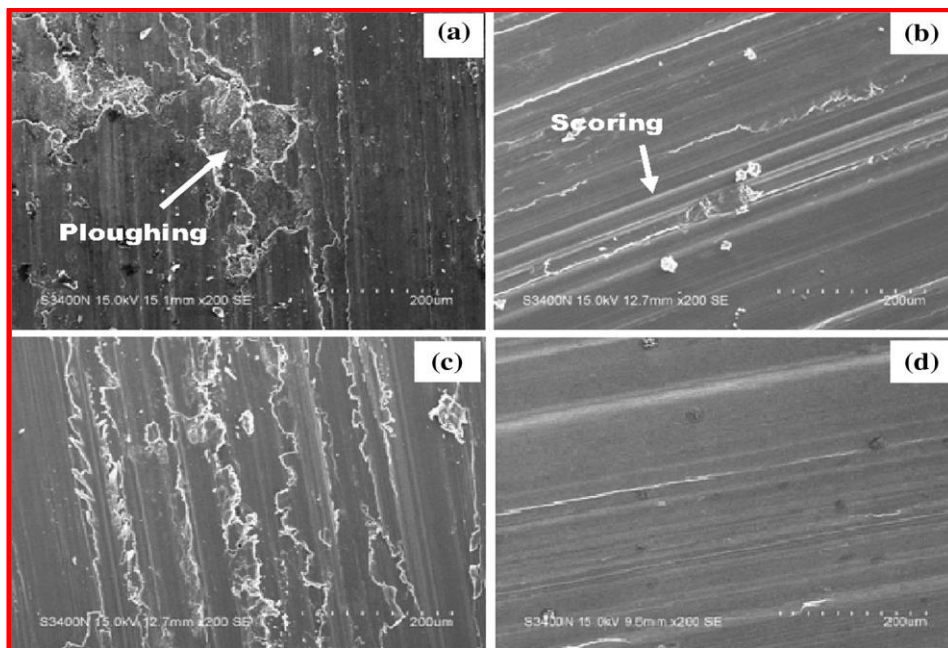
Figure 2.31: Worn-out surfaces of (a) as-cast Al–17Si alloy (b) spray formed Al–17Si alloy (c) as-cast Al–17Si–10Sn alloy (d) spray formed Al–17Si–10Sn alloy (Goudar et al., 2015)

32

`

Muthaiah et al. (2016), investigated the solid solubility extension of zirconium in aluminium silicon matrix and to study its thermal stability. Miedema's semi-empirical model is used to verify the formation of disordered solid solutions. X-ray diffraction investigation confirms the formation of disordered solid solution up to 1% zirconium, while Al3Zr and Al9.83Zr0.17 intermetallic phases shape according to the XRD pattern of 2-10% zirconium composites. The thermal stability of Al-Zr solid solutions with intermetallic compounds was excellent, particularly for the 10% Zr alloy. TEM analysis of Al-10%Zr sample annealed at 550 ^{0}C can be observed in the Figure 2.32. The aluminium-zirconium solid solution contained up to 1% zirconium, and the excess of zirconium resulted in the formation of intermetallic compounds such as L12-Al3Zr, which were critical in the stabilisation of the nanocrystalline grains. The authors came to the conclusion that the kinetic process, namely Zener pinning (Muthaiah et al., 2016) by second phase particles(e.g., L12-Al3Zr), was responsible for the high thermal stability.
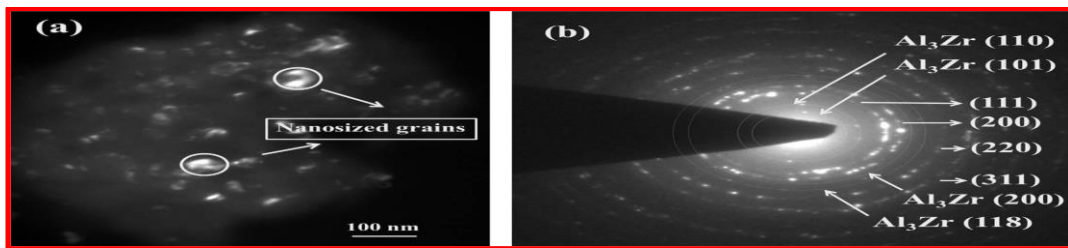
Figure 2.32: TEM analysis of Al-10%Zr sample annealed at 550 ^{0}C: (a) Dark field image (b) SAED pattern (Muthaiah et al., 2016)

Liu et al. (2016), fabricated large-scale spray deposited Al-Zn-Mg-Cu-Zr alloy rods. They were were found to have equiaxed grains, and the grain size in the spray-deposited ingot was smaller than the commercial product. High strength-to-elongation ratio (11.9 GPa·%.) was obtained. Spray deposition, hot extrusion, and solvent treatment were used to create the alloy. As a result, there was a strong combination of strength and elongation (Ultimate tensile strength: 684 MPa; Elongation: 17.4%). Hot extrusion improved the mechanical properties, while T6 treatment improved the tensile strength but decreased the elongation. The fracture of spray deposited Al-Zn-Mg-Cu-Zr alloys is shown in the Figure 2.33. The authors concluded that the transgranular and intergranular fracture are the main mechanisms in T6 treatment samples and extrusion state. Due to their reduced ductility, the brittle secondary-phase particles cracked during the tension test process.
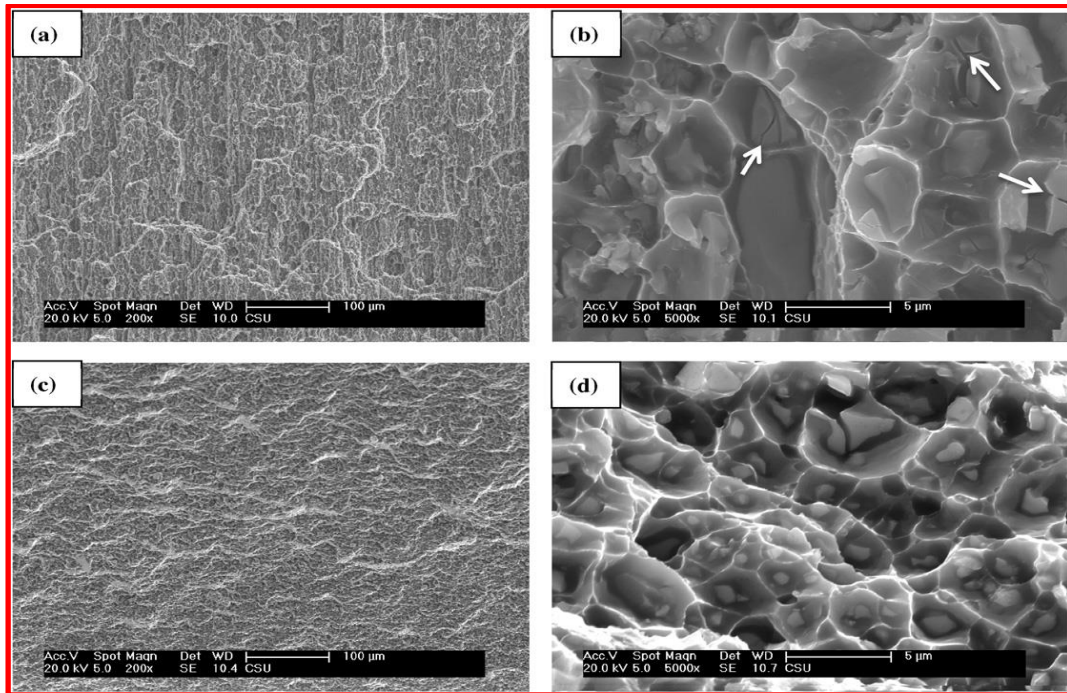
Figure 2.33: Fracture of spray deposited Al-Zn-Mg-Cu-Zr alloys (a) and (b): hot extrusion state; (c) and (d): extrusion and T6 treatment state. (b) and (d): the high magnification images of the same sample of (a) and (c), respectively (Liu et al., 2016)

Investigating the wear properties of the composites is a very difficult phenomena because it dependents on many factors such as reinforcement (nature, size, weight fraction and shape) (Rao et al., 2010), applied load (Umasankar et al., 2014), sliding distance (Rao et al., 2011a) and sliding speed (Rao et al., 2011b). Rovira et al. (1999) studied behaviour of both thixo-forging and thixo-extrusion using the aluminium– 4.5copper alloys. The author's reported that the evolution of a fine globular morphology of microstructure was observed in both the tests. In the line of works on using reinforced material, Kaushik et al. (2016) investigated wear behaviour of Al6082-SiC-Gr composites using stir casting method. The results were compared with Al 6082–SiC composites and Al6082 alloy. The study found that wear of Al–SiC–Gr composites surpassed all other developed metal matrix composites. Kiuchi and Sugiyana, 1991 & Herbert et al. (2006) investigated mushy state rolling of Al alloys and cast iron. Moreover, there exists little information about the properties of wear in aluminium alloys and the corresponding composites were subjected to mushy state rolling. The author's reported the refinement in the grain structure and enhancement in bulk hardness in case of the mushy state rolled Al–4.5Cu alloy and its composite with 5 wt.% TiB_2 particles (Herbert et al., 2006; 2007a; 2007b; 2008). Marigoudar et al. (2011) used Al-Zin alloy reinforced with SiC to investigate the wear behaviour. The study found that using SiC particles will enhance

`

the material wear property. Additionally, the wear of the metal matrix composite decresed with increase in SiC composition. The behaviour of deformation in plastic at mushy state rolling is different from that involving dislocation movement in cold or hot working. Therefore, relative sliding and rotation across the grains is possible in the former. Therefore, by reducing the concentration of micro particles and increasing the nanoparticles in synergistic arrangement will improve the wear properties. Sahin, (2003) investigated the wear rate by increasing sliding distance, abrasive size and applied load for SiC paper. They reported that the wear rate is proportional to abrasive particle size and applied load and inversely proportional to the fight distance for Al_2O_3 paper. It was note that the effect of interaction between the variables exhibited a mixed behaviour towards the wear properties. Wear rate in peak aged as well as in overaged composites drastically decreased in comparison with the respective as-cast composites by (Grigoris et al., 2002). The artificial neural networks is non-linear statistical analysis technique used for intelligent product design which are hard to be described by physical models (Ray et al., 2020). The selection proper neural network is one main aspects in ANN modelling (Altinkok et al., 2004; Karimzadeh et al., 2006; Lisboa et al., 2006; Singh et al., 2010; Hassan et al., 2009; Shabani et al., 2011b). Akbari et al., (2017a) investigated the wear properties of aluminium-silicon alloy using different types of reinforcement materials namely B_4C, TiC, SiC and ZrO_2 using friction stir processing method. The pin-on-disk results revealed that, at higher sliding velocity and applied load, the wear loss weight of the developed composite increased gradually.

The effect of flight distance, gas velocity, droplet size, melt flow rate and super heat, and compositions are studied on cooling and solidification of spray overlay (Grant, 1993). However, the developed model limit to predict the surface temperature and solid fractions, but they have neglected the factors influence and determining optimal values on mechanical and wear properties. Particle swarm optimization has been applied to optimize the wear rate of aluminium matrix composites subjected to melt superheat, nozzle distance, metal gas flowrate, droplet-gas interface and heat removal rate (Shabani et al., 2013). However, their work does not explain the factors (individual and interaction) effect on wear rate. Artificial neural networks are applied to predict the grain diameter of metal droplets of aluminium alloy with different sets of gas pressure and melt temperature (Liu et al., 2020). The major weakness of above research work is that they have neglected the other important parameters namely melt super heat and nozzle distance influence on mechanical properties. The mathematical simulation model (differential equations) and fractional design of experiments

`

are applied to determine the optimal ranges of parameters namely, gas velocities, flight distance, melt flow rate and melt temperature for high-density deposits of copper-zinc based metals (Pariona et al., 2020). Akbari et al., (2017b) optimized microstructural and mechanical properties of aluminium composites using the neural network and NSGA-II. These materials consolidated with various reinforcing particles namely B4C, TiC, ZrO_2 and SiC. To acquire the optimized mechanical and microstructural properties of these materials, different consolidating particles, traverse and rotational speed are selected as ANN inputs in the developed ANN model. The ANN approach is prone to local convergence, but the genetic algorithm (GA) provides global searching capability by concluding the ANN's first weight and bias (Murthy et al., 2018).

2.5 Research gap

It is clearly shown from the literature survey that spray deposition process is effective in controlling the physical, mechanical and wear properties of alloys in comparison to conventional metal casting technique. As evident from the literature review, considerable attention is being drawn to the study of the microstructural evolution and the structure property correlation of the Al Si13alloys mainly for the automotive applications. There exists knowledge about influence of alloying on the microstructure, mechanical and wear properties of spray deposited materials. Although there are large number of investigations on Al alloys, the systematic and detailed research reports on microstructural control and the effect of processing route on the properties of Al alloys for automotive applications remain to be understood clearly.

It is noted that from the research survey that no significant research is carried out on an aluminium- silicon alloy and zirconium oxide as a reinforcing material. So, the future work is to be carried out on Al-Si12.5ZrO_2 evaluating the microstructural, mechanical and wear properties. In the next chapter, the manufacturing of Al-Si+ZrO_2 using spray and stir casting methods is discussed.

`

2.6 Objectives

The main aim of the present research is to explore the use of zirconium oxide as reinforcement particles in aluminum silicon matrix. The following objectives have been identified for the present research work:

1. To prepare AlSi12.5ZrO$_2$ metal matrix composite by stir casting as well as spray deposition process, followed by hot pressing.
2. To carry out comparative study on the mechanical properties of AlSi12.5 ZrO$_2$ composite, formed by stir cast and spray deposition.
3. To assess the wear behavior of spray formed AlSi12.5 ZrO$_2$ composite, in comparison to that of stir cast AlSi12.5ZrO$_2$ composite
4. To investigate the effect of flight distance of spray deposition process on fabrication of AlSi12.5ZrO$_2$ composite. .
5. To develop an intelligent prediction model for spray deposit process based on above studies.

`

CHAPTER 3

EXPERIMENTAL METHODOLOGY

This chapter presents details about the experimental procedure and the experimental setup for preparing Al+12.5Si+ZrO$_2$ composite. Information about different equipment or instruments used for measuring the performance characteristics, selection of process parameters is also presented here.

3.1 Selection of work material

The commercially available 99.9 % pure aluminium and silicon 12.5 wt. % alloy was used as the matrix material. Zirconium oxide powder was used as the reinforcement. The composites were produced using spray deposition techniques (Goudar et al., 2013). The microstructures were examined for all the specimens under optical microscope and Scanning electron microscope (S–3400 N Hitachi Model), (SEM) equipped with energy dispersive X-ray analysis (EDX). It is worthy to note that the Al-12.5% Si binary alloys are in the eutectic range. The nominal composition of the matrix and filler material are tabulated in Table 3.1 and chemical composition of the ZrO$_2$ reinforced powder is shown in Table 3.2. Further, the substrate plate was cleaned with acetone and subsequently emery paper was used to remove the surface oxide layer before executing the spray deposition.

Table 3.1: Chemical comosition of Al-Si alloy Metal matrix (wt%)

Alloy	Si	Fe	Mn	Mg	Zn	Pb	Al	Others
Value	12.50	0.18	0.005	0.006	0.017	0.004	87.288	0.088

Table 3.2:Chemical composition of ZrO$_2$ reinforced powder (wt %)

Constiuent	ZrO$_2$	SiO$_2$	TiO$_2$	Fe$_2$O$_3$	Others
(wt%)	99.5	0.10	0.008	0.002	0.39

Al-12.5% Si alloy is used as matrix material due to their industrial relevance applications (Zalensas 1993; Hernandez et al., 2017b). ZrO$_2$ as reinforcement material possesses excellent hardness and wear resistance properties that might be well suited for load bearing applications (Anil et al., 2010). Stir casting composites are prepared by reinforcing ZrO$_2$ to

Al-12.5%Si alloy. The average particle size of ZrO_2 was found to be equal to 50 ± 5 µm. Energy dispersive x-ray spectra (SEM: TESCAN Vega 3 LMU) analysis confirms the presence of ZrO_2 reinforcement, Al and Si on the composite samples (refer Figure 3.1).
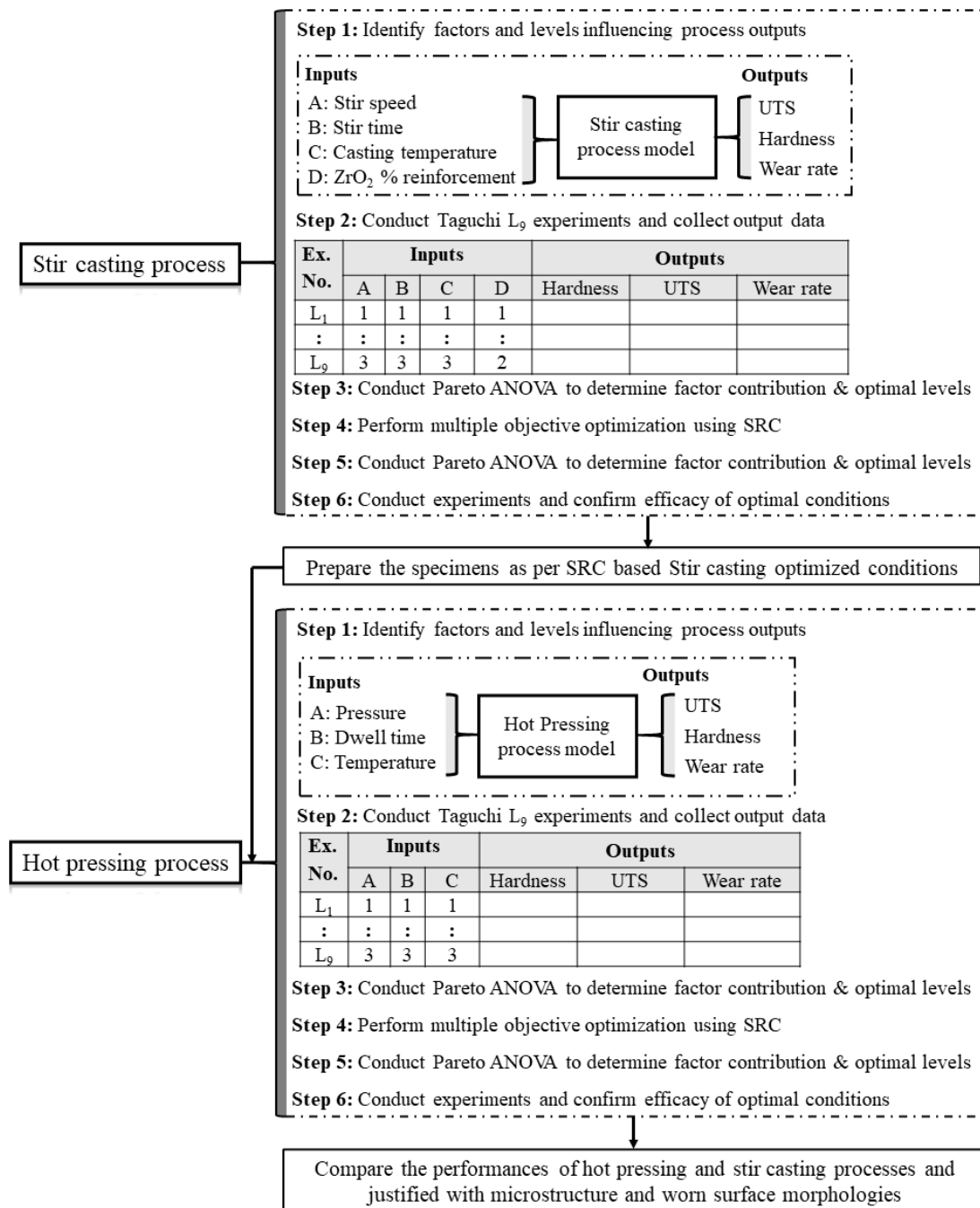
Figure 3.1: Experimental and optimization methodology for stir casting and hot-pressing processes (Patil et al., 2021)

3.2 Stir casting test rig

Good number of investigations on Al-Si alloy metal matrix have been reported in the literature. However, use of Al-Si with ZrO_2 particles have been not been investigated more

`

comprehensively. Therefore, in this study different compositions of ZrO₂ with Al-Si have been studied. Al-Si alloy metal matrix having 12.5 wt. % silicon reinforced with 0 wt. % ,5 wt. %, 10 wt. % and 15 wt. % of ZrO₂ particles of mean diameter 25µm are manufactured using spray deposition processing techniques and stir casting (Kumaraswamy et al., 2018). The properties of the composites are shown in Table 3.1.The schematic and photograph of the stir casting are shown in Figure 3.2.

(a)   (b)
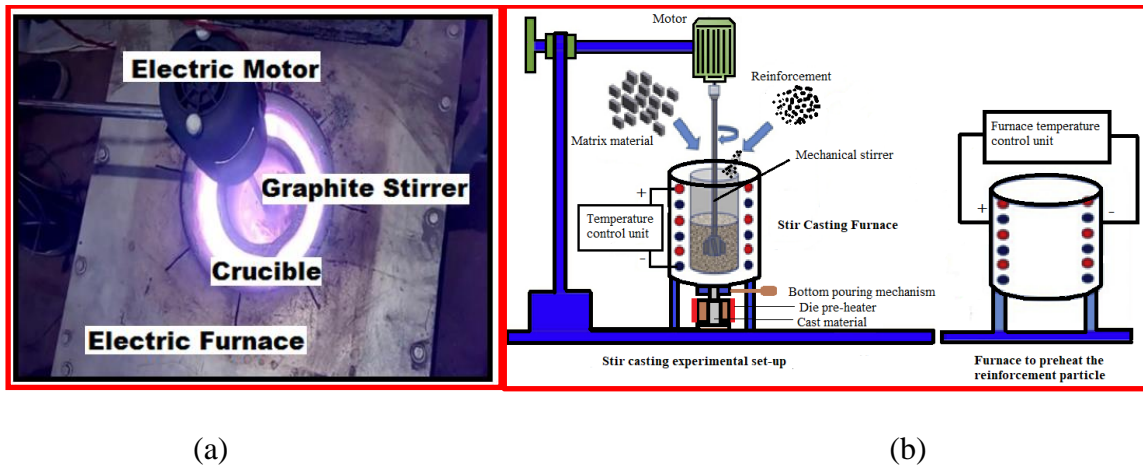
Figure 3.2: (a) Photograph of the stir casting; (b) Schematic of the stir casting (Patil et al., 2021)

Figure 3.2 shows the stir casting of Al-Si alloy matrix having 10 wt. %, 11 wt. %, 12 wt. % and 12.5 wt. % silicon composites. The vortex-free high-speed electromagnetic-mechanical stirring equipment for slurry is used. Matrix alloy Al-12.5 Si is placed on a graphite crucible in a furnace and heated to a temperature of 700 °C. These particles are wrapped in Al foil at the bottom of the crucible which was preheated to 800°C. Crucible is connected with an atomizing chamber and inert nitrogen gas. Switching on the 35-kW graphite stirrer and adjusting the temperature of melt to 850°C at which the melt gradually turned into semisolid slurry. Meanwhile, uninterruptedly screwing the cover into the crucible with the cooling of slurry under a constant torque. The matrix material becomes semisolid at 650°C and then scum powder is added to remove the impurities on the surface of the liquid. The reinforcement ZrO₂ is preheated to a temperature of 300°C and then mixed in the AlSi alloy. Stirring is carried out for 15 min. The stirring speed was 510, 520 and 550 rpm were used and mixture is poured in to the melted die to produce Ø50mm cylindrical bars. The uncertainty of thermocouple was ± 1°C. MMC's fabrication with liquid state processing route (i.e., stir casting) is popular in industries due to their robustness, simplicity and economy (Kumaraswamy et al., 2018). In the present work, melt stirring aided die casting method is

`

employed for the production of Al-12.5%SiZrO$_2$ composites. Here, ZrO$_2$ particles with varying wt.% (5, 10, 15) was dispersed in a molten Al-12.5%Si matrix metal with the help of mechanical stirring. For better mechanical properties and uniform dispersion of ZrO$_2$ particles in the molten matrix, the right choice of stir speed, stir time, reinforcement preheating and melt temperature are of practical relevance (Hashim et al. 2002; Prabu et al.2006; Dirisenapu et al. 2019; Hendronursito et al. 2020; Prabaharan et al. 2020; Yigezu et al. 2013). Al-12.5% Si ingot material supplied by FENFE Metallurgical Laboratory; Bangalore was sliced to small parts and are then placed in a graphite crucible equipped with electric resistance furnace. The ingots were initially subjected to temperature up to 800 ^{o}C. Hexachloroethane (C$_2$Cl$_6$) tablets prepared in powder form are packed in aluminium foil and dipped to the bottom of molten metal with the help of Zirconium coated chromium steel rod. This helps to degas the melt to remove the presence of possible casting defects (voids and porosity), present if any. The ZrO$_2$ powder reinforcements (size: 50 $\pm$ 5 µm) were preheated to 500 ^{o}C for 30 mins in an electric muffle furnace such that the particles are free from moisture, residues and scales. The preheated particles are transferred to prepared melt at the rate of 25-30 gm/min through the funnel, followed by mechanical stirring to create a vortex operated at the speed of 500-600 rpm. The prepared melt (say 680, 720 and 760 ^{o}C) was then transferred to the preheated mould (temperature: 250 ^{o}C and mould material: H13 die steel). After ensuring complete solidification the casting was ejected from the split die halves.

Taguchi experiments composed of nine different combinations of stir speed, stir time, casting temperature and ZrO$_2$ wt. % (5, 10, 15) were designed. Three replicates corresponding to each experimental trial ensures reduced experimental variations that leads to precise results. The process stir casting is shown is Figure 3.3.

`
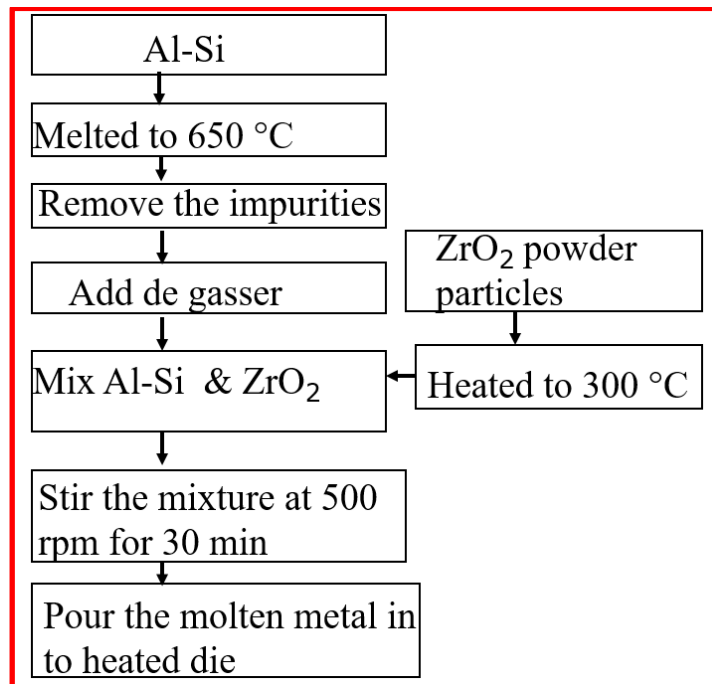
Figure 3.3: Flow chart of stir casting process (Patil et al., 2021)

3.3 Spray deposition

3.3.1 Procedure

Spray atomization and deposition process also known as spray casting or spray forming process and in-situ compaction is a method of casting near net shape metal components with homogeneous microstructures via deposition of semi-solid sprayed droplets onto a shaped substrate. Spray forming process possesses several advantages in effective microstructural control together with producing a near net shape, preform in a smaller number of processing steps. Because of high cooling rate, the material produced by this process has finer equiaxed grains without segregation. Extremely fine precipitants, modified primary and secondary phases, chemical homogeneity and increased solid solubility can be achieved by this method

This process is in competition with established metal forming technologies like casting and forging. This technique has to offer several advantages concerning the material properties of its products. The important characteristics of spray forming alloy (refer Figure 3.4) are as follows:

(i) High density, typically 96-99% of theoretical density

(ii) Oxygen content is decreased compared to P/M products and degassing operations are not needed

(iii) Superior fracture properties are obtained in comparison to P/M and I/M products

The spray casting process consists of two distinct but integral processes of atomization and deposition. In the atomization stage, the melt is disintegrated into a spray of micron sized droplets using an inert gas. The droplets in the spray are propelled away from the atomization zone under the effect of a high velocity gas jet. Droplets are thus experiencing a high cooling rate usually in rapid solidification regime i.e. of the order of 10^3-10^6 C$^\circ$s^{-1} due to increased surface to volume ratios of small sized droplets. These droplets generated during atomization stage are collected over a substrate to form a coherent and dense preform.

2   Various process parameters involved in spray forming play a vital role in refining the microstructure of the preform and achieving the desired properties.

3   Although, this process utilizes the same methodology as that used in the powder metallurgy, the difference lies in that the atomized droplets in the melt spray are not allowed to fully solidify to form powder particles

4   These are collected in a semi solid state on a deposition substrate. (The microstructural features of the preforms are fine and drastically modified compared to that of conventionally cast alloys.

5   A comparison of the steps involved in various processes for Al alloys is shown in Figure 3.1. It is obvious from the figure that the spray deposition process involves a smaller number of steps in producing a near net shape component compared to the other processing methods such as I/M and P/M route. This process can be applied to a variety of ferrous and non-ferrous alloys and composites. It is clear from the above discussion that though there are various processing routes available, the spray forming process has several beneficial effects concerning material properties and their processing methodology.

Ingot Metallurgy (I/M)

- Liquid metal
- Continuous casting
- Preform
- Scalping
- Billet
- Reheating
- Extrusion /forging
- Stock

Yield :30% ---35%

Powder Metallurgy (P/M)

- Liquid metal
- Atomization
- Powder
- Screening
- Canning
- Green compact
- Degassing
- Preheated preform
- Consolidation
- Compacted preform
- Decanning
- Billet
- Extrusion
- Stock

Yield : < 80%

Spray Forming

- Liquid metal
- Atomization and deposition
- Preform
- Scalping
- Billet
- Extrusion/Rolling /Hot pressing
- Stock

Yield : > 80%

Figure 3.4: Comparison of spray deposition process and P/M process (Patil et al., 2022)

3.3.2 Test rig of spray forming

As discussed earlier, the spray forming process consists of two distinct but integral processes of atomization and deposition. The proposed schematic representation of spray forming set up is shown in Figure 3.5 The spray set up mainly consists of an atomization chamber wherein atomization takes place in an inert gas atmosphere. It also consists of control system to regulate the temperature and gas/melt flow ratio and mechanical arrangement for proper positioning of substrate so as to get desired net shape of preform. The substrate can have both rotational as well as translational motion.

The desired amount of charge (Al-Si) was heated in a crucible at elevated temperature. This temperature is higher than melting point of Al alloy and also ensures superheat in each test case. The heating was carried out for about one and half hour. The flow of molten metal to delivery tube is controlled using stopper rod. The tube is located at the bottom of the crucible. The temperature of the molten metal is measured using type T thermocouple during the experiments. When a predetermined temperature is reached, the molten metal and highly

`

compressed nitrogen gas start flowing along with the ZrO_2 particulate reinforcement simultaneously through the nozzle assembly and delivery tube respectively. The molten metal streams enter into the spray chamber. The metal streams were converted into different sizes of the droplets using pressurized gas stream. Further, the atomized droplets were then collected over a stationary copper substrate which was inclined to 0° from the central axis of the nozzle assembly to achieve a disk shape preform. Spray forming is complete when the molten metal flow is stopped. The experimental conditions are shown in Table 3.3
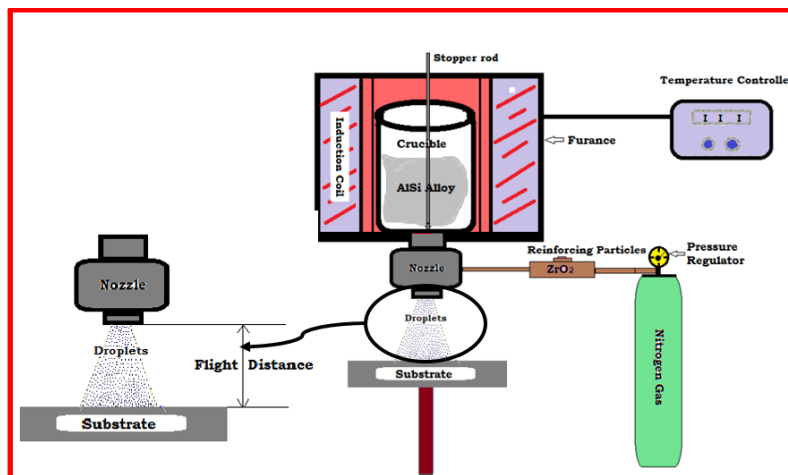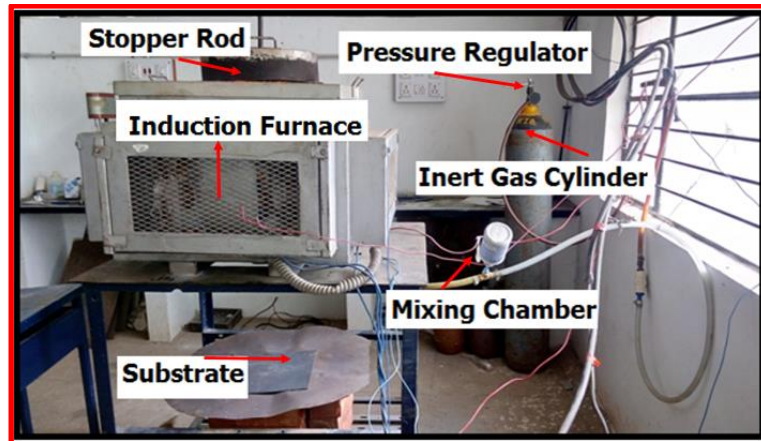
Figure 3.5: Spray deposition test rig (Patil et al., 2022)

`

Table 3.3: Spray experimental conditions

Sl. No	Alloy composition (wt. %)	Inert nitrogen gas pressure (MPa)	Flight Distance (atomizer to substrate) in mm	Superheat temperature (°C)
1	Al-Si+5% ZrO_2	4.5	370-480	850
2	Al-Si+10% ZrO_2	4.5	370-480	850
3	Al-Si+15% ZrO_2	4.5	370-480	850

3.4 Wear Testing

The details of spray deposition test rig used this study have been described by (Raju et al., 2011). The spray deposition method is employed with an annular divergent-convergent nozzle in order to create a spray of melt. It is worthy to note that during each trial 1.2 kg of alloy has been melted to a temperature of 800°C. The molten metal is atomized by a free fall atomizer using inert gas (Nitrogen). The resultant spray is deposited over a copper substrate resulting in a required shaped preform. The operating condition used in spray deposition method which is used for producing the preforms are tabulated in Table 3.4.

Table 3.4: Operating conditions used in spray forming

Nozzle diameter (mm)	Gas pressure (MPa)	Melt temperature (°C)	Atomization gas	Nozzle to substrate distance (m)	Molten metal flow rate (kg/min)
4.1	0.46	820	N_2	0.38	2.4

The sliding wear testing of hybrid composites was analysed at room temperature on pin-on-disc wear device (Ducom, Model No: TR-201CL, Bangalore, India) according to ASTM G99-95a (reapproved) standards. The test rig and the specimens are shown in Figure 3.6. The polishing disc shaped paper was made by abrasive material. It consists of Al-12.5Si of 80 mesh grit size. The abrasive material was a polishing disc-shaped paper consisted of Al_2O_3 particles of 60 mesh grit size. The minimum and maximum grit size of the composite is 170 μm and 335 μm. The sliding duration of the disc was 2 min. The study was conducted was three sliding speeds: u_1=0.18 m/s, u_2=0.26 m/s and u_3=0.33 m/s. The wear test was

`

conducted with various input parameters like sliding distance (1200 to 4100 m). The nominal applied loads used were 10, 20, 30 and 40 N. The weight loss was measured with an accuracy of 0.1 mg. During the end of each test, the abrasive disc was replaced with a new one in order to avoid data scattering. This ensures safe interpretations and repeatability of tests. Each test was conducted at least five times and average readings were used to analyse the wear behaviour.

(a)

(b)

Figure 3.6: Test rig of pin on disc machine; (b) Wear test specimens

The aluminium 12.5% of silicon alloy reinforced with 5%, 10% and 15 wt. % ZrO_2 reinforced of 45 μm in size were fabricated with the spray deposition method. The required silicon, aluminium and zirconium oxide were measured using a digital weighing machine

(Precisa, Swiss Made, ES 225SM-DR) with a count of 0.1 mg. The composition of the Al-Si alloy and ZrO_2 reinforced powder is tabulated in Table 3.1 and 3.2.

The plain alloy and the developed metal matrix composites specimens were subjected to heat treatment process. The corrected weighed powders were properly mixed at ambient temperature (32°C) using a centrifugal ball mill (FRITSCH, Germany) for 20 min and at a speed of 125 rpm. The mixed powder was compacted using uniaxial hydraulic pallet press (Type KE, Sr. No. 1327, Kimaya Engineers, India) at 585 MPa pressure at the ambient temperature. Cylindrical pellets of dimension 10 mm diameter and 30 mm height were fabricated for sintering operation. The applied load is normal to the component direction. The measurement instrument is equipped with a load cell at appropriate position in order to measure the frictional forces. The linear variable differential transducer is integrated with load cell to measure the depth of wear in microns. The testing specimens were fixed to the sample holder during the experiment trails. The track diameter was kept constant and sliding distance, sliding speed and applied normal load were varied for all metal matrix composite samples.

Wear surfaces and debris of selected samples have been characterized using scanning electron microscope (SEM) (Model: S-3400N Hitachi Model). The pin disc during the test was operated at 300 rpm. After each run, the test specimens were removed from the machine and weighed accurately to determine the loss of weight. The weight loss is measured for every 1200 rpm. The weight loss during the wear is calculated (refer Equation 3.1) by taking the difference between the initial weight and the final weight.

$$\text{Wear weight loss} = W_{21} - W_{12} \qquad (3.1)$$

where, W_{12}, W_{21} is the initial and final weight

The coefficient of friction is calculated using Equation 3.2

$$\mu = \frac{F_N}{W} \qquad (3.2)$$

where, μ, F_N, W is the coefficient of friction, frictional force and nominal load, respectively.

It is worthy to note that the density of spray formed composites were calculated using Archimedes principle as per ASTM: B962-08.

The wear rate and specific wear rate of the sample are calculated using Equation 3.3(a) &3(b)

$$\text{Wear rate} \left(\frac{mm^3}{m}\right) = \frac{\frac{Mass\ loss}{Density}}{Sliding\ distance} \qquad (3.3a)$$

$$\text{Specific wear rate} \left(\frac{mm^3}{Nm}\right) = \frac{\frac{Mass\ loss}{Density}}{Sliding\ distance \times Load} \qquad (3.3b)$$

`

Specific wear rate is defined as ratio of the wear rate to the unit load. It is used to represent the materials load bearing ability.

The hardness testing of Al-12.5Si+15ZrO$_2$ was determined using LECO LV700AT Vickers hardness tester. The test specimens were prepared by polishing using standard metallographic techniques of grinding on emery paper specifications with 1/0, 2/0, 3/0 and 4/0. Final polishing of the sample was done on a wheel cloth using kerosene and brasso. The polished samples were etched with Keller's reagent 1.5% vol. hydrochloric acid (HCl), (1% vol. hydrofluoric acid (HF), 2.5% vol. nitric acid (HNO3) and rest water). Every tested samples were polished before conducting each trial.

3.5 Hot pressing method

The specimens were then hot pressed using hydraulic hot press machine at a pressure of 50 MPa and at a temperature of 480°C for 8 hours. The hydraulic hot press machine is shown in Figure 3.7. The hot pressing is the secondary operation after stir casting and spray forming involves simultaneous application of heat and uniaxial pressure. The prepared specimen is machined and kept in a furnace and the specimens are heated to the temperature of 525°C and the specimens are held at that temperature for two hours and pressed with a pressure of 50 MPa. The hot-pressing technique applies pressure and heat to the as-cast specimens at the same time. 100-Tonne hydraulic press was used for pressure application. The as-received stir cast samples were placed in an electric muffle furnace. Temperature control unit maintains the desired temperature (say 400 - 480 °C) required for experimentation. Once the set furnace temperature is attained, it is maintained for 2 hours to ensure uniform distribution of temperature throughout the specimen. The specimens are then transferred to the split die halves made of H13 Hot work steel (45 HRC) for pressing. The dies and the punch are also pre-heated to the required temperature (same as specimen temperature). Hot pressing process is done for varying combinations of pressure (60, 80, 100 MPa), temperature (400, 440 and 480 °C) and dwell time (20, 30, 40 mins). After the desired dwell time, the application of pressure and heat was withdrawn. Later, the specimens were allowed to cool to room temperature. The specimens ejected from the split die halves were then examined for wear resistance, hardness and tensile strength.

`
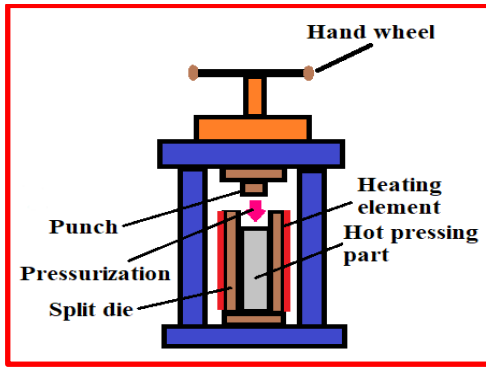
(a)   (b)

Figure 3.7: (a) Schematic of the hot-pressing machine; (b) Photograph of the hot press machine

Tensile specimens with dimensions conforming to the ASTM E8 standard were prepared out bar-shaped SLM samples. Experiments were performed at room temperature and were repeated three times for each material to confirm repeatability. After processing, the strength of aluminium silicon alloy matrix reinforced with zirconium particulates composite specimens was measured using Matsuzawa micro-hardness testing machine. The Compressive strength (MPa) and tensile strength (MPa) of the specimen were measured using a 3-point measuring method (ASTM E8) with a Universal Testing Machine (Instron 3366, 10 kN capacity, 0.005 -500 mm/min). The Figures 3.8 & 3.9 shows the specimen used for experimentation as per ASTM standards. The gauge length is the reference length used in the elongation calculations.
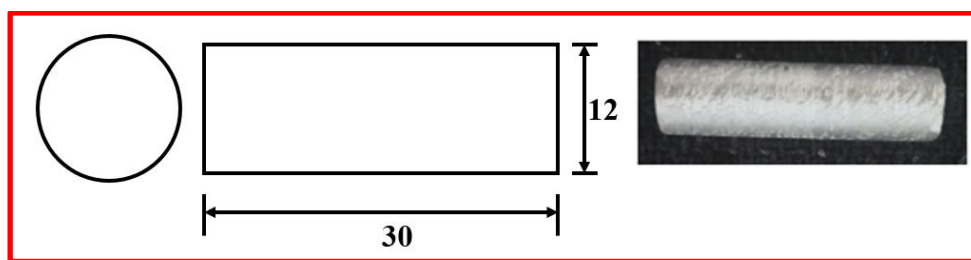
Figure 3.8: Compression test sample
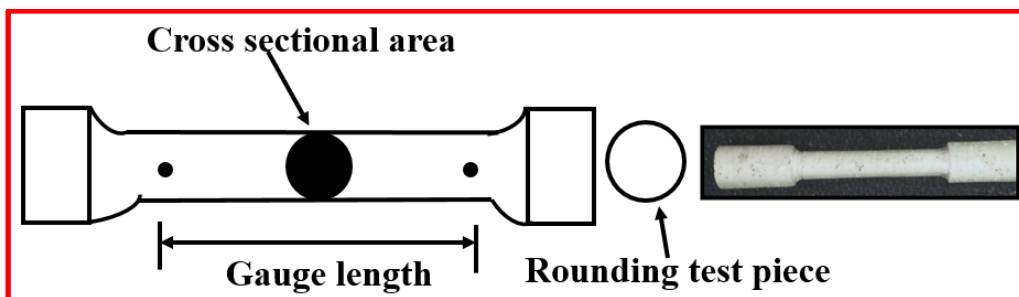
Figure 3.9: Tensile test samples

The specifications of the specification are shown below:

- Gauge length G =   45+ 0.1mm
- Diameter   D =   9 + 0.1mm
- Radius of   R=   8mm
- Length of reduced cross sectional area A =54 mm^2

3.6 Vickers Hardness Test

The stir cast and hot-pressed composites were subjected to micro-hardness examination as per ASTM E384 viz. Vickers hardness testing machine. The specimens were and flat and polished. Hardness measurement was performed on the face perpendicular to pressurized direction of hot pressing and pouring direction of stir casting technique. 1 Kgf load, was applied for 10 seconds through the rectangular pyramid diamond indenter (136^0) on the composite specimens. Average of eight indentations per samples were taken during Vickers hardness test (Figure 3.10).

Figure 3.10: Vickers Micro hardness Tester

3.7 Metallographic examination

SEM was used to measure the tool wear, chip-morphology and the surface defects of the machined surface. 'JEOL-JSM-638OLA' model SEM with 30KV resolution is as shown in Figure 3.11. It was used to measure the performance characteristics and the images were procured with different magnifications for investigation and extensive analysis.

`

Figure 3.11: Scanning Electron Microscope

3.8 Mechanical properties (Tensile strength)

The tensile tests of the specimens were carried out using precision controlled computerized universal testing machine (UNITEK 9450 PC, Blue Star India Ltd.) as shown in Figure 3.12.

Figure 3.12: Universal Testing Machine

3.9 Mechanical properties (Micro hardness)

The micro hardness of commercially available Al-12.5Si alloy before and after the addition of grain refiner and modifier was measured using automatic Vickers Micro hardness tester as shown in Figure 3.13 (Model: MVH-I, METATECH Industries, Pune, India) in as cast condition.

`

Figure 3.13: Micro hardness tester

This chapter gives an overview of the Al-Si alloy material and its chemical compositions as well as mechanical properties. It also explains the experimental set up with stir casting and spray deposition methods. The chapter briefly elaborates on the experimental design plans and describes the various equipment's which are used to measure the performance characteristics and the procedure of measurement. The next chapter gives the detail explanation of prediction system using ANN and ANN-GA, which has been developed to validate the experimental results. The Taguchi L27 orthogonal array is considered for development of correlation models between input parameters and output responses.

`

CHAPTER 4

OPTMIZATION STRATEGY

To determine set of optimal conditions that add value to their product performances are of industrial relevance for any manufacturing processes (Rao 2010). Trial-and-error-method or one-factor-at-a-time approach results in undesired performances, in addition to material wastage as well as time and money (Mukherjee et al. 2006; Patel et al. 2020a; Patel 2020b). Taguchi method has proven its success due to their robust experimental design and solve practical problems with minimum experimental trials, where multiple factors influencing the process performances (Mukherjee et al. 2006; Fei et al. 2013).

4.1 Taguchi Method

Taguchi method has been employed for both stir casting and hot-pressing processes. Taguchi L_9 experiments are conducted to explore the influence the multiple factors (stir speed, stir time, temperature and ZrO_2 reinforcements) on wear rate, ultimate tensile strength and hardness of the stir casting fabricated Al-12.5%SiZrO$_2$ composites. Stir casting factors and the respective operating levels were finalized after conducting thorough literature review (Dirisenapu et al. 2019; Hendronursito et al. 2020; Prabaharan et al. 2020; Yigezu et al. 2013; Jokhio et al. 2016). Similarly, Taguchi L_9 experiments were performed to examine the influence of hot-pressing parameters (dwell time, pressure and temperature) on hardness, ultimate tensile strength and wear rate. The hot-pressing parameters and operating levels were set based on pilot experiment study and consulting literature (Azimi et al. 2015; Zheng et al. 2015; Asl et al. 2015a; Asl et al. 2015b). Stir casting and hot-pressing processes factors and levels used for experimentation and optimization are presented in Table 4.1.

`

Table 4.1: Stir casting and hot-pressing process factors and levels

Stir casting process		Hot pressing process	
Input factors	**Levels (1, 2 and 3)**	**Input factors**	**Levels (1, 2 and 3)**
A: Stir speed, rpm	500, 550, and 600	E: Temperature, ^{o}C	400, 440 and 480
B: Stir time, min	4, 8, and 12	F: Pressure, MPa	60, 80 and 100
C: Casting temperature, ^{o}C	680, 720, and 760	G: Dwell time, min	20, 30 and 40
D: ZrO$_2$ reinforcement, %	5, 10, and 15		

4.2 Super Ranking Concept (SRC)

Taguchi method is efficient enough to improve product/process performances, but is limited to analyse and optimize single response at a time (Arunachalam et al. 2020; Patel 2020b). Multi criteria decision making (MCDM) methods solve such engineering problems where multiple factors affecting the responses which are conflict to one another (Stojčić et al. 2019). MCDM techniques namely GRA, TOPSIS, MOORA, COPRAS and VIKHOR were solved effectively to counter such multi-objective optimization problems (Arunachalam et al. 2020; Patel 2020b; Kumari et al 2020). However, these methods dependent on determining weights for assigning individual responses by weighting methods like CRITIC, PCA, Entropy, Fuzzy, AHP, ANP and so on (Singh et al. 2020a; Singh et al. 2020b). Hybridization of MCDM with weight methods increases complexity, loses transparency and requires skilled mathematician to solve large computational steps in evaluating the conflicting optimization criteria. Industry based working professionals require quick predictive tools that determine optimal solutions with simple mathematical steps. Super Ranking Concept (SRC) is neither dependent on weighting methods, nor requires complex computational steps to solve multi-objective optimization problems. Steps to solve the multi-objective optimization problem by SRC are shown in Figure 4.1.
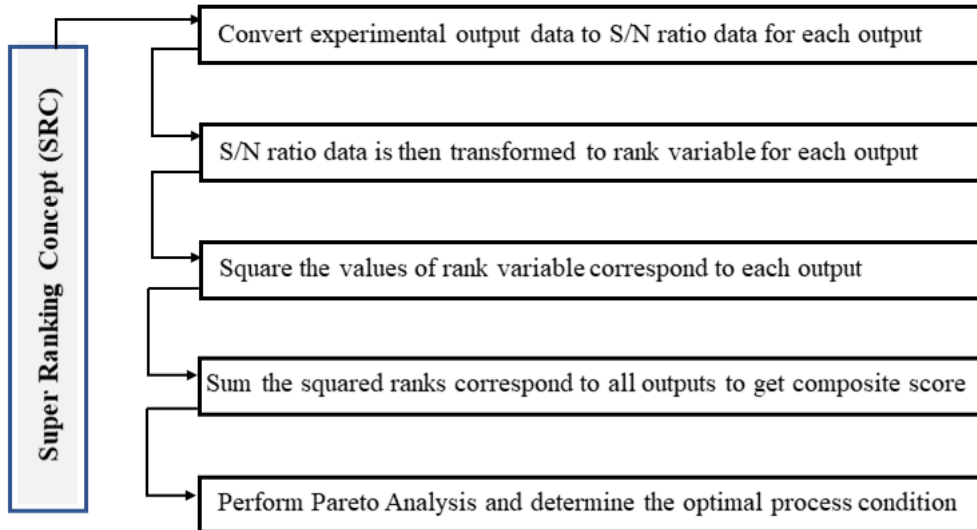
Figure 4.1: Methodology illustrating computational steps of SRC

4.3 Artificial Neural Network Model

4.3.1 Multilayer perceptron neural network (MLPNN)

Artificial Neurons are the building blocks of neural networks which contain activation, bias, weights and outputs. Neurons are arranged into network of neurons and a layer consists of row of neurons. The developed neural network is composed of two neurons at the input layer (composition of ZrO_2 and flight distance). The output layer consists of seven neurons corresponding to tensile strength, compression strength, and degree of porosity, strip thickness, yield strength, elongation and micro hardness. This MLPNN network consists of single hidden layer with H_n (number of hidden neurons) as shown in Figure 4.2(a). Hidden layer consists of weights and biases represented by W_{ij} and b_{ij}. The output layer also consists of weights and biases represented by W_{jk} and b_{jk}. The non-linear activation function namely sigmoidal activation function was selected for both inputs and outputs. The structure of MLPNN is shown in Figure 4.2(a). Back-propagation (BP) algorithm was used for training in MLPNN. Gradient descent with momentum and adaptive learning rate back propagation (GDX) was used as training function in the MLPNN. GDX has the ability to add weights and biases and also update other factors like learning rate (g) and momentum rate (m) as shown in Figure 4.2(b). The Performance of MLPNN was validated through MSE (Mean Square Error) as given in Equation 4.1. Other factors that affect the performance of MLPNN were the number of hidden neurons and momentum rate. The learning rate, iterations, time and number of epochs were controlled in the present study. The overall MLPNN record is shown in the Table 4.2.

56

$$MSE = \frac{sum(y-targets)^2}{length(y)} \qquad (4.1)$$

where y is the net of input values and targets expected output value.
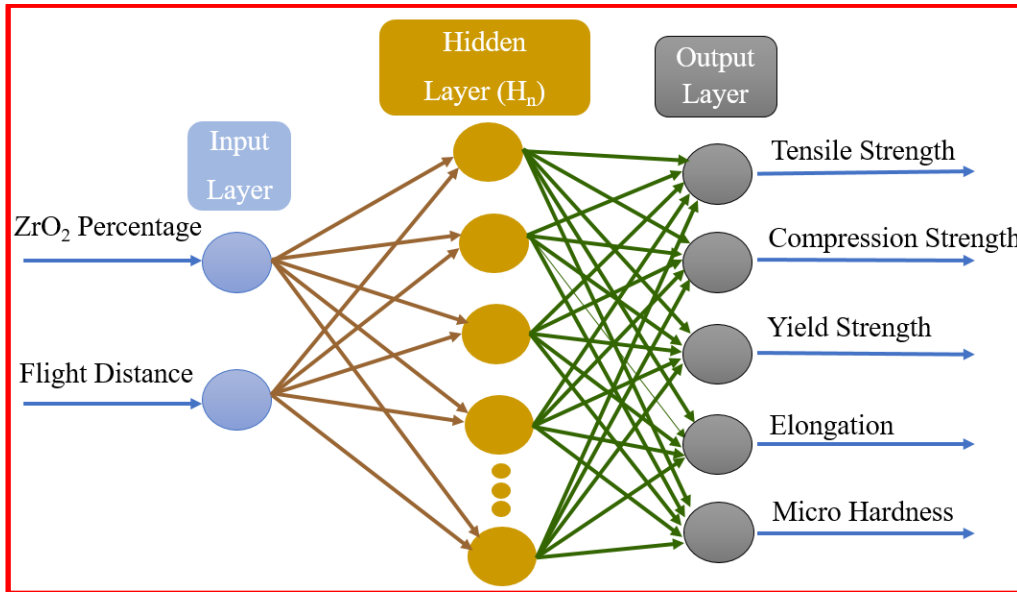
(a)
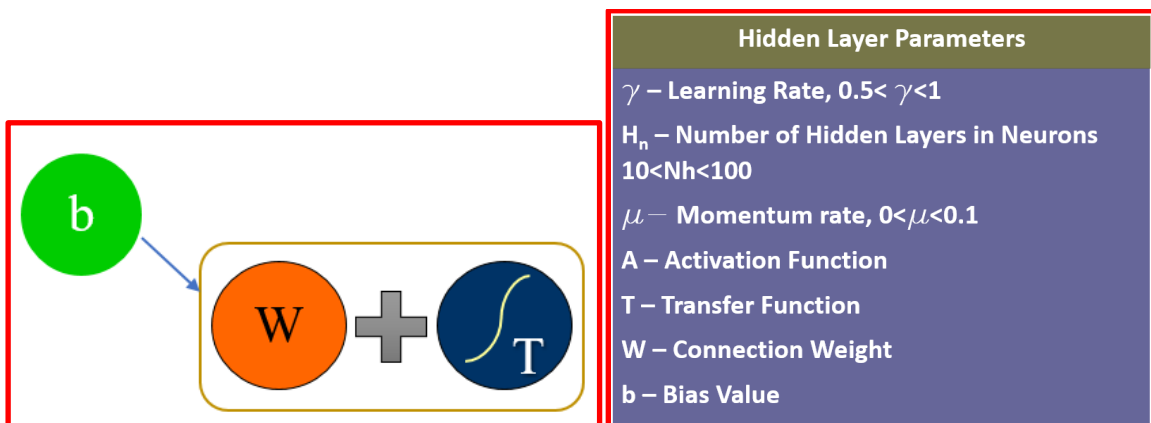
(b)

Figure 4.2: (a) Structure of MLPNN; (b) Structure of hidden and output neuron with sigmoid activation function

where b – bias, W – weight, T- Transfer function or Activation Function.

`

Table 4.2: MLPNN Training Record

Parameter	Value
trainFcn	'traingdx'
performFcn	'mse'
derivFcn	'defaultderiv'
divideFcn	'dividerand'
divideMode	'sample'
stop	'Maximum epoch reached.'
num_epochs	5000
learning rate	0.65-0.85
momentum rate	0.0025
Number of neurons in hidden layer	17

4.3.2 Radial basis functional neural network (RBFNN)

The structure of RBFNN consists of an input layer, two-layered feed forward network (hidden layer) and an output layer. Input layer distributes the inputs to the network. The hidden layer contains a non-linear radial basis function called Gaussian activation function. The output layer contains a linear summation function. The radial basis function is expressed as $\phi_1, \phi_2, \phi_3 ... ... \phi_N$, where $\{\phi_i(x)\}_{i=1}^{N}$ is the hidden space.

One-dimensional Gaussian form is shown in the Equation 4.2.

$$\phi(x, \mu) = e^{\frac{||x - \mu||^2}{sd^2}} \qquad (4.2)$$

Where μ is the center of the mean value of x, i.e. the centre of the Gaussian function. The Spread of the Gaussian curve is given by the distance between the center of $\phi(x, \mu)$ which is represented by d. The hidden unit contains Gaussian function whose output is the distance between input x and the center μ. The number of basis functions (N) and the number of training data points need not be equal. It is better if number of training data points is more than the number of basis functions (N). During the training phase, centre μ arranges the distribution of spread d in hidden layer such that it is sensitive to the data points near the center. We can fine tune this sensitivity by varying the value of spread d. The radial basis should be enough sensitive to the input data and it can be achieved by keeping the region of the spread d smaller. This sensitivity of spread d enables solving complex non-linear problems by non-linear mapping of the data set. The complexity of the mapping decides the

number of radial basis functions. Number of radial basis functions does not depend on the size of the data set. Hence, it can be said that RBFNN is similar to MLPNN, but both are not the same. There is no training required because RBF uses linear combination of radial basis functions between input and target value. This linear combination always renders infinite number of zero error solutions. In this RBFNN, there are two neurons in the input layer corresponding to four input process parameters (ZrO_2 Composite and Flight Distance). The output layer consists of five neurons corresponding to Tensile Strength, Compression Strength, Yield Strength, Elongation and Micro Hardness as shown in .
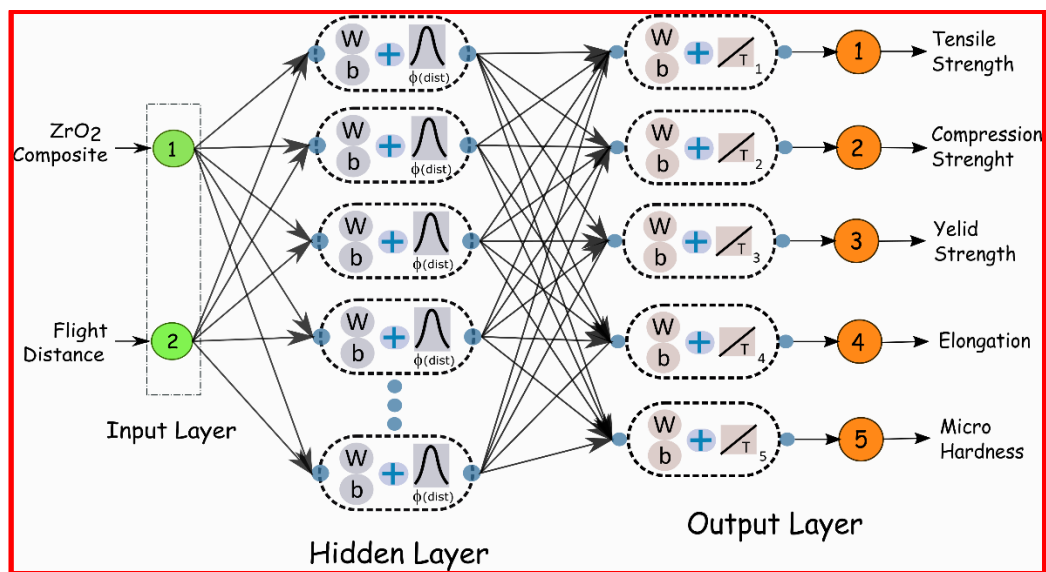
Figure 4.3: Structure of RBFNN

Where, $\phi(dist) = \phi(x, \mu)$, T = summation of output layer

4.3.3 ANN optimized by genetic algorithm (GA-ANN)

Genetic algorithm is a meta-heuristic algorithm best known for global searching and evolution of parameters. The development of genetic algorithm was inspired by the nature theories, i.e., evolution of chromosomes and Natural selection theory. Therefore, similar principles from these theories are used to find the solution in GA. The structure of RBFNN and flow chart of RBFNN-GA is shown in the . For the initial population a fitness value is assigned for each chromosome. From this initial population (parents), new set of chromosomes (offspring) are created which have a better fitness value. In the next step, the selected chromosomes undergo mutation and crossover to generate the offspring. During crossover, two randomly selected chromosomes with best fitness value are divided and exchanged to produce new offspring. Mutation is expressed as mutation rate which explores

`

the solution space in a random manner. Mutation rate is the rate at which the part of selected chromosome undergoes changes. This mutation is the reason as to why the GA does not settle to the local minima like the other conventional algorithms. After crossover and mutation, the new population undergoes fitness evaluation where, if value of new population is less than the fitness value, the GA cycle is repeated. The fitness value is evaluated through Mean Square Error (MSE). IF MSE is less than 0.005, the new population is rejected, and the cycle is repeated until we get the best population. In this research a population size of 25 was used and GA was run for 115 generations. Mutation rate of 0.25 and crossover rate of 0.87 were selected.
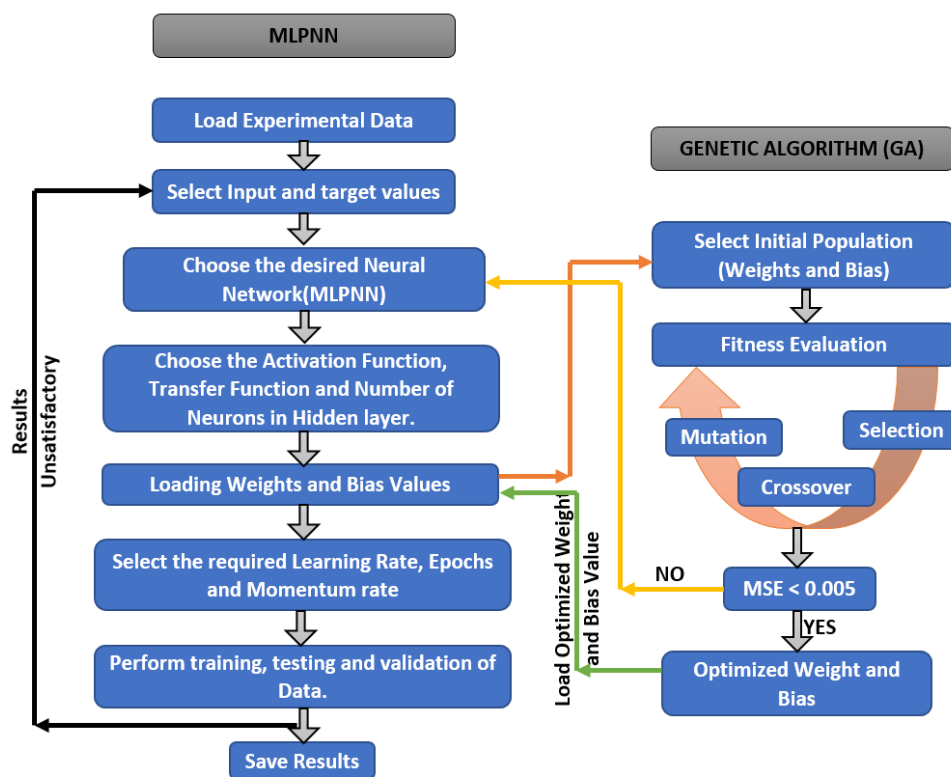
Figure 4.4: Flow Chart of ANN-GA

4.4 Design of Experiments:

Face-centred Central Composite Design (CCD) was used for experimental plan to perform series of experiments with multiple factors varied simultaneously and are analysed to identify factors effect (i.e., individual and interaction) and optimal spray forming conditions are determined. Four input variables (control variables) operating at three respective levels represented in un-coded form of spray forming technique are presented in Table 4.3. It is to be noted that spray forming levels and factors are selected after conducting comprehensive

`

pilot experiments, based on previous research literature (Guo et al., 2020). Thereby, CCD matrices of 27 experiments (16 factorial point experiments, 3 centre point or replicate experiments, and 8-star point experiments) covering the full design for four factors at three levels were used to build full quadratic (individual or linear, square, and interactions) models (refer Table 4.3). Three replicate experiments are carried out on each experimental trial that increase precision analysis for fit second order polynomial model.

Table 4.3: Spray forming factors and operating levels

Control variables	Symbols	Levels & Units
Flight distance, FD	A	0.37, 0.40 and 0.48 m
Melt temperature, MT	B	720, 760 and 800 $^{\circ}$C
Gas pressure, GP	C	0.4, 0.7 and 1.0 MPa
ZrO_2 reinforcement, ZR	D	5, 10, and 15 %
Fixed factors		
Atomization gas		Nitrogen, N_2
Disc material		Copper
Disc diameter		300 mm
Disc thickness		6 mm
Nozzle diameter		4 mm

4.4.1 Response Surface Methodology (RSM)

In the present work, RSM main function is to estimate the factor effects (individual, interaction and curvature) of spray forming variables such as melt temperature, gas pressure, flight distance and percent reinforcement of ZrO_2 on output performances (i.e. hardness and ultimate tensile strength). CCD follows five stages to perform optimization of process viz. experiments:

1. Perform experiments according to standard matrix plan and collect output data.
2. Derive empirical models or regression equations relating input-output based on experimental data.
3. Estimate the factor effects based on experimental data after conducting analysis of variance test.

`

4. Conduct tests such as full quadratic terms of factor significance or contributions, followed by surface plot analysis on outputs.

5. The derived empirical equations are checked subjected to coefficient of correlation tests and prediction accuracy tests with random experimental cases.

4.4.2 Multi-objective Particle Swarm Optimization based Crowding Distance (MOPSO-CD)

Eberhart and Kennedy proposed artificial intelligence-based swarm intelligence technique (which mimic the social behaviour of bird's flock search for food source) for solving multi-objective optimization problem (Kennedy et al., 1995). PSO starts with set of generation of random population of particles with assigning random velocity to individual particle and the particle fly towards optimal solutions in a global search space (Nagarkar et al., 2016). Each particle flies through solution space with certain velocity and update their positions in search space based on per particles current position and personal or self-flying best experience (P_{best}) and best location in its group (G_{best}). The updates correspond to velocity and position of individual particle is done by using Equation 4.3.

$$V_{ij}^{t+1} = \omega V_{ij}^{t} + C_1 rand_1\left(P_{best\,ij}^{t} - \chi_{ij}^{t}\right) + C_2 rand_2\left(g_{best\,ij}^{t} - \chi_{ij}^{t}\right) \tag{4.3}$$

$$P_{ij}^{t+1} = P_{ij}^{t} + P_{ij}^{t+1} \tag{4.4}$$

Terms, $rand_1$ and $rand_2$ refers to the random numbers varied between the ranges of 0-1. Let ω be the inertia weight whose value ranges between 0.4-0.9, C_1 and C_2 refers to the acceleration coefficients whose value kept fixed to 2 (Kumar et al., 2020).

The computation of *P_{best}* and *G_{best}* values necessary to determine the optimal condition for single objective optimization is relatively easy compared to multiple output optimization (Nagarkar et al., 2016). This occurs due to difference in nature of behaviour of input variables on multiple outputs (Patel et al., 2018). Thereby, search algorithms are often difficult for an objective function to hit global maximum or minimum simultaneously. Thus, search algorithms generate multiple optimal solutions different from one another (Patel et al., 2016). Thereby, Pareto ranking methods are introduced to simple PSO to solve multi-objective optimization, wherein the potential solutions are stored in the external archive or repository which contains the previous best solutions. At each iteration of swarm, the solutions of the updated and stored in external archive only when the solutions are non-dominated. Note that, the archive size is to be kept fixed that could limit the computation cost. Selection of G_{best}

`

swarm solution in a stored repository is done by applying global best selection method such as (Ding et al., 2018), 1. Crowding distance CD; 2. Adaptive grids and 3. Comprehensive ranking. Use of crowding distance mechanism ensures appropriate choice of global best positions G_{best} with deletion of non-dominated solutions in repository. Mutation operator introduced to MOPSO-CD, that conduct exhaustive search which limit towards premature convergence of a solution (Coello et al., 2004). The use of crowding distance with mutation parameter could help MOPSO-CD to converge towards Pareto optimal front with the potential set of nondominated solutions.

`

CHAPTER 5

RESULTS AND DISCUSSION

5.1 Mechanical and microstructure behaviour of stir cast and as cast hot-pressed

Taguchi L_9 based experiments with different sets of influencing parameters of stir casting and hot-pressing were carried out. Pareto analysis of variance examine each parameter influence and determine optimal levels for conflicting nature of outputs (minimum WR, maximum hardness and UTS). SRC determines single set of optimal factors for all conflicting outputs. Microstructure examinations were carried out to justify the statistical results that clearly distinguish the efficacy of stir casting and hot-pressing processes. Confirmation experiments evaluate the performances of optimal conditions determined by Taguchi and SRC. Most of the information in this section has been published.

(**https://doi.org/10.1080/2374068X.2021.1927648**).

5.1.1 Stir casting

Stir casting technique (Goudar et al., 2013) was employed to fabricate the Al-12.5%SiZrO$_2$ composites. The factors such as stir speed, stir time, cast temperature and (ZrO$_2$ reinforcements 5, 10, 15%) influence of on wear loss, hardness and UTS were studied with the help of Taguchi L_9 experiment method (four factors operating at three levels). Each experiment was repeated thrice and average values correspond to 24 indentations of hardness, three wear loss and UTS are recorded and presented in Table 5.1. The actual output data were transformed to S/N ratio data. For better composite properties, larger-the-better quality characteristics were used for hardness and UTS, whereas smaller-the-better was adopted for wear loss. The S/N ratio data correspond to output quality characteristics of stir casting process and are presented in Table 5.1.

Table 5.1: Experimental conditions for stir casting process

Exp. No.	Experimental Input				Experimental output			Signal-to-noise ratio, dB		
	A	B	C	D	Hardness	UTS	WL	Hardness	UTS	WL
	rpm	min	^oC	%	HV	MPa	mg	HV	MPa	mg
L_1	500	4	680	5	63.8	162.7	13.8	36.10	44.23	-22.80
L_2	500	8	720	10	64.4	176.2	12.9	36.18	44.92	-22.21
L_3	500	12	760	15	61.8	141.4	15.1	35.82	43.01	-23.58
L_4	550	4	720	15	63.6	153.4	14.7	36.07	43.72	-23.35
L_5	550	8	760	5	66.5	174.6	13.2	36.46	44.84	-22.41
L_6	550	12	680	10	66.8	180.1	10.1	36.50	45.11	-20.09
L_7	600	4	760	10	64.9	178.3	12.2	36.24	45.02	-21.73
L_8	600	8	680	15	64.3	169.9	13.3	36.16	44.60	-22.48
L_9	600	12	720	5	67.0	198.1	8.8	36.52	45.94	-18.89

The S/N ratio data were used to construct the Pareto ANOVA (refer Table 5.1). Pareto analysis of variance enables investigator to determine the of factors contribution and optimal levels for hardness, wear loss and UTS (refer Table 5.2).

`
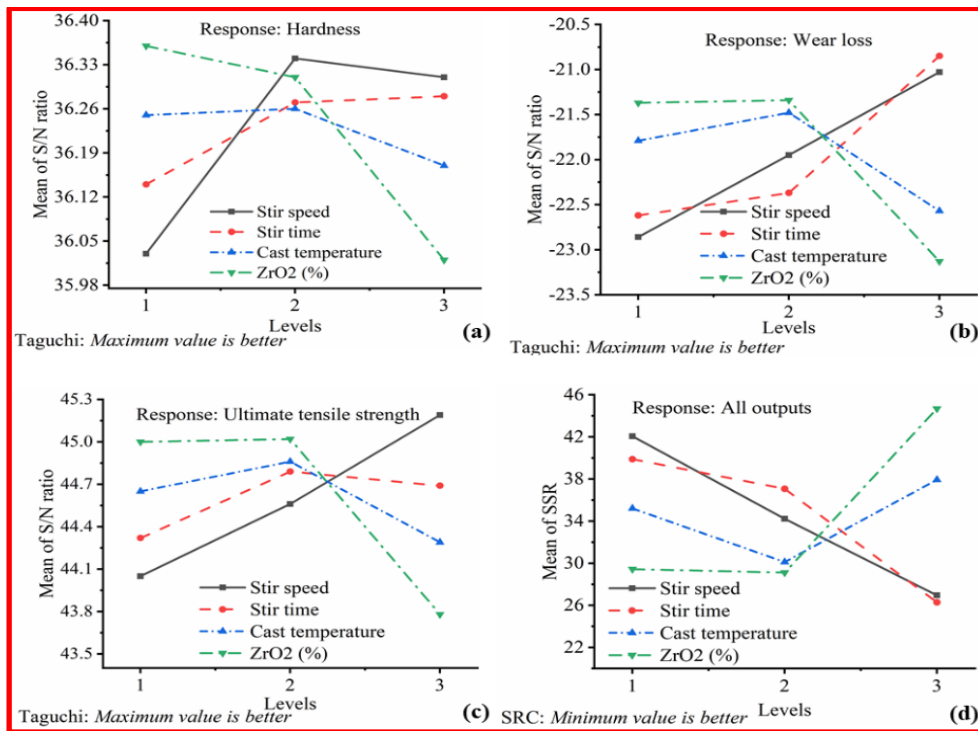
Figure 5.1: Main effect plots of S/N ratio of responses: a) Hardness, b) Wear loss, c) Ultimate tensile strength, and d) All outputs

5.1.1.1 Effect of factor on hardness

Figure 5.1(a) explain the hardness behaviour with mean S/N ratio correspond to each factor and levels. The results showed increased proportion of ZrO_2 (after 10%) in Al-12.5%Si matrix resulted in decreasing trend in hardness values. The probable reasons could be the presence of trapped air inside the cluster of ZrO_2 particles in the entire melt increases with increased percent reinforcement of ZrO_2. The agglomerated ZrO_2 particles do not break during melt mixture stirring. In MMCs, few reinforced particles may float and get agglomerated on the melt surface due to difference in properties (such as, density and surface tension) (Goudar et al., 2013). Shearing action of rotating blade at higher stirring speed for enough duration helps the reinforcement particles distributed inside the melt mixture to deagglomerate and ensures homogeneous particle distribution in composites. Higher speed and stir time resulted in better hardness values. It is noted that stir speed after crossing the mid value does not show any appreciable improvement in hardness. Increase in casting temperature showed improved hardness values. This might be due to the improved wettability and ensures homogeneous mixing. ZrO_2 reinforcement showed dominant effect, followed by stir speed, stir time and pouring temperature (refer Table 5.2). Pareto ANOVA suggested optimal stir casting conditions that maximizes the hardness value was found equal to

`

$A_2B_3C_2D_1$ (i.e. stir speed: 550 rpm, stir time: 12 min, cast temperature: 720 °C and ZrO_2: 5 wt.%) (refer Table 5.2). The suggested optimal levels are different from those of L_9 experiments and this occurs due to multi-factor nature of experiments (i.e., levels ^{factors} = 3^4: 81 experiments set).

5.1.1.2 Effect of factors on wear loss

Figure 5.1(b) shows the main effect factors on wear loss. Increase in weight percentage of ZrO_2 reinforced to Al-12.5%Si after 10%, showed increase in wear loss. Increase in Wt. % of ZrO_2 reinforcement leads to large particle clusters resulting in low wettability with the matrix material and tends to pull out from the matrix subjected to loading conditions. Large voids or pores occur in such fabricated composites. The increase in stir speed and stir time enable homogeneous particle distribution and increases inter-particle distribution by providing sufficient space between the reinforcement particles which reduces the wear loss. Conversely, particle agglomeration may take place at low stir speed and stir time. Low and higher levels of casting temperature results in increase in wear loss. Low pouring temperature results in particle agglomeration and premature solidification. However, too high pouring temperature tends to undergo prolonged solidification which results in undesired microstructure. All the factors showed dominant effect towards wear loss, of which ZrO_2 reinforcement showed highest contribution, followed by stirring time, stir speed and pouring temperature. Optimal factor levels for reducing wear loss of the composites were found to be $A_3B_3C_2D_2$ (i.e., stir speed: 600 rpm, stir time: 12 min, cast temperature: 720 °C and ZrO_2: 10% Wt.). It is noted that the optimal levels determined for minimum wear loss are not one among the Taguchi L_9 experiments.

5.1.1.3 Effect of factors on ultimate tensile strength

The main effect of stir casting variables on ultimate tensile strength of the Al-12.5%SiZrO_2 composites were presented in Figure 5.1(c). Negligible change in ultimate tensile strength values was observed with increased percent of ZrO_2 reinforcement from 5 to 10%. However, beyond the critical limit of reinforcement (i.e., after 10% wt. of ZrO_2), the advantages in reinforcing particles were weakened probably due to the porosity or voids as a result of particle clusters which resulted in reduced UTS. Increased values of stirring speed create vortex in an aluminium melt by setting up centrifugal currents. This helps to disperse the reinforcement particles deep inside the melt homogeneously that results in higher UTS of the composites. The reinforced particle's distribution in aluminium matrix is reliant on creation

of vortex by stir speed and stir time. If stir time is not sufficient then some of the reinforcement particles may float or agglomerate due to difference in density, and surface tension between the matrix and reinforcement. Conversely, prolonged stirring duration results in porosity (because vortex possess has tendency to suck air in to the aluminium melt) in composites. The cast temperature influences the viscosity and gas pick up in the aluminium melt. It is important to note that, ZrO_2 reinforcement is found to have maximum percent contribution followed by stir speed, casting temperature and stir time (refer Table 5.2). Higher ultimate tensile strength could be expected from the set of optimal stir casting conditions i.e. $A_3B_2C_2D_2$ (i.e., stir speed: 600 rpm, stir time: 8 min, cast temperature: 720 ºC and ZrO_2: 10% wt.). The determined optimal values that maximize the ultimate tensile strength were not the set of Taguchi L_9 experiments.

Table 5.2: Pareto ANOVA results of stir casting technique

Output	Factors	Levels	Stir speed (rps)	Stir time (s)	Cast temperature (°C)	ZrO_2 %
Hardness	Mean	1	36.03	36.14	36.25	36.36
	Factor	2	36.34	36.27	36.26	36.31
	Levels	3	36.31	36.28	36.17	36.02
	Mean square deviation		0.17	0.04	0.01	0.20
	Percent contribution		40.90	8.70	3.04	47.36
	Optimal levels					
Wear loss	Mean	1	-22.86	-22.62	-21.79	-21.37
	Factor	2	-21.95	-22.37	-21.48	-21.34
	Levels	3	-21.03	-20.85	-22.57	-23.13
	Mean square deviation		5.03	5.50	1.90	6.34
	Percent contribution		26.81	29.30	10.11	33.77

	Optimal levels					
Ultimate tensile strength	Mean	1	44.05	44.32	44.65	45.00
	Factor	2	44.56	44.79	44.86	45.02
	Levels	3	45.19	44.69	44.29	43.78
	Mean square deviation		1.94	0.36	0.49	3.04
	Percent contribution		33.28	6.16	8.44	52.12
	Optimal levels					

5.1.1.4 Multiple-objective optimization of stir casting process

The limitations of Taguchi method in simultaneous optimization of multiple outputs were overcome effectively by applying Super ranking Concept (SRC). In the current study, multi-objective optimization corresponds to three responses with conflicting requirements (minimize: wear loss (WL); maximize: Ultimate Tensile Strength (UTS) and hardness) were solved for stir casting process. The experimental output data are transformed to S/N ratio data (refer Table 5.1). Ranks were assigned for each response corresponding to S/N ratio data. For each experimental trial, the assigned ranks of each response variable were then squared and added to obtain the composite value referred to as sum of squared rank (SSR). Pareto ANOVA was constructed corresponding to SSR values to determine the factor contribution and optimal levels considering all outputs. In SRC computation, the highest rank (low value: 1) is assigned corresponding to highest S/N ratio. Higher values correspond to stir speed and stir time resulted in better quality in stir cast composites (refer Figure 5.1(d)). The casting temperature and ZrO_2 reinforcements maintained at middle values showed improved performance, considering all outputs (refer Figure 5.1(d)). The percentage contribution of each factor on individual output and considering all output was found to be different and was expected due to their nature of influence (refer Table 5.4). It is to be noted that, all factors (stir speed: 28.06%; stir time: 25.32%; cast temperature: 7.72% and ZrO_2 wt.%: 38.9%) contributed more towards optimizing the multiple outputs (refer Figure 5.2). The optimal factor levels in achieving better quality, considering outputs are found to be $A_3B_2C_2D_2$ (i.e., stir speed: 600 rpm, stir time: 8 min, cast temperature: 720 ºC and ZrO_2: 10% wt.). The SRC and Pareto ANOVA proved their efficacy in determining optimal factor levels which are not the set of L_9 experiments (refer Table 5.1 and 5.4).

Table 5.3: Summary of results of super ranking concept: stir casting process

Exp. No.	Signal-to-noise ratio, dB			Ranking			Square ranking			Sum of squared rank
	Hardness HV	UTS MPa	WL mg	Hardness HV	UTS MPa	WL mg	Hardness HV	UTS MPa	WL mg	
L_1	36.10	44.23	-22.80	7	7	7	49	49	49	147
L_2	36.18	44.92	-22.21	5	4	4	25	16	16	57
L_3	35.82	43.01	-23.58	9	9	9	81	81	81	243
L_4	36.07	43.72	-23.35	8	8	8	64	64	64	192
L_5	36.46	44.84	-22.41	3	5	5	9	25	25	59
L_6	36.50	45.11	-20.09	2	2	2	4	4	4	12
L_7	36.24	45.02	-21.73	4	3	3	16	9	9	34
L_8	36.16	44.60	-22.48	6	6	6	36	36	36	108
L_9	36.52	45.94	-18.89	1	1	1	1	1	1	3

`

Table 5.4 Pareto ANOVA results: stir casting process

Factors	Levels	Stir speed (rps)	Stir time (s)	Cast temperature (°C)	ZrO_2 (%)
Mean	1	42.06	39.88	35.20	29.44
Factor	2	34.22	37.07	30.11	29.11
Levels	3	26.95	26.28	37.92	44.68
Mean square deviation		342.71	309.29	94.33	475.06
Percent contribution		28.06	25.32	7.72	38.90
Optimal levels					
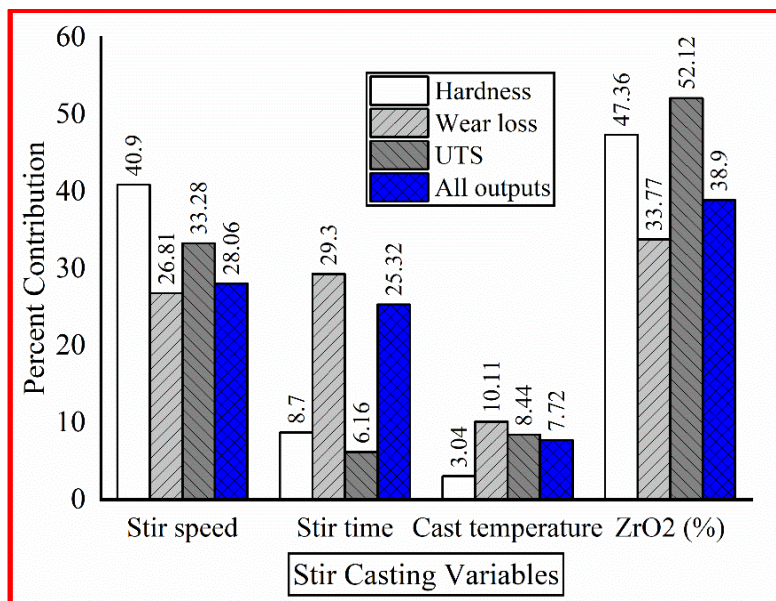
Figure 5.2: Percent contribution of factors on different responses (Hardness in HV; Wear loss in mg and UTS in MPa)

5.1.1.5 Confirmation experiments

Table 5.5 shows the comparison of experimental results obtained for initial and optimal conditions. The optimal conditions for stir casting process for individual responses were determined through Taguchi method, whereas the optimal conditions corresponding to multiple responses were determined through SRC. Taguchi method based one at a time optimal condition resulted with improved hardness, wear loss and UTS was found equal to

71

`

6.58%, 37.68, and 29.26%, respectively. Single optimal conditions for multi-objective functions are determined viz. SRC resulted with improvement in 37.68% of wear loss, 25.02% of UTS and 5.64% of hardness, compared to initial experimental conditions of stir casting process (refer). The improved results justify the efficacy of Taguchi and SRC techniques.

Table 5.5: Confirmation experimental results for optimal conditions of stir casting process

Condition	Stir casting condition	Responses	Percent improvement
Initial (Table 2)	Stir speed: 500 rpm Stir time: 4 min Cast temperature: 680 °C ZrO$_2$ %wt.: 5	WL: 13.8 gm UTS: 162.7 MPa Hardness: 63.8	
Optimal condition for hardness	Stir speed: 550 rpm Stir time: 12 min Cast temperature: 720 °C ZrO$_2$ %wt.: 5% wt.	Hardness: 68	6.58%
Optimal condition for wear loss	Stir speed: 600 rpm Stir time: 12 min Cast temperature: 720 °C ZrO$_2$ %wt.: 10% wt.	WL: 8.6 gm	37.68%
Optimal condition for UTS	Stir speed: 600 rpm Stir time: 8 min Cast temperature: 720 °C ZrO2 %wt.: 10% wt.	UTS: 210.3 MPa	29.26%

Optimal condition for all outputs	Stir speed: 600 rpm	WL: 8.6 gm	WL: 37.68%
	Stir time: 12 min	UTS: 203.4 MPa	UTS: 25.02%
	Cast temperature: 720 ºC		Hardness: 5.64%
	ZrO_2 %wt.: 10% wt.	Hardness: 67.4	

5.1.2 Hot Pressing Technique

Hot pressing technique ensures fine grain structure with low porosity that further enhances the properties of stir cast composite samples (prepared as per optimized condition), reinforced by 10% wt. of ZrO_2 to Al-12.5%Si matrix. Therefore, hot pressing technique was applied on stir cast Al-12.5%Si-10%ZrO_2 specimens. Hot pressing technique with different sets of influencing parameters (pressure, temperature and dwell time) were studied to examine their factor's contribution and optimal levels on wear loss, hardness and UTS. Taguchi L_9 experiments were carried out to collect the experimental input-output data corresponding to hot pressing process (refer Table 5.5). S/N ratio values corresponding to the experimental data are presented in Table 5.6.

Table 5.6: Taguchi experimental conditions for hot-pressing process

Exp.	Experimental Input			Experimental output			Signal-to-noise ratio, dB		
No.	E, ^{o}C	F, MPa	G, min	Hardness, HV	UTS, MPa	WL, mg	Hardness HV	UTS MPa	WL mg
L_1	400	60	20	70.2	216.1	8.4	36.93	46.69	-18.49
L_2	400	80	30	72.3	233.6	7.5	37.18	47.37	-17.50
L_3	400	100	40	72.7	236.5	7.1	37.23	47.48	-17.03
L_4	440	60	30	71.7	227.5	8.0	37.11	47.14	-18.06
L_5	440	80	40	72.8	239.1	6.6	37.24	47.57	-16.39
L_6	440	100	20	73.3	241.9	5.2	37.30	47.67	-14.32
L_7	480	60	40	70.6	220.9	8.3	36.98	46.88	-18.38
L_8	480	80	20	71.3	233.4	7.9	37.06	47.36	-17.95
L_9	480	100	30	72.3	228.9	8.2	37.18	47.19	-18.28

Pareto ANOVA was used to estimate the hot-pressing factor effects and corresponding optimal levels. The summary of results of hot-pressing techniques are presented in Table 5.7.

Table 5.7: Pareto ANOVA results for hot-pressing process

Output	Factors	Levels	Temperature (°C)	Pressure (MPa)	Dwell time (min)	Total
Hardness	Mean	1	37.20	37.11	37.16	111.59
	Factor	2	37.25	37.19	37.21	
	Levels	3	37.15	37.29	37.23	
	Mean square deviation		0.014	0.049	0.008	0.071
	Percent contribution		19.47	69.08	11.46	100
	Optimal levels		$E_2F_3G_3$ (Not the combination of L_9 experiments)			
Wear loss	Mean	1	-17.67	-18.31	-16.92	
	Factor	2	-16.26	-17.28	-17.95	-52.13
	Levels	3	-18.20	-16.54	-17.27	
	Mean square deviation		06.07	04.74	01.64	12.44
	Percent contribution		48.77	38.07	13.17	100.00
	Optimal levels		$E_2F_3G_1$			
Ultimate tensile strength	Mean	1	47.18	46.91	47.24	
	Factor	2	47.46	47.43	47.23	141.79
	Levels	3	47.15	47.45	47.31	
	Mean square deviation		0.18	0.57	0.01	0.76
	Percent contribution		23.52	75.09	1.39	100
	Optimal levels		$E_2F_3G_3$ (Not the combination of L_9 experiments)			

`

5.1.2.1 Effect of factors on Hardness

Figure 5.3(a) explains the influence of hot-pressing factors on the material hardness. Increased values of pressure showed linear increase in hardness values. Pressure on composite samples tend to force the part close to die surface walls and thereby full densification could be achieved resulting in better hardness. At low temperature, the composites undergo premature solidification, whereas significant grain growth might take place due to slow cooling at high temperatures and also causing lower hardness values. Higher dwell time under pressurization is always desirable to attain full compaction (i.e., pore closure, if any) that improves hardness values. The impact of dwell time or holding time on hardness values are negligibly small compared to pressure and temperature. The contributions of pressure, temperature and dwell time were found equal to 69.08%, 19.47% and 11.46%, respectively (refer Table 5.7). The optimal hot-pressing conditions that maximize the hardness values were found to be $E_2F_3G_3$ (temperature: 400 ^oC, pressure: 100 MPa, and dwell time: 40 min).

5.1.2.2 Effect of factors on Wear loss

Figure 5.3(b) explains the main factor effects on wear loss under hot-pressing conditions. High values of pressure with corresponding lower dwell time are responsible for low values of wear loss. Higher pressure forces the metal close to die surface walls, resulted in better heat transfer, fine grain structure and closure of pores in composites. Minimum wear loss was observed when the temperature is set at fixed middle level. The pressure is found to have dominant effect with contribution of 48.77%, temperature of 38.07%, and dwell time of 13.17% towards wear loss (refer Table 5.7). The optimal factors and levels ($E_2F_3G_1$: temperature: 480 ^oC, pressure: 100 MPa, and dwell time: 20 min) are responsible for minimum wear loss.
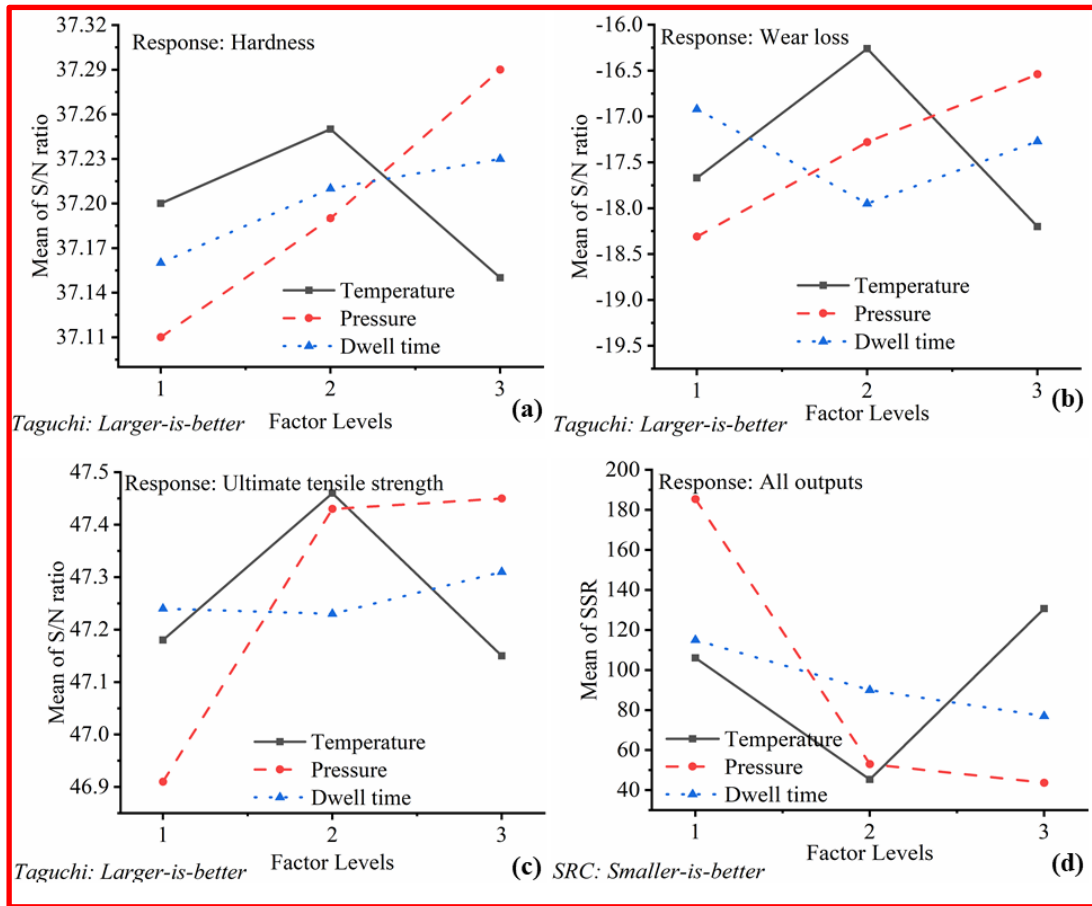
Figure 5.3: Main effect plots of S/N ratio of responses: a) Hardness, b) Wear loss, c) Ultimate tensile strength, and d) All outputs (Temperature in °C, Pressure in Pa,Dwell time in seconds)

5.1.2.3 Effect of factors on UTS

The ultimate tensile strength also showed similar trend to that of hardness values as observed in Figure 5.3(c). This occurs probably due to strong correlation between the hardness and ultimate tensile strength. It should be noted that, the pressure after crossing the middle level showed no significant benefit. Temperature set at middle level and dwell time at higher level resulted in improved ultimate tensile strength of composites. The percent of contribution of pressure, dwell time, and temperature were found to be 75.09%, 1.39% and 23.52%, respectively (refer Table 5.7). The optimal factors and levels that maximize the ultimate tensile strength were found to be $E_2F_3G_3$ (temperature: 440 ^{o}C, pressure: 100 MPa, and dwell time: 40 min), responsible for maximum strength in the composites.

5.1.2.4 Multiple-objective optimization of hot-pressing process

Super ranking concept is adopted to optimize the hot-pressing condition for conflicting responses (*Minimum:* WL, *Maximum:* UTS and hardness). The steps in super ranking concept applied for hot-pressing conditions are similar to the stir casting process and the results obtained are presented in Table 5.8 and 5.9. The optimal hot-pressing conditions responsible for better quality composites was found to be $E_2F_3G_3$ (temperature: 440 ℃, pressure: 100 MPa, and dwell time: 40 min). The pressure and temperature showed maximum contribution equal to 73.18% and 22.48%, and dwell time of 4.35%, respectively (refer Figure 5.4 & Table 5.9). It is important to note that, percent of contribution and optimal factor levels corresponding to each individual output and multiple outputs were found to be different and this might be due to nature of influence of input factors on outputs (refer Figure 5.4). It was also observed that the optimal factors and levels for both individual outputs (excluding wear loss) and multiple outputs are often different from those of L_9 experiments.

Table 5.8: Summary of results of super ranking concept

Exp. No.	Signal-to-noise ratio, dB			Ranking			Square ranking			Sum of squared rank
	Hardness HV	UTS MPa	WL mg	Hardness HV	UTS MPa	WL mg	Hardness HV	UTS MPa	WL mg	
L_1	36.93	46.69	-18.49	9	9	9	81	81	81	243
L_2	37.18	47.37	-17.50	4	4	4	16	16	16	48
L_3	37.23	47.48	-17.03	3	3	3	9	9	9	27
L_4	37.11	47.14	-18.06	6	7	6	36	49	36	121
L_5	37.24	47.57	-16.39	2	2	2	4	4	4	12

L_6	37.30	47.67	-14.32	1	1	1	1	1	1	3
L_7	36.98	46.88	-18.38	8	8	8	64	64	64	192
L_8	37.06	47.36	-17.95	7	5	5	49	25	25	99
L_9	37.18	47.19	-18.28	4	6	7	16	36	49	101

Table 5.9: Results of Pareto ANOVA Analysis

Factors	Levels	Temperature (°C)	Pressure (MPa)	Dwell time (min)	Total
Mean	1	106.00	185.33	115.00	282.00
Factor	2	45.33	53.00	90.00	
Levels	3	130.67	43.67	77.00	
Mean square deviation		11570.67	37668.67	2238.00	51477.3
Percent contribution		22.48	73.18	4.35	100
Optimal levels		$E_2F_3G_3$ (Not the combination of L_9 experiments)			

`
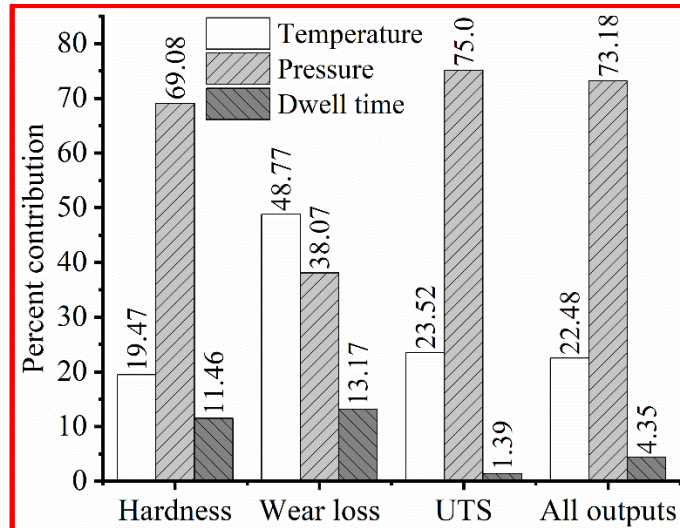
Figure 5.4: Percent contribution of Hot-pressing Variables (Hardness in HV; Wear loss in mg and UTS in MPa)

5.1.2.5 Confirmation experiments

Table 5.10 shows the comparative results of initial and optimal experimental conditions for hot-pressing technique. Taguchi method determined identical optimal condition for both hardness and UTS resulted in increase of 4.7% and 13.05%, respectively, for the output responses (refer Table 5.10). The optimal conditions for minimum wear loss resulted with an improvement of 42.9% (refer Table 5.10). It is important to note that, the optimal conditions corresponding to SRC resulted in 39.29% decrease in WL, whereas increase in UTS, and hardness by 11.54% and 4.88%, respectively (refer Table 5.10). Taguchi and SRC are an effective technique to perform optimization task.

`

Table 5.10: Confirmation experimental results for optimal conditions of hot-pressing process

Condition	Hot pressing condition	Responses	Percent improvement
Initial (Table 7)	Temperature: 400 ºC Pressure: 60 MPa Dwell time: 20 min	WL: 8.4 gm UTS: 216.1 MPa Hardness: 70.2	
Optimal condition for hardness	Temperature: 440 ºC Pressure: 100 MPa Dwell time: 40 min	Hardness: 73.5	4.7%
Optimal condition for wear loss	Temperature: 440 ºC Pressure: 100 MPa Dwell time: 20 min	WL: 4.8 gm	42.9%
Optimal condition for UTS	Temperature: 440 ºC Pressure: 100 MPa Dwell time: 40 min	UTS: 244.3 MPa	13.05%
Optimal condition for all outputs	Temperature: 440 ºC Pressure: 100 MPa Dwell time: 40 min	WL: 5.1 gm UTS: 243.5 MPa Hardness: 73.8	WL: 39.29% UTS: 11.54% Hardness: 4.88%

5.1.3 Comparison of Hot-pressing and Stir casting process

Table 5.11 compare the optimized properties obtained from stir casting and hot-pressing process. Hot-pressing technique was applied on the composites prepared according to the optimized parametric conditions of stir casting process. Hot-pressing technique in

comparison with stir casting process resulted with reduced WL of 40.7%, and increased with 19.71% of UTS and 9.5% of hardness values.

Table 5.11: Comparison of properties of Hot-pressed and Stir cast composites

Optimized properties of processes		Percent Improvement
Stir casting	Hot-pressing	
Wear loss: 8.6 gm	Wear loss: 5.1 gm	40.70%
UTS: 203.4 MPa	UTS: 243.5 MPa	19.71%
Hardness: 67.4	Hardness: 73.8	09.50%

Table 5.12: Confirmation experimental results for optimal conditions of stir casting process

Condition	Process variables	Responses	Composite Designation
Initial (Table 4.1)	Stir speed: 500 rpm Stir time: 4 min Cast temperature: 680 ºC ZrO_2 %wt.: 5	WL: 13.8 gm UTS: 162.7 MPa Hardness: 63.8	S1 (Al-12.5%Si-5% ZrO_2)
Optimal condition for all outputs	Stir speed: 600 rpm Stir time: 12 min Cast temperature: 720 ºC ZrO_2 %wt.: 10% wt.	WL: 8.4 gm UTS: 203.4 MPa Hardness: 67.4	S2 (Al-12.5%Si-10% ZrO_2)

`

Initial (Table 7) Hot Pressing	Temperature: 400 ºC Pressure: 60 MPa Dwell time: 20 min	WL: 8.4 gm UTS: 216.1 MPa Hardness: 70.2	S1-HP (Al-12.5%Si-10%ZrO$_2$)
Optimal condition for all outputs Hot Pressing	Temperature: 440 ºC Pressure: 100 MPa Dwell time: 40 min	WL: 5.1 gm UTS: 243.5 MPa Hardness: 73.8	S2-HP (Al-12.5%Si-10%ZrO$_2$)

5.1.4 Microstructure Characterization

Microstructural characterization of Stir cast and Hot-pressed Al-12.5%Si-ZrO$_2$ composites are depicted in Figure 5.5. Optical and SEM micrographs have been used to describe the surface morphology of the ZrO$_2$ particles. Bright silvery nearly spherical particle resembles ZrO$_2$ particles. Figures 5.5(a-d) shows the OM and SEM of S1 (Al-12.5%Si-5%ZrO$_2$) and S2 (Al-12.5%Si-10%ZrO$_2$) composites in stir cast condition. From Figures 5.5(a-d), it can be observed that the development of dendritic structures in which dendrite arm expand parallel to favourable growth patterns. Grains are driven by the direction of heat flow, that will grow faster and inhibit the development of several other grains, contributing to a columnar morphology (Hogan 2001; Dann 1979). Figures 5.5(a-d)indicates the dispersal of the ZrO$_2$ particles in the Al-12.5%Si matrix. The morphology of most of the ZrO$_2$ particles is almost spherical in nature. We can also observe strong interfacial bonding of ZrO$_2$ with the Al-12.5%Si alloy which further helps in achieving better mechanical properties (Avinash et al. 2016a; Parthasarathy et al. 2017).

Figures 5.5 (e-h) shows the OM and SEM of S1-HT (Al-12.5%Si-10%ZrO$_2$) and S2-HT (Al-12.5%Si-10%ZrO$_2$) composites in Hot-Pressing condition. Even dispersal of reinforcement particles (ZrO$_2$) in the matrix alloy is required to visualise composite with good mechanical properties (Qingping et al. 2014). Hot-Pressing and applying high values of pressure would have led to the absence of pores and grain refinement of composites indicating sound castings (Elias et al. 2004). Homogeneity of ZrO$_2$ particles along the surface is observed. Figures 5.5 (e-h) shows the uniform dispersal of the ZrO$_2$ particles in the Al-12.5%Si matrix. Uniform dispersion has a better adhesion contact area between both the matrix and the reinforcement,

`

thereby enhancing the mechanical properties of the composites. Figure 5.5 (i) shows the Energy dispersive x-ray spectra analysis of Al-12.5%Si-ZrO$_2$ composites. In Figure 5.5 (h), Zr and O, peaks confirm the presence of ZrO$_2$ as reinforcement. Also, Al and Si correspond to Al-12.5%Si alloy.
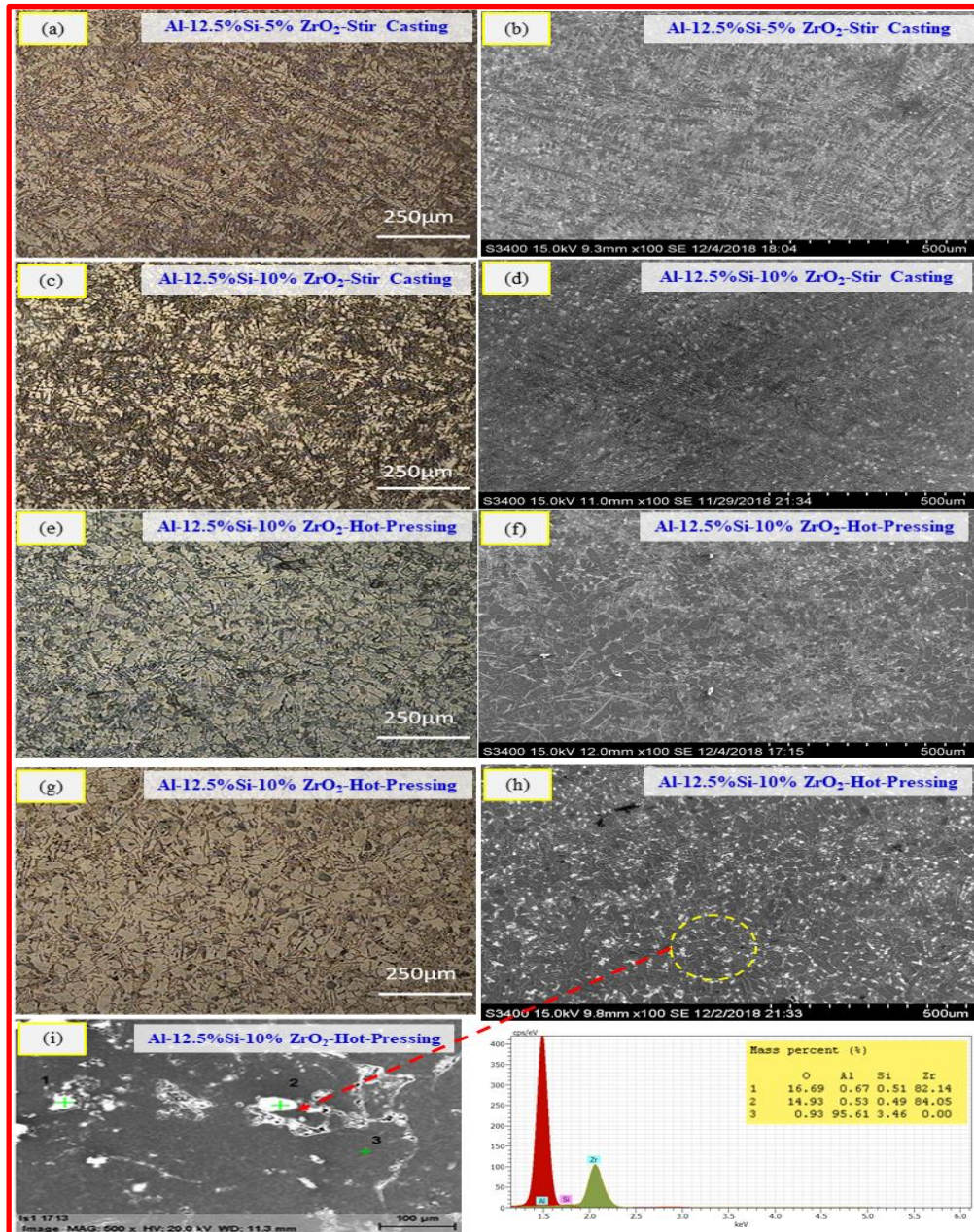
Figure 5.5: Microstructural characterization of Stir cast and Hot-pressed Al-12.5%Si-ZrO$_2$ composites (Table 5.10): (a-b) Optical & SEM micrographs of stir cast Al-12.5%Si-5% ZrO$_2$- as cast, (c-d) Optical & SEM micrographs of stir cast Al-12.5%Si-10%ZrO$_2$- optimal condition, (e-f) Optical & SEM micrographs of Hot pressed Al-12.5%Si-10%ZrO$_2$- as cast, (g-h) Optical & SEM micrographs of Hot pressed Al-12.5%Si-10% ZrO$_2$ optimal condition

`

5.1.5 Wear Surface Morphology

Wear tracks of Stir cast and Hot-pressed Al-12.5%Si-ZrO$_2$ composites are shown in Figure 5.6. Figure 5.6 (a) denotes delaminated area, Figure 5.6 (b) denotes Narrow abrasive grooves, Figure 5.6 (c) denotes Dense abrasive grooves, Figure 5.6 (d) denotes Debris. The wear tracks of Al-12.5%Si-ZrO$_2$ composites exhibited dissimilar wear profile when subjected to stir casting (refer Figure 5.6(a-b)) and hot-pressed (Figure 5.6(c-d)). This confirms the change in wear mechanism dominating abrasion wear. A large number of delaminated area, cavities and thick grooves have been observed on the surface of the Al-12.5%Si-ZrO$_2$ composites fabricated by stir casting as shown in Figure 5.6 (a-b). But the surface of the Al-12.5%Si-ZrO$_2$ composites subjected to hot-pressing show thin abrasive grooves, few debris, and mild abrasion areas. Figure 5.6 (a) shows higher degree of plastic deformation on the stir cast S1 composite (Al-12.5%Si-5%ZrO$_2$) due to the rubbing of wear pin and disc at a high load (Yadav et al. 2020) which is confirmed by SEM micrograph. It can also be observed that the width of the wear groves is showing maximal wear loss (13.8 g) which is well augmented with the attained results viz. maximal wear loss at 30 N load.

Figure 5.6 (b) shows plastic deformation of minor extent on the stir cast S2 composite (Al-12.5%Si-10%ZrO2) at a high load of 30N, which is confirmed by SEM micrograph. It can also be observed that the wear groves are showing minimal wear loss, i.e., 8.6 g and higher hardness of 67.4 VHN which is well augmented with the attained results viz. minimal wear loss at 30 N load. Also, the presence of hard and higher percentage of ceramic particles in S2 composites are more when compared to S1 composites. These ceramic particles act as load-bearing material which further helps in mitigating wear. Many researchers have observed similar findings (Avinash et al. 2016b; Lakshmikanthan et al. 2019; Lakshmikanthan et al. 2020).

Figure 5.6 (c) shows a mild abrasion region on the hot pressed S1-HP composite (Al-12.5%Si-10%ZrO$_2$) which is confirmed by SEM micrograph. Compared to Figure 5.6 (a-b), it can be witnessed from Figure 5.6 (c), the wear groves width is less with marginal wear loss, i.e., 8.4 g. Also, the hardness of 70.2 VHN higher than that of those produced via stir casting method which could be another reason for the improved of wear resistance. The samples produced via simultaneous applying of high values of pressure with corresponding lower dwell time are responsible for low values of wear loss (Moazami-Goudarzi et al. 2016). The wear track surface was concealed with numerous thin and narrow grooves running parallel to

sliding direction and a few wear debris particles as seem in Figure 5.6 (c), which is an indicative of mild abrasive wear mechanism (Sajjan et al., 2017).
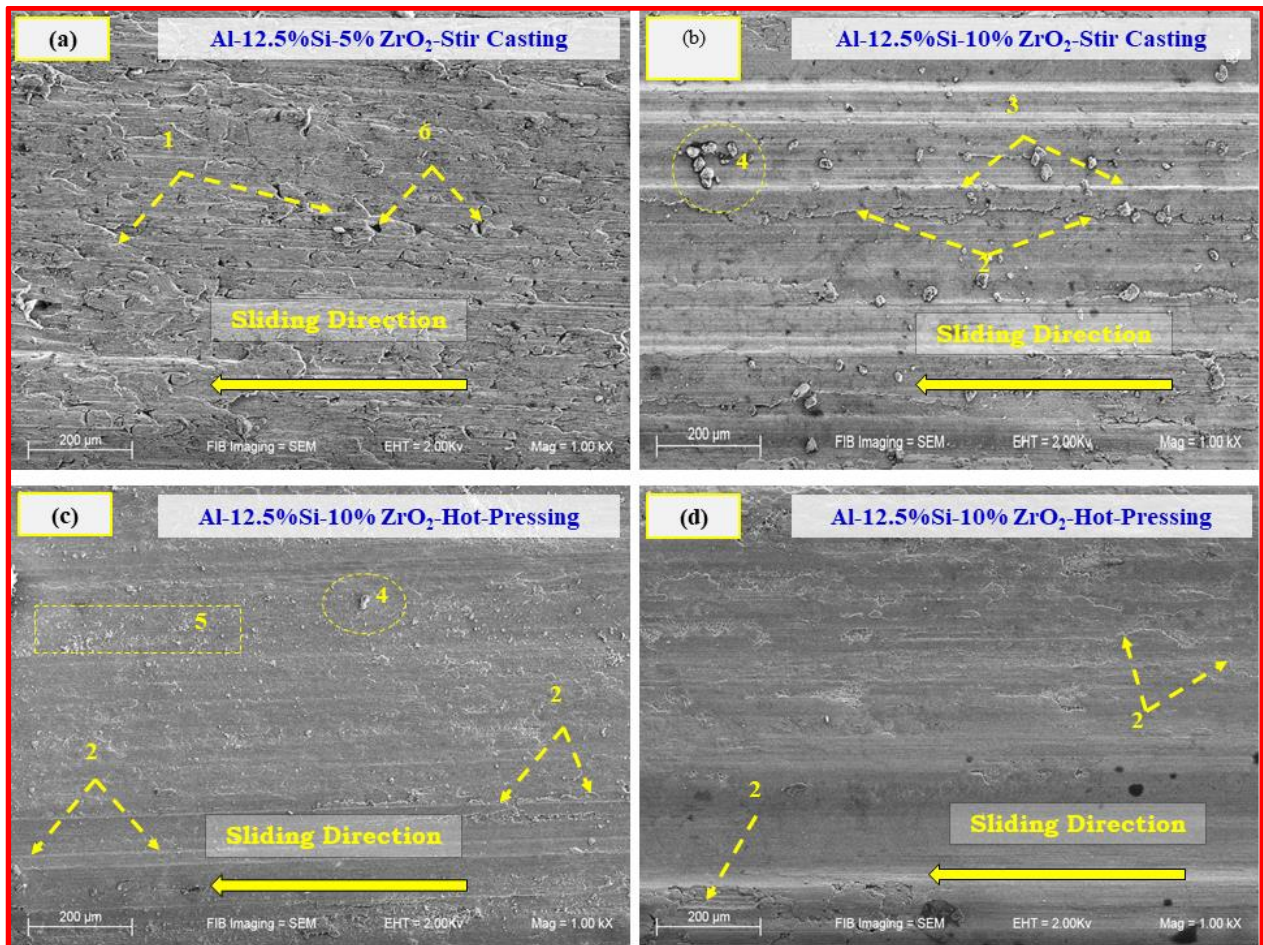
Figure 5.6: Wear surface Morphology of Stir cast and Hot-pressed Al-12.5%Si-ZrO₂ composites (Table 5.13) Where (a) stir cast Al-12.5%Si-5% ZrO₂ as cast, (b) stir cast Al-12.5%Si-10%ZrO₂ optimal condition, (c) Hot pressed Al-12.5%Si-10%ZrO₂ as castm, (d) Hot pressed Al-12.5%Si-10% ZrO₂- optimal condition

Figure 5.6 (d) shows a similar surface to that of S1-HP composite (i.e., mild abrasion region) which is confirmed by SEM micrograph. Compared to Figure 5.6 (a-c), it can be witnessed that in Figure 5.6 (d) the wear tracks are smooth with thin grooves showing least wear loss of 5.1 grams. The higher hardness (73.8 VHN) compared to other composites and grain refinement due to hot pressing may be one of the causes for the superior of wear rate (Kavimani et al. 2017).

`

Summary

For sustainable use of natural resources and mitigation of cast defects, the present work employs two-step process i.e., stir-casting followed by hot pressing. The remarks on obtained results are discussed below,

- Stir casting is an ideal processing route employed to prepare Al-12.5%Si composites reinforced with varying wt. percentage of ZrO_2 particles. ZrO_2 reinforcements showed maximum impact followed by stir speed, stir time and casting temperature on casting properties (ultimate tensile strength, hardness, and wear loss).

- Super ranking concept determine optimal stir casting conditions which resulted in 37.68% reduction in wear loss (13.8 g to 8.4 g), 25.02% and 5.64% increase in UTS (162.7 to 203.4 MPa) and hardness (63.8 to 67.4) values compared to initial stir casting conditions. Pareto ANOVA determined optimal stir casting conditions, and corresponding resultant properties justify the effectiveness of models developed and the analysis performed.

- The samples prepared as per stir cast optimized conditions are subjected to hot pressing technique to heal or reduce the pores that could results in enhanced properties. The influence of hot-pressing variables (i.e., temperature, pressure, and dwell time) on properties (wear loss, UTS and hardness) were studied experimentally. The effect of pressure contributions are more to close pores that results in better properties, followed by temperature and dwell time.

- Super ranking concept based optimal conditions resulted in 39.29% reduction in wear loss (8.4 gm to 5.1 gm), 11.54% increase in UTS (216.1 to 243.5 MPa) and 4.88% rise in hardness values (70.2 to 73.8) when compared with initial hot-pressing conditions.

- The optimized stir cast components subjected to hot-pressing technique results in 40.7% reduced wear loss, 19.71% increase in UTS, and 9.5% increase in hardness values. Therefore, based on results even stir cast optimized conditions have greater probability to improve properties subjected to hot-pressing technique.

- The statistical results of composite properties obtained for initial and optimized conditions of stir cast and hot-pressing techniques are strongly justified based on the findings of microstructure and worn surface morphologies.

5.2 Investigation of the mechanical properties and evolution of microstructure of spray formed and stir cast composites

5.2.1 Evaluation of micro hardness
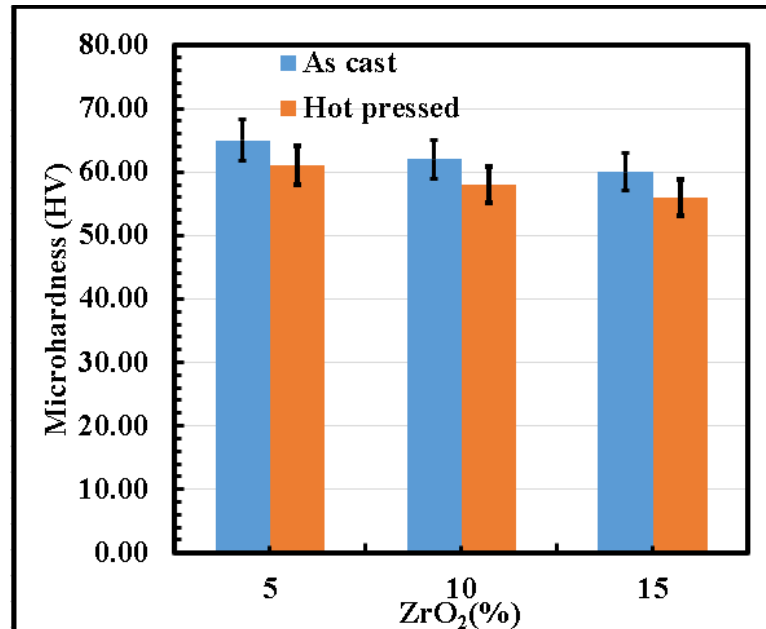
Figure 5.7: Micro hardness of AlSi-ZrO₂ composite

It can be inferred from Figure 5.7 that as cast reinforced zirconium oxide exhibits better hardness as compared to hot pressed. This is explained by the observation of decrease in the grain size and heating slightly above the recrystallization temperature. With a rise in zirconium oxide, hot pressing's hardness reduces. This is due to limited reduction in the porosity and unable to break up the agglomeration after hot pressing. Most of the information in this section has been published (**https://doi.org/10.1080/14484846.2021.1913872**).

`
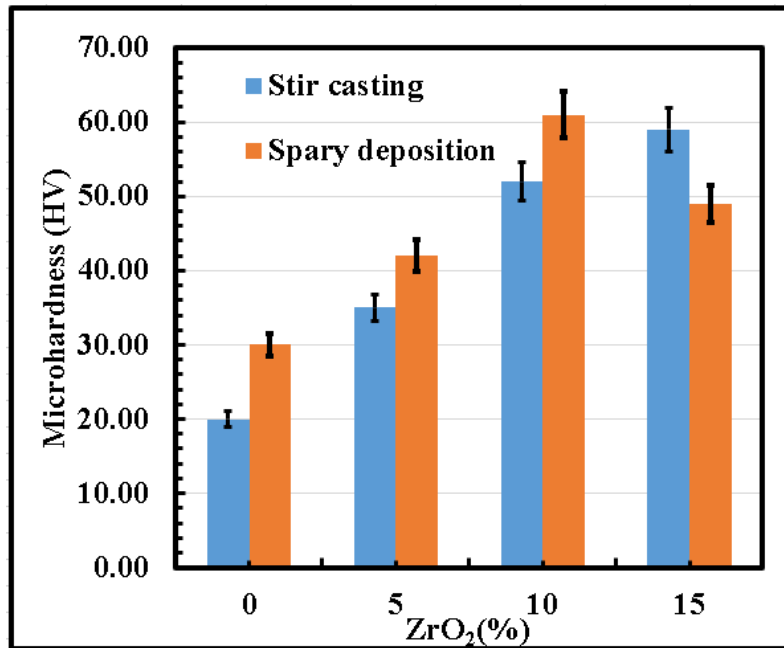
Figure 5.8: Micro Hardness plot of stir cast and spray deposited Al-12.5Si alloy matrix composite reinforced with ZrO₂ particles

Figure 5.8 shows the micro hardness values for stir cast and spray deposition treated composites with varying percentage of weight of ZrO_2 particles and silicon particles. For both stir cast and spray deposition treated composites, the micro hardness value increases linearly up to 10 wt. percent ZrO_2 particles and then begins to decrease. With increasing ZrO_2 and silicon weight percentage, this phenomenon was observed in all cases. This clearly indicates that the hardness of the Al matrix will increase as the number of hard ZrO_2 particles increases. ZrO_2 particles serve as a barrier to dislocation flow in the aluminium matrix. (Kumarswamy et al., 2018). As a result, increasing the number of ZrO_2 particles increases the density of barriers and dislocations. In addition, as opposed to stir casting manufacturing, spray deposition results in a more uniform distribution and homogeneous dispersion of ZrO_2 particles, resulting in higher micro hardness values. As a result, we can deduce that under spray deposition, an Aluminium Silicon alloy matrix reinforced with 12.5% ZrO_2 particles can be the optimum choice for obtaining larger micro hardness value.
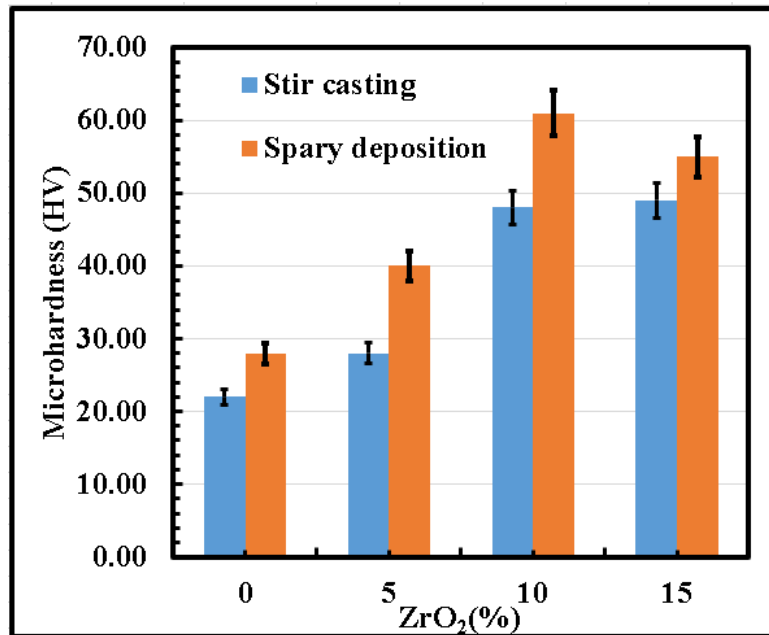
Figure 5.9: Micro Hardness interaction plot of stir cast and spray deposited Al-12.5Si alloy matrix composite reinforced with ZrO₂ particles

Figure 5.9 shows the micro hardness strength interaction plot obtained from Taguchi's design of experiments for stir cast and spray deposition of AlSi alloy matrix reinforced with ZrO_2 particles for 12.5 wt. % of Silicon. From the interaction plot, it can be observed that reinforcement of 15 wt. % of ZrO_2 particles in composite results in the maximum micro hardness value under spray deposition processing method. The micro hardness test specimens of spray deposition and stir casting method of AlSi-ZrO_2 alloy are shown in Figure 5.10 & 5.11.
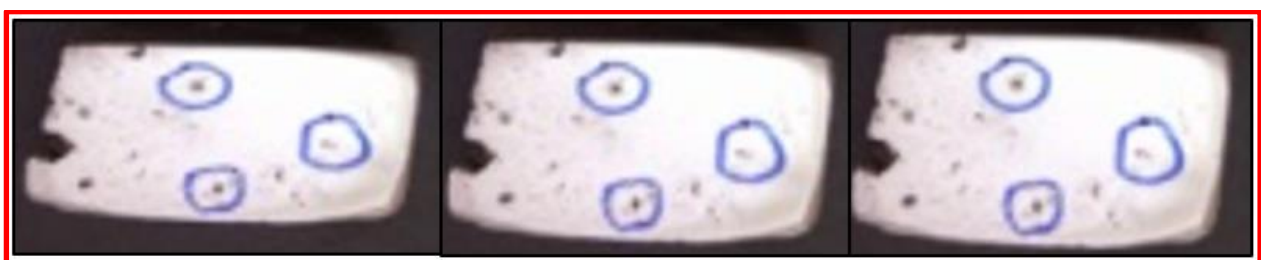
| (a) | (b) | (c) |

Figure 5.10: Images of micro hardness test specimens of stir cast Al-Si alloy matrix composite reinforced with a) 5% b) 10% c) 15% ZrO₂ particles for 12.5 wt. % of Silicon

`

<div align="center">

(a)   (b)   (c)

Figure 5.11: Images of micro hardness test specimens of spray deposited Al-Si alloy matrix composite reinforced with a) 5% b) 10% c) 15% ZrO2 particles for 12.5 wt. % of Silicon

</div>

In Figure 5.12, the effect of weight percentage of silicon and reinforced ZrO_2 particles on micro hardness is presented. As it could be seen, for the silicon wt. %, this trend was always in an increasing mode with increase in silicon percentage. The percentage of contribution (P %) of different factors selected for micro hardness is reported in Table 5.13. The values of P % for Zirconium were 62.82%, Silicon 22.06% and processing technique 14.18%. Therefore, it is fair to conclude that Zirconium gave the maximum contribution towards micro hardness.
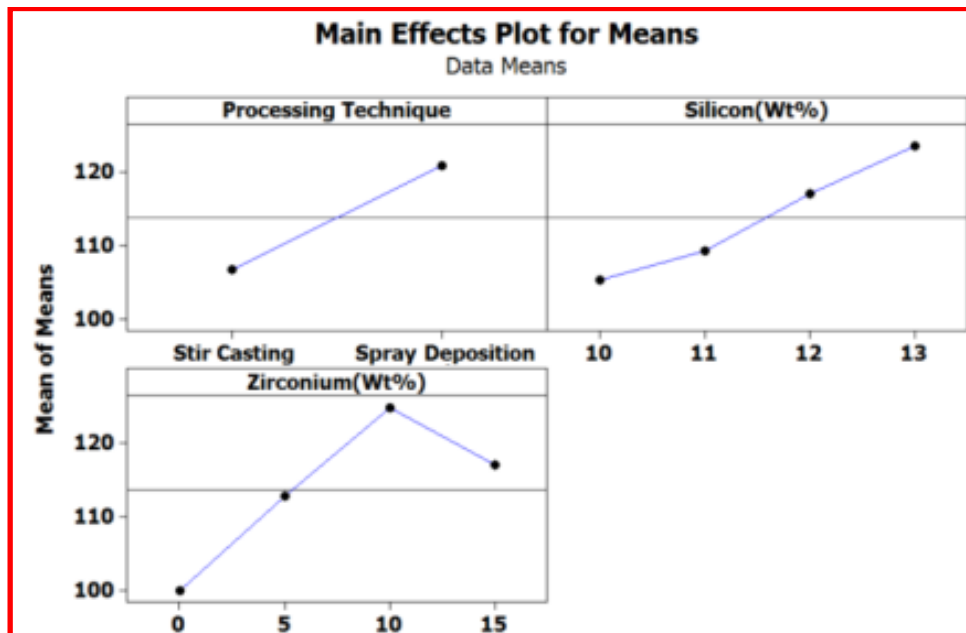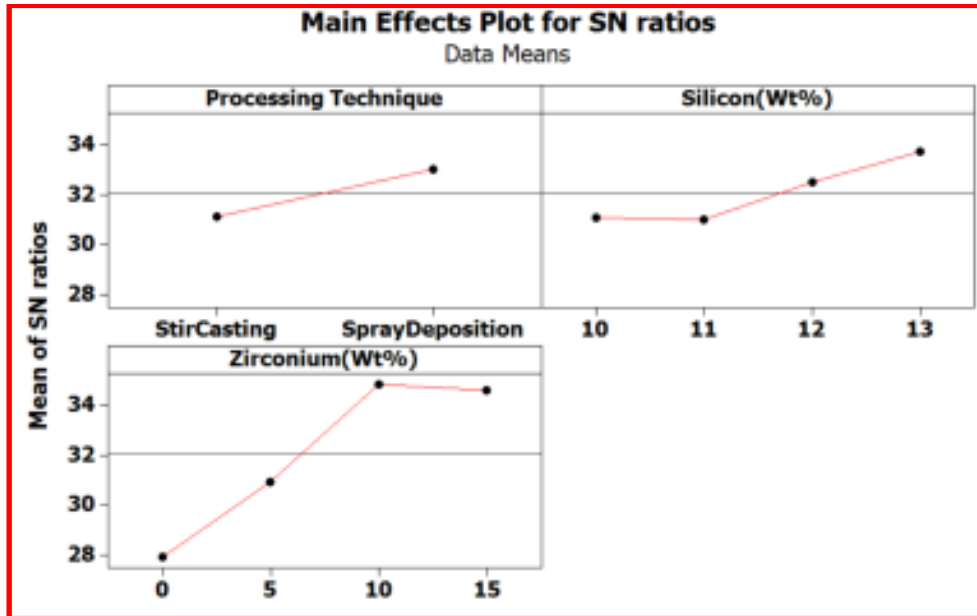
Figure 5.12: Main effects plot for Means and SN ratios for Micro Hardness

Table 5.13: Analysis of Variance for SN ratios for Micro Hardness

Source	DF	Seq SS	Adj SS	Adj MS	F	P	P (%)
Processing Technique	1	23.39	23.39	23.39	174.9	0.00	14.18
Silicon (Wt %)	3	109.1	109.1	36.38	272.0	0.00	22.06
Zirconium (Wt %)	3	310.8	310.8	103.61	774.7	0.00	62.82
AXB	3	0.754	0.754	0.251	1.88	0.20	0.16
AXC	3	1.704	1.704	0.568	4.25	0.04	0.35
BXC	9	6.368	6.368	0.708	5.29	0.01	0.43
Residual Error	9	1.204	1.204	0.134			
Total	31	453.4					
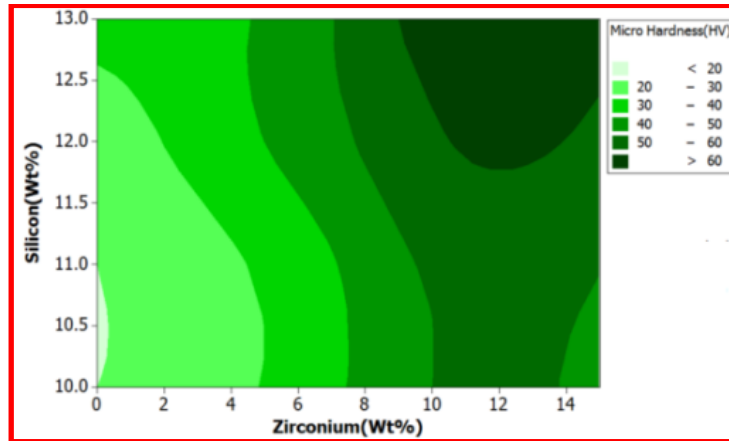
Figure 5.13: Micro Hardness contour plot at Zirconium – Silicon planes of spray deposited Al-Si alloy matrix reinforced with ZrO$_2$ particles

It is worthy to note that spray deposition method gives better results compared to stir casting. Figure 5.13 shows the Micro Hardness contour plot at Zirconium – Silicon planes under spray deposition processing techniques of Al-Si alloy matrix reinforced with ZrO$_2$ particles. From the contour plot, it was observed that increase of ZrO$_2$ particles (10 wt. % to 15 wt. %) and silicon (12.5 wt. %) resulted in optimum parameters for obtaining maximum micro hardness.

Hardness measurements of the developed specimens with varying composition of the reinforced material were conducted on a HV-5 Vickers hardness tester (Instron 3366) under 2 kg load for 15s. To reduce experimental errors, the average of at least seven hardness measurements at room temperature with a chuck extension rate of 2 mm/min was calculated.

5.2.2 Compression test of the samples of hot pressed and as cast composites

Compression test samples were prepared and conducted the tests were conducted on specimens having a diameter 12mm and length of 30mm as per the ASTM E8 Standard, as is shown in Figure 5.14.
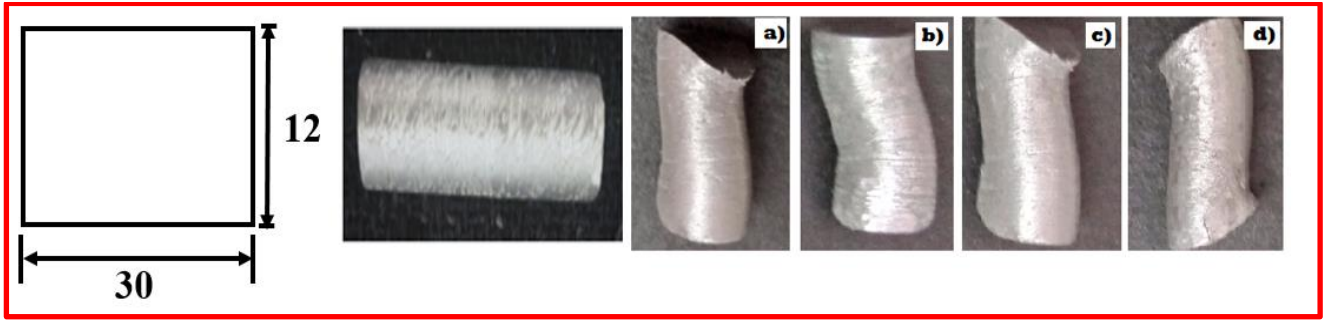
Figure 5.14: Images of compressive strength test specimens of spray deposited Al-Si alloy matrix composite reinforced with a) 0% b) 5% c) 10% d) 15% ZrO₂ particles for 12.5 wt. % of Silicon

(a)   (b)
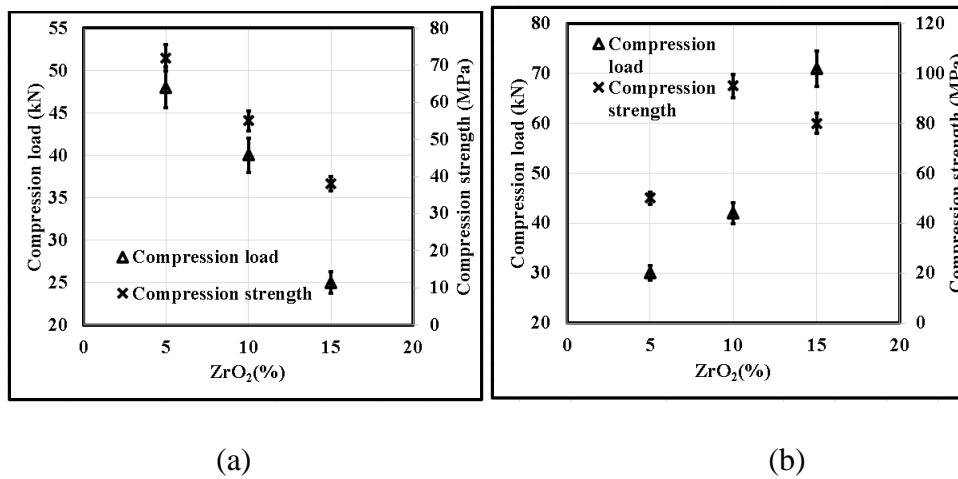
Figure 5.15 (a): Compressive load and compressive strength of hot pressed; (b) Compressive load and compressive strength of hot pressed (as cast)

The increase in the percentage of ZrO₂ did not affect the diameter and area of the samples, but a change was observed in the compression strength with different loads applied, as shown in Figure 5.15. For the as cast sample, with the increasing loads the compressive strength increased to 274.87 MPa for 5%, 380.54MPa for 10% of ZrO₂. But the compressive strength reduced to 347.42 MPa for 15% of ZrO₂ even though the load applied was the highest for this case since the material had reached its fracture point for the previous case itself. It can be observed, that in the case of hot-pressed samples the compression strength increases for a higher percentage of the zirconium oxide. The hardness of developed AlSi-ZrO₂ is improved by the resistance which appears in the motion of dislocation under testing.

5.2.3 Compression test of the samples of spray deposition and stir casting of Al-12.5Si+ZrO₂ composite
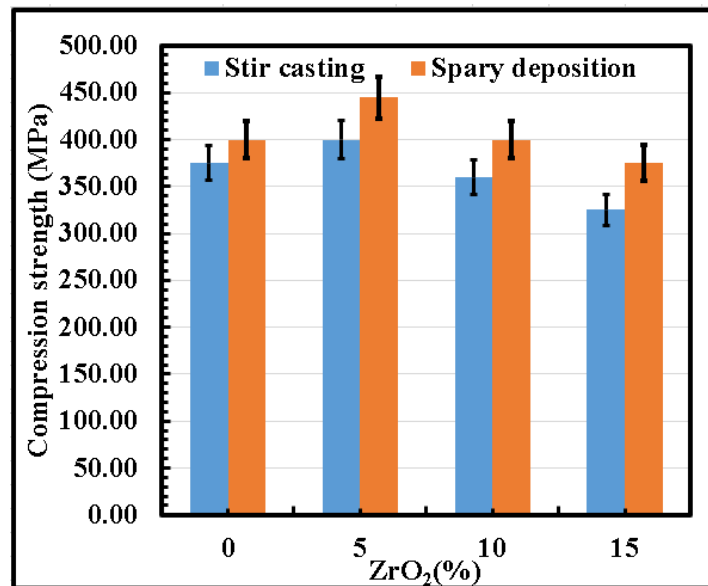
Figure 5.16: Experimental compressive strength plot of stir cast and spray formed Al-12.5Si alloy matrix composite reinforced with ZrO₂ particles

Figure 5.16 depicts the compressive strength values of different weight fractions of ZrO_2 reinforced particles during spray deposition and stir casting methods. For all samples, the compressive strength increased with addition of up to 5 wt. % ZrO_2. It can be explained by the fact that the increase in ZrO_2 particle prevents the decrease in the distance between the ZrO_2 particles resulting in dislocation movement in Al-Si alloy. Therefore, compressive strength decreases through dispersion strengthening mechanism in case of both spray deposition and stir casting.

`
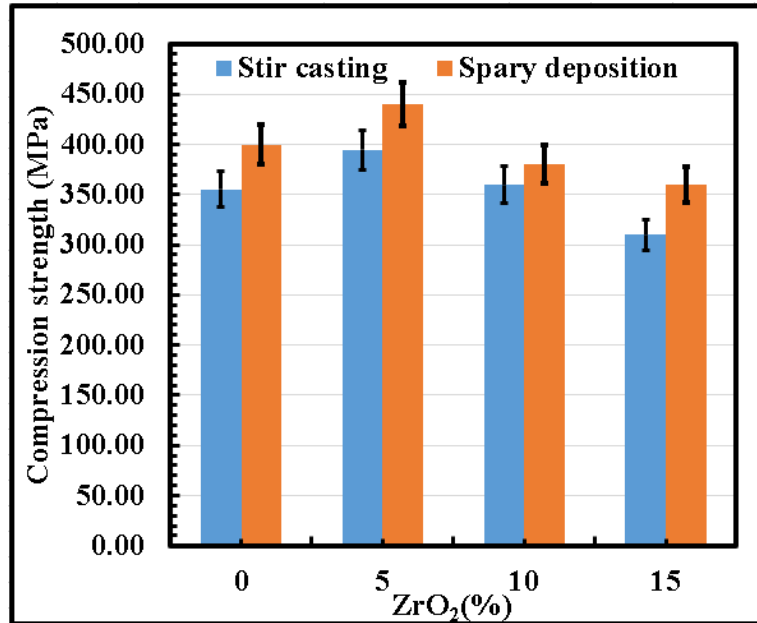
Figure 5.17: Compressive Strength interaction plot of Al-12.5Si alloy matrix reinforced with ZrO₂particles

Figure 5.17 shows the compressive strength interaction plot obtained from Taguchi's design of experiments for stir cast and spray deposited Al-Si alloy matrix composite reinforced with ZrO_2 particles for 12.5 wt. % of Silicon. The study found that the 5 wt. % of ZrO_2 particles led to maximum compression strength value under spray deposition processing technique. Figure 5.18 depicts the effect of weight percentage of silicon and reinforced ZrO_2 particles on compression strength. As it could be seen, for the silicon wt. %, this trend was always in an increasing mode with increase in silicon percentage. The percentage of contribution (P %) of different factors selected for micro hardness are reported in Table 5.14. The value of P % for Zirconium was 50.0%, for Silicon 9.9% and processing technique 39.3%.
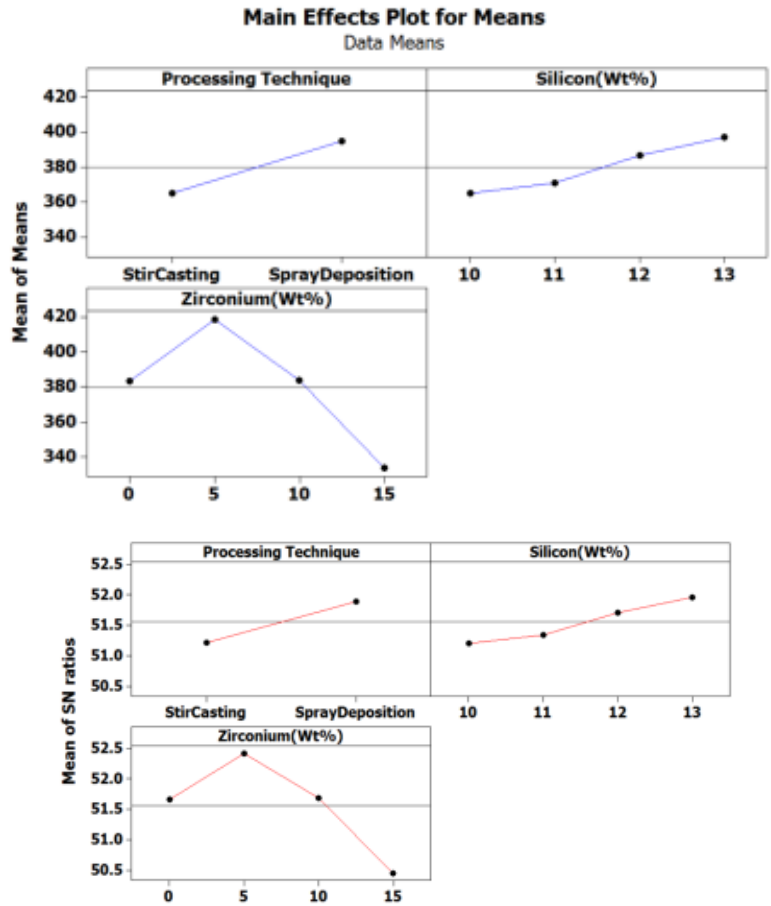
Figure 5.18: Main effects plot for Means and SN ratio for Compressive Strength

Table 5.14: Analysis of Variance for SN ratios for Compressive Strength

Source	DF	Seq SS	Adj SS	Adj MS	F	P	P (%)
Processing Technique	1	3.726	3.726	3.726	410.7	0.00	39.3
Silicon (Wt %)	3	2.827	2.827	0.9425	103.8	0.00	9.9
Zirconium (Wt %)	3	16.01	16.01	5.3395	588.5	0.00	50.0
AXB	3	0.005	0.005	0.0017	0.20	0.89	0.02
AXC	3	0.017	0.017	0.0058	0.64	0.60	0.05
BXC	9	0.570	0.570	0.0633	6.98	0.00	0.61
Residual Error	9	0.081	0.081	0.0090			
Total	31	23.24					
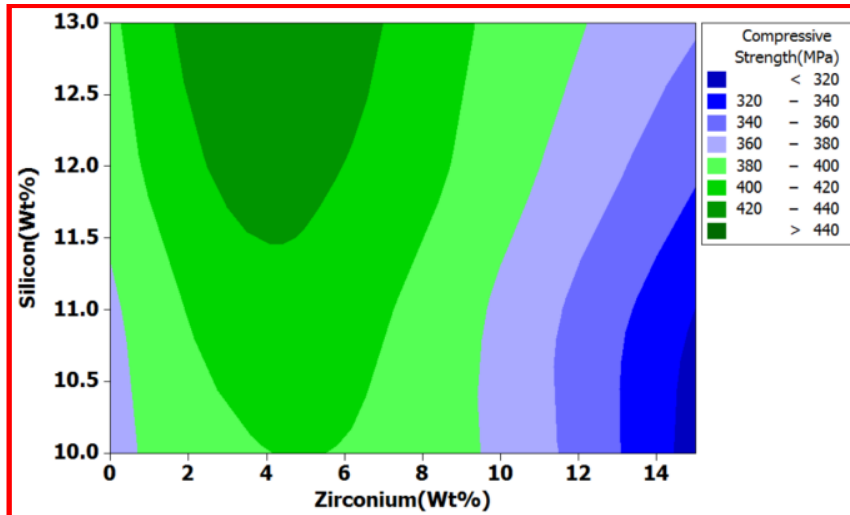
Figure 5.19: Compressive Strength contour plot at Zirconium – Silicon planes of spray deposited Al-Si alloy matrix reinforced with ZrO$_2$ particles

Figure 5.19 shows the Micro Hardness contour plot at Zirconium – Silicon planes under spray deposition processed Al-Si alloy matrix composite reinforced with ZrO$_2$ particles. From the contour plot, it was observed that increase of ZrO$_2$ particles (1.75 wt. % to 6 wt. % and silicon 12.5 wt. %) resulted in optimum process parameters for obtaining maximum micro hardness value.

5.2.4 Tensile test of the samples of hot pressed and as cast of Al-12.5Si alloy

The samples were prepared and tests conducted as per ASTM E8 is shown in Figure 5.20. The Figure 5.21(a) shows the tensile strength of aluminium silicon alloys, with and without reinforcements. These results indicate that addition of zirconium oxide increases the brittleness. The presence of ZrO$_2$ will lead to localized crack initiation. Clear interfaces in composite will enhance the load bearing capacity and delay in crack formation but reverse tendency is observed in hot pressed samples and corresponding results are presented in this section.

`
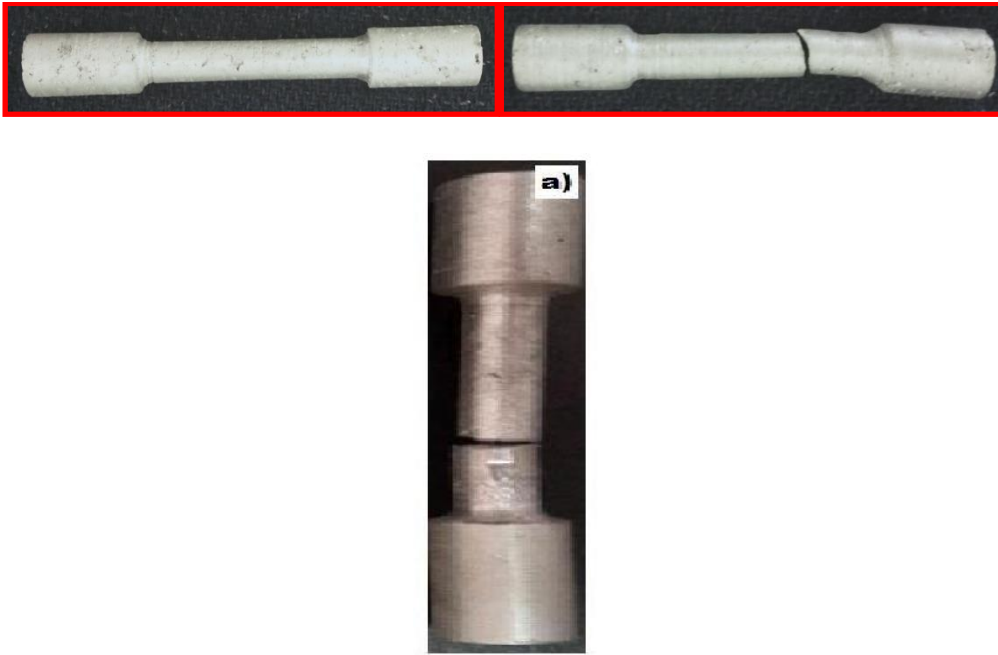
Figure 5.20: Tensile Strength test specimens of spray deposited Al-Si alloy matrix composite reinforced with 12.5% of Silicon

(a)	(b)
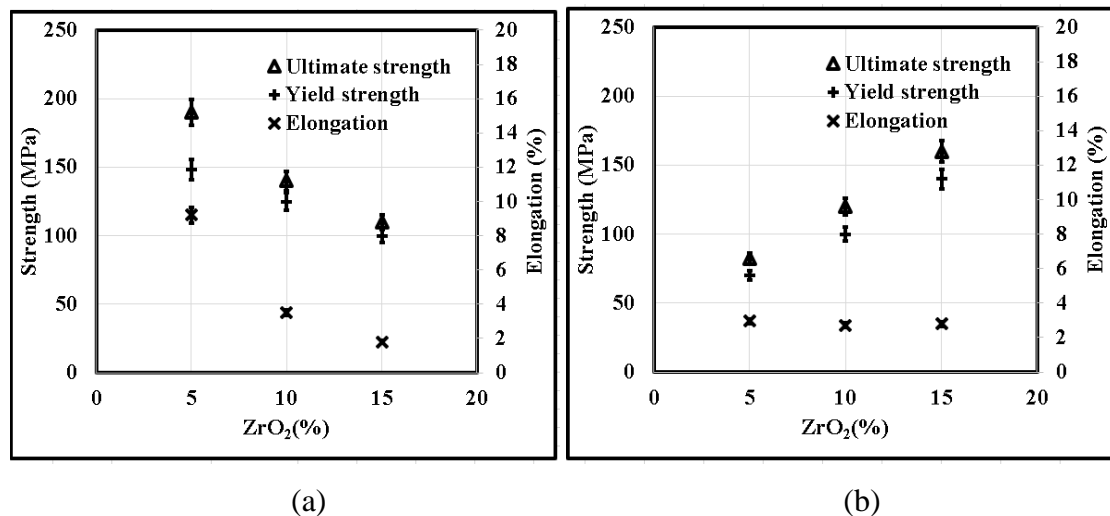
Figure 5.21: Tensile strength and elongation of a) hot pressed; (b) as cast composite

The mechanical properties include the elongation, yield strength and ultimate tensile strength under different ZrO_2 compositions. Yield strength and ultimate strength for the aluminium silicon alloy with the reinforcement were found to be higher than those of the unreinforced material. This is due to simultaneous reduction of the elongation and enhancement of the ultimate strength in the size of Si phases in the aluminium matrix. This is probably tied to the size of Al matrix and Si particles. Another reason may be the dendrite arm spacing in the microstructure, when the heat treatment was applied to the material (Jiang et al., 2014).

5.2.5 Tensile test of the samples of spray deposited and stir cast Al-12.5Si+ZrO$_2$ composite
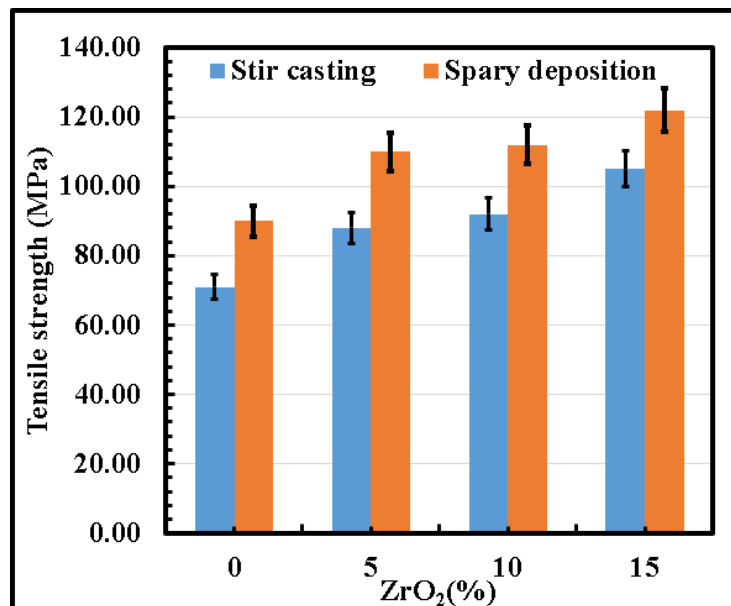
Figure 5.22: Experimental tensile Strength plot of Al-12.5Si alloy matrix composite reinforced with ZrO$_2$particles

As mentioned in section 5.2, the tensile test results of Al-12.5Si alloys reinforced with ZrO$_2$ powder particles are shown in Figure 5.22. The tensile strength increased with increase in weight fraction of ZrO$_2$ powder particles. It can be observed that for 15 wt. % of ZrO$_2$ particles and 12.5 wt. % silicon, a maximum tensile strength of 139.87 MPa was attained for spray deposition processed composites. This is due to decrease of ferrite, and increase of pearlite content. This may be due to larger work hardening rate, structure of dislocation tangles around the particles, uniform distribution of reinforcement and plastic incongruity between the reinforcement and matrix (Daoud et al., 2002)

Figure 5.23 depicts the tensile strength interaction plot obtained from Taguchi's design of experiments for stir cast and spray deposition of Al-Si alloy matrix reinforced with ZrO$_2$ particles for 12.5 wt. % of Silicon. From the interaction plot 15 wt. % of ZrO$_2$ particles gave the maximum tensile strength value under spray deposition processing technique.

`
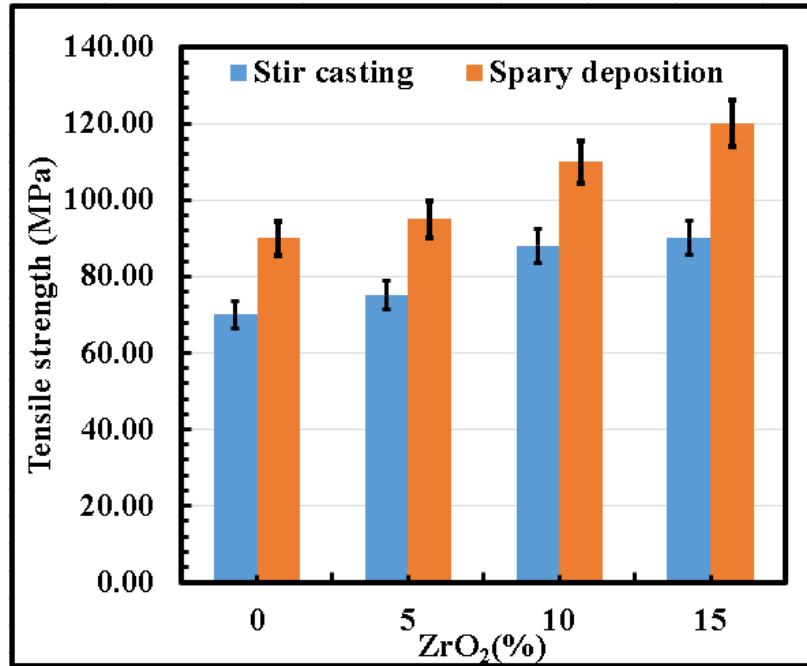
Figure 5.23: Tensile strength interaction plot of stir cast and spray deposited Al-12.5Si alloy matrix composite reinforced with ZrO$_2$ particles

Figure 5.24 depicts the effect of weight percentage of silicon and reinforced ZrO$_2$ particles on compression strength. As it could be seen, for the silicon wt. %, this trend was always in an increasing mode, with increase in silicon percentage. The percentage contribution (P %) of different factors selected for micro hardness is reported in Table 5.15. The values of P % for Zirconium were 23.7%, for Silicon 17.1% and for processing technique is 57.3%.
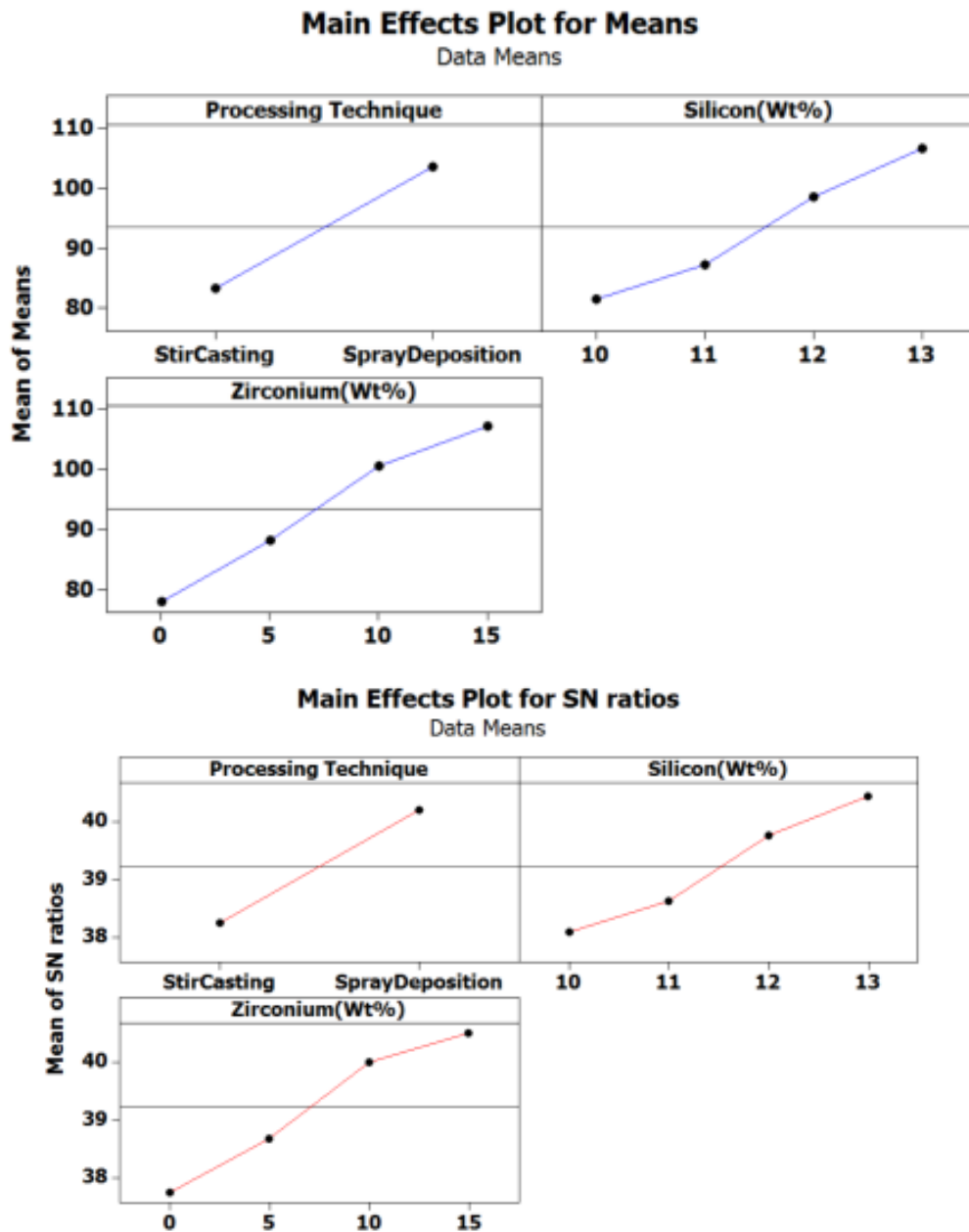
Figure 5.24: Main effects plot for means and SN ratio for tensile strength

`

Table 5.15: Analysis of Variance for SN ratios for Tensile Strength

Source	DF	Seq SS	Adj SS	Adj MS	F	P	P (%)
Processing Technique	1	30.52	30.52	30.52	296.1	0.000	57.33
Silicon (Wt %)	3	27.26	27.26	9.088	88.1	0.000	17.07
Zirconium (Wt %)	3	37.86	37.85	12.61	122.4	0.000	23.74
AXB	3	0.126	0.126	0.042	0.41	0.750	0.08
AXC	3	0.367	0.366	0.122	1.19	0.369	0.29
BXC	9	7.178	7.177	0.797	7.74	0.003	1.49
Residual Error	9	0.928	0.927	0.103			
Total	31	104.25					
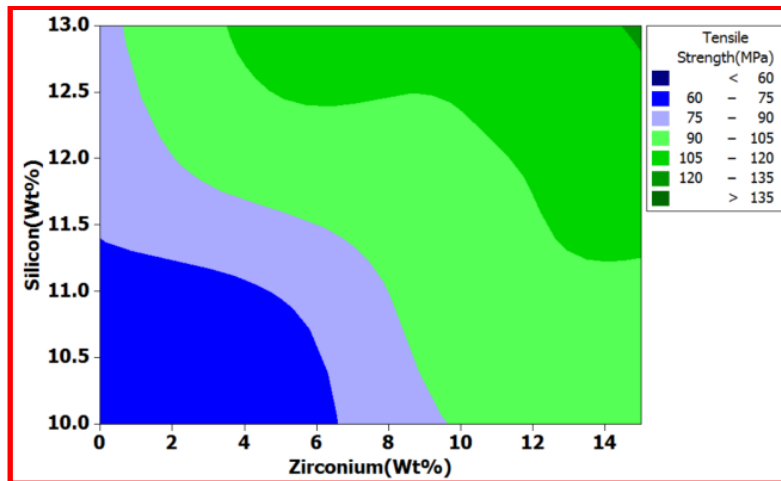
Figure 5.25: Tensile strength contour plot at Zirconium – Silicon planes for spray deposited Al-Si alloy matrix reinforced with ZrO_2 particles

Figure 5.25 shows the Micro Hardness contour plot at Zirconium – Silicon planes under spray deposited Al-Si alloy matrix reinforced composite with ZrO_2 particles. From the contour plot it was observed that increase of ZrO_2 particles (15 wt. % and silicon 12.5 wt. %) resulted in optimum condition for obtaining maximum micro hardness.

5.2.6 Evaluation of the Microstructure

The microstructures of the fabricated sample of as-cast, hot pressed and spray formed composite are evaluated with the aid of a scanning electron microscope (SEM). Figures 5.26 to 5.28 show the microstructures of the AlSi and AlSi-ZrO_2 alloy for 5%, 10% and 15% observed by scanning electron microscope. The Microscope and peripheral regions of the spray formed disc for all percentages of ZrO_2 are shown in Figure 5.26 to 5.28.
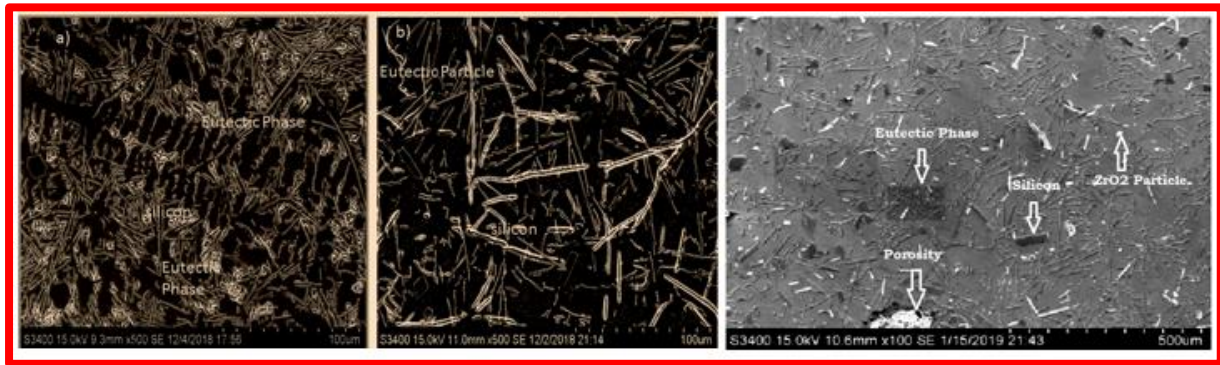
Figure 5.26: Microstructure of Al+12.5Si alloy (a) as cast (b) composite with 5% hot pressed ZrO_2 (c) composite with 5% spray deposited ZrO_2

Figure 5.26(a), 5.27(a) and 5.28(a) show the image of the powder particles of the as cast. It is to be noted that the equiaxed grain morphology of primary Aluminium was observed in contrast to typical dendritic morphology often observed in the as-cast alloy. The eutectic phase is seen in the sample (see Figures 5.27(b) & 5.28(c)). No obvious precipitates or in homogeneous structures were observed, but periodic traces of laser scanning were observed which were created by the difference of microstructure between the centre and boundary regions of the trace. The SEM images of spray formed and AlSi- ZrO_2 alloy are shown in Figure 5.28(c). It is observed that the size of silicon particles is refined.
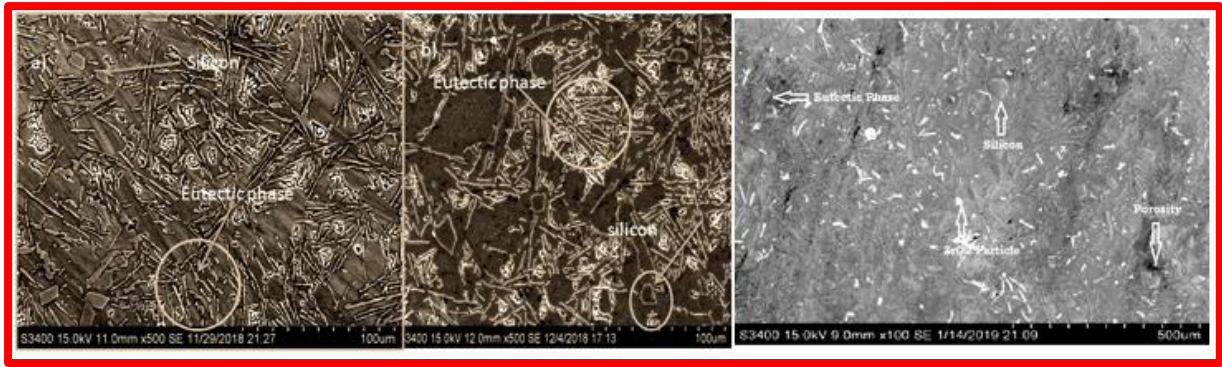
Figure 5.27: Microstructure of Al+12.5Si alloy (a) as cast (b) composite with 10% hot pressed ZrO₂ (c) composite with 10% spray deposited ZrO₂
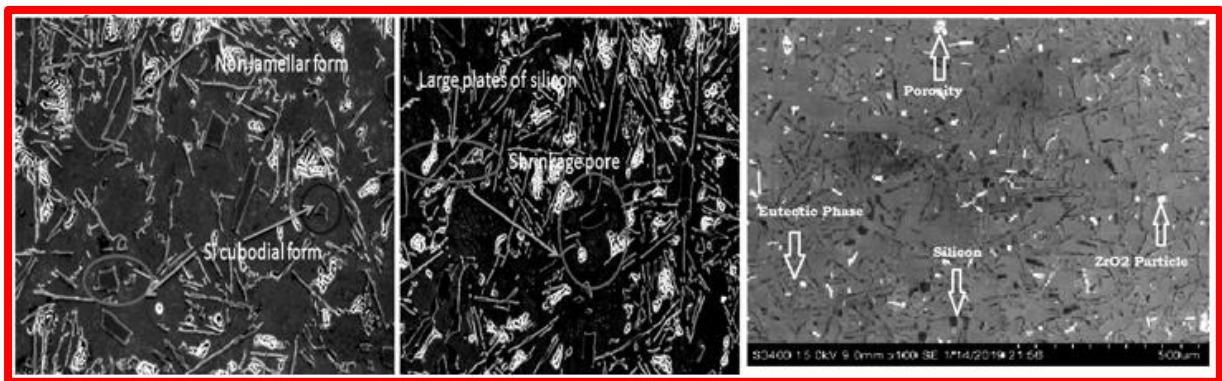
Figure 5.28: Microstructure of Al+12.5Si alloy (a) as cast (b) composite with 15% hot pressed ZrO₂ (c) composite with 15% spray deposited ZrO₂

It is worthy to note that the size of ZrO_2 particles increased with increasing the content of ZrO_2 as shown in Figure 5.27(b), 5.27(c), 5.28(b) & 5.28(c). The AlSi- ZrO_2 alloys exhibit a typical elongated fibrous structure along the extrusion direction. The grain size of ZrO_2 and Aluminium are slightly bigger in the central area as compared to peripheral area. This can be explained by the concept of heat transfer rate. There is fairly a uniform distribution of zirconium oxide in the matrix. The Figure 5.26(a), 5.27(a) & 5.28(a) depicts that presence of primary eutectic phase and silicon in a needle like structure. Figures 5.26 (b) & 5.27(b) depict the primary eutectic phase and silicon gray plates. Figure 5.26(b), 5.27(b) & 5.28(b) shows the silicon in a cuboidal form and large plate of silicon. Figure 5.26(c), 5.27(c) & 5.28(c) indicates the silicon of cuboidal form.The eutetic mixture though non lamellar in form appears to be in section and the large plates of silicon which can be used to determine the mechanical properties. The Al-Si and zirconium oxide particles act as heterogeneous nucleation during solidification as a result of the addition of zirconium and also results in to good bonding between AlSi-ZrO_2. It is interesting to note that the heat transfer rate from the

`

spray deposition by convection form is almost similar throughout the disc. However, in the case of conduction form (q α dT/dx), the rate of heat transfer varies with area of the disc. Therefore, higher rate of heat transfer is expected in the peripheral region. This is because the peripheral region's thickness is smaller than the central regions. As a result, the peripheral area solidified more quickly than the central region. The finer grain shaped in the peripheral region is due to this (Grant et al., 1991; Raju et al., 2011).

In conclusion, the systematic fabrication of Al-Si composites reinforced with ZrO_2 using the technique of stir casting, spray deposition indicated that the method is an effective option for metal casting. The SEM images showed a considerably uniform distribution of the zirconium oxide in the matrix. The SEM images also indicated the rich interface among the metal matrix and AlSi-ZrO_2 particles and depicts the agglomeration of reinforced phase resulting in poor wettability of ZrO_2 and decohesion is observed.

Summary

The present study indicates that stir casting, followed by spray deposition is one of the promising processing methods of producing metal matrix composite. The ZrO_2 (5, 10 and 15 wt. %) was reinforced in the Al-Si composites, was systematically fabricated by spray deposition and stir casting process. Study indicates that stir casting is one of the promising processing methods of producing metal matrix composite. Figure 5.26 to 5.28 show the uniform distribution of zirconium oxide in the matrix. Figure 5.27 indicates the silicon is incuboidal form. The eutetic mixture, though non lamellar in form, appears to be in section. UTS, YS, and percentage elongation in cast exhibit better results compared to hot pressed samples with the increase in weight percentage zirconium oxide. The enhancement of mechanical property is due to the combined effect of refinement strengthening and precipitate formation. Hot pressed samples exhibit decrease in the hardness as the zirconium oxide increases. The following conclusion can be drawn from the study.

1)   The hardness and tensile strength measurements illustrated the enhancement in the mechanical properties due to the addition of ZrO_2 to as cast composite, compared to hot press composite. SEM images shows the uniform distribution of zirconium oxide in the matrix. Gray plates of silicon in a rich aluminum matrix are observed, with 5% of ZrO_2.

2)   The study showed that the micro hardness of the developed composite increases as the percentage of ZrO_2 particles increases. In Aluminum-matrix, fine equiaxed grain morphology with a uniform distribution of ZrO2 and Silicon Phase was observed.

3)   When spray deposition is used instead of stir casting, it was discovered that uniform distribution and homogeneous dispersion of ZrO_2 particles results in higher micro hardness values.

4)   In both spray deposition and stir casting, an increase in ZrO_2 particle prevents a decrease in the distance between the ZrO_2 particles, resulting in dislocation movement in Al-Si alloy. As a result, compressive strength decreases due to the dispersion strengthening mechanism.

5)   The more the ZrO_2 contents in the $AlSi + ZrO_2$ composite, the higher is the tensile strength of the composite. However, for 15 wt. percentage of ZrO_2 particles, the tensile strength value went maximum up to 139.87 MPa for spray deposition processed composites. This may be due to larger work hardening rate, structure of dislocation tangles around the particles, uniform distribution of reinforcement and plastic incongruity between the reinforcement and matrix.

5.3 Effect of flight distance on mechanical and microstructure properties

5.3.1. Mechanical properties of AlSi-ZrO$_2$ composite as a function of flight distance

The samples were prepared and tests conducted as per ASTM E8. For all the cases, the tensile strength increased with increase in weight fraction of ZrO$_2$ powder particles. As ZrO$_2$ content increases from 5% to 15%, the tensile strength shows more variations in tensile behaviour. It can be observed that for 15% of ZrO$_2$ particles, the maximum value of tensile strength is 144.87 MPa. This may be due to structure of dislocation tangles around the particles, uniform distribution of reinforcement and plastic incongruity between the reinforcement and matrix (Daoud et al., 2002). It can clearly observe in Figure 5.29 that the developed MLPNN-GA was able to sufficiently predict the values based on the experimental values. This implies that the developed optimized MLPNN-GA model is not over fitted by the trained data. The average error in MLPNN and MLPNN-GA is 2.2% and 1.5%, respectively. Most of the information in this section has been published (**https://doi.org/10.1016/j.mtcomm.2021.102398**).

Table 5.16(a): Tensile strength of Al+12.5Si+ZrO$_2$ composite

5% ZrO$_2$					
Flight distance (mm)	Experiment	ANN	ANN-GA	RR (ANN) (%)	RR (ANN-GA) (%)
320	108.78	110.98	110.015	-2.02	-0.87
330	110.78	112.98	112.015	-1.98	-0.85
340	112.78	114.98	114.015	-1.91	-0.84
350	113.78	115.98	115.015	-1.93	-0.83
360	114.78	116.98	116.015	-1.91	-0.82
370	115.78	117.98	117.015	-1.90	-0.82
380	116.78	118.98	118.015	-1.88	-0.81
390	118.78	120.98	120.015	-1.85	-0.8
400	120.78	122.98	122.015	-1.82	-0.78
410	123.78	125.98	125.015	-1.77	-0.77
420	122.62	124.82	123.855	-1.79	-0.77
430	121.62	123.82	122.855	-1.80	-0.78

440	119.62	121.82	120.855	-1.83	-0.79
450	117.62	119.82	118.855	-1.87	-0.81
460	115.62	117.82	116.855	-1.90	-0.82
470	110.62	112.82	111.855	-1.98	-0.86
480	107.52	109.72	108.755	-2.04	-0.88
10% ZrO₂					
320	107.2	109.77	109.135	-2.39	-0.57
330	108.2	110.77	110.135	-2.37	-0.57
340	109.2	111.77	111.135	-2.35	-0.56
350	110.2	112.77	112.135	-2.33	-0.56
360	111.2	113.77	113.135	-2.31	-0.55
370	112.2	114.77	114.135	-2.29	-0.55
380	113.2	115.77	115.135	-2.27	-0.54
390	114.2	116.77	116.135	-2.25	-0.54
400	118.2	120.77	120.135	-2.17	-0.52
410	119.2	121.77	121.135	-2.15	-0.52
420	120.5	123.07	122.435	-2.13	-0.51
430	118	120.57	119.935	-2.17	-0.52
440	116	118.57	117.935	-2.21	-0.53
450	114	116.57	115.935	-2.25	-0.54
460	112	114.57	113.935	-2.29	-0.55
470	110	112.57	111.935	-2.33	-0.56
480	108.2	110.77	110.135	-2.37	-0.57
15% ZrO₂					
320	122.5	125.4053	123.845	-2.37	-1.24
330	124.5	127.4053	125.845	-2.33	-1.22
340	126.5	129.4053	127.845	-2.29	-1.21
350	129.5	132.4053	130.845	-2.24	-1.18
360	130.5	133.4053	131.845	-2.22	-1.17
370	132.5	135.4053	133.845	-2.19	-1.15
380	134.5	137.4053	135.845	-2.16	-1.14
390	136.5	139.4053	137.845	-2.12	-1.12

400	140.5	143.4053	141.845	-2.06	-1.09
410	143.5	146.4053	144.845	-2.02	-1.07
420	146.5	149.4053	147.845	-1.98	-1.04
430	140.5	143.4053	141.845	-2.06	-1.09
440	137.4	140.3053	138.745	-2.11	-1.11
450	135.4	138.3053	136.745	-2.14	-1.13
460	132.4	135.3053	133.745	-2.19	-1.15
470	128.4	131.3053	129.745	-2.26	-1.19
480	125.2	128.1053	126.545	-2.32	-1.22

Table 5.16(b): Tensile strength of Al+12.5Si+ZrO$_2$ composite

Flight distance (mm)	Experiment	ANN	ANN-GA
5% ZrO$_2$			
370	115.78±1.5	117.98	117.015
420	122.62±0.9	124.82	123.855
480	107.52±1.4	109.72	108.755
10% ZrO$_2$			
370	112.2±2.5	114.77	114.135
420	120.5±1.2	123.07	122.435
480	108.2±1.4	110.77	110.135
15% ZrO$_2$			
370	132.5±1.6	135.4053	133.845
420	146.5±1.1	149.4053	147.845
480	125.2±0.9	128.1053	126.545
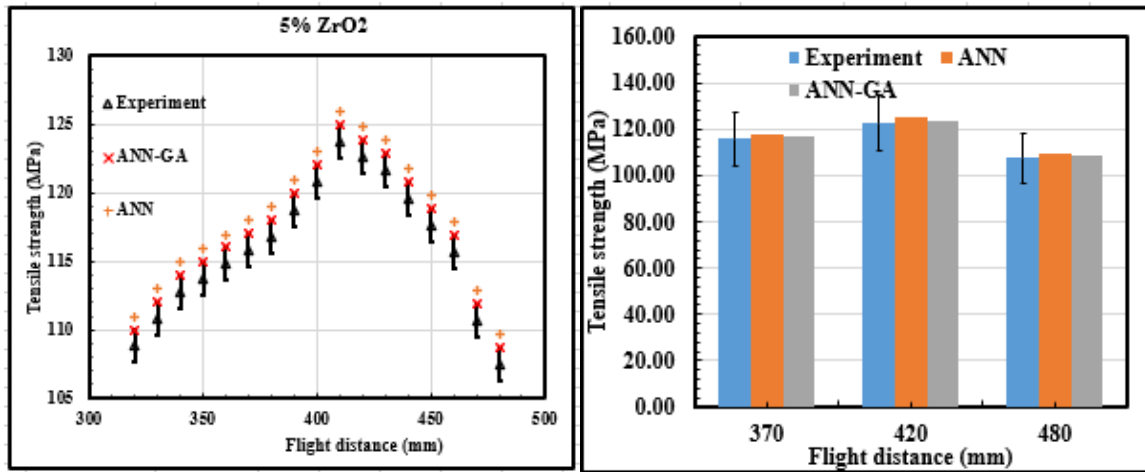
(a)
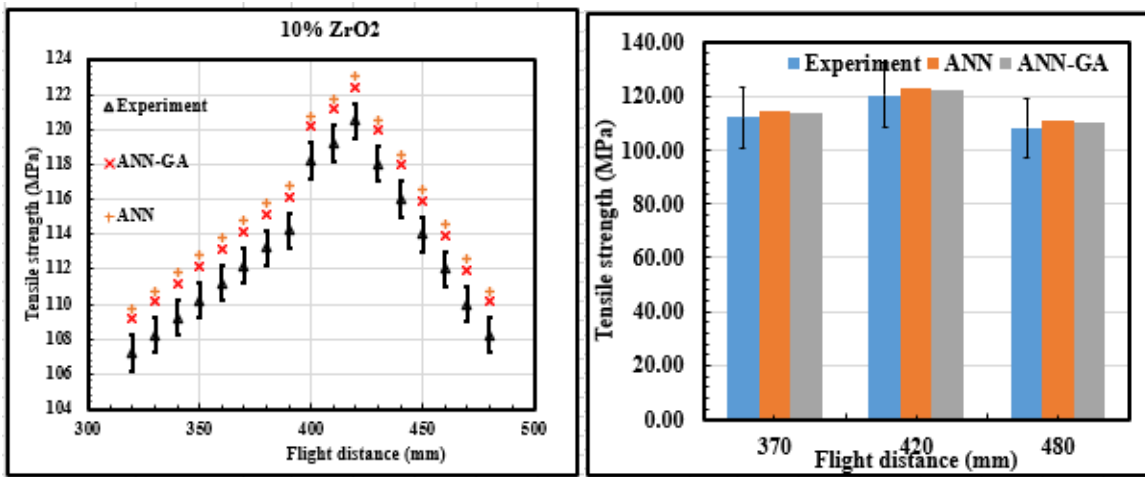
(b)
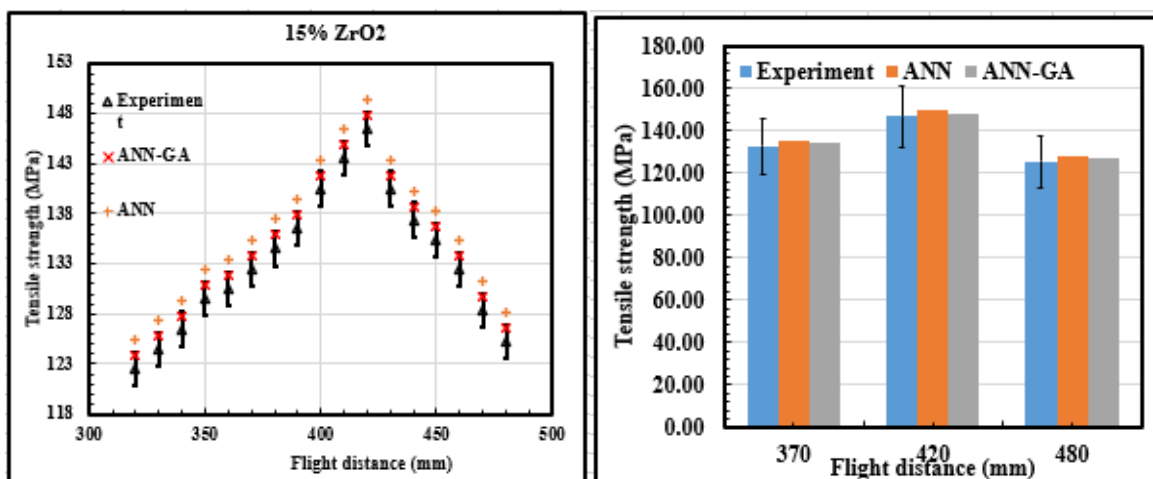
(c)

Figure 5.29: Tensile strength of Al+12.5Si+ZrO₂ composites (a) 5%, (b) 10% and (c)

15% reinforcements

111

`

Figure 5.29 shows the tensile strength with respect to the flight distance for different weight fractions of ZrO_2 reinforced particles. For all samples, the tensile strength increased with addition of weight percentage of zirconium oxide particles and prevents the decrease in the distance between the ZrO_2 particles resulting in dislocation movement in Al-Si alloy. Therefore, compressive strength decreases through dispersion strengthening mechanism. In addition, it was found that the 15% ZrO_2 sample displayed the highest compressive strength. It is evident in all the cases, the compressed strength peaked at 420 mm flight distance. The high strength may be attributed to the refinement and modification in the microstructural features during spray deposition (Wu et al., 1995). According to the theory, thermal spray process is a common method to transfer powder material to a continuous coating onto a supporting substrate. The average error in MLPNN and MLPNN-GA is 2.8% and 1.9%, respectively.

Table 5.17: Compressive strength of Al+12.5Si+ZrO₂ composite

5% ZrO₂					
Flight distance (mm)	**Experiment**	**ANN**	**ANN-GA**	**RR (ANN) (%)**	**RR (ANN-GA) (%)**
320	355	359.424	358.15	-1.25	-0.88
330	382	386.424	385.15	-1.16	-0.82
340	395	399.424	398.15	-1.12	-0.79
350	402	406.424	405.15	-1.13	-0.78
360	408	412.424	411.15	-1.08	-0.77
370	412	416.424	415.15	-1.07	-0.76
380	416	420.424	419.15	-1.06	-0.75
390	423	427.424	426.15	-1.05	-0.74
400	430	434.424	433.15	-1.03	-0.73
410	435	439.424	438.15	-1.02	-0.72
420	445	449.424	448.15	-0.99	-0.7
430	430	434.424	433.15	-1.03	-0.73
440	400	404.424	403.15	-1.11	-0.78
450	385	389.424	388.1594	-1.15	-0.81
460	365	369.424	368.1594	-1.21	-0.86
470	352	356.424	355.1594	-1.26	-0.89

480	348	352.424	351.1594	-1.27	-0.9
10% ZrO₂					
320	375	380.2	379.235	-1.39	-1.12
330	385	390.2	389.235	-1.35	-1.09
340	395	400.2	399.235	-1.32	-1.06
350	405	410.2	409.235	-1.28	-1.03
360	415	420.2	419.235	-1.25	-1.01
370	425	430.2	429.235	-1.22	-0.99
380	435	440.2	439.235	-1.21	-0.96
390	445	450.2	449.235	-1.17	-0.94
400	455	460.2	459.235	-1.14	-0.92
410	468	473.2	472.235	-1.11	-0.9
420	475	480.2	479.235	-1.09	-0.88
430	455	460.2	459.235	-1.14	-0.92
440	435	440.2	439.235	-1.21	-0.96
450	415	420.2	419.235	-1.25	-1.01
460	395	400.2	399.235	-1.32	-1.06
470	382	387.2	386.235	-1.36	-1.1
480	378	383.2	382.235	-1.38	-1.11
15% ZrO₂					
320	401	406.2	405.235	-1.31	-1.05
330	410	412.2	411.235	-0.54	-0.3
340	421	423.2	422.235	-0.52	-0.29
350	432	434.2	433.235	-0.51	-0.29
360	443	445.2	444.235	-0.51	-0.28
370	450	452.2	451.235	-0.49	-0.27
380	463	465.2	464.235	-0.48	-0.27
390	470	472.2	471.235	-0.47	-0.26
400	478	480.2	479.235	-0.46	-0.26
410	489	491.2	490.235	-0.45	-0.25
420	495	497.2	496.235	-0.44	-0.25
430	475	477.2	476.235	-0.46	-0.26

440	455	457.2	456.235	-0.48	-0.27
450	435	437.2	436.235	-0.51	-0.28
460	425	427.2	426.235	-0.52	-0.29
470	413	415.2	414.235	-0.53	-0.3
480	409	411.2	410.235	-2.35	-1.06

Table 5.17(b): Compressive strength of Al+12.5Si+ZrO$_2$ composite

Flight distance (mm)	Experiment	ANN	ANN-GA
5% ZrO$_2$			
370	412±1.3	416.424	415.1594
420	445±1.4	449.424	448.1594
480	348±1.7	352.424	351.1594
10% ZrO$_2$			
370	425±1.5	430.2	429.235
420	475±1.2	480.2	479.235
480	378±1.1	383.2	382.235
15% ZrO$_2$			
370	450±1.7	452.2	451.235
420	495±1.2	497.2	496.235
480	409±1.3	411.2	410.235
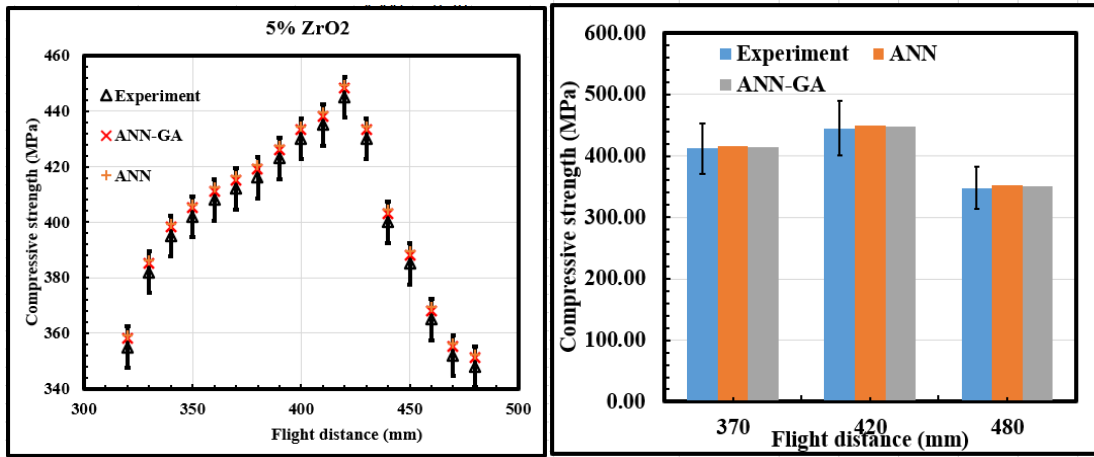
(a)
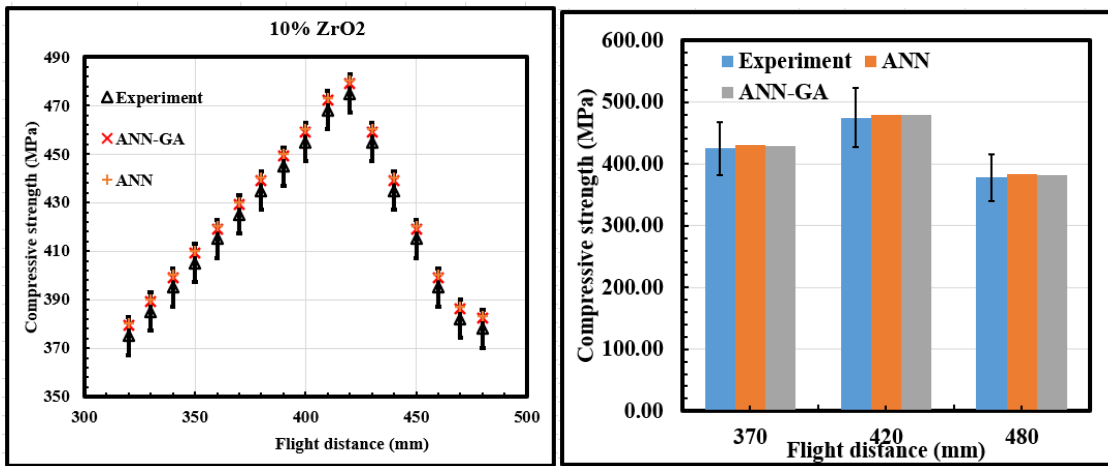
(b)
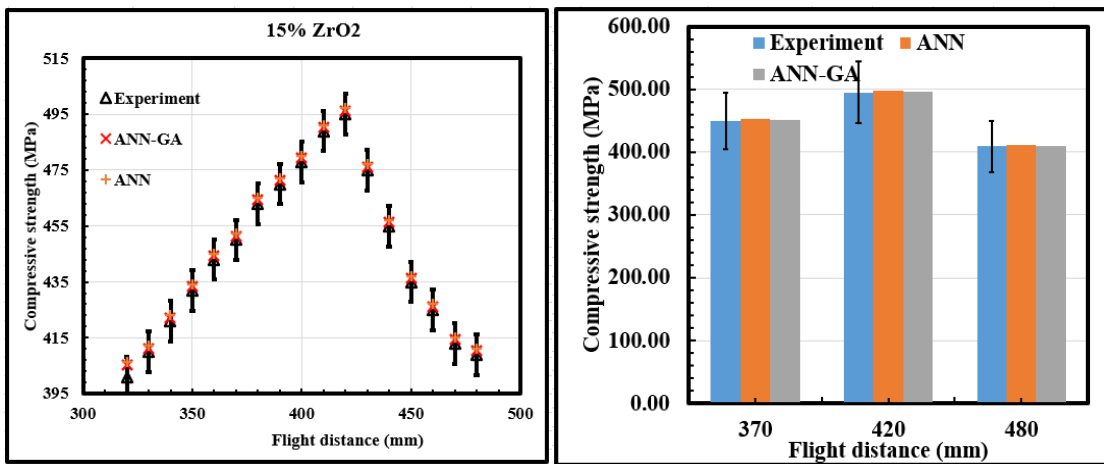
(c)

Figure 5.30: Compressive of Al+12.5Si+ZrO₂ composites (a) 5%, (b) 10% and (c) 15% reinforcements

`

To further investigate the mechanical properties, the yield strength study was performed for the Al-12.5Si alloy reinforced with 5%, 10% and 15% ZrO_2. The results of yield strength are shown in Figure 5.31. From these results one can draw the conclusion that there exists a critical grain size irrespective of ZrO_2 composition, which give rise to higher yield strength for the developed material. These results provide an additional interpretation of the tensile test. Qualitatively, increasing surface roughness reduces cohesion by limiting the closest separation particles can reach (Zwol et al. 2008). The average error in MLPNN and MLPNN-GA is 3.1% and 2.3%, respectively.

Table 5.18: Yield strength of Al+12.5Si+ZrO_2 composite

5% ZrO_2					
Flight distance (mm)	**Experiment**	**ANN**	**ANN-GA**	**RR (ANN) (%)**	**RR (ANN-GA) (%)**
320	89	91.563	90.135	-2.88	-1.26
330	90	92.563	91.135	-2.85	-1.25
340	91	93.563	92.135	-2.82	-1.23
350	92	94.563	93.135	-2.79	-1.22
360	93	95.563	94.135	-2.76	-1.21
370	95	97.563	96.135	-2.71	-1.18
380	96	98.563	97.135	-2.67	-1.17
390	97	99.563	98.135	-2.64	-1.16
400	99	101.563	100.135	-2.59	-1.13
410	102	104.563	103.135	-2.51	-1.1
420	104	106.563	105.135	-2.46	-1.08
430	103	105.563	104.135	-2.49	-1.09
440	100	102.563	101.135	-2.56	-1.12
450	98	100.563	99.135	-2.62	-1.14
460	96	98.563	97.135	-2.67	-1.17
470	94	96.563	95.135	-2.73	-1.19
480	92	94.563	93.135	-2.79	-1.22
10% ZrO_2					
320	94	96.315	95.435	-2.46	-1.50

330	97	99.315	98.435	-2.39	-1.46
340	100	102.32	101.435	-2.32	-1.41
350	105	107.32	106.435	-2.21	-1.35
360	110	112.32	111.435	-2.11	-1.29
370	114	116.32	115.435	-2.03	-1.24
380	119	121.32	120.435	-1.95	-1.19
390	120	122.32	121.435	-1.93	-1.18
400	121	123.32	122.435	-1.91	-1.17
410	123	125.32	124.435	-1.88	-1.15
420	125	127.32	126.435	-1.85	-1.13
430	120	122.32	121.435	-1.93	-1.18
440	118	120.32	119.435	-1.96	-1.2
450	115	117.32	116.435	-2.01	-1.23
460	105	107.32	106.435	-2.21	-1.35
470	101	103.32	102.435	-2.29	-1.4
480	97	99.315	98.435	-2.39	-1.46
15% ZrO$_2$					
320	102	104.5153	103.145	-2.47	-1.11
330	104	106.5153	105.145	-2.42	-1.09
340	106	108.5153	107.145	-2.37	-1.07
350	110	112.5153	111.145	-2.29	-1.03
360	112	114.5153	113.145	-2.25	-1.01
370	114	116.5153	115.145	-2.21	-0.99
380	116	118.5153	117.145	-2.17	-0.98
390	118	120.5153	119.145	-2.13	-0.96
400	122	124.5153	123.145	-2.06	-0.93
410	125	127.5153	126.145	-2.01	-0.91
420	127	129.5153	128.145	-1.98	-0.89
430	120	122.5153	121.145	-2.12	-0.95
440	117	119.5153	118.145	-2.15	-0.97
450	114	116.5153	115.145	-2.21	-0.99
460	111	113.5153	112.145	-2.27	-1.02

| 470 | 109 | 111.5153 | 110.145 | -2.31 | -1.04 |
| 480 | 107 | 109.5153 | 108.145 | -2.35 | -1.06 |

Table 5.18(b): Yield strength of Al+12.5Si+ZrO₂ composite

Flight distance (mm)	Experiment	ANN	ANN-GA
5% ZrO₂			
370	95±0.9	97.563	96.135
420	104±0.5	94.563	93.135
480	92±1.2	106.563	105.135
10% ZrO₂			
370	114±1.8	116.32	115.435
420	125±1.3	99.315	98.435
480	97±1.4	127.32	126.435
15% ZrO₂			
370	114±1.6	116.5153	115.145
420	127±1.8	109.5153	108.145
480	107±0.4	129.5153	128.145

`
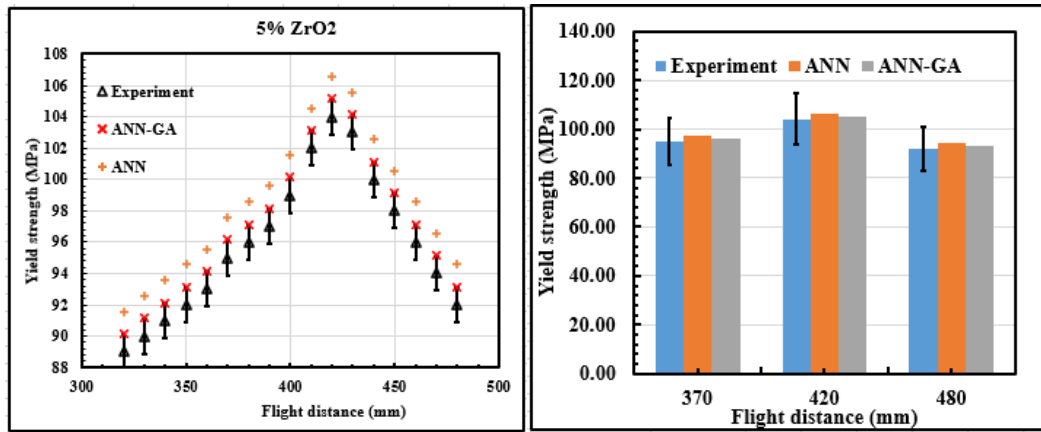
(a)
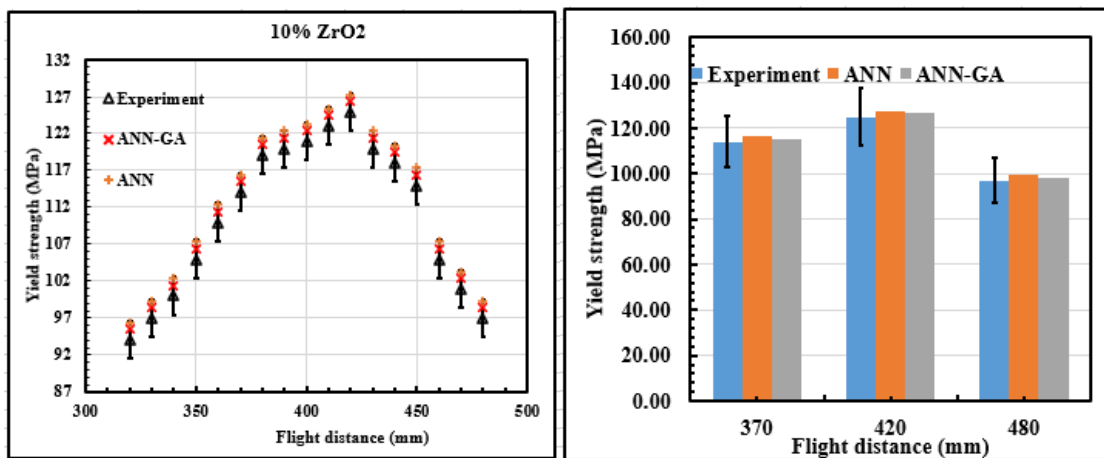
(b)
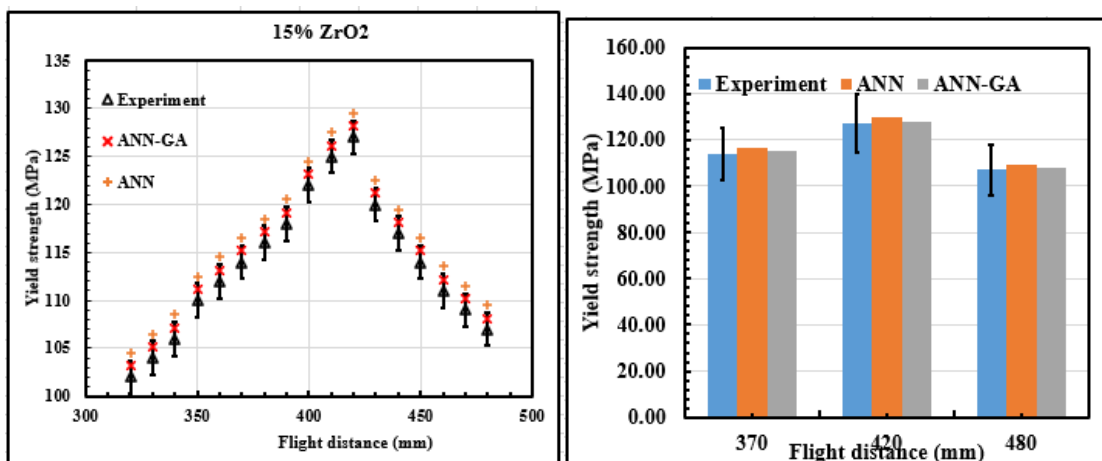
Figure 5.31: Yield strength Al+12.5Si+ZrO$_2$ composites as a function of different composition of ZrO$_2$ with (a) 5%, (b) 10% and (c) 15% reinforcements

Figure 5.32 shows the elongation of AlSi-ZrO$_2$ composites with different flight distances are presented. These results indicates that addition of zirconium oxide increases the brittleness.

`

The presence of ZrO_2 will be prone to localized crack initiation. Clear interfaces in composite will enhance the loading bearing capacity and delay in crack formation but reverse tendency is observed in hot pressed samples and corresponding results are presented in this section. This is due to simultaneous reduction of the elongation and increase in the size of Si phases in the aluminium matrix. This is probably tied to the size of Al matrix and Si particles. Another reason is due to dendrite arm spacing in the microstructure, which also reported by other researcher (Jiang et al., 2014). The average error in MLPNN and MLPNN-GA is 3.8% and 1.9%, respectively.

Table 5.19 (a): Elongation of Al+12.5Si+ZrO_2 composite

5% ZrO_2					
Flight distance (mm)	**Experiment**	**ANN**	**ANN-GA**	**RR (ANN) (%)**	**RR (ANN-GA) (%)**
320	0.38	0.53	0.4113	-39.47	-7.61
330	0.68	0.83	0.7113	-22.06	-4.4
340	1	1.15	1.0313	-15.21	-3.04
350	1.3	1.45	1.3313	-11.54	-2.35
360	1.5	1.65	1.5313	-10.54	-2.04
370	1.6	1.75	1.6313	-9.37	-1.92
380	1.7	1.85	1.7313	-8.82	-1.81
390	1.8	1.95	1.8313	-8.33	-1.71
400	1.9	2.05	1.9313	-7.89	-1.62
410	2.05	2.2	2.0813	-7.32	-1.5
420	2.18	2.33	2.2113	-6.88	-1.42
430	1.9	2.05	1.9313	-7.89	-1.62
440	1.6	1.75	1.6313	-9.37	-1.92
450	1.5	1.65	1.5313	-10.54	-2.04
460	1.4	1.55	1.4313	-10.71	-2.19
470	1.3	1.45	1.3313	-11.54	-2.35
480	1.3	1.45	1.3313	-11.54	-2.35
10% ZrO_2					
320	0.58	0.73	0.68	-25.86	-14.71

330	0.98	1.23	1.08	-25.51	-9.26
340	1.2	1.45	1.3	-20.83	-7.69
350	1.6	1.85	1.7	-15.63	-5.88
360	1.8	2.05	1.9	-13.89	-5.26
370	2.3	2.55	2.4	-10.87	-4.17
380	2.6	2.98	2.86	-14.62	-9.09
390	2.9	3.15	3.16	-8.62	-8.23
400	3.3	3.55	3.56	-7.58	-7.3
410	3.8	4.05	4.06	-6.58	-6.4
420	4.18	4.43	4.44	-5.98	-5.86
430	3.75	4.14	4.01	-10.41	-6.48
440	3.5	3.75	3.76	-7.14	-6.91
450	2.8	3.22	3.06	-15.54	-8.5
460	2.3	2.55	2.56	-10.87	-10.16
470	1.9	2.33	2.16	-22.63	-12.04
480	1.3	1.55	1.56	-19.23	-16.67
15% ZrO$_2$					
320	1.2	1.62	1.4353	-35.54	-16.39
330	1.4	1.82	1.6353	-30.45	-14.39
340	1.6	2.02	1.8353	-26.25	-12.82
350	1.8	2.22	2.0353	-23.33	-11.56
360	2.2	2.62	2.4353	-19.09	-9.66
370	2.5	2.92	2.7353	-16.8	-8.6
380	2.8	3.22	3.0353	-15.24	-7.75
390	3.2	3.62	3.4353	-13.13	-6.85
400	3.8	4.22	4.0753	-11.05	-6.76
410	4.1	4.52	4.3753	-10.24	-6.29
420	4.7	5.09	4.9753	-8.32	-5.53
430	4.1	4.49	4.3753	-9.51	-6.29
440	3.5	3.89	3.7753	-11.14	-7.29
450	2.9	3.29	3.1753	-13.45	-8.67
460	2.3	2.69	2.5753	-16.96	-10.69

| 470 | 1.9 | 2.29 | 2.1753 | -20.53 | -12.66 |
| 480 | 1.6 | 1.99 | 1.8753 | -24.38 | -14.68 |

Table 5.19(b): Elongation of Al+12.5Si+ZrO$_2$ composite

Flight distance (mm)	Experiment	ANN	ANN-GA
5% ZrO$_2$			
370	1.6±0.05	1.75	1.6313
420	2.18±0.04	2.33	2.2113
480	1.3±0.1	1.45	1.3313
10% ZrO$_2$			
370	2.3±0.02	2.55	2.4
420	4.18±0.03	4.43	4.44
480	1.3±0.02	1.55	1.56
15% ZrO$_2$			
370	2.5±0.04	2.92	2.7353
420	4.7±0.07	5.09	4.9753
480	1.6±0.08	1.99	1.8753
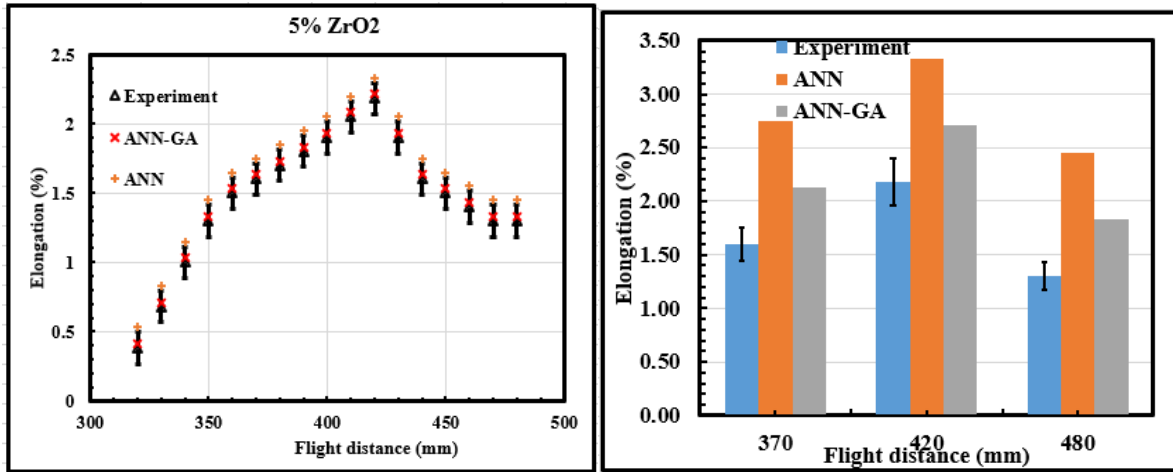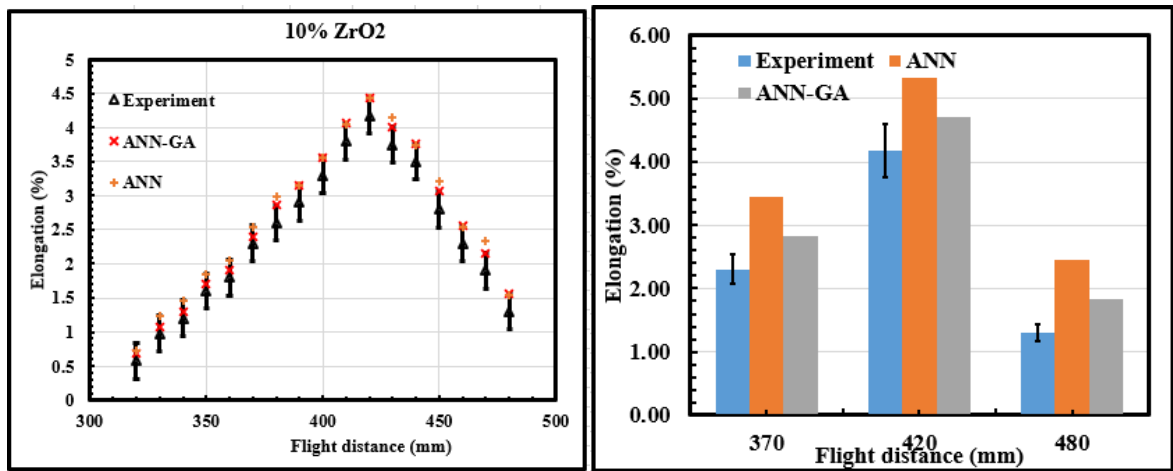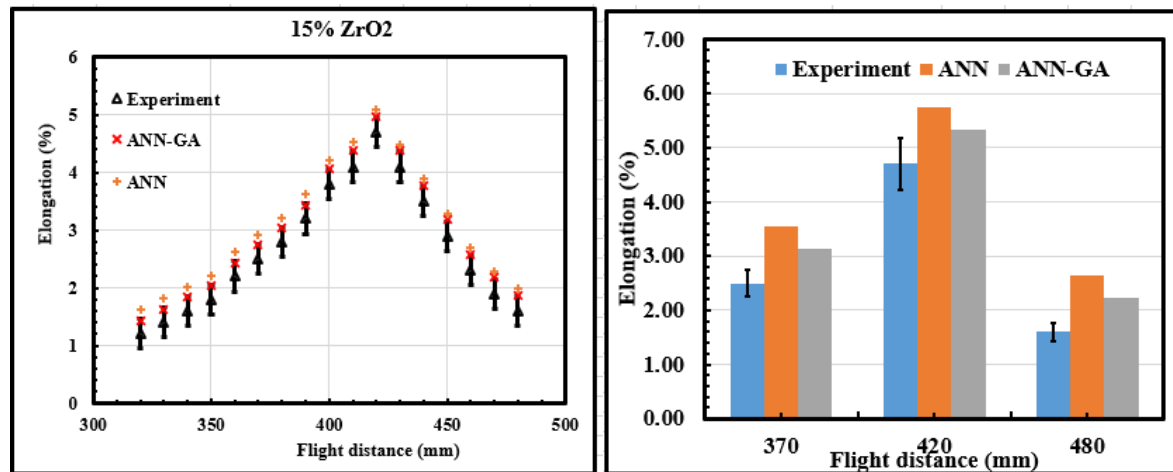
Figure 5.32: Elongation of Al+12.5Si+ZrO₂ composites with ZrO₂ (a) 5%, (b) 10% and (c) 15% reinforcements

`

Hardness testing of AlSi-ZrO$_2$ composites was carried out on META TECH Micro Vickers hardness tester. The tested samples were polished before conducting the test. The weight of 1 kg was used in the current study. The experiments were repeated five times for each sample and the average values of hardness have been reported. The results obtained from MLPNN and MLPNN-GA was compared against the experimental readings for varying flight distance is represented in Figure 5.33. It is interesting to note that at most points around the tests, the increase in flight distance from 320 mm to 420 mm led to increase in micro hardness value. The micro hardness peaked at 71 (HV) at about 420 mm. The addition of ZrO$_2$ into AlSi alloy causes more impact to hardness as observed in Figure 5.33(c). This can be explained by the effect of microstructural refinement in the former owing to the rapid solidification and hot isostatic pressing. The improvement of micro hardness attributes to the change of constituent phase as shown in Figure 5.38(c) for 420 mm flight distance. The developed MLPNN model can predict the micro hardness with the average percentage of deviation of 4.1%, whereas MLPNN-GA optimized neural network predicts within 2.4% deviation with respect to the experimental readings.

Table 5.20(a): Hardness of Al+12.5Si+ZrO₂ composite

5% ZrO₂					
Flight distance (mm)	**Experiment**	**ANN**	**ANN-GA**	**RR (ANN) (%)**	**RR (ANN-GA) (%)**
320	44	46.2	45.235	-5.21	-2.73
330	46	48.2	47.235	-4.78	-2.61
340	48	50.2	49.235	-4.58	-2.51
350	50	52.2	51.235	-4.42	-2.41
360	52	54.2	53.235	-4.23	-2.32
370	54	56.2	55.235	-4.07	-2.24
380	56	58.2	57.235	-3.93	-2.16
390	58	60.2	59.235	-3.79	-2.08
400	60	62.2	61.235	-3.67	-2.02
410	61	63.2	62.235	-3.61	-1.98
420	63	65.2	64.235	-3.49	-1.92
430	60	62.2	61.235	-3.67	-2.02
440	57	59.2	58.235	-3.86	-2.12
450	56	58.2	57.235	-3.93	-2.16
460	53	55.2	54.235	-4.15	-2.28
470	50	52.2	51.235	-4.42	-2.41
480	47	49.2	48.235	-4.68	-2.56
10% ZrO₂					
320	46	48.2	47.235	-4.78	-2.61
330	48	50.2	49.235	-4.58	-2.51
340	50	52.2	51.235	-4.42	-2.41
350	53	55.2	54.235	-4.15	-2.28
360	56	58.2	57.235	-3.93	-2.16
370	58	60.2	59.235	-3.79	-2.08
380	60	62.2	61.235	-3.67	-2.02
390	62	64.2	63.235	-3.55	-1.95
400	65	67.2	66.235	-3.38	-1.86

410	67	69.2	68.235	-3.28	-1.81
420	69	71.2	70.235	-3.19	-1.76
430	63	65.2	64.235	-3.49	-1.92
440	60	62.2	61.235	-3.67	-2.02
450	58	60.2	59.235	-3.79	-2.08
460	56	58.2	57.235	-3.93	-2.16
470	53	55.2	54.235	-4.15	-2.28
480	50	52.2	51.235	-4.42	-2.41
15% ZrO_2					
320	48	50.2	49.235	-4.58	-2.51
330	50	52.2	51.235	-4.4	-2.41
340	52	54.2	53.235	-4.23	-2.32
350	56	58.2	57.235	-3.93	-2.16
360	58	60.2	59.235	-3.79	-2.08
370	60	62.2	61.235	-3.67	-2.02
380	62	64.2	63.235	-3.55	-1.95
390	64	66.2	65.235	-3.44	-1.89
400	67	69.2	68.235	-3.28	-1.81
410	69	71.2	70.235	-3.19	-1.76
420	72	74.2	73.235	-3.06	-1.69
430	68	70.2	69.235	-3.24	-1.78
440	65	67.2	66.235	-3.38	-1.86
450	62	64.2	63.235	-3.55	-1.95
460	59	61.2	60.235	-3.73	-2.05
470	56	58.2	57.235	-3.93	-2.16
480	53	55.2	54.235	-4.15	-2.28

Table 5.20(b): Hardness of Al+12.5Si+ZrO₂ composite

Flight distance (mm)	Experiment	ANN	ANN-GA
5% ZrO₂			
370	54±1.5	56.2	55.235
420	63±0.9	65.2	64.235
480	47±1.36	49.2	48.235
10% ZrO₂			
370	58±0.5	60.2	59.235
420	69±0.9	71.2	70.235
480	50±1.2	52.2	51.235
15% ZrO₂			
370	60±1.1	62.2	61.235
420	72±0.4	74.2	73.235
480	53±0.9	55.2	54.235
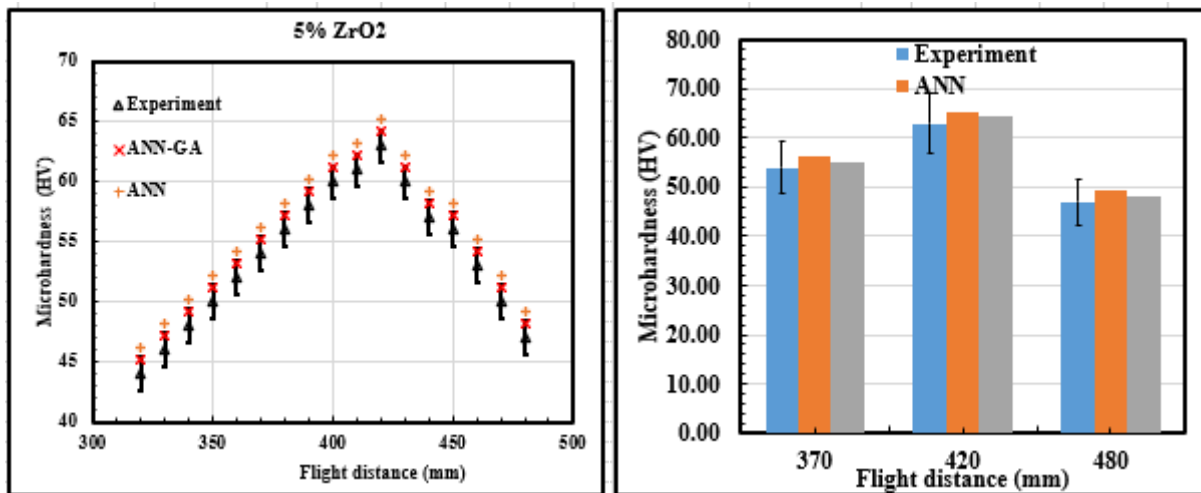
(a)

`
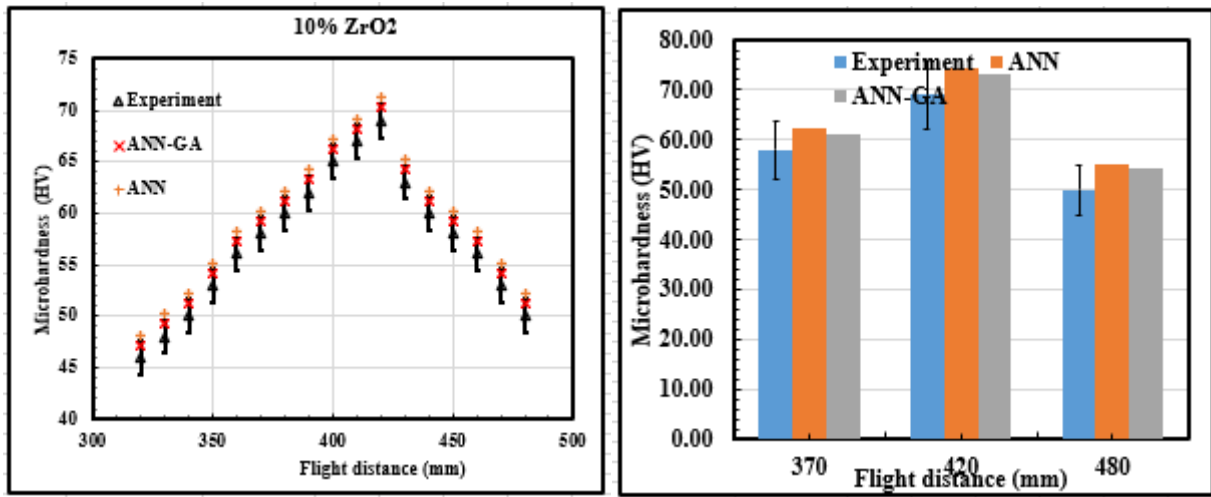
(b)
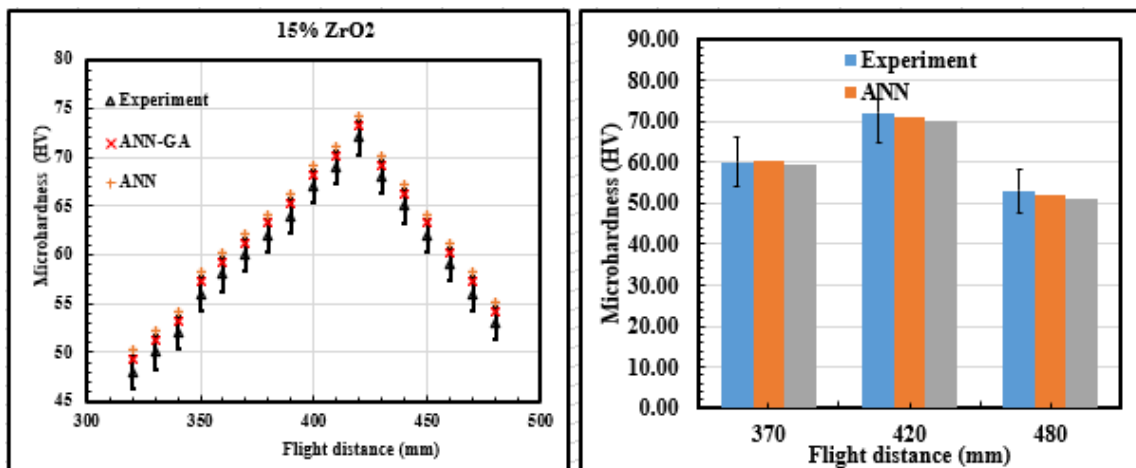
(c)

Figure 5.33: Micro hardness of Al+12.5Si+ZrO$_2$ composites with ZrO$_2$(a) 5%, (b) 10% and (c) 15% reinforcements

5.3.2 Strip thickness and metal flowrate of AlSi-ZrO$_2$ composite as a function of flight distance

The strip thickness of the specimen was measured with a precision micrometre. The strip thickness at the edge and centreline of AlSi-ZrO$_2$ with respect to flight distance is shown in Figure 5.34. Considering the strip thickness trends for centreline at the edge as shown in Figure 5.34, the strip thickness decreased with an increase in flight distance. Considering the trend of the experimental readings of strip thickness, MLPNN needs intensive training algorithm and notable to keep up with the small intermittent changes. The developed MLPNN-GA was able to track the trend of the experimental readings fairly good. The average deviation between the MLPNN-GA optimized model results with the experimental

`

results for strip thickness at centre and strip thickness at edge is found be 6.1% and 4.2%, respectively.

Table 5.20(a): Strip thickness (centre and edge) of Al+12.5Si+ZrO₂ composite

Flight distance (mm)	Experiment	ANN	ANN-GA	RR (ANN) (%)	RR (ANN-GA) (%)
Strip thickness (center)					
320	45	47.2	46.235	-4.89	-2.67
330	44	46.2	45.235	-5.65	-2.73
340	43	45.2	44.235	-5.12	-2.79
350	42	44.2	43.235	-5.24	-2.86
360	41	43.2	42.235	-5.37	-2.92
370	40	42.2	41.235	-5.52	-3.54
380	39	41.2	40.235	-5.64	-3.07
390	38	40.2	39.235	-5.79	-3.15
400	35	37.2	36.235	-6.29	-3.41
410	34	36.2	35.235	-6.47	-3.51
420	32	34.2	33.235	-6.88	-3.72
430	30	32.2	31.235	-7.33	-3.95
440	29	31.2	30.235	-7.59	-4.08
450	28	30.2	29.235	-7.86	-4.22
460	27	29.2	28.235	-8.15	-4.37
470	26	28.2	27.235	-8.46	-4.53
480	25	27.2	26.235	-8.81	-4.71
Strip thickness (edge)					
320	15	17.15385	16.5335	-14.36	-9.28
330	14.75	16.90385	16.2835	-14.62	-9.42
340	14	16.15385	15.5335	-15.38	-9.87
350	14	16.15385	15.5335	-15.38	-9.87
360	13.75	15.90385	15.2835	-15.66	-10.03
370	13.5	15.65385	15.0335	-15.95	-10.21
380	13.25	15.40385	14.7835	-16.26	-10.37

390	13	15.15385	14.5335	-16.57	-10.55
400	12.75	14.90385	14.2835	-16.89	-10.74
410	12.5	14.65385	14.0335	-17.23	-10.93
420	12	14.15385	13.5335	-17.95	-11.33
430	11.5	13.65385	13.0335	-18.73	-11.77
440	11	13.15385	12.5335	-19.58	-12.24
450	10.5	12.65385	12.0335	-20.51	-12.74
460	10	12.15385	11.5335	-21.54	-13.32
470	9.5	11.65385	11.0335	-22.67	-13.92
480	9	11.15385	10.5335	-23.93	-14.56

RR: Relative error

Table 5.20(b): Strip thickness of Al+12.5Si+ZrO$_2$ composite

Flight distance (mm)	Experiment	ANN	ANN-GA	RR (ANN) (%)	RR (ANN-GA) (%)
Strip thickness (center)					
370	40±1.5	42.2	41.235	-5.51	-3.52
420	32±1.2	34.2	33.235	-6.88	-3.72
480	25±1.1	27.2	26.235	-8.82	-4.71
Strip thickness (edge)					
370	13.5±0.5	15.65385	15.0335	-15.95	-10.21
420	12±1.3	14.15385	13.5335	-17.95	-11.33
480	9±1.2	11.15385	10.5335	-23.93	-14.56
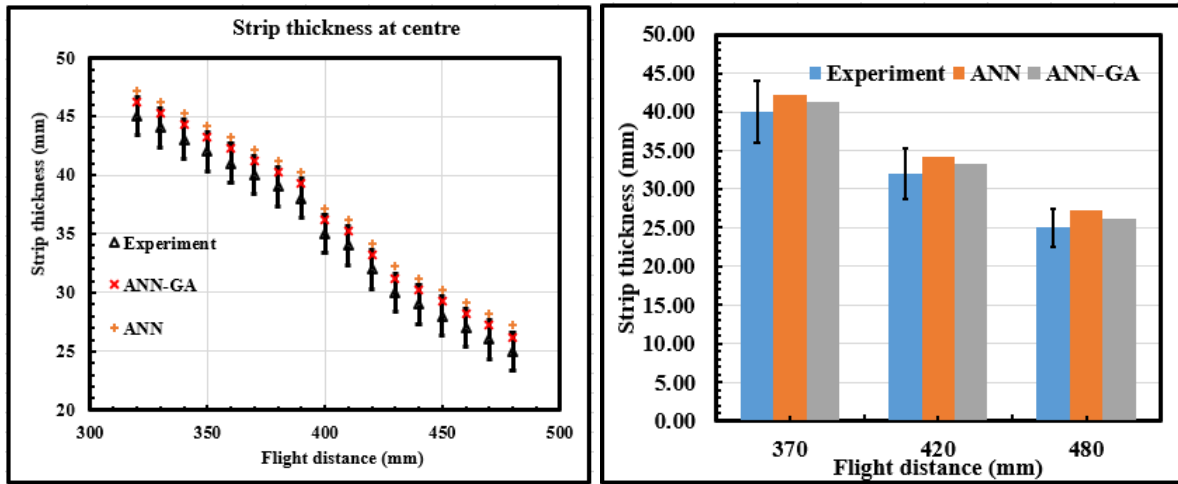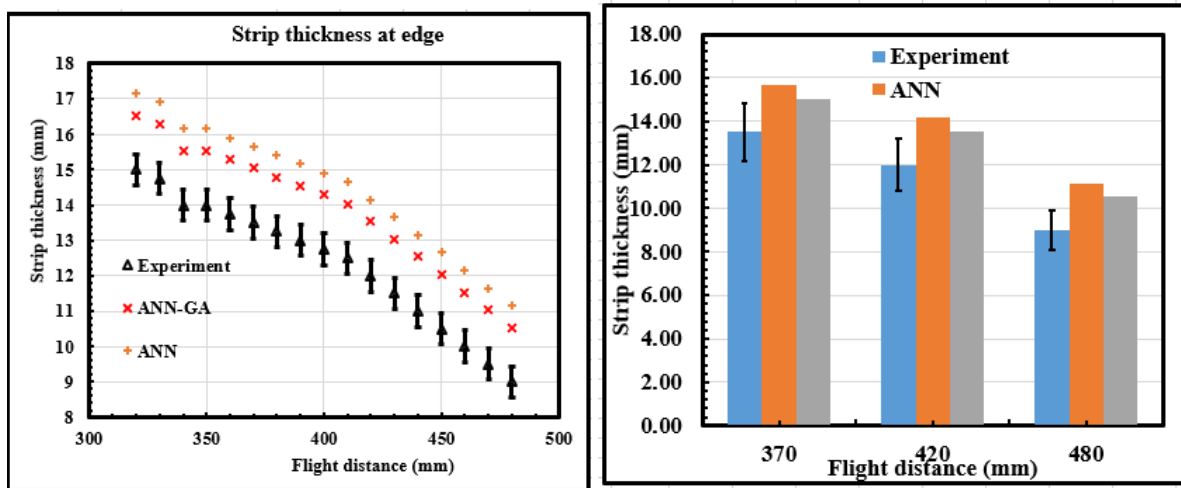
Figure 5.34 (a): Variation of strip thickness at centre, as a function of flight distance; (b) Variation of strip thickness at edge as a function of flight distance

Figure 5.35(a) shows the variation of metal flowrate with respect to the flight distance. It can be observed that the metal flow decreases with increasing the flight distance. The pressure is integral to the performance of the nozzle. It is worthy to note that operating condition for spray forming should be properly selected to ensure a large fraction of partially solid droplets. The higher flight distance consists a large fraction of solidified droplets prior to spray deposition. Therefore, the amount of liquid available to flow into the substrate is very minimal. Conversely, at small deposition substrate, the larger fraction of liquid more accurately replicates the substrate surface profile. The deviation between the MLPNN and MLPNN-GA with respect to experimental readings is 10.2% and 5.8%, respectively.

`

Table 5.21(a): Spray flowrate of Al+12.5Si+5% ZrO$_2$ composite

Flight distance (mm)	Experiment	ANN	ANN-GA	RR (ANN) (%)	RR (ANN-GA) (%)
320	18.9423077	21.09630769	19.9973	-11.37	-5.28
330	18.5660377	20.72003774	19.621	-11.6	-5.38
340	18.2037037	20.3577037	19.2587	-11.83	-5.48
350	17.8363636	19.99036364	18.8914	-12.08	-5.58
360	17.4821429	19.63614286	18.5371	-12.32	-5.69
370	17.1578947	19.31189474	18.2129	-12.55	-5.79
380	16.8448276	18.99882759	17.8998	-12.79	-5.89
390	16.5423729	18.69637288	17.5974	-13.02	-6
400	16.2333333	18.38733333	17.2883	-13.27	-6.1
410	15.9508197	18.10481967	17.0058	-13.5	-6.2
420	15.6612903	17.81529032	16.7163	-13.75	-6.31
430	15.3809524	17.53495238	16.436	-14	-6.42
440	15.109375	17.263375	16.1644	-14.26	-6.53
450	14.8615385	17.01553846	15.9165	-14.49	-6.63
460	14.6212121	16.77521212	15.6762	-14.73	-6.73
470	14.3731343	16.52713433	15.4281	-14.99	-6.84
480	14.1176471	16.27164706	15.1726	-15.26	-6.95

RR: Relative error

Table 5.21(b): Spray flowrate of Al+12.5Si+5% ZrO$_2$ composite

Flight distance (mm)	Experiment	ANN	ANN-GA	RR (ANN) (%)	RR (ANN-GA) (%)
370	17.1578947±1.2	19.31189474	18.2129	-12.55	-5.79
420	15.6612903±1.1	17.81529032	16.7163	-13.75	-6.31
480	14.1176471±1.9	16.27164706	15.1726	-15.26	-6.95

`
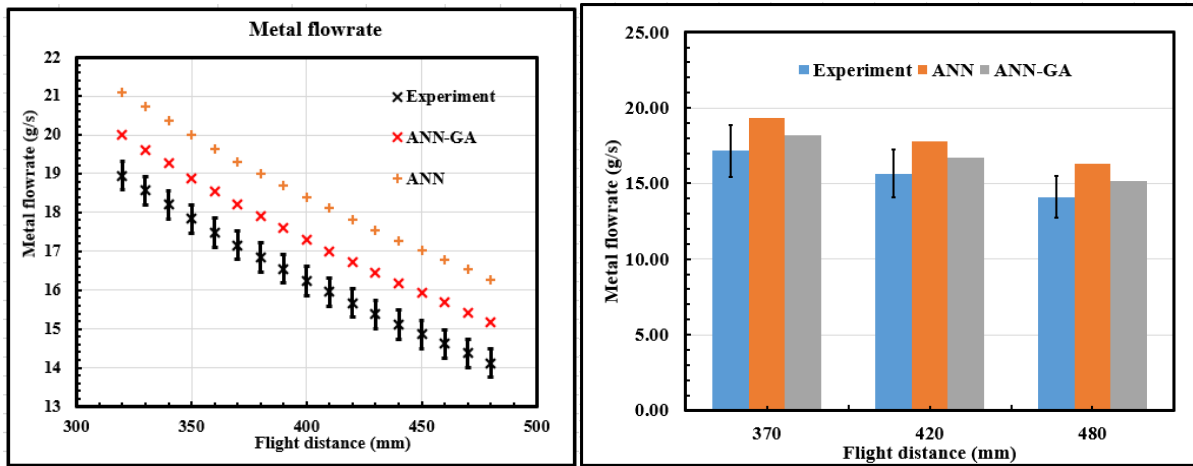
Figure 5.35: Variation of metal flowrate as a function of flight distance

The degree of porosity as a function of flight distance is shown in Figure 5.36(b). The degree of porosity is small for the lower flight distance. The larger spray height of 480 mm, the degree of porosity level is higher indicating that the pores are evenly distributed across the strip thickness. The porosity is measured by preparation the sample, which is cut from the centre portion (5 mm x 10 mm x 10 mm). The measurements were carried out by vacuum Xylene impregnated method. It can be observed that the degree of porosity at the edge of the strip doubles as the flight distance increases from 320 mm to 480 mm. The corresponding increase in the degree of porosity level at the centreline of the strip is fourfold. From the Figure 5.36 (a) & (b), it can be seen that the MLPNN-GA model predicated lower variations than the MLPNN model. The average error before optimization of initial weights and biases using MLPNN was found to be of 7.8%. The optimized weight and biases updated using MLPNN-GA model, the average error was decreased to 6.2%. It is worthy to note that for all the training sets, the number of required training the MLPNN-GA significantly decreased. The properties of sprayed AlSi-ZrO$_2$ can hence be adjusted, including strength, hardness and porosity.

Table 5.22(a): Degree of porosity of Al+12.5Si+ZrO₂ composite

Flight distance (mm)	Experiment	ANN	ANN-GA	RR (ANN) (%)	RR (ANN-GA) (%)
Strip thickness (center)					
320	8	10.2	9.235	-27.5	-13.37
330	8.2	10.4	9.435	-26.83	-13.09
340	8.6	10.8	9.835	-25.58	-12.56
350	8.9	11.1	10.135	-24.72	-12.19
360	9.2	11.4	10.435	-23.91	-11.84
370	9.5	11.7	10.735	-23.16	-11.5
380	9.9	12.1	11.135	-22.22	-11.09
390	10.2	12.4	11.435	-21.57	-10.8
400	10.5	12.7	11.735	-20.95	-10.52
410	11	13.2	12.235	-20	-10.09
420	11.5	13.7	12.735	-19.13	-9.7
430	12.2	14.4	13.435	-18.03	-9.19
440	12.8	15	14.035	-17.19	-8.8
450	13.5	15.7	14.735	-16.3	-8.38
460	13.8	16	15.035	-15.94	-8.21
470	14.1	16.3	15.335	-15.6	-8.05
480	14.4	16.6	15.635	-15.28	-7.9
Strip thickness (edge)					
320	0.5	0.8	0.8	-60	-37.5
330	1	1.3	1.3	-30	-23.08
340	1.4	1.7	1.7	-21.43	-17.65
350	1.6	1.9	1.9	-18.75	-15.79
360	1.8	2.1	2.1	-16.67	-14.29
370	1.9	2.2	2.2	-15.79	-13.64
380	2.1	2.4	2.4	-14.29	-12.5
390	2.2	2.5	2.5	-13.64	-12
400	2.3	2.6	2.6	-13.04	-11.54

410	2.5	2.8	2.8	-12	-10.71
420	2.8	3.1	3.1	-10.71	-9.68
430	3.1	3.4	3.4	-9.68	-8.82
440	3.3	3.6	3.6	-9.09	-8.33
450	3.5	3.8	3.8	-8.57	-7.89
460	3.6	3.9	3.9	-8.33	-7.69
470	3.8	4.1	4.1	-7.89	-7.32
480	4	4.3	4.3	-7.5	-6.98

Table 5.22(b): Degree of porosity of Al+12.5Si+ZrO$_2$ composite

Flight distance (mm)	Experiment	ANN	ANN-GA	RR (ANN) (%)	RR (ANN-GA) (%)
Strip thickness (center)					
370	9.5±0.8	11.7	10.735	-23.16	-11.5
420	11.5±1.2	13.7	12.735	-19.13	-9.7
480	14.4±1.8	16.6	15.635	-15.28	-7.9
Strip thickness (edge)					
370	1.9±1.9	2.2	2.2	-15.79	-13.64
420	2.8±1.4	3.1	3.1	-10.71	-9.68
480	4±1.7	4.3	4.3	-7.5	-6.98
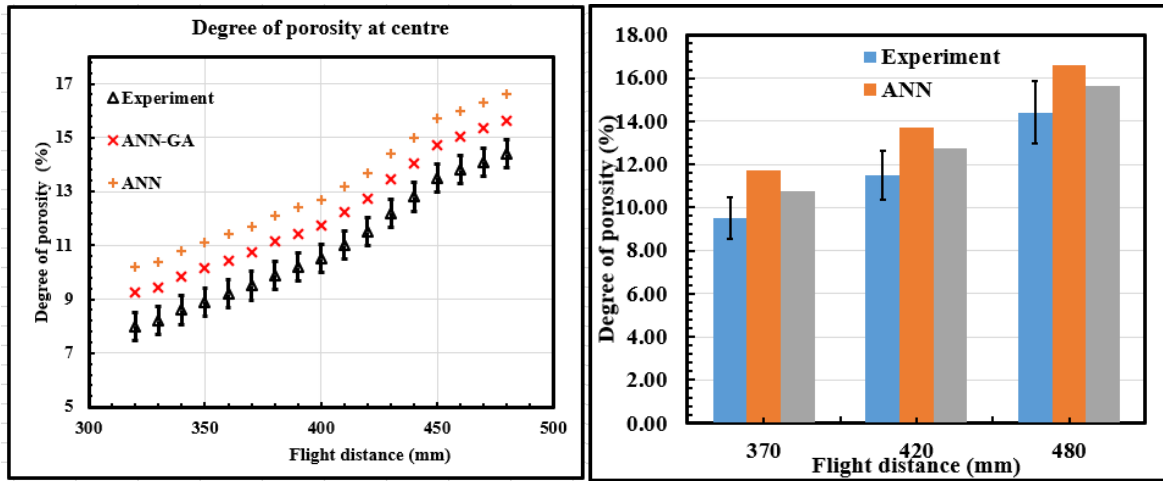
(a)
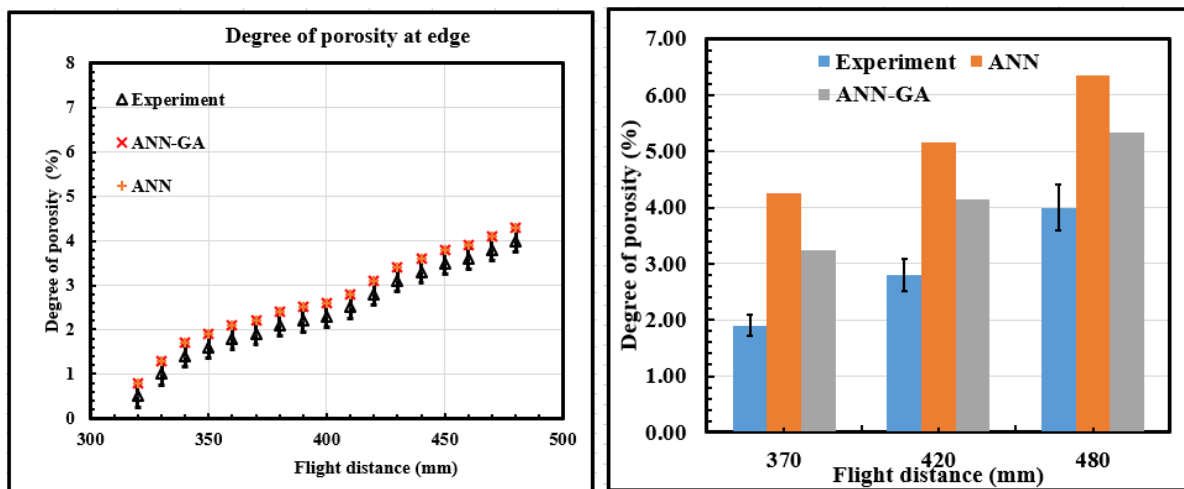
(b)

Figure 5.36 (a): Degree of porosity at centre as a function of flight distance; (b) Degree of porosity at edge as a function of flight distance

5.3.3 Evaluation of the Microstructure and EDS as a function of flight distance

The microstructures of the 5%, 10% and 15% AlSi-ZrO$_2$ composites for the flight distance 370 mm are shown in Figure 5.37. From Figure 5.37(a-c), it can be observed that the AlSi-ZrO$_2$ is mainly composed of Al matrix and Si phases, and the two-phase interface is bonded strongly. At the start of spray deposition, the droplets splat on the substrate and the deposit experiences a higher cooling rate. This mainly depends on the temperature and thermal conductivity of the substrate.

Therefore, the deposit exhibits a fine microstructure in the vicinity of the substrate as shown in Figure 5.37. It is worthy to note that the top layer of the growing preform during spray

`

deposition at lesser distances receives both the semi-solid and undercooled droplet particles. A non-uniform distribution of these liquids may follow a different solidification path. Smaller flight distance results in insufficient gas filling time to interact with the spray so that a larger fraction of the droplet flux is completely molten. Additionally, the nuclei were remelted and this is due to the larger temperature of the liquid layer. This results in an extremely thick molten layer on the top of the deposit. Therefore, optimizing a proper flight distance is highly essential. The different flight distances for the developed composites were discussed in Figure 5.38 & 5.39, respectively.

(a)   (b)

(c)
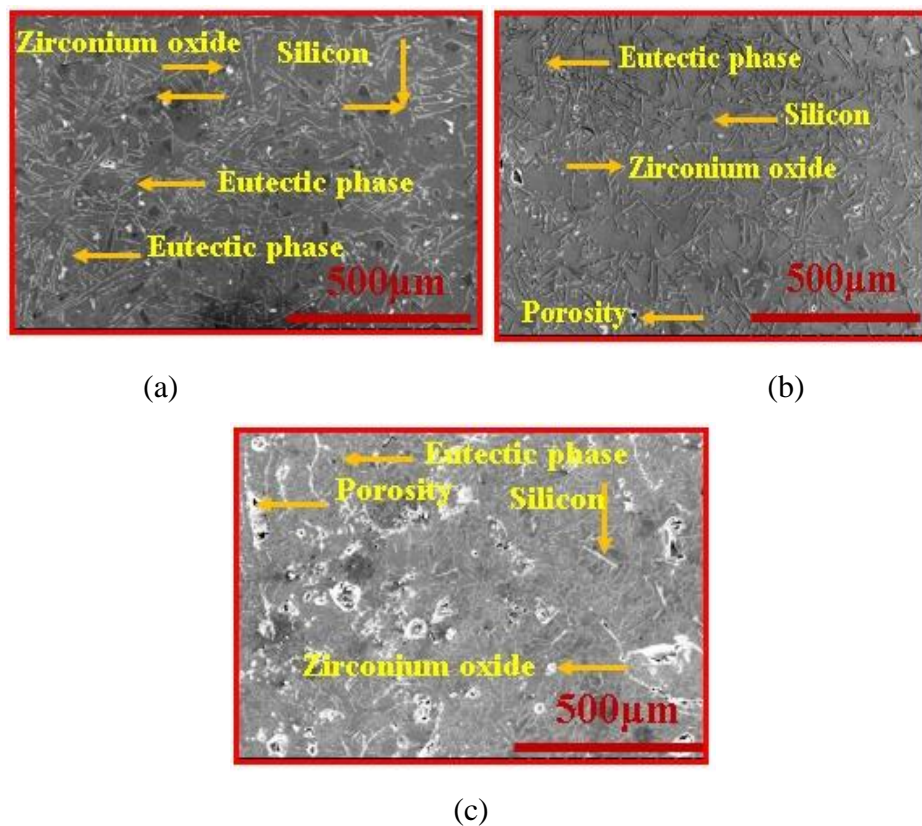
Figure 5.37: Microstructure of Al+12.5Si+ZrO₂ composites with ZrO₂(a) 5%, (b) 10% and (c) 15% reinforcements, for the flight distance 370 mm

It is observed that the Si particles have been finely divided and are globular in shape (420 mm flight distance). The composites mainly composed of block like primary Si, needle-like eutectic Si phases and well distributed ZrO_2 reinforced particles in the dendritic Al-matrix. It was observed that increase in ZrO_2 content resulted in clustering of reinforcement particles at grain junctions as well as continuous network along the grain boundaries. It consists of coarse primary Si, needle-like eutectic Si phases and small agglomerated ZrO_2 particles dispersed

`

uniformly in the matrix. It is interesting to note that with the addition of 15% ZrO_2, there is decrease in eutectic temperature of Al–Si alloy that accelerates the growth of the Si phase during rapid solidification. The average particle size is about 25 μm, which was calculated based on particle count fraction. Conversely, the liquid phase formed due to the addition of ZrO_2 facilitates the small-sized Si phase attached to the surface of the large-sized Si phase by diffusion, resulting in a slight growth of the Si phase. The eutectic Si also depicted round shape in the deposit near the substrate-deposit interface. The volume fraction of normal eutectic microstructure was observed to grow with its subsequent coarsening in the deposit at a distance of 420 mm from the deposition substrate. The morphology of most of the ZrO_2 particles is almost spherical in nature. Strong interfacial bonding of ZrO_2 with the Al-12.5%Si alloy is observed, which further helps in achieving better mechanical properties. Figure 5.38 shows considerable microstructure uniformity with round shape of the eutectic Si particle throughout the deposit. They showed that the thickness of the preform grows as it proceeds with the deposition. This results an impediment for the heat flow through the preform. An additional increase in deposit thickness results in improved thermal resistance. The heat transfer rate by the cooling substrate decreases, i.e. under cooling will be less from the spray deposited materials. This decrease in the rate of heat extraction might be responsible for the observed increase in microstructural scale with increasing deposit thickness, i.e. at the central region of the preform (Grant et al., 1991; Raju et al., 2011) as shown in Figure 5.37. Uniform dispersion has a better adhesion contact area between both the matrix and the reinforcement, thereby enhancing the mechanical properties of the composites. This results in refined microstructural features compared to other flight distances.
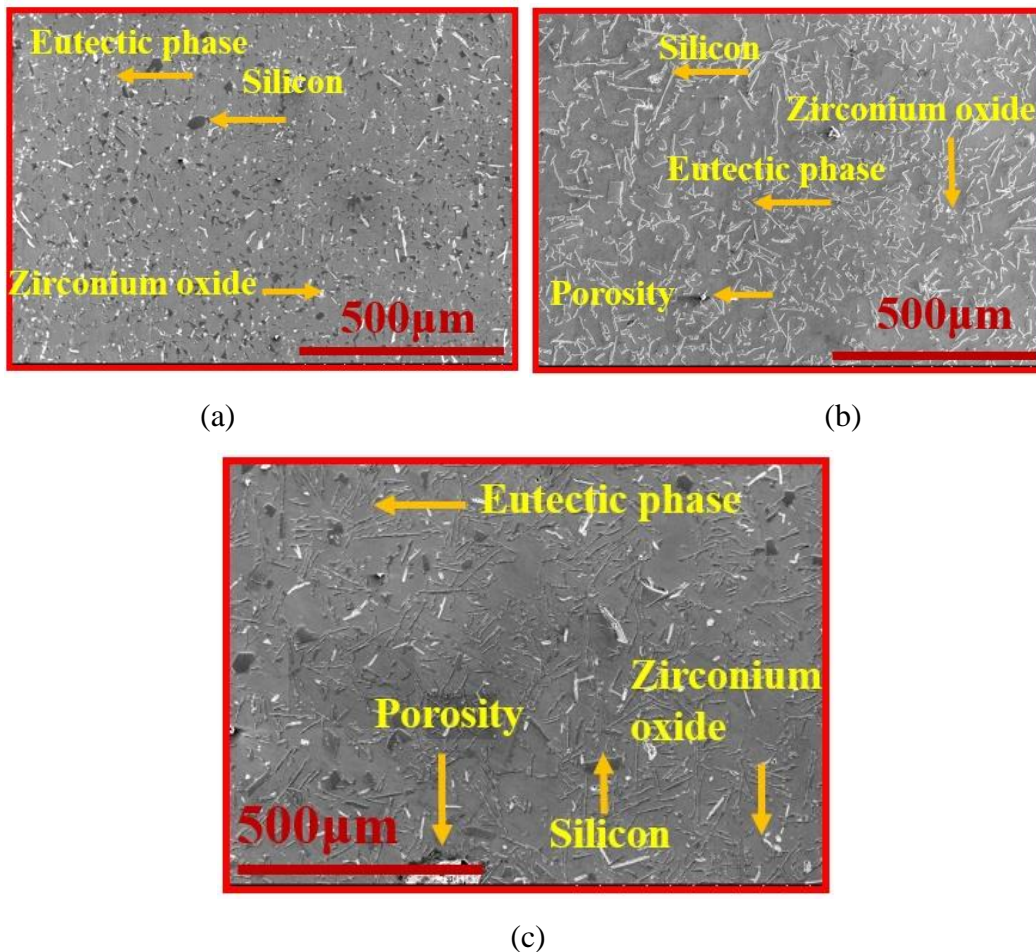
Figure 5.38: Microstructure of Al+12.5Si+ZrO$_2$ composites with ZrO$_2$(a) 5%, (b) 10% and (c) 15% reinforcements, for the flight distance 420 mm

The higher flight distance makes the spray droplets to reduce the lower enthalpy, which is prior to the spray deposition. Moreover, as mentioned above, if the flight distance is less, a higher fraction of the large size droplets come on the growing preform in undercooled state. It is worthy to note that with the increase in flight distance, the grain morphology in the middle of the strip changes from columnar to equiaxed as shown Figure (5.37-5.39). At higher flight distance of 480 mm, the degree of porosity level is larger. This leads to the uniform distortion of the more pores across the strip thickness. It is interesting to note that the central region of the deposit consists of larger size droplets (Lavernia et al., 1989; 1992; Srivastava et al., 2001). This particular portion receives highly undercooled droplets and the same phenomena is observed by other researchers (for eg. Xu and Lavernia, 1999 and Ojha et al., 1991). Srivastava et al., (2001) results showed that a 120um droplet remains in undercooled state up to 300 mm deposition distance. On the whole flight distance determines the amount of cooling of the droplets by the atomizing gas. From the aforementioned phenomena of the

observations of SEM microstructure, it is fair to conclude that the optimized flight distance is 420 mm. To qualitatively analyse the phases in the AlSi-ZrO$_2$, the energy dispersive spectroscopy (EDS) was employed to characterize the evolution of the phases with the addition of ZrO$_2$ as illustrated in Figure 5.39 for the compositions of 5% ZrO$_2$, 10% ZrO$_2$ and 15% ZrO$_2$, respectively.

(a) (b)

(c)
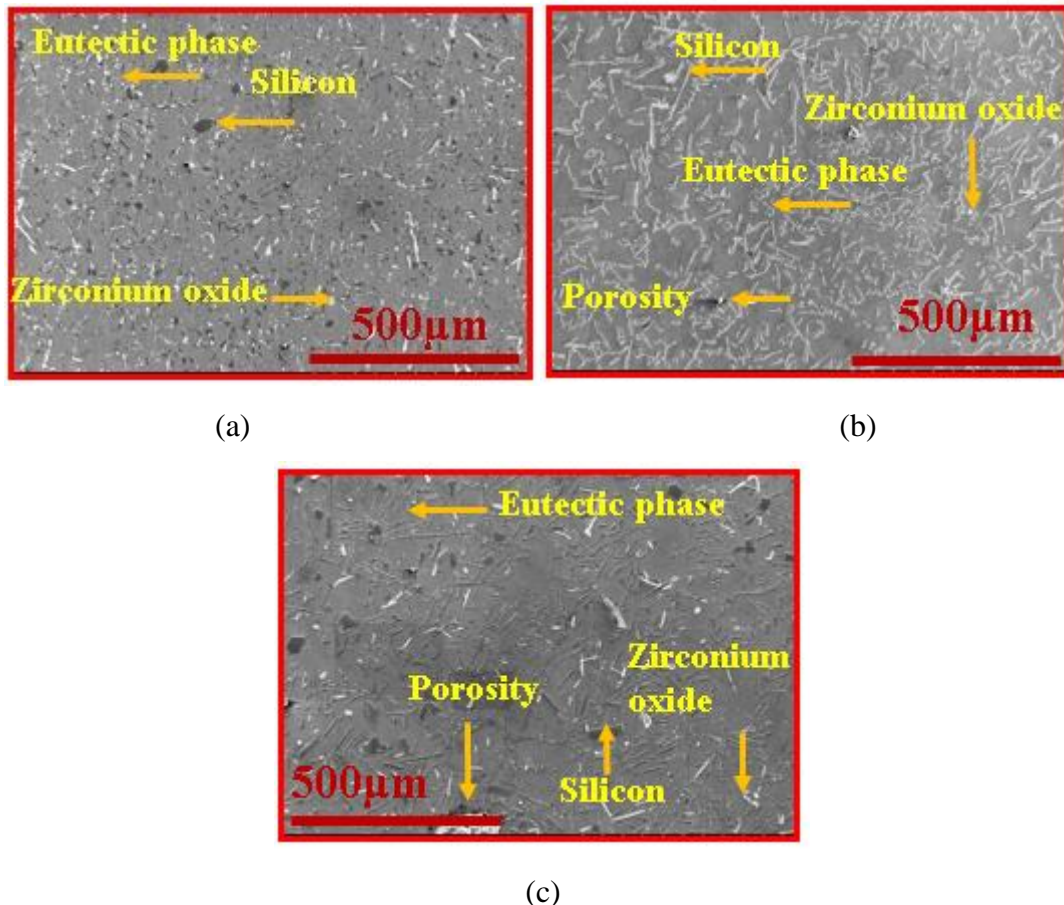
Figure 5.39: Microstructure of Al+12.5Si+ZrO$_2$ composites with ZrO$_2$(a) 5%, (b) 10% and (c) 15% reinforcements, for the flight distance 480 mm

The actual composition of the AlSi-ZrO$_2$ is determined by EDS. The diffraction peaks corresponding to α-Al and Si phases are detected in both samples as observed in the Figure 5.40(a), (b) & (c). However, diffraction peaks correlate to ZrO$_2$ are detected in all the different compositions. EDS spectra confirmed the existence of ZrO$_2$ in the AlSi alloy. It can be observed that highest ZrO$_2$ atomic composition is found in 15%. It is worthy to note that the highest observed weight percentages are 17.12%, 0.52%, 0.57% and 81.80% with corresponding to O$_2$, Al, Si and Zr elements, respectively. It shows the incorporation of Zr

`

ions into AlSi structure. This incorporation factor can influence the mechanical and structural properties. Based on the observations of mechanical strength, degree of porosity and microstructure, it is fair to conclude that the preferred flight distance for the developed AlSi-ZrO_2 alloy is 420 mm.
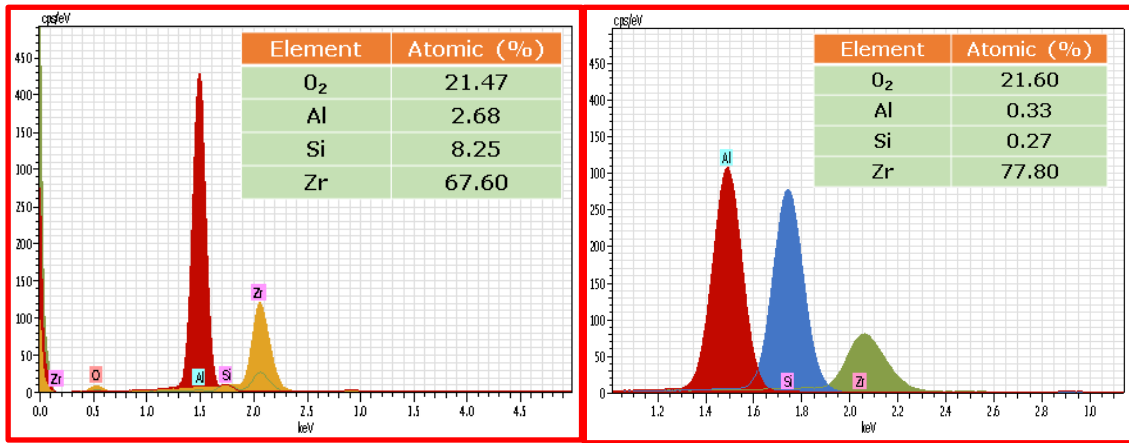
(a)

(b)
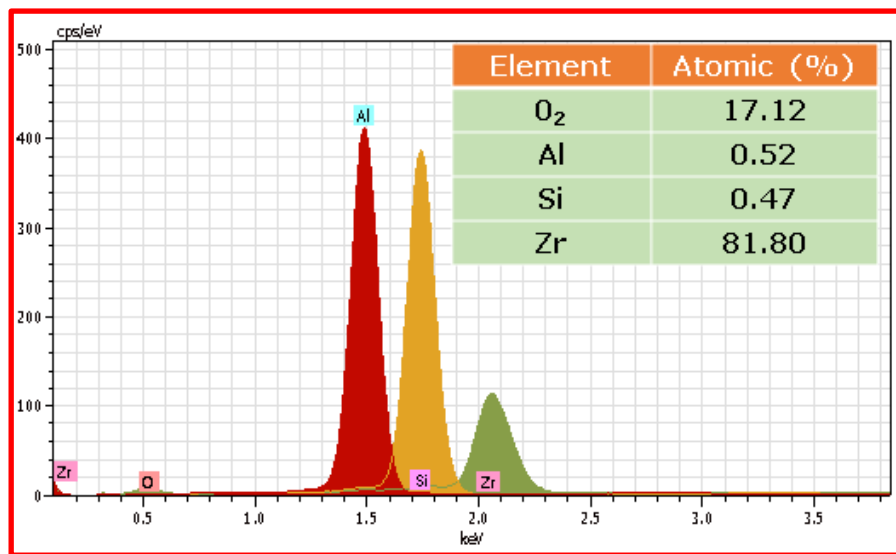
(c)

Figure 5.40: The EDS spectrum of Al+12.5Si+ZrO_2 composites (a) 5% (b) 10% (c) 15% ZrO_2, for the flight distance 420 mm

141

`

Summary:

AlSi-ZrO$_2$ composite with varying the percentage of reinforcement material using spray deposition material has been developed successfully. The effect of flight of distance on the mechanical and microstructural properties of AlSi-ZrO$_2$ composite were investigated and following are the outcomes of the work:

- The microstructure of the spray deposited AlSi-ZrO$_2$ alloy is significantly affected by deposit substrate and the nozzle distance. At lesser flight distance (320 mm), needle and α-Al like constituent of eutectic Si phase are observed and the reason is due to higher undercooling experienced by the liquid pool. Interestingly, at the optimized flight distance of 420 mm, well-defined pre-solidified particles were noticed.

- Evaluation of hardness and mechanical properties of spray formed composites exhibits higher tensile, compressive and yield strength. The combination of AlSi-ZrO$_2$ precipitation and strengthening results in the improved mechanical properties.

- The degree of porosity at the center and at the edge surface of the strip is strongly dependent upon the surface preparation of the substrate. The degree of porosity level will be higher at larger flight distance. At this stage the pores are more uniformly distributed across the strip thickness

- In summary, the smaller flight distance leads to a large scale of compositional inhomogeneity in the preform. The thickness of the deposit increases with the increase in incoming fraction of liquid at the deposition surface. A refined and uniform microstructure is evolved at intermediate distances. In addition, the thickness of liquid pool is comparable to the thickness of the interaction domain formed during spray deposition.

- In addition, the experimental data were compared with the developed neural network models for validation. Optimized MLPNN-GA model was found to be more robust and efficient. The model estimates the values close to the experimental readings, which signified the accuracy of the developed model. Overall, MLPNN, MLPNN-GA methods and experimental study gave valuable thoughts on the use of reinforced particle of ZrO$_2$ in AlSi metal composite.

`

5.4 Wear behaviour of Al-12.5Si composite reinforced with ZrO₂ composite using spray deposition and ANN-GA methods

5.4.1 Wear characteristics as a function of sliding velocity

The coefficient of friction (COF) of the fabricated composites are plotted as a function of sliding velocity in Figure 5.41 with a fixed load 40 N. It can be noted that coefficient of friction (COF) is increases with increase in sliding velocity. At lower sliding velocity, the friction between the two contact surfaces is less and can prevent the scratch and cut from the surface. The higher sliding velocity increase the touch area between the counter disk surface and the pin, increasing the friction coefficient (Mazahery et al., 2012; Shabani et al., 2011a). On the other hand, friction coefficient is related to the interaction of asperities between the counter disk surface and the pin. However, the COF varies within specific range throughout the test period in microscale. It can be noted that as sliding velocities is lower, more amount of time is available for the formation of micro welds. This in turn increases the frictional force which shears off micro welds in order to maintain the relative motion. Therefore, friction coefficient increases. The average error in MLPNN and MLPNN-GA is 3.6% and 1.3%, respectively. Most of the information in this section has been published. (**https://doi.org/10.1016/j.mtcomm.2022.103217**)

`

Table 5.23(a): Coefficient of friction for Al+12.5Si+ZrO₂ composite

Sliding velocity (m/s)	Coefficient of friction	Coefficient of friction (ANN	Coefficient of friction ANN-GA	RR (ANN) (%)	RR (ANN-GA) (%)
5% ZrO₂					
0.91	0.14	0.19	0.18	-36.36	-22.54
1.27	0.17	0.22	0.21	-30.30	-19.51
1.64	0.20	0.25	0.24	-27.18	-17.02
2.00	0.21	0.26	0.25	-23.53	-14.14
2.36	0.23	0.29	0.27	-25.93	-14.95
2.73	0.27	0.32	0.31	-18.52	-12.90
3.09	0.29	0.34	0.33	-17.39	-12.21
3.45	0.31	0.36	0.35	-16.00	-11.10
3.82	0.33	0.39	0.37	-18.48	-10.81
4.18	0.37	0.42	0.41	-13.51	-9.76
4.55	0.40	0.46	0.44	-15.60	-10.37
10% ZrO₂					
0.91	0.11	0.14	0.13	-22.22	-10.36
1.27	0.14	0.17	0.15	-17.86	-8.50
1.64	0.17	0.20	0.18	-14.71	-7.10
2.00	0.19	0.22	0.20	-15.47	-6.48
2.36	0.20	0.23	0.22	-12.35	-6.68
2.73	0.25	0.27	0.27	-10.20	-9.26
3.09	0.26	0.29	0.29	-12.19	-8.70
3.45	0.29	0.31	0.31	-8.70	-8.00
3.82	0.31	0.33	0.33	-8.20	-7.58
4.18	0.35	0.38	0.37	-9.57	-6.76
4.55	0.37	0.41	0.40	-9.93	-6.29
15% ZrO₂					
0.91	0.09	0.12	0.12	-37.71	-25.53
1.27	0.12	0.15	0.15	-28.70	-20.69
1.64	0.15	0.18	0.18	-22.76	-17.14
2.00	0.16	0.19	0.19	-19.69	-15.67
2.36	0.18	0.21	0.21	-18.59	-14.46
2.73	0.20	0.25	0.25	-29.74	-22.00
3.09	0.21	0.27	0.27	-27.11	-20.35
3.45	0.24	0.30	0.29	-24.42	-18.30
3.82	0.26	0.31	0.31	-22.75	-17.74
4.18	0.30	0.35	0.35	-19.15	-15.18
4.55	0.32	0.38	0.38	-17.67	-14.57

RR: Relative error

Table 5.23(b): Coefficient of friction for Al+12.5Si+ZrO₂ composite

Sliding velocity (m/s)	Coefficient of friction	Coefficient of friction (ANN	Coefficient of friction ANN-GA	RR (ANN) (%)	RR (ANN-GA) (%)
5% ZrO₂					
0.91	0.14±0.03	0.19	0.18	-36.36	-22.54
2.73	0.27±0.02	0.32	0.31	-18.52	-12.90
4.55	0.40±0.01	0.46	0.44	-15.60	-10.37
10% ZrO₂					
0.91	0.11±0.05	0.14	0.13	-22.22	-10.36
2.73	0.25±0.02	0.27	0.27	-10.20	-9.26
4.55	0.37±0.03	0.41	0.40	-9.93	-6.29
15% ZrO₂					
0.91	0.09±0.01	0.12	0.12	-37.71	-25.53
2.73	0.20±0.03	0.25	0.25	-29.74	-22.00
4.55	0.32±0.03	0.38	0.38	-17.67	-14.57

(a)

`

(b)

(c)
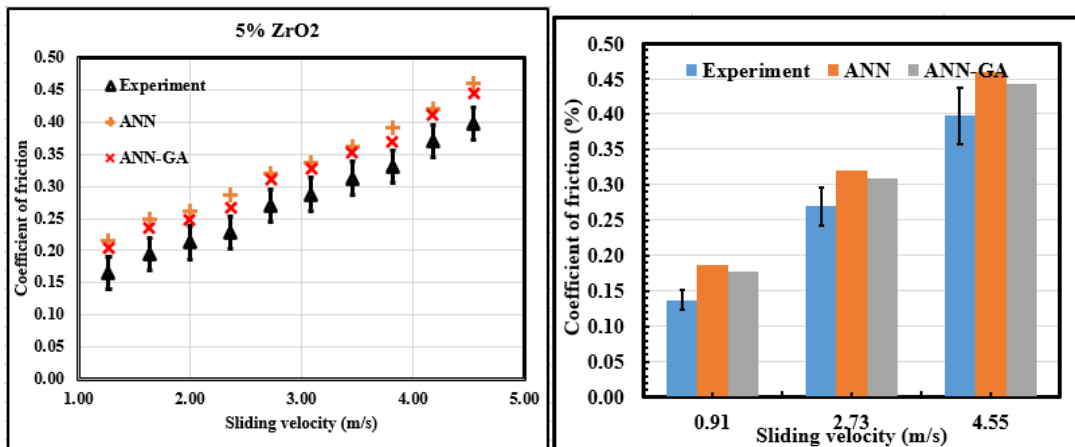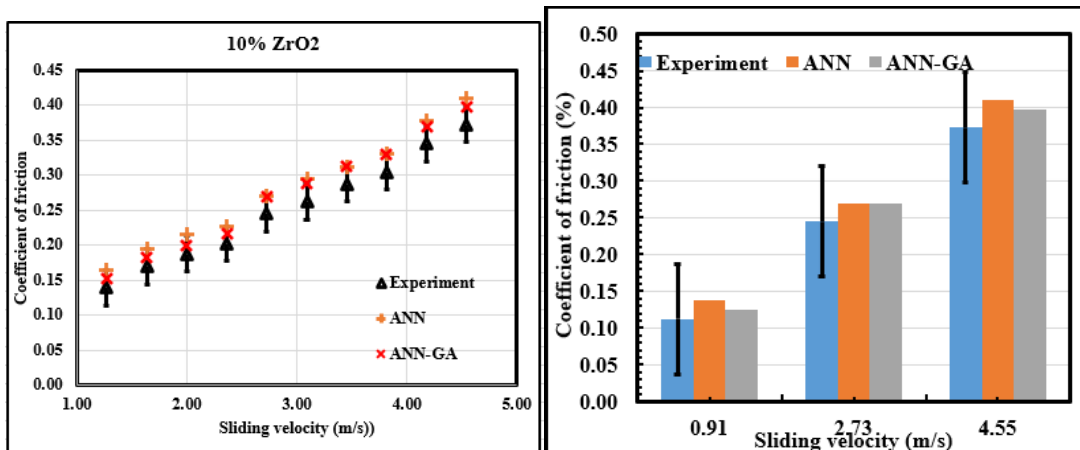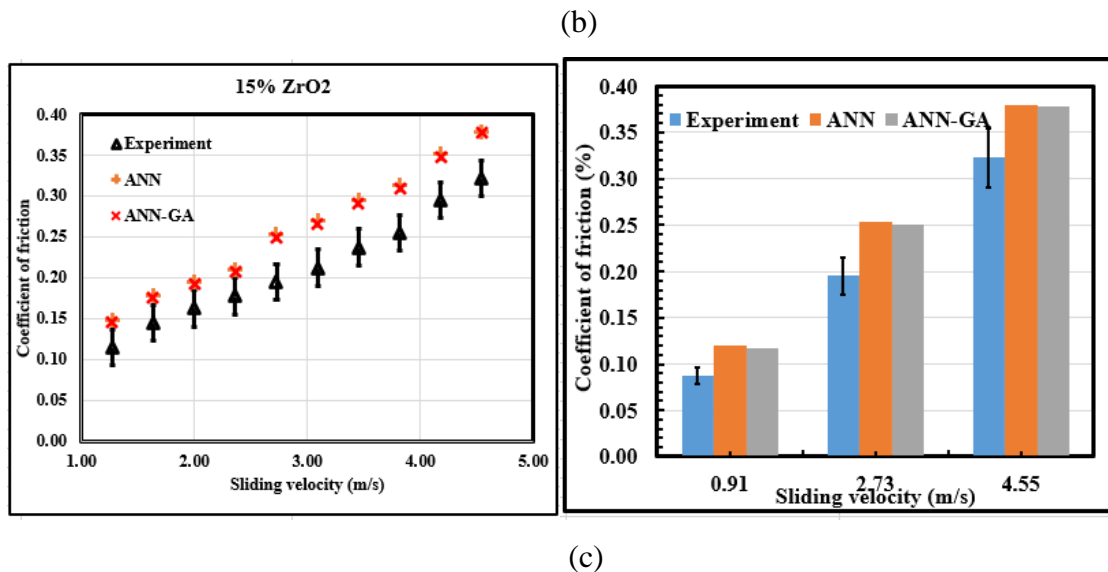
Figure 5.41: Coefficient of the friction with respect to sliding velocity of Al+12.5Si+ZrO₂ composites with (a) 5 wt. % (b) 10 wt.% (c) 15 wt.% ZrO₂ reinforcements

The variation of wear rates as a function of sliding velocity is plotted in Figure 5.42. It is to noted that the wear behaviour depends on asperity-to-asperity contact between the two surfaces (counter disk and pin surface). These surfaces are in relative motion which rub against each other. This is primarily due to the occurrence of seizure. It can be observed that the wear rates are decreased as the sliding velocity is increased. It is worthy to note that the wear properties can be improved by heat treatment process (Rao et al., 2001b). For 15% ZrO₂, the wear rate is 37.7% and 15.6% less compared to 5% and 10% ZrO₂ composition. This behaviour is consistent with (Anil, 2007). The same author reported that aluminium silicon wear rate decreased with higher sliding velocities. The other reasons for this phenomenon are the competing effects of temperature and strain rate developed during the sliding between the pin and counter disk surfaces (Raju et al., 2011). This can be accomplished by the microstructural modifications in the aluminium silicon alloy. The tiny silicon and globular shaped particles controlled the wear rate during the spray forming method (Anil, 2007). In the line of this context, Kori et al., (2007) investigated grain modified/refined aluminium silicon alloy in eutectic alloy. Their study found that the wear rate decreased in both the cases, which is consistent with our results. The average error in MLPNN and MLPNN-GA is 3.2% and 2.5%, respectively.

Table 5.24(a): Wear rate for Al+12.5Si+ZrO$_2$ composite

Sliding velocity (m/s)	Wear rate (mm^3/m)	Wear rate (mm^3/m) ANN	Wear rate (mm^3/m) ANN-GA	RR (ANN) (%)	RR (ANN-GA) (%)
5% ZrO$_2$					
0.91	0.003293	0.003853	0.003543	-17.01	-7.06
1.27	0.002587	0.003147	0.002837	-21.65	-8.81
1.64	0.002195	0.002755	0.002445	-25.51	-10.22
2.00	0.001946	0.002506	0.002196	-28.78	-11.39
2.36	0.001773	0.002193	0.001923	-23.69	-7.80
2.73	0.001646	0.002066	0.001896	-25.51	-13.18
3.09	0.001550	0.001970	0.001800	-27.11	-13.89
3.45	0.001473	0.001893	0.001723	-28.51	-14.51
3.82	0.001411	0.001801	0.001701	-27.64	-17.05
4.18	0.001360	0.001780	0.001610	-30.88	-15.53
4.55	0.001317	0.001737	0.001637	-31.89	-19.55
10% ZrO$_2$					
0.91	0.002963	0.003443	0.003193	16.20	-7.20
1.27	0.002352	0.002832	0.002702	20.41	-12.95
1.64	0.002012	0.002492	0.002362	23.85	-14.82
2.00	0.001796	0.002076	0.002146	15.59	-16.31
2.36	0.001646	0.001796	0.001996	9.11	-17.53
2.73	0.001537	0.002017	0.001887	31.24	-18.55
3.09	0.001453	0.001933	0.001733	33.04	16.16
3.45	0.001386	0.001866	0.001596	34.62	-13.15
3.82	0.001333	0.001813	0.001563	36.02	-14.72
4.18	0.001288	0.001608	0.001638	24.84	-21.36
4.55	0.001251	0.001731	0.001601	38.36	-21.86
15% ZrO$_2$					
0.91	0.001646	0.001946	0.001856	18.22	-11.31
1.27	0.001411	0.001711	0.001571	21.26	-10.18
1.64	0.001281	0.001581	0.001491	23.43	-14.09
2.00	0.001197	0.001447	0.001337	20.88	-10.47
2.36	0.001140	0.001440	0.001350	26.32	-15.56
2.73	0.001098	0.001398	0.001308	27.33	-16.06
3.09	0.001065	0.001385	0.001275	30.04	-16.47
3.45	0.001040	0.001340	0.001280	28.85	-18.75
3.82	0.001019	0.001379	0.001229	35.32	-17.08
4.18	0.001002	0.001302	0.001242	29.94	-19.32
4.55	0.000988	0.001288	0.001198	30.37	-17.53

RR: Relative error

Table 5.24(b): Wear rate for Al+12.5Si+ZrO$_2$ composite

Sliding velocity (m/s)	Wear rate (mm^3/m)	Wear rate (mm^3/m) ANN	Wear rate (mm^3/m) ANN-GA	RR (ANN) (%)	RR (ANN-GA) (%)
5% ZrO$_2$					
0.91	0.003293±0.0002	0.003853	0.003543	-17.01	-7.06
2.73	0.001646±0.0001	0.002066	0.001896	-25.51	-13.18
4.55	0.001317±0.0003	0.001737	0.001637	-31.89	-19.55
10% ZrO$_2$					
0.91	0.002963±0.0002	0.003443	0.003193	16.20	-7.20
2.73	0.001537±0.0001	0.002017	0.001887	31.24	-18.55
4.55	0.001251±0.0005	0.001731	0.001601	38.36	-21.86
15% ZrO$_2$					
0.91	0.001646±0.0002	0.001946	0.001856	18.22	-11.31
2.73	0.001098±0.0001	0.001398	0.001308	27.33	-16.06
4.55	0.000988±0.0007	0.001288	0.001198	30.37	-17.53
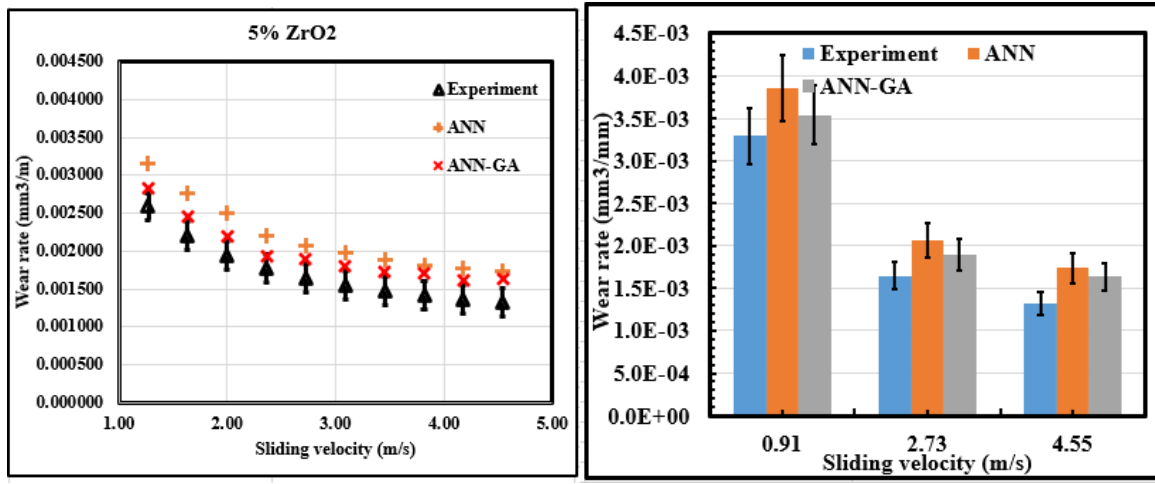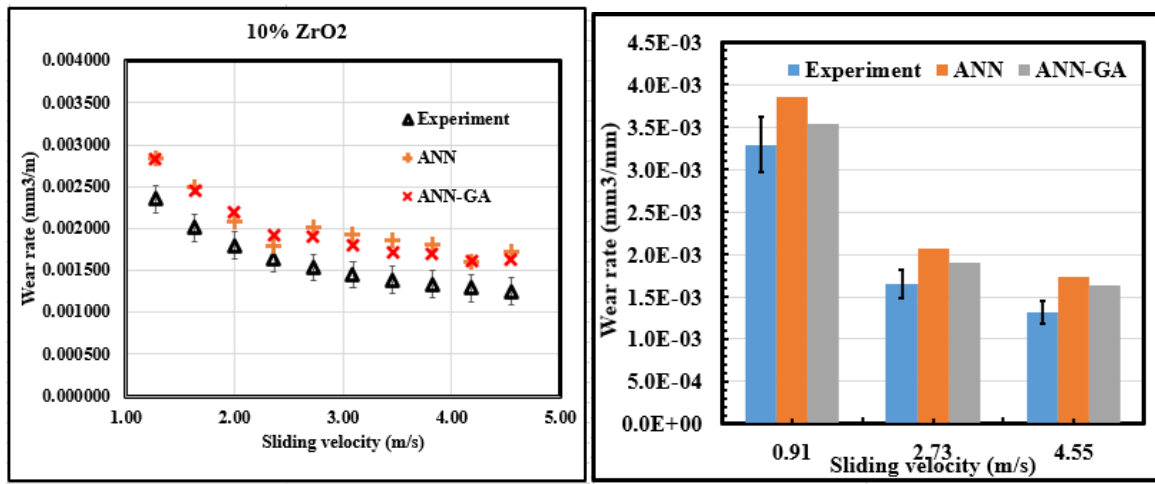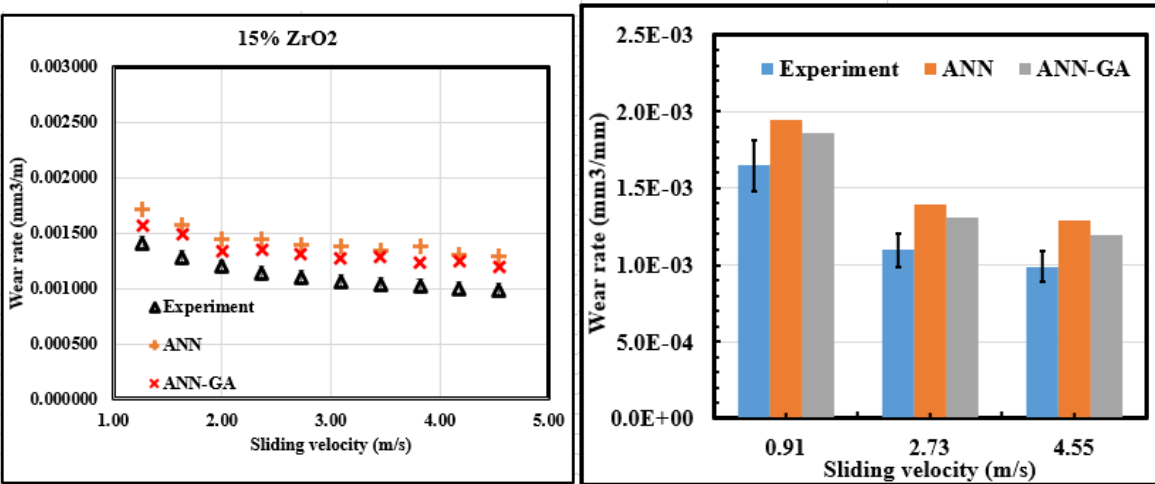
Figure 5.42: Wear rate with respect to sliding velocity of Al+12.5Si+ZrO₂ composites with(a) 5 wt. % (b) 10 wt.% (c) 15 wt.% ZrO₂ reinforcements

`

Figure 5.43(a), (b) & (c) depict the variation of specific wear rate of the composites with respect to sliding velocity. It is worthy to note that the specific wear rate is more accurate parameter to determine the wear properties (sliding pin on disk), since all the parameters affecting the wear behaviour were considered for calculation. The specific wear rate follows the similar trend as the wear rate. It can be noticed from the Figure 5.45 that the specific wear rates of the metal matrix composites were lower under the same operating conditions, which implies that much of the higher load is utilized in deformation of the plastic rather than wear (Herbert et al., 2008). It can be clearly observed in Figure 5.43 that the developed MLPNN-GA was able to sufficiently predict the values based on the experimental values. This implies that the developed optimized MLPNN-GA model is not over fit by the trained data. The average error in MLPNN and MLPNN-GA is 1.9% and 0.9%, respectively.

Table 5.25(a): Specific wear rate of Al+12.5Si+ZrO₂ composite

Sliding velocity (m/s)	Specific wear rate (mm³/Nm)	Specific wear rate (mm³/Nm) ANN	Specific wear rate (mm³/Nm) ANN-GA	RR (ANN) (%)	RR (ANN-GA) (%)
5% ZrO₂					
0.91	0.000082	0.000093	0.000091	-13.36	-9.86
1.27	0.000065	0.000076	0.000074	-17.01	-12.22
1.64	0.000055	0.000066	0.000064	-20.04	-14.09
2.00	0.000049	0.000060	0.000058	-22.61	-15.61
2.36	0.000044	0.000055	0.000053	-24.82	-16.88
2.73	0.000041	0.000052	0.000050	-26.73	-17.94
3.09	0.000039	0.000052	0.000046	-33.56	-15.30
3.45	0.000037	0.000048	0.000046	-29.87	-19.64
3.82	0.000035	0.000046	0.000044	-31.18	-20.33
4.18	0.000034	0.000048	0.000043	-41.18	-20.93
4.55	0.000033	0.000047	0.000042	-42.52	-21.47
10% ZrO₂					
0.91	0.000074	0.000085	0.000083	-14.85	-10.83
1.27	0.000059	0.000070	0.000068	-18.71	-13.27
1.64	0.000050	0.000061	0.000059	-21.87	-15.18
2.00	0.000045	0.000056	0.000054	-24.50	-16.70
2.36	0.000041	0.000052	0.000050	-26.73	-17.94
2.73	0.000038	0.000049	0.000047	-28.63	-18.98
3.09	0.000036	0.000047	0.000045	-30.29	-19.86
3.45	0.000035	0.000046	0.000044	-31.74	-20.61
3.82	0.000033	0.000044	0.000042	-33.01	-21.27
4.18	0.000032	0.000043	0.000041	-34.15	-21.84
4.55	0.000031	0.000042	0.000040	-35.17	-22.34
15% ZrO₂					
0.91	0.000041	0.000045	0.000043	-9.48	-4.23
1.27	0.000035	0.000039	0.000037	-11.05	-4.91
1.64	0.000032	0.000036	0.000034	-12.18	-5.38
2.00	0.000030	0.000034	0.000032	-13.03	-5.73
2.36	0.000028	0.000032	0.000030	-13.69	-6.00
2.73	0.000027	0.000031	0.000029	-14.21	-6.22
3.09	0.000027	0.000031	0.000028	-14.64	-6.40
3.45	0.000026	0.000030	0.000028	-15.00	-6.54
3.82	0.000025	0.000029	0.000027	-15.31	-6.67
4.18	0.000025	0.000029	0.000027	-15.57	-6.77
4.55	0.000025	0.000029	0.000027	-15.79	-6.86

RR: Relative error

`

Table 5.25(b): Specific wear rate of Al+12.5Si+ZrO$_2$ composite

Sliding velocity (m/s)	Specific wear rate (mm^3/Nm)	Specific wear rate (mm^3/Nm) ANN	Specific wear rate (mm^3/Nm) ANN-GA	RR (ANN) (%)	RR (ANN-GA) (%)
5% ZrO$_2$					
0.91	0.000082±0.00002	0.000093	0.000091	-13.36	-9.86
2.73	0.000041±0.00001	0.000052	0.000050	-26.73	-17.94
4.55	0.000033±0.00005	0.000047	0.000042	-42.52	-21.47
10% ZrO$_2$					
0.91	0.000074±0.00003	0.000085	0.000083	-14.85	-10.83
2.73	0.000038±0.00007	0.000049	0.000047	-28.63	-18.98
4.55	0.000031±0.00009	0.000042	0.000040	-35.17	-22.34
15% ZrO$_2$					
0.91	0.000041±0.00004	0.000045	0.000043	-9.48	-4.23
2.73	0.000027±0.00009	0.000031	0.000029	-14.21	-6.22
4.55	0.000025±0.00002	0.000029	0.000027	-15.79	-6.86
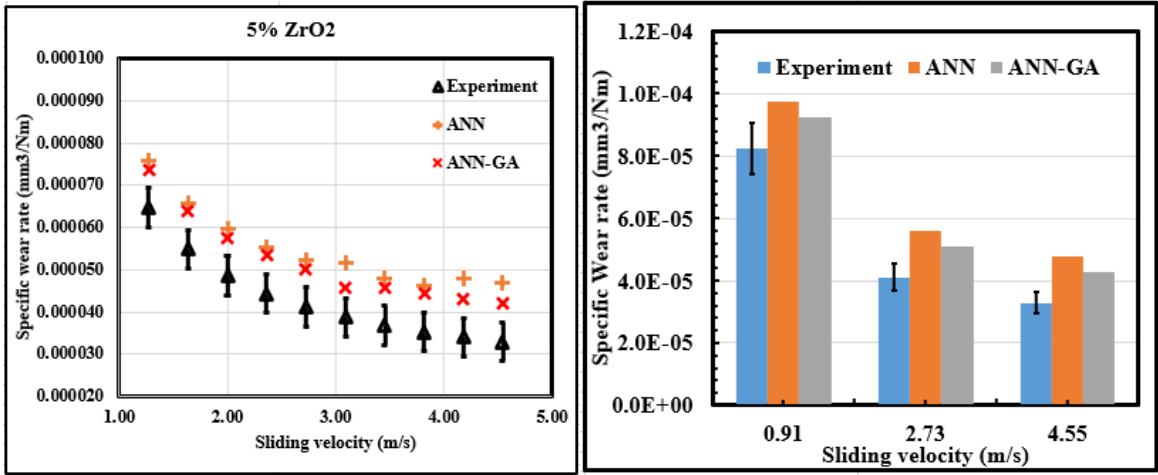
(a)
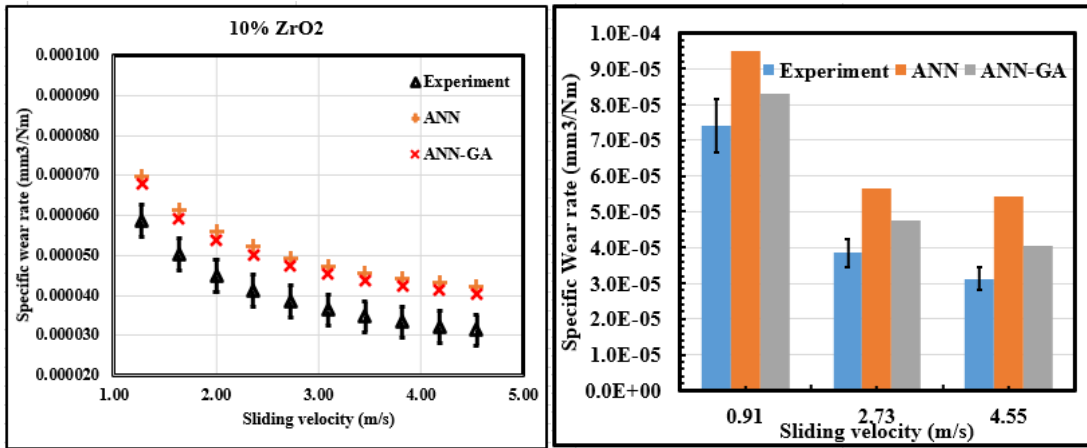
(b)
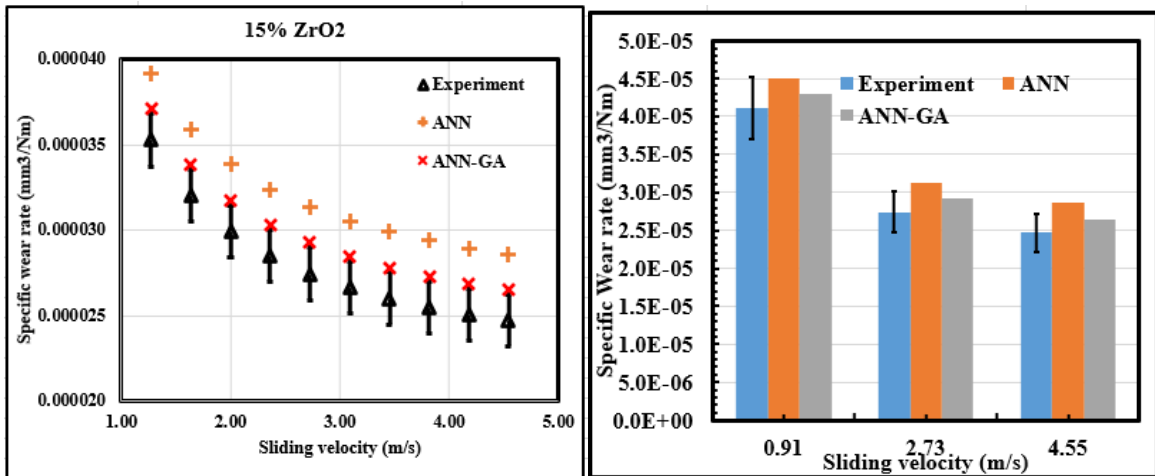
(c)

Figure 5.43: Specific wear rate with respect to sliding velocity of Al+12.5Si+ZrO₂ composites with (a) 5 wt. % (b) 10 wt.% (c) 15 wt.% ZrO₂ reinforcements

153

5.4.2 Wear characteristics as a function of applied load

It may be noted that in <u>Figure 5.44</u>, the coefficient of friction in all the developed samples decreases with increasing the applied nominal load. Larger loads tend to increase the penetration of hard asperities between the pin and counter disk surface. Other reasons could be higher significant frictions between the contact surface, which in turn creates localized adhesion of the counter disc and the pin surface. Also, there is an increase in softening of the surface material and thus more penetration of the asperities. The coefficient of friction decreased from 0.41 to 0.25 for the load of 10 N to 60 N, respectively. The average error in MLPNN and MLPNN-GA is 2.9% and 1.3%, respectively.

Table 5.26(a): Coefficient of friction of Al+12.5Si+ZrO$_2$ composite

Load (N)	Coefficient of friction	Coefficient of friction (ANN	Coefficient of friction ANN-GA	RR (ANN) (%)	RR (ANN-GA) (%)
5% ZrO$_2$					
10	0.55	0.67	0.62	-20.91	-10.57
15	0.44	0.56	0.47	-26.14	-5.38
20	0.39	0.51	0.46	-29.49	-14.29
25	0.34	0.44	0.41	-27.94	-16.05
30	0.30	0.40	0.37	-31.32	-17.65
35	0.31	0.36	0.37	-17.82	-17.40
40	0.29	0.34	0.35	-19.13	-18.44
45	0.28	0.33	0.34	-19.80	-18.96
50	0.26	0.32	0.30	-20.83	-11.71
55	0.27	0.32	0.33	-20.44	-19.46
60	0.27	0.32	0.29	-20.75	-7.02
10% ZrO$_2$					
10	0.45	0.54	0.50	-19.33	-10.00
15	0.37	0.46	0.42	-23.30	-11.81
20	0.34	0.42	0.39	-22.06	-12.82
25	0.30	0.38	0.33	-25.00	-9.09
30	0.27	0.32	0.30	-19.26	-10.00
35	0.28	0.33	0.31	-18.57	-9.68
40	0.26	0.31	0.28	-19.81	-7.73
45	0.26	0.31	0.28	-20.35	-7.93
50	0.24	0.30	0.27	-21.31	-8.27
55	0.25	0.30	0.27	-20.72	-8.06
60	0.25	0.30	0.27	-20.94	-8.14
15% ZrO$_2$					
10	0.35	0.43	0.47	-22.29	-26.00
15	0.31	0.36	0.40	-16.96	-22.62
20	0.29	0.34	0.36	-17.93	-18.77
25	0.26	0.31	0.32	-20.00	-17.98
30	0.24	0.29	0.29	-21.97	-17.54

35	0.22	0.28	0.29	-27.82	-22.89
40	0.21	0.27	0.27	-29.18	-21.73
45	0.21	0.27	0.26	-29.37	-20.20
50	0.20	0.27	0.25	-30.39	-19.37
55	0.21	0.28	0.26	-28.90	-17.45
60	0.22	0.28	0.26	-28.84	-16.45

RR: Relative error

Table 5.26(b): Coefficient of friction of Al+12.5Si+ZrO$_2$ composite

Load (N)	Coefficient of friction	Coefficient of friction (ANN	Coefficient of friction ANN-GA	RR (ANN) (%)	RR (ANN-GA) (%)
5% ZrO$_2$					
10	0.55±0.1	0.67	0.62	-20.91	-10.57
40	0.29±0.02	0.34	0.35	-19.13	-18.44
60	0.27±0.05	0.32	0.29	-20.75	-7.02
10% ZrO$_2$					
10	0.45±0.02	0.54	0.50	-19.33	-10.00
40	0.26±0.03	0.31	0.28	-19.81	-7.73
60	0.25±0.07	0.30	0.27	-20.94	-8.14
15% ZrO$_2$					
10	0.35±0.01	0.43	0.47	-22.29	-26.00
40	0.21±0.06	0.27	0.27	-29.18	-21.73
60	0.22±0.07	0.28	0.26	-28.84	-16.45
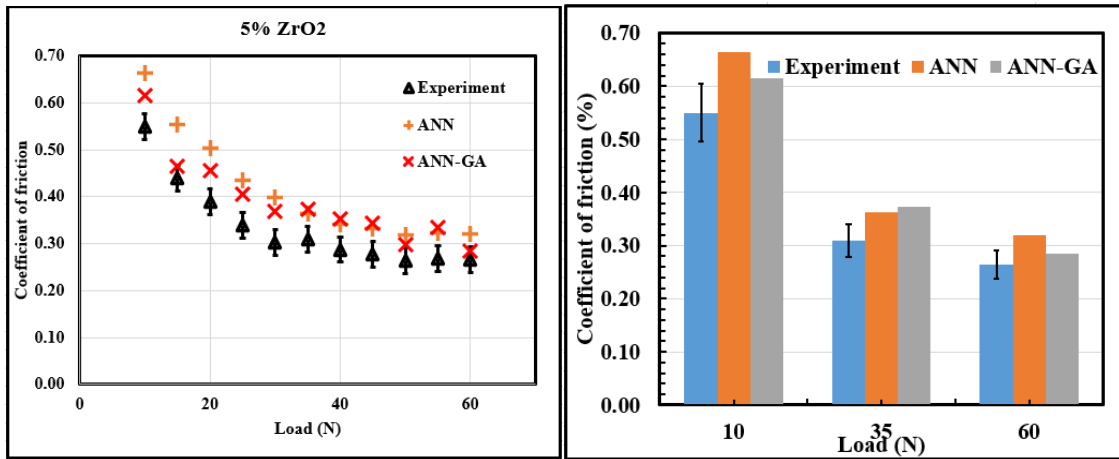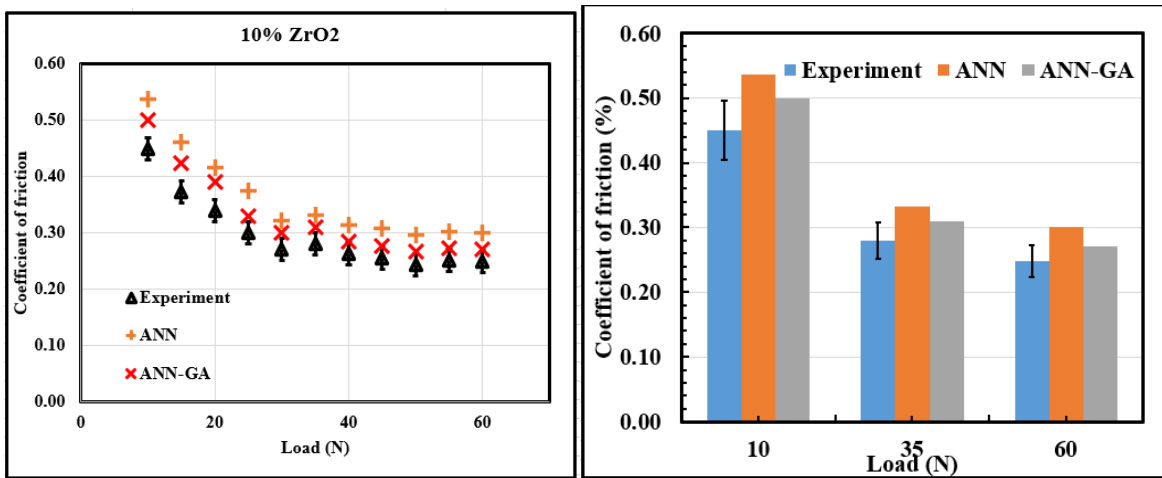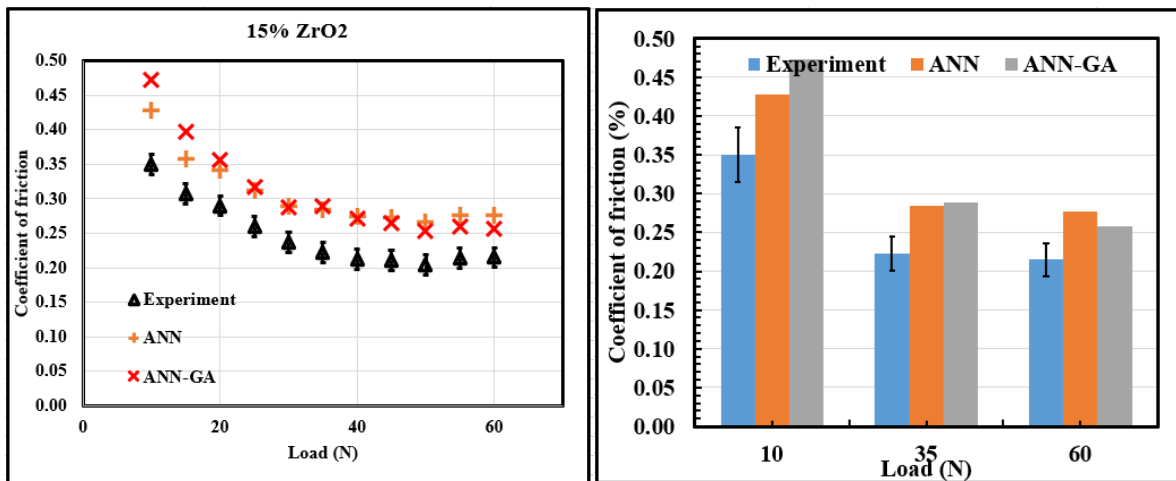
Figure 5.44: Coefficient of the friction with respect to load of Al+12.5Si+ZrO₂ composites with (a) 5 wt. % (b) 10 wt.% (c) 15 wt.% ZrO₂ reinforcements

156

The wear rate of the developed composite is plotted as a function of applied nominal load as shown in [Figure 5.45](). Conversely to [Figure 5.42](), the wear rate in all the composite specimens increases marginally with increasing nominal applied load ([Shabani et al., 2011a](); [2011b]()). This is due to the higher frictional heating. The removal of material due to delamination of adhered areas ([Ludema et al., 1984]()) at larger loads, the difference between the wear rates of the Al+12.5Si+5% ZrO_2 and Al+12.5Si+15% ZrO_2 is the most significant. The variations of wear rates with nominal load (N) for the developed metal matrix composites, subjected to spray deposition conditions, is depicted in the plots representing the wear rate of 6.2%, 5.2% and 5.4%, respectively.

Table 5.27(a): Wear rate for Al+12.5Si+ZrO$_2$ composite

Load (N)	Wear rate (mm³/m)	Wear rate (mm³/m) ANN	Wear rate (mm³/m) ANN-GA	RR (ANN) (%)	RR (ANN-GA) (%)
5% ZrO₂					
10	0.001432	0.002032	0.001722	-41.91	-16.84
15	0.001575	0.002175	0.001865	-38.10	-15.55
20	0.001718	0.002318	0.002008	-34.93	-14.44
25	0.001861	0.002361	0.002191	-26.87	-15.06
30	0.002004	0.002504	0.002294	-24.95	-12.64
35	0.002147	0.002647	0.002437	-23.28	-11.90
40	0.002291	0.002791	0.002651	-21.83	-13.58
45	0.002434	0.002734	0.002724	-12.33	-10.65
50	0.002577	0.002877	0.002867	-11.64	-10.12
55	0.002720	0.003020	0.003080	-11.03	-11.69
60	0.002863	0.003163	0.003153	-10.48	-9.20
10% ZrO₂					
10	0.001288	0.001788	0.001518	-38.81	-15.15
15	0.001432	0.001932	0.001662	-34.93	-13.84
20	0.001575	0.002075	0.001835	-31.75	-14.17
25	0.001718	0.002218	0.002008	-29.11	-14.44
30	0.001861	0.002361	0.002121	-26.87	-12.26
35	0.002004	0.002454	0.002324	-22.45	-13.77
40	0.002147	0.002597	0.002467	-20.96	-12.97
45	0.002291	0.002711	0.002611	-18.34	-12.26
50	0.002434	0.002854	0.002754	-17.26	-11.62
55	0.002577	0.002997	0.002897	-16.30	-11.05
60	0.002720	0.003140	0.003040	-15.44	-10.53
15% ZrO₂					
10	0.000716	0.001016	0.000896	-41.91	-20.09
15	0.000859	0.001159	0.001039	-34.93	-17.33
20	0.001002	0.001282	0.001182	-27.94	-15.23
25	0.001145	0.001445	0.001355	-26.19	-15.49
30	0.001288	0.001528	0.001468	-18.63	-12.26

35	0.001432	0.001732	0.001652	-20.96	-13.32
40	0.001575	0.001875	0.001755	-19.05	-10.26
45	0.001718	0.002018	0.001898	-17.46	-9.48
50	0.001861	0.002151	0.002101	-15.58	-11.42
55	0.002004	0.002304	0.002244	-14.97	-10.69
60	0.002147	0.002477	0.002387	-15.37	-10.05

RR: Relative error

Table 5.27(b): Wear rate for Al+12.5Si+ZrO$_2$ composite

Load (N)	Wear rate (mm^3/m)	Wear rate (mm^3/m) ANN	Wear rate (mm^3/m) ANN-GA	RR (ANN) (%)	RR (ANN-GA) (%)
5% ZrO$_2$					
10	0.001432±0.0005	0.002032	0.001722	-41.91	-16.84
40	0.002291±0.0002	0.002791	0.002651	-21.83	-13.58
60	0.002863±0.0004	0.003163	0.003153	-10.48	-9.20
10% ZrO$_2$					
10	0.001288±0.0001	0.001788	0.001518	-38.81	-15.15
40	0.002147±0.0007	0.002597	0.002467	-20.96	-12.97
60	0.002720±0.0008	0.003140	0.003040	-15.44	-10.53
15% ZrO$_2$					
10	0.000716±0.0003	0.001016	0.000896	-41.91	-20.09
40	0.001575±0.0004	0.001875	0.001755	-19.05	-10.26
60	0.002147±0.0006	0.002477	0.002387	-15.37	-10.05
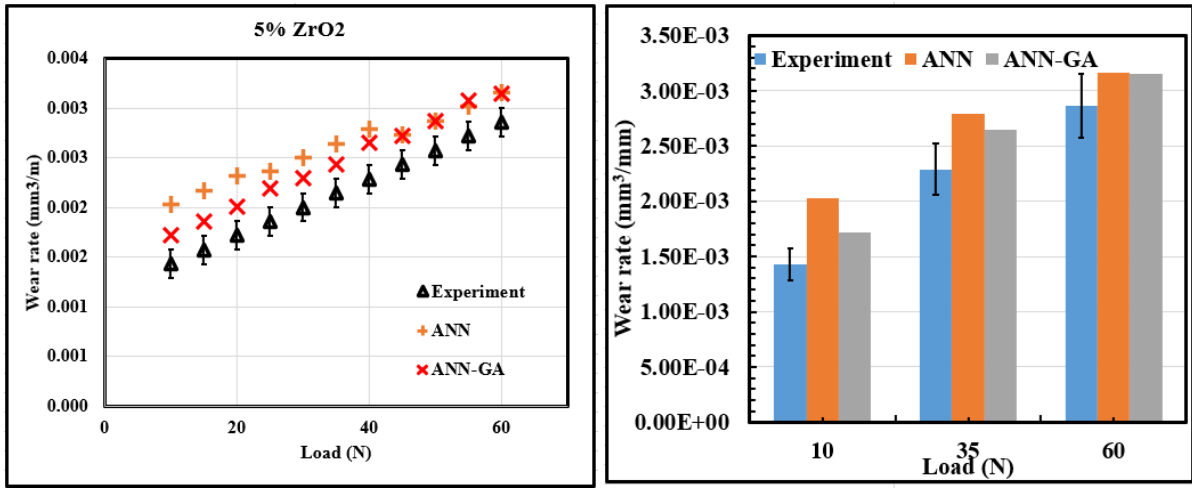
(a)
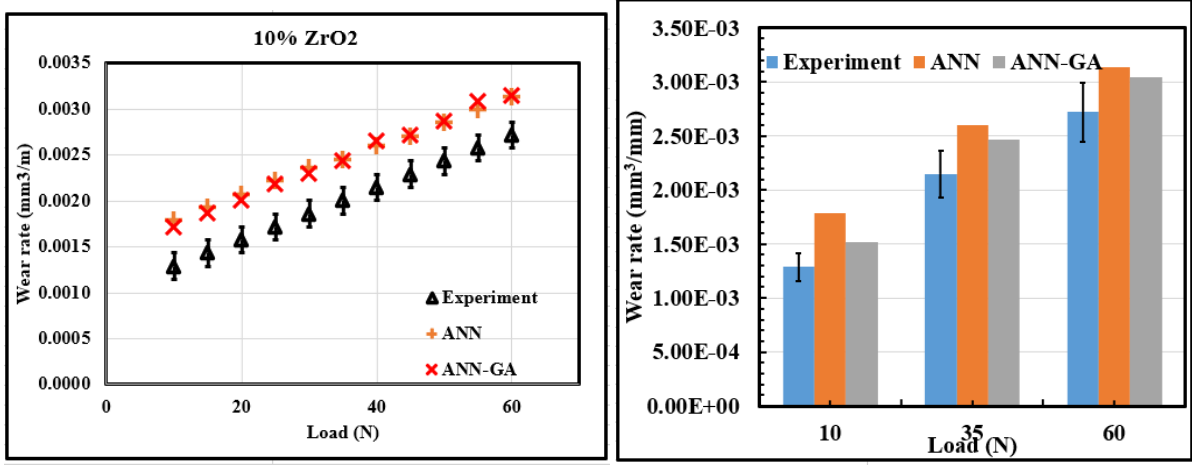
(b)
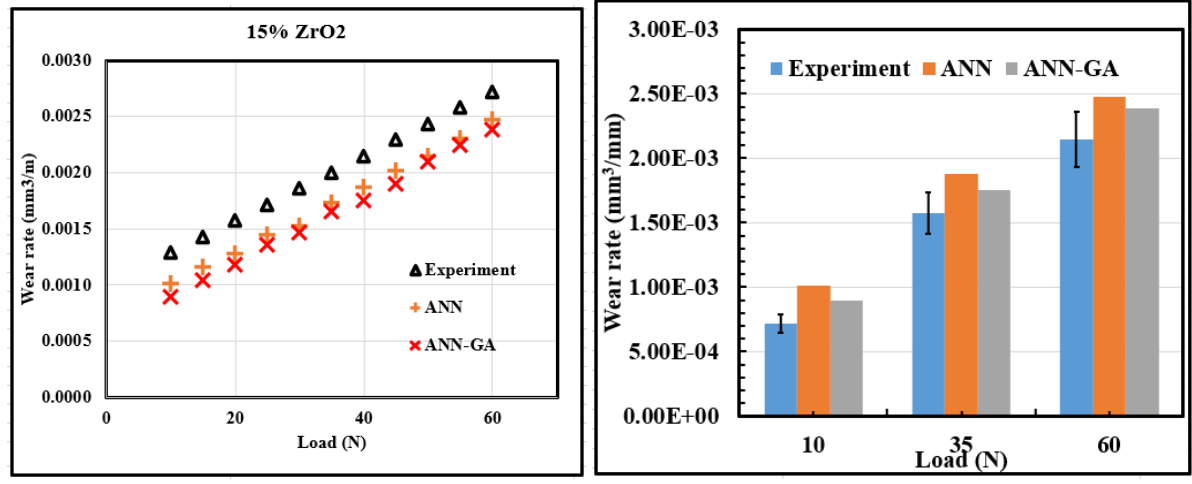
(c)

Figure 5.45: Wear rate with respect to load of Al+12.5Si+ZrO₂ composites with (a) 5 wt. % (b) 10 wt.% (c) 15 wt.% ZrO₂ reinforcements

`

Interestingly, the specific wear rate is inversely proportional to the wear rate as observed in [Figure 5.45](). The variations of specific wear rate as a function of load are shown in [Figure 5.46](). It can be seen that specific wear rate decreases with increasing load. However, stress concentration is the main factor for wear debris. This mainly occurs in sharp edges of zirconium oxide particles which can initiate cracks in the adjacent metal matrix. These propagate further parallel to direction of sliding and forms debris. But in case of 15% ZrO_2 composition, it decreased by almost 19.5%. The specific wear rate to decrease with increase in nominal applied load, if deformation of asperities does not occur and the actual area of contact remains unchanged ([Herbert et al., 2007a]). The average error in MLPNN and MLPNN-GA is 3.1% and 2.3%, respectively.

Table 5.28(a): Specific wear rate for Al+12.5Si+ZrO$_2$ composite

Load (N)	Specific wear rate (mm³/Nm)	Specific wear rate (mm³/Nm) ANN	Specific wear rate (mm³/Nm) ANN-GA	RR (ANN) (%)	RR (ANN-GA) (%)
5% ZrO$_2$					
10	0.000260	0.000310	0.000295	-19.2308	-13.4615
15	0.000239	0.000289	0.000274	-20.9205	-14.6444
20	0.000220	0.000270	0.000255	-22.7273	-15.9091
25	0.000219	0.000272	0.000254	-24.2009	-15.9817
30	0.000220	0.000273	0.000255	-24.0909	-15.9091
35	0.000199	0.000247	0.000234	-24.1206	-17.5879
40	0.000199	0.000247	0.000234	-24.1206	-17.5879
45	0.000195	0.000243	0.000230	-24.6154	-17.9487
50	0.000195	0.000243	0.000226	-24.6154	-15.8974
55	0.000184	0.000232	0.000219	-26.087	-19.0217
60	0.000180	0.000228	0.000203	-26.6667	-12.7778
10% ZrO$_2$					
10	0.000286	0.000345	0.000328	-20.61	-12.79
15	0.000256	0.000315	0.000289	-23.08	-11.43
20	0.000232	0.000294	0.000264	-26.77	-12.14
25	0.000229	0.000291	0.000271	-27.07	-15.50
30	0.000230	0.000292	0.000283	-26.98	-18.74
35	0.000205	0.000267	0.000258	-30.32	-20.58
40	0.000205	0.000267	0.000242	-30.32	-15.32
45	0.000199	0.000252	0.000252	-26.61	-21.02
50	0.000199	0.000252	0.000234	-26.57	-14.93

55	0.000187	0.000240	0.000212	-28.38	-11.81
60	0.000183	0.000236	0.000208	-29.03	-12.05
15% ZrO$_2$					
10	0.000205	0.000250	0.000223	-22.00	-8.17
15	0.000187	0.000232	0.000205	-24.10	-8.88
20	0.000173	0.000218	0.000191	-26.04	-9.53
25	0.000176	0.000221	0.000194	-25.54	-9.36
30	0.000181	0.000216	0.000200	-19.29	-9.12
35	0.000184	0.000219	0.000202	-19.07	-9.02
40	0.000185	0.000212	0.000203	-14.57	-8.94
45	0.000181	0.000216	0.000199	-19.35	-9.14
50	0.000182	0.000217	0.000201	-19.18	-9.07
55	0.000170	0.000199	0.000188	-17.07	-9.68
60	0.000166	0.000201	0.000185	-21.03	-9.86

RR: Relative error

Table 5.28(b): Specific wear rate for Al+12.5Si+ZrO$_2$ composite

Load (N)	Specific wear rate (mm^3/Nm)	Specific wear rate (mm^3/Nm) ANN	Specific wear rate (mm^3/Nm) ANN-GA	RR (ANN) (%)	RR (ANN-GA) (%)
5% ZrO$_2$					
10	0.000260±0.0006	0.000310	0.000295	-19.2308	-13.4615
40	0.000199±0.0001	0.000247	0.000234	-24.1206	-17.5879
60	0.000180±0.0004	0.000228	0.000203	-26.6667	-12.7778
10% ZrO$_2$					
10	0.000286±0.0002	0.000345	0.000328	-20.61	-12.79
40	0.000205±0.0001	0.000267	0.000242	-30.32	-15.32
60	0.000183±0.0007	0.000236	0.000208	-29.03	-12.05
15% ZrO$_2$					
10	0.000205±0.0001	0.000250	0.000223	-22.00	-8.17
40	0.000185±0.0002	0.000212	0.000203	-14.57	-8.94
60	0.000166±0.0009	0.000201	0.000185	-21.03	-9.86
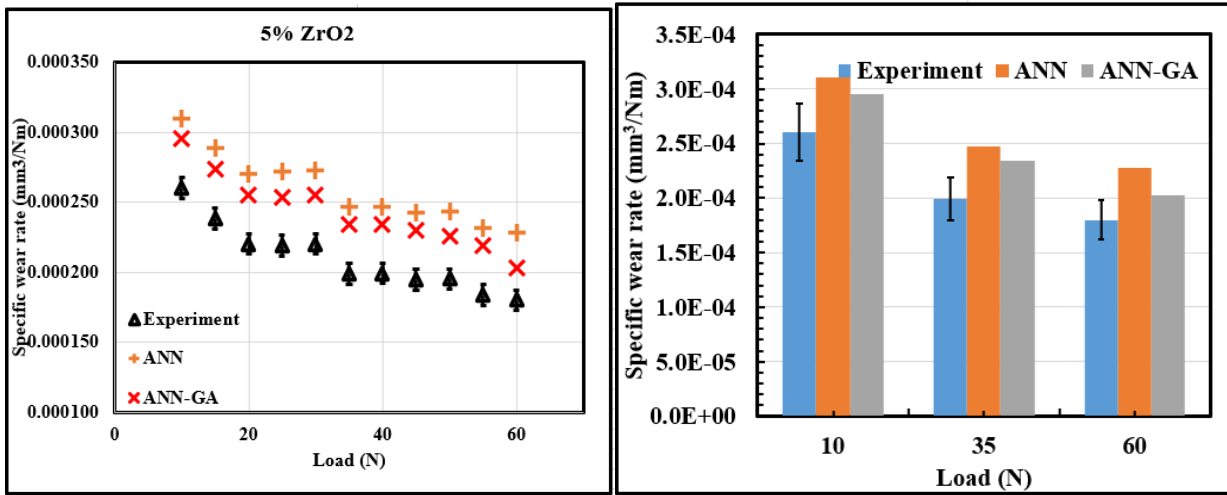
(a)
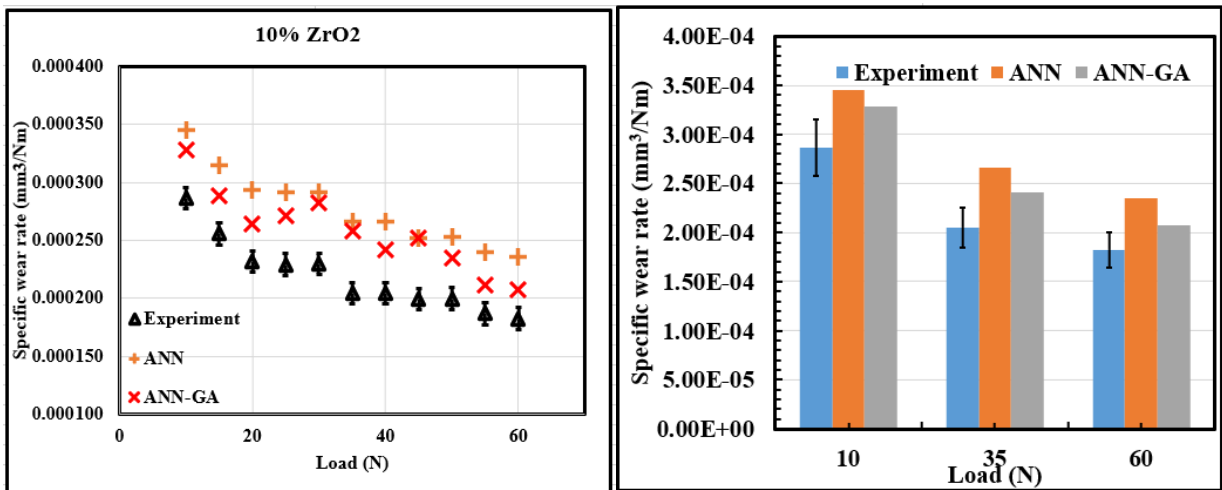
(b)
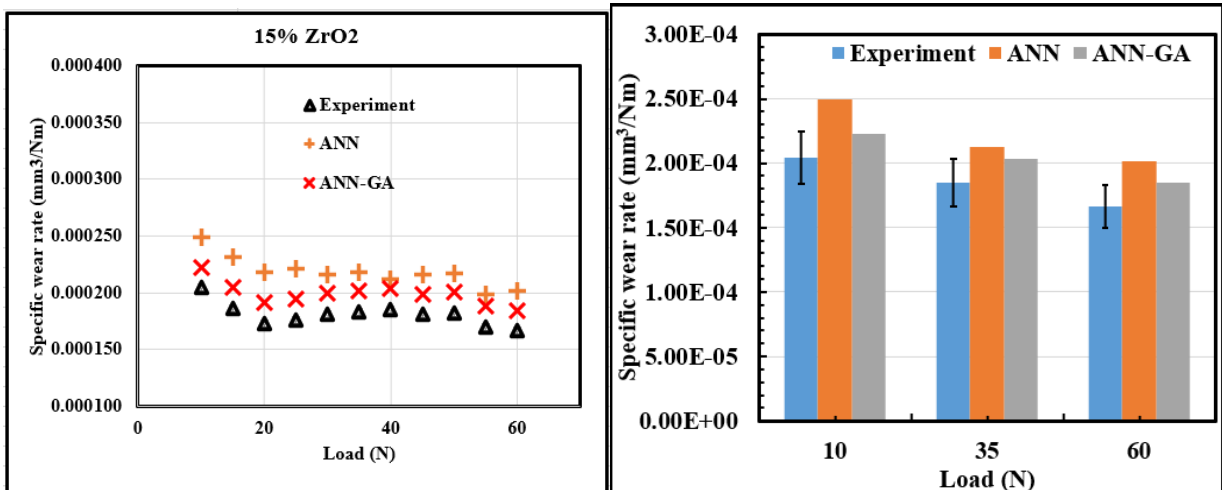
(c)

Figure 5.46: Specific wear rate with respect to load ofAl+12.5Si+ZrO₂ composites with

(a) 5 wt. % (b) 10 wt.% (c) 15 wt.% ZrO₂ reinforcements

`

5.4.3 Wear characteristic s as a function of flight distance

The optimum flight is an important attain criteria to get the good properties of the material during spray forming method. Therefore, this study is conducted to determine the optimum flight distance for this Al+12.5Si-ZrO2 composition. It is evident from <u>Figure 5.47</u> that the coefficient of friction increases with increasing distance between the nozzle to the substrate with a fixed load and sliding distance of 40 N and 2300 m, respectively. It can be observed that the flight distance significantly influences the friction coefficient. At 380 mm flight distance for 10 N (15% ZrO_2), the coefficient of friction is 0.08. These are relative lower values compared to other compositions. It is to be noted that the well distribution of zirconium oxide in aluminium silicon matrix reduces the wear rates. The average error in MLPNN and MLPNN-GA is 3.1% and 2.1%, respectively

Table 5.29(a): Coefficient of friction ofAl+12.5Si+ZrO₂ composite

Flight distance (mm)	Coefficient of friction	Coefficient of friction (ANN	Coefficient of friction ANN-GA	RR (ANN) (%)	RR (ANN-GA) (%)
5% ZrO₂					
370	0.4152	0.4652	0.4316	-10.82	-4.82
380	0.4225	0.4825	0.4525	-14.20	-6.63
390	0.395	0.445	0.425	-12.66	-7.06
400	0.355	0.405	0.385	-14.08	-7.79
410	0.3375	0.3875	0.3535	-14.81	-4.53
420	0.3125	0.3625	0.3425	-16.00	-8.76
430	0.295	0.365	0.325	-23.73	-9.23
440	0.2525	0.3425	0.2825	-35.64	-10.62
450	0.2375	0.2775	0.2675	-16.84	-11.21
460	0.195	0.199	0.22	-2.05	-11.36
470	0.165	0.169	0.195	-2.42	-15.38
480	0.1125	0.1185	0.1425	-5.33	-21.05
10% ZrO₂					
370	0.4156	0.4425	0.4325	-6.82	-4.58
380	0.3725	0.4225	0.4025	-13.42	-7.45
390	0.345	0.395	0.375	-14.49	-8.00
400	0.305	0.355	0.335	-16.39	-8.96
410	0.2875	0.3475	0.3575	-20.87	-19.58
420	0.2625	0.3225	0.3325	-22.86	-21.05
430	0.245	0.305	0.305	-24.49	-19.67
440	0.2025	0.2525	0.2625	-24.69	-22.86
450	0.1875	0.2575	0.2775	-37.33	-32.43
460	0.17	0.21	0.2	-23.53	-15.00
470	0.14	0.18	0.17	-28.57	-17.65
480	0.1125	0.1525	0.1425	-35.56	-21.05

		15% ZrO₂			
370	0.3456	0.3751	0.3658	-6.52	-4.58
380	0.3225	0.3575	0.3525	-10.85	-8.51
390	0.295	0.33	0.325	-11.86	-9.23
400	0.255	0.29	0.285	-13.73	-10.53
410	0.2375	0.2725	0.2675	-14.74	-11.21
420	0.2125	0.2475	0.2275	-16.47	-6.59
430	0.195	0.246	0.225	-26.15	-13.33
440	0.1775	0.2125	0.2075	-19.72	-14.46
450	0.1625	0.2095	0.1925	-28.92	-15.58
460	0.145	0.18	0.159	-24.14	-8.81
470	0.115	0.15	0.145	-30.43	-20.69
480	0.0875	0.1225	0.1085	-40.00	-19.35

RR: Relative error

Table 5.29(b): Coefficient of friction ofAl+12.5Si+ZrO₂ composite

Flight distance (mm)	Coefficient of friction	Coefficient of friction (ANN	Coefficient of friction ANN-GA	RR (ANN) (%)	RR (ANN-GA) (%)
		5% ZrO₂			
370	0.4152±0.05	0.4652	0.4316	-10.82	-4.82
420	0.3125±0.03	0.3625	0.3425	-16.00	-8.76
480	0.1125±0.01	0.1185	0.1425	-5.33	-21.05
		10% ZrO₂			
370	0.4156±0.02	0.4425	0.4325	-6.82	-4.58
420	0.2625±0.04	0.3225	0.3325	-22.86	-21.05
480	0.1125±0.05	0.1525	0.1425	-35.56	-21.05
		15% ZrO₂			
370	0.3456±0.01	0.3751	0.3658	-6.52	-4.58
420	0.2125±0.03	0.2475	0.2275	-16.47	-6.59
480	0.0875±0.06	0.1225	0.1085	-40.00	-19.35
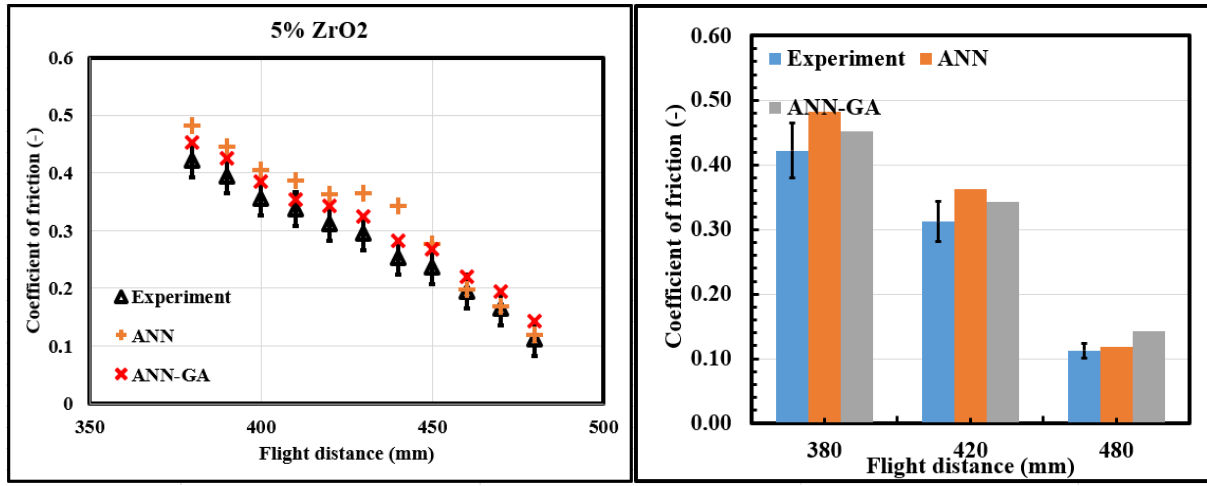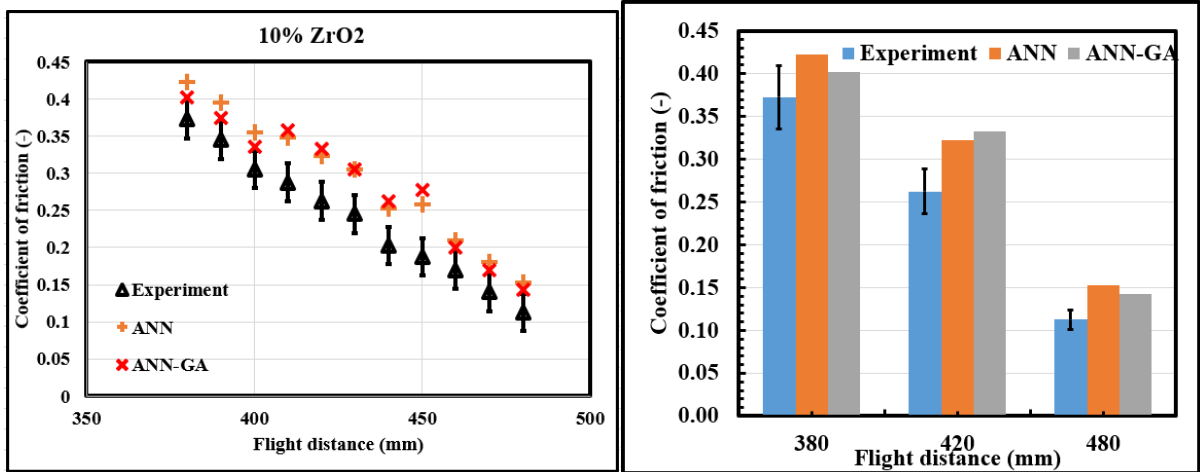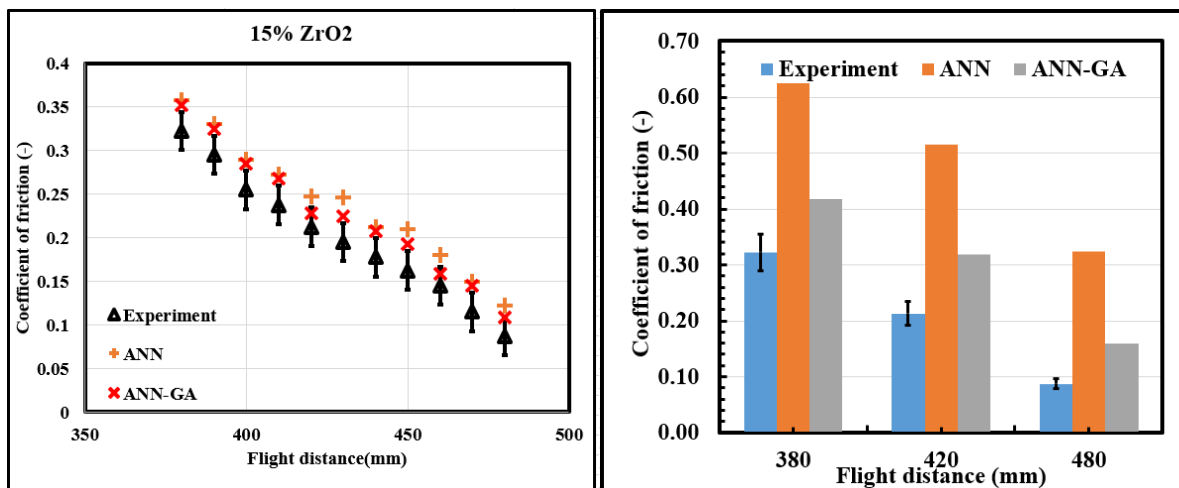
Figure 5.47: Coefficient of the friction with respect to flight distance of Al+12.5Si+ZrO₂ composites with (a) 5 wt. % (b) 10 wt.% (c) 15 wt.% ZrO₂ reinforcements

165

`

The wear rate of the developed composite is plotted as a function of flight distance in Figure 5.48. It was observed that the wear rate is directly proportional to flight distance. As reported above, the wear rate is less in Al+12.5Si+15% ZrO_2 compared to 5% and 10% ZrO_2. It is noted that the wear rate of composite decrease to 2.8% by addition of ZrO_2 particles in aluminium silicon alloy. This trend is attributed by agglomeration of zirconium oxide particles during the spray deposition process. The zirconium oxide particles were highly dense with non-homogenous distribution of zirconium oxide in aluminium silicon alloy. This results in dense network of zirconium oxide particles, which prevents specimens to be dense (Shen et al., 2001). The average error in MLPNN and MLPNN-GA is 2.9% and 1.3%, respectively.

Table 5.30(a): Wear rate of Al+12.5Si+ZrO$_2$ composite

Flight distance (mm)	Wear rate (mm^3/m)	Wear rate (mm^3/m) ANN	Wear rate (mm^3/m) ANN-GA	RR (ANN) (%)	RR (ANN-GA) (%)
			5% ZrO$_2$		
370	0.002925462	0.003255465	0.00308755	-8.25	-3.43
380	0.002720043	0.003020043	0.002840043	-11.03	-4.23
390	0.002576913	0.003076913	0.002696913	-19.40	-4.45
400	0.002433739	0.002933739	0.002553739	-20.54	-4.70
410	0.002147435	0.002647435	0.002267435	-23.28	-5.29
420	0.001574783	0.002274783	0.001924783	44.45	-18.18
430	0.001717913	0.002217913	0.002067913	-29.11	-16.93
440	0.002147435	0.002647435	0.002497435	-23.28	-14.01
450	0.002576913	0.003376913	0.002696913	-31.04	-4.45
460	0.003006391	0.003506391	0.003126391	-16.63	-3.84
470	0.00343587	0.00433587	0.00384587	-26.19	-10.66
480	0.004151652	0.004651652	0.004361652	-12.04	-4.81
			10% ZrO$_2$		
370	0.002659876	0.00316546	0.002846564	-19.23	-7.69
380	0.002433739	0.003033739	0.002533739	-24.65	-3.95
390	0.001861087	0.002461087	0.001961087	-32.24	-5.10
400	0.001431609	0.002031609	0.001731609	-41.91	-17.32
410	0.001145304	0.001745304	0.001245304	-52.39	-8.03
420	0.001717913	0.002117913	0.002117913	-23.28	-18.89
430	0.002147435	0.002547435	0.002547435	-18.63	-15.70
440	0.002290565	0.002690565	0.002690565	-17.46	-14.87
450	0.002576913	0.002876913	0.002976913	-11.64	-13.44
460	0.002720043	0.003020043	0.003120043	-11.03	-12.82
470	0.003006391	0.003406391	0.003506391	-13.30	-14.26
480	0.003292696	0.003492696	0.003492696	-6.07	-5.73
			15% ZrO$_2$		
370	0.00254699	0.00276569	0.002656464	-8.52	-4.21
380	0.002433739	0.002833739	0.002663739	-16.44	-8.63
390	0.001717913	0.002017913	0.001947913	-17.46	-11.81
400	0.001288435	0.001788435	0.001518435	-38.81	-15.15
410	0.00100213	0.00150213	0.00129213	-49.89	-22.44
420	0.000858957	0.001358957	0.001088957	-58.21	-21.12
430	0.001574783	0.002174783	0.001884783	-38.10	-16.45
440	0.001861087	0.002311087	0.002091087	-24.18	-11.00
450	0.002004261	0.002304261	0.002234261	-14.97	-10.29
460	0.002290565	0.002590565	0.002450565	-13.10	-6.53
470	0.002433739	0.002733739	0.002623739	-12.33	-7.24
480	0.002576913	0.002876913	0.002806913	-11.64	-8.19

RR: Relative error-

Table 5.30(b): Wear rate of Al+12.5Si+ZrO$_2$ composite

Flight distance (mm)	Wear rate (mm^3/m)	Wear rate (mm^3/m) ANN	Wear rate (mm^3/m) ANN-GA	RR (ANN) (%)	RR (ANN-GA) (%)
5% ZrO$_2$					
370	0.002925462±0.0005	0.003255465	0.00308755	-8.25	-3.43
420	0.001574783±0.0003	0.002274783	0.001924783	44.45	-18.18
480	0.004151652±0.0001	0.004651652	0.004361652	-12.04	-4.81
10% ZrO$_2$					
370	0.002659876±0.0002	0.00316546	0.002846564	-19.23	-7.69
420	0.001717913±0.0006	0.002117913	0.002117913	-23.28	-18.89
480	0.003292696±0.0001	0.003492696	0.003492696	-6.07	-5.73
15% ZrO$_2$					
370	0.00254699±0.0003	0.00276569	0.002656464	-8.52	-4.21
420	0.000858957±0.0008	0.001358957	0.001088957	-58.21	-21.12
480	0.002576913±0.0002	0.002876913	0.002806913	-11.64	-8.19
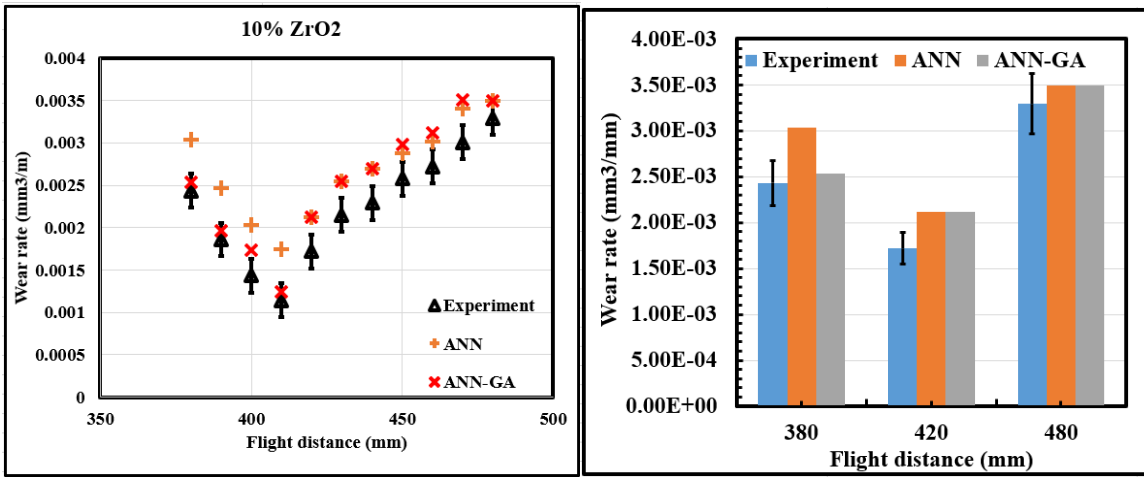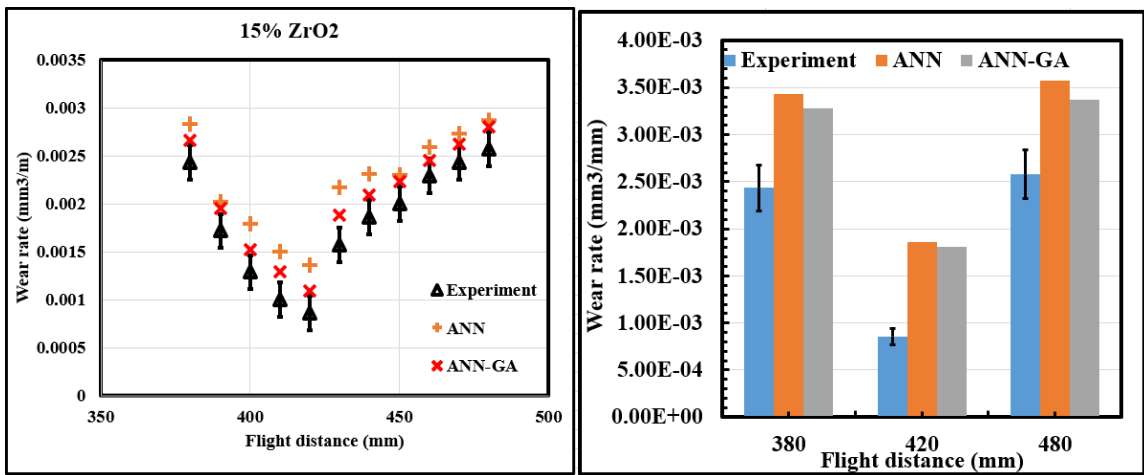
Figure 5.48: Wear rate with respect to flight distance of Al+12.5Si+ZrO₂ composites with (a) 5 wt. % (b) 10 wt.% (c) 15 wt.% ZrO₂ reinforcements

`

The interaction of specific wear rates against the flight distance from 380 mm to 480 mm is shown in Figure 5.49. It is noted that the specific wear rate trend is similar to the applied nominal load (refer Figure 5.46). The reason is due to the increase in the penetration of hard asperities between the two contact surfaces (pin and counter disk surfaces). Because of the combined effect of sliding velocity and applied load, subsurface micro cracks are generated. This results in removal of wear debris which can be observed in (Figure 5.49 to 5.51). Increasing the flight distances results in non-uniform distribution of zirconium oxide particles in aluminium silicon matrix. This significantly affects the wear behaviour and mechanical strength of the composite. The average error in MLPNN and MLPNN-GA is 2.8% and 1.7%, respectively.

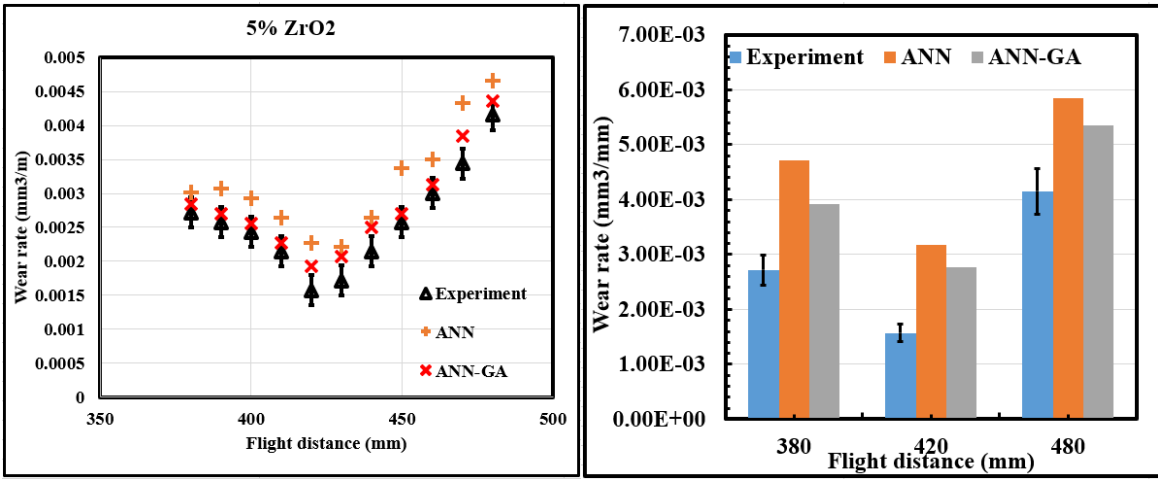**Table 5.31(a): Specific wear rate of Al+12.5Si+ZrO$_2$ composite**

Flight distance (mm)	Specific wear rate (mm^3/Nm)	Specific wear rate (mm^3/Nm) ANN	Specific wear rate (mm^3/Nm) ANN-GA	RR (ANN) (%)	RR (ANN-GA) (%)
5% ZrO$_2$					
370	0.000074	0.000086	0.000081	-16.26	-9.49
380	0.000068	0.000083	0.000078	-22.06	-12.82
390	0.000064	0.000079	0.000074	-23.28	-13.44
400	0.000061	0.000076	0.000071	-24.65	-14.12
410	0.000054	0.000069	0.000064	-27.94	-15.70
420	0.000039	0.000054	0.000049	-38.10	-20.26
430	0.000043	0.000058	0.000053	-34.93	-18.89
440	0.000054	0.000069	0.000064	-27.94	-15.70
450	0.000064	0.000079	0.000074	-23.28	-13.44
460	0.000075	0.000090	0.000085	-19.96	-11.74
470	0.000086	0.000101	0.000096	-17.46	-10.43
480	0.000104	0.000119	0.000114	-14.45	-8.79
10% ZrO$_2$					
370	0.000074	0.000094	0.000082	-27.20	-10.82
380	0.000061	0.000082	0.000070	-34.51	-12.89
390	0.000047	0.000068	0.000056	-45.13	-16.21
400	0.000036	0.000048	0.000045	-33.53	-20.09
410	0.000029	0.000041	0.000038	-41.91	-23.92
420	0.000043	0.000055	0.000052	-27.94	-17.33
430	0.000054	0.000064	0.000063	-18.63	-14.36
440	0.000057	0.000069	0.000066	-20.96	-13.58
450	0.000064	0.000074	0.000073	-15.52	-12.26
460	0.000068	0.000080	0.000077	-17.65	-11.69
470	0.000075	0.000085	0.000084	-13.30	-10.69
480	0.000082	0.000094	0.000091	-14.58	-9.86
15% ZrO$_2$					
370	0.000068	0.000081	0.000073	-19.51	-7.53
380	0.000061	0.000065	0.000063	-6.41	-3.21
390	0.000043	0.000047	0.000045	-9.08	-4.07
400	0.000032	0.000036	0.000034	-12.11	-5.35
410	0.000025	0.000029	0.000027	-15.57	-6.77
420	0.000021	0.000025	0.000023	-18.16	-8.21
430	0.000039	0.000043	0.000041	-9.91	-4.42
440	0.000047	0.000050	0.000049	-8.38	-4.36
450	0.000050	0.000054	0.000054	-7.78	-7.08
460	0.000057	0.000061	0.000061	-6.81	-6.25
470	0.000061	0.000065	0.000071	-6.41	-13.90
480	0.000064	0.000068	0.000074	-6.05	-13.23

RR: Relative error

Table 5.31(b): Specific wear rate of Al+12.5Si+ZrO$_2$ composite

Flight distance (mm)	Specific wear rate (mm^3/Nm)	Specific wear rate (mm^3/Nm) ANN	Specific wear rate (mm^3/Nm) ANN-GA	RR (ANN) (%)	RR (ANN-GA) (%)
5% ZrO$_2$					
370	0.000074±0.000005	0.000086	0.000081	-16.26	-9.49
420	0.000039±0.000001	0.000054	0.000049	-38.10	-20.26
480	0.000104±0.000003	0.000119	0.000114	-14.45	-8.79
10% ZrO$_2$					
370	0.000074±0.000002	0.000094	0.000082	-27.20	-10.82
420	0.000043±0.000003	0.000055	0.000052	-27.94	-17.33
480	0.000082±0.000007	0.000094	0.000091	-14.58	-9.86
15% ZrO$_2$					
370	0.000068±0.000006	0.000081	0.000073	-19.51	-7.53
420	0.000021±0.000002	0.000025	0.000023	-18.16	-8.21
480	0.000064±0.000001	0.000068	0.000074	-6.05	-13.23
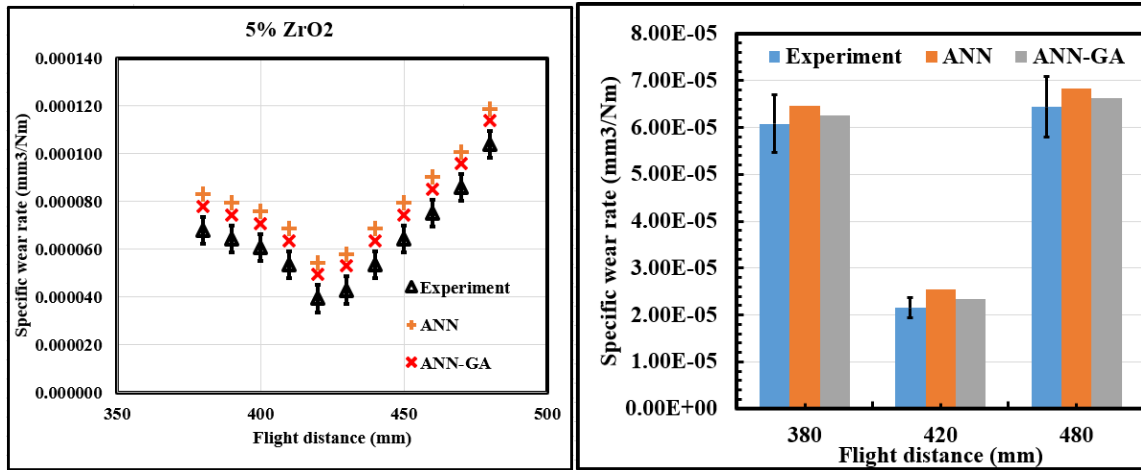
(a)
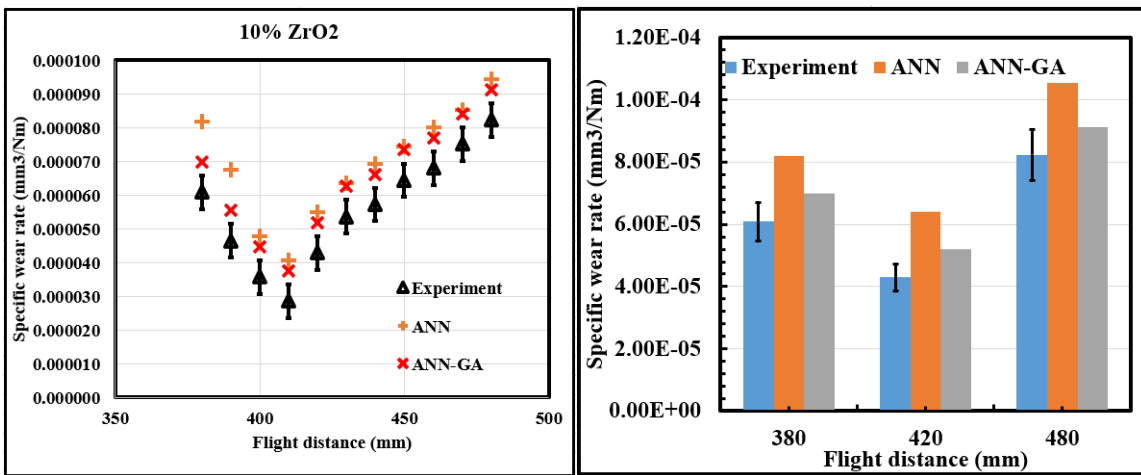
(b)
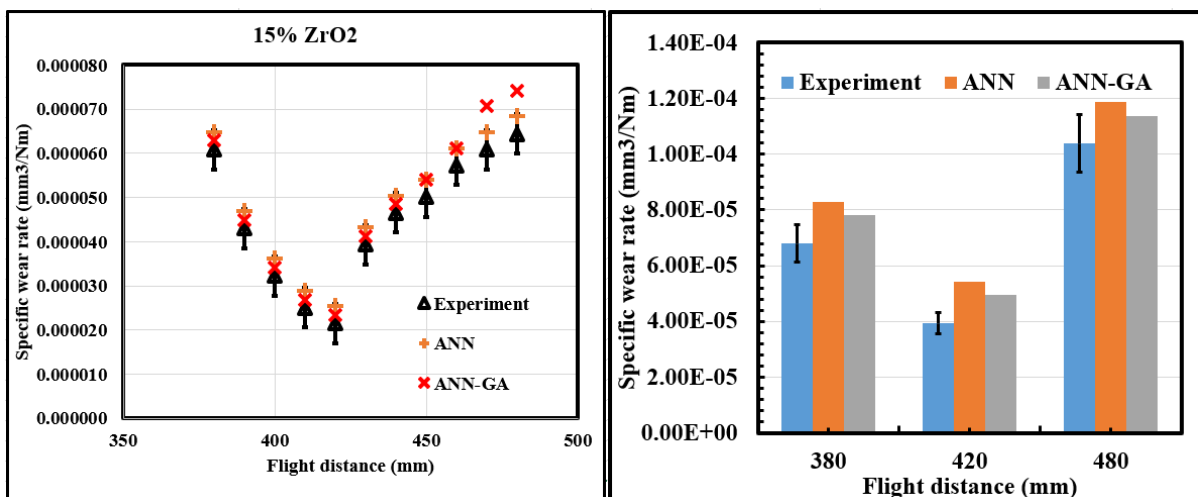
(c)

Figure 5.49: Specific wear rate with respect to flight distance of Al+12.5Si+ZrO₂ composites with (a) 5 wt. % (b) 10 wt.% (c) 15 wt.% ZrO₂ reinforcements

5.4.4 Evaluation of the Microstructure features of Al-12Si+ ZrO₂ composite

Composite material is a combination of two or more phases, with their mechanical, chemical and physical characteristics. The properties of these materials are mainly influenced by metal matrix alloy and reinforcing phase (minor phase). The chemistry and microstructure of the alloy have significant influence on the wear and mechanical properties of the composite. In order to investigate the influence of reinforcement material in aluminium silicon alloy and dry wear behaviour of the composites, these composite materials, namely Al+12.5Si+ (5%, 10% and 15% ZrO_2) for different flight distances 370 mm, 420 mm and 480 mm are used in the present study. It is worthy to note that the aluminium silicon alloy and reinforced zirconium oxide are processed in similar manner for each experimental trails (i.e., varying weight fraction of ZrO_2) under same experimental condition. The size of ZrO_2 particles was measured using SEM images and it has been noted that ZrO_2 particles varied between 42 and 84 μm, but majority of the particles are in the range of 45-50 μm. The Figure 5.50 shows the microstructure for the flight distance 370 mm. It can be observed that more or less uniform distribution reinforced zirconium oxide in aluminium silicon matrix. The reason for this is due to the particles which are trapped within the primary aluminium dendrites instead of inter-dendritic region. The main reason is having very small amount of inter-dendritic phase. Another possibility is due to the dimension of inter-dendritic region being less compared to the particle diameter. The interface between ZrO_2 particle and aluminium silicon matrix acts as nucleation agent for the intermetallic precipitates during heat-treatment. Therefore, at the interfacial region a greater number of precipitates of relatively larger size were observed. The higher dislocation of density around zirconium oxide particle leads to growth of precipitates, which are larger in these regions resulting in coarser precipitates. It is worth to note that smaller flight distance results in insufficient gas filling time to interact with the spray so that a larger fraction of the droplet flux is completely molten (Annavarapu, 1988; Srivastava et al., 2004). In order to investigate the change in morphology of the used zirconium oxide in detail during spray forming, the flight distance of 420 mm and 480 mm are examined which are shown in Figure 5.51 and 5.52, which is very much essential for uniform distribution of ZrO_2 particles.
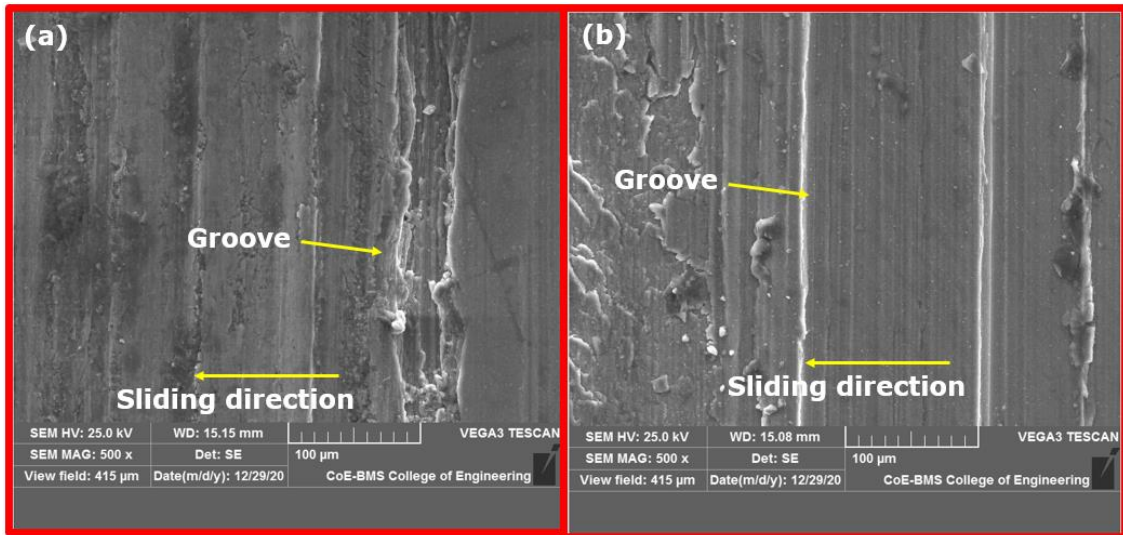
(a)

(b)
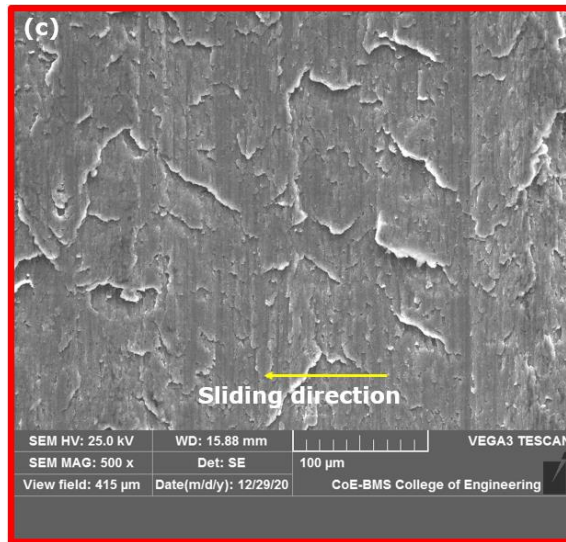
(c)

Figure 5.50: Microstructure image of Al+12.5Si+ZrO₂ composites with (a) 5 wt. % (b) 10 wt.% (c) 15 wt.% ZrO₂ reinforcements for the flight distance 370 mm

The microstructure of the spray formed composite (5%, 10% and 15% AlSi-ZrO₂) for the flight distance 420 mm is shown in Figure 5.51. The interfaces between the ZrO₂ particles and AlSi matrix are clearly observed, and also the uniform distribution of ZrO₂ particles is observed along the grain boundaries with the appearance of some ZrO₂ particles dispersed inside the aluminium silicon matrix. This change in the morphology is mainly due to the presence of AlSi composite powders. It seems that addition of ZrO₂ on wear track leads to the development of various oxide layers such as aluminium and iron oxide. These formed layers have significantly influenced the wear and friction factors of contact pairs. The findings are

`

inline of another research works reported ([Arif et al., 2017](); [Arif et al., 2020]()). The composites consisted of block like primary Si, needle-like eutectic Si phases and uniformly distributed ZrO_2 reinforced particles in the dendritic Al-matrix. The increase in ZrO_2 particles leads of clustering of reinforcement particles at grain junctions as well as continuous network along the grain boundaries. It is to be noted that individual zirconium oxide component measuring around 5 μm is clearly seen with its boundary and also the interfaces between the zirconium oxides were observed at higher magnification. These results are probably tied up with earlier works, which shows the formation of reinforcement with size in few microns, uniform distribution of reinforcement particles and strong and clear interface between matrix and reinforcement particles were the main advantages of in situ formation of reinforcement over ex situ processes ([Tjong et al., 2000](); [Sheibani et al., 2007](); [Ramesh et al., 2011]()). Another reason is due to decrease in the rate of heat extraction leads to increase in microstructural scale with increasing deposit thickness, i.e., at the central region of the preform ([Grant et al., 1991](); [Raju et al., 2011]()) as shown in [Figure 5.51](). This results in refined microstructural features as compared other flight distances.
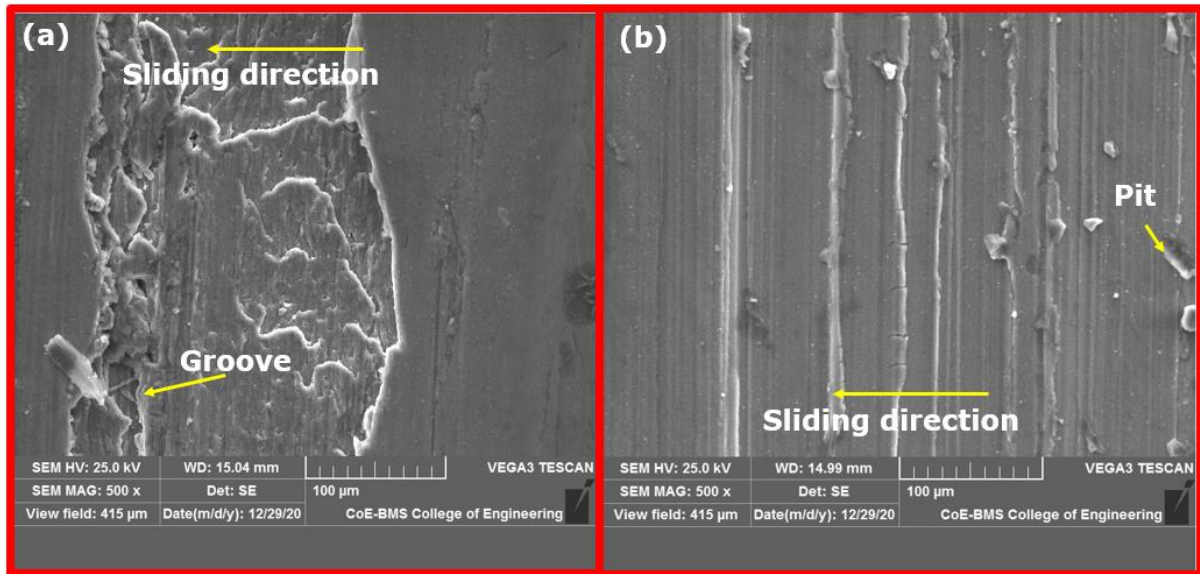
(a)   (b)
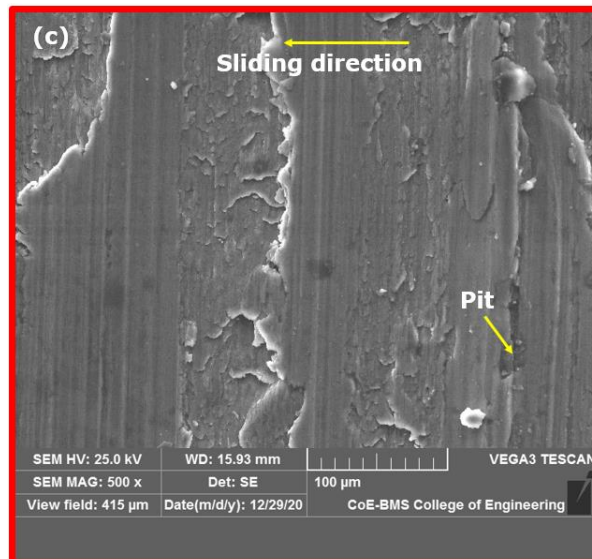
(c)

Figure 5.51: Microstructure image of the Al+12.5Si+ZrO$_2$ composites with (a) 5 wt. %

(b) 10 wt.% (c) 15 wt.% ZrO$_2$ reinforcements for the flight distance 420 mm

In contrast to previous Figure 5.51, more ploughing action, irregularities and material transfer are observed at a flight distance of 480 mm as shown in Figure 5.52. Due to the ploughing action, some of the zirconium oxide particles are flushed out from the surface, which is confirmed by the very low amount of zirconium oxide on the wear track. The central region of the deposit consists of larger size droplets (Lavernia et al., 1989; 1992; Srivastava et al., 2001) and undercooled droplets and the same phenomena is observed by other researchers (for eg. Xu and Lavernia, 1999 and Ojha et al., 1991). These results shows that the cooling of

the droplets by the atomizing gas is mainly influenced by the flight distance. From the phenomena of the observations of SEM microstructure, it is fair to conclude that the optimized flight distance is 420 mm.

(b) (b)

(c)
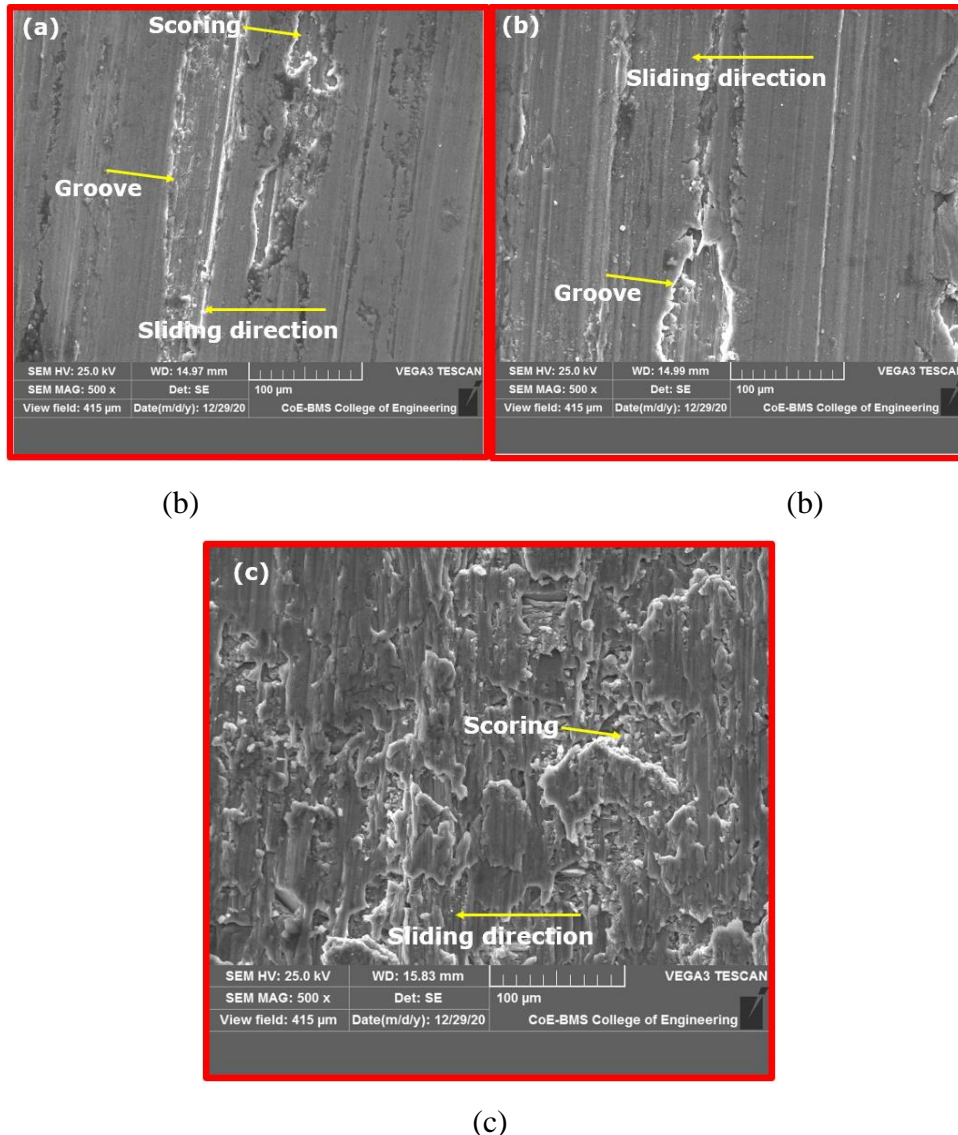
Figure 5.52: Microstructure image of the Al+12.5Si+ZrO₂ composites with (a) 5 wt. % (b) 10 wt.% (c) 15 wt.% ZrO₂ reinforcements for the flight distance 480 mm

5.5 Fractography of Al-12.5Si composite reinforced with ZrO₂ particles using spray deposition

5.5.1 Analysis of fractography microstructure and mechanical properties

Analysis of the results of spray forming experiments are discussed here, to establish relationship among process parameters. The Pareto optimal front corresponding to spray forming process determined viz. MOPSO-CD were also discussed. Confirmation experiments are conducted to justify the developed model (predictions and optimization) performances. Table 5.32 presents the spray forming input-output data collected according to CCD experiments for spray forming. A total 27 experiments ($2^4 = 16$ corner or cube experiments, 8-star point experiments, and 3 replicate experiments at centre point) were conducted with three replicates at each trial. Minitab 17 software platform was used to perform (statistical, regression and graphical) analysis on the collected spray forming input-output data.

Table 5.32: DOE conditions for spray forming process

Exp. No.	Input variables				Outputs		Exp. No.	Input variables				Outputs	
	FD, m	MT, ºC	GP, MPa	ZR, %	Hardness, HV	UTS, MPa		FD, m	MT, ºC	GP, MPa	ZR, %	Hardness, HV	UTS, MPa
1	0.40	760	0.7	10	78.0	166.2	15	0.35	720	1.0	05	67.0	139.7
2	0.48	720	1.0	15	74.0	158.9	16	0.40	760	1.0	10	77.9	164.8
3	0.48	800	0.4	15	73.0	157.8	17	0.40	800	0.7	10	76.5	164.4
4	0.48	720	0.4	15	74.0	160.1	18	0.35	800	0.4	15	73.0	155.4
5	0.37	800	1.0	05	68.0	145.7	19	0.35	720	1.0	15	74.0	153.5
6	0.37	800	0.4	05	67.0	140.8	20	0.40	760	0.7	15	74.2	158.8
7	0.48	800	1.0	15	75.0	161.2	21	0.35	760	0.7	10	77.9	165.9
8	0.48	760	0.7	10	77.0	166.6	22	0.45	720	0.4	05	67.0	142.1
9	0.40	760	0.7	10	78.0	166.5	23	0.40	760	0.7	10	77.5	164.6
10	0.40	760	0.4	10	77.5	165.6	24	0.35	720	0.4	15	73.0	155.5
11	0.37	720	0.4	05	69.0	144.7	25	0.40	720	0.7	10	76.7	164.5
12	0.37	800	1.0	15	76.0	162.4	26	0.45	720	1.0	05	67.0	140.4
13	0.48	800	1.0	05	67.0	141.3	27	0.45	800	0.4	05	65.8	135.6
14	0.40	760	0.7	05	67.3	142.3							

`

The RSM application derives the second-order regression equation that is empirical relationship between output variables (UTS and Hardness) and input (spray forming) variables shown in Equation 5.1 and 5.2 (Goudar et al., 2013)

$$
\begin{aligned}
\text{Hardness} = {} & \text{-189- 49 FD} + 0.699 \text{ MT} - 39.56 \text{ GP} + 4.407 \text{ ZR} + 93 \text{ FD*FD} - \\
& 0.000472 \text{ MT*MT} + 3.83 \text{ GP*GP} - 0.2642 \text{ ZR*ZR} - 0.0591 \text{ FD*MT} \quad (5.1) \\
& + 1.30 \text{ FD*GP} + 0.922 \text{ FD*ZR} + 0.04271 \text{ MT*GP} + 0.001313 \text{ MT*ZR} \\
& + 0.2417 \text{ GP*ZR}
\end{aligned}
$$

$$
\begin{aligned}
\text{UTS} = {} & \text{-295+ 61 FD+ 1.144 MT- 118.9 GP+ 8.56 ZR+ 264 FD*FD} \quad - \\
& 0.000722 \text{ MT*MT- 4.51 GP*GP- 0.6022 ZR*ZR- 0.450 FD*MT+ 8.1 FD*GP} \quad (5.2) \\
& + 5.071 \text{ FD*ZR+ 0.1609 MT*GP+ 0.00384 MT*ZR+ 0.137 GP*ZR}
\end{aligned}
$$

5.5.2 Response: Hardness

Table 5.17 presents the analysis of variance (i.e., significance and F-tests) test results of the response, hardness. Note that, larger F-values and lower P-values (i.e., < 0.05) are treated to be significant for that term. For Hardness, all linear terms (except, melt temperature), square terms (except flight distance and gas pressure), and 2-term interactions (excluding, flight distance interaction with gas pressure and melt temperature) were significant terms, as their P-values are less than 0.05. Although, two individual terms such as flight distance and gas pressure were found significant but their interaction among themselves was insignificant towards the response-hardness. ZrO_2 reinforcements are found to have maximum contribution followed by gas pressure, and flight distance, respectively (refer F-value of Table 5.34). The square terms of gas pressure and flight distance were found insignificant and their relationship is found to have linear relationship with other parameters (refer Figure 5.53(c) and (f)). Interesting to note that, graphical plots of Figure 5.53(a, b, d) and (c, e, f) were appeared in identical form might be due to large influence (magnitude of F-values) of ZrO_2 and almost similar with negligible influence by melt temperature, flight distance and gas pressure, respectively. Higher hardness was observed at the mid-values of gas pressure and flight distance (refer Figure 5.53(b)). Lower flight distance ensures the spray deposits are nearer to atomiser, wherein spray deposits encounters larger atomization gas cooling impact than that of larger flight distances. It is also observed that, faster cooling rate ensures higher mechanical properties (hardness) with combined effect of gas pressure and flight distance.

`

Figure 5.53c shows the flight distance impact is negligible and the resulted surface plot is almost flat. The findings are statistically in good agreement with Table 5.33. Zirconium dioxide (ZrO_2) reinforcements showed maximum percent contributions compared to that of flight distance, melt temperature and gas pressure (refer Figure 5.53(c), (e) and (f). Increased reinforcements tend to increase melt viscosity, generate large thermal expansion coefficient differences among aluminium matrix and ZrO_2 reinforcement. This causes formation of interfacial microporosity. Beyond the critical limit of ZrO_2 reinforcements (>10% wt.), the porosities will lower the interfacial bonding between reinforcements-matrix phases. Furthermore, gasses accumulate on the rough part of ZrO_2 reinforcements may enter inside the melt droplets resulting in gas porosity and thereby reducing composite hardness. The results are in good agreement with similar confounding factor effects in published literature (Srivastava et al., 2005). The model F-values were found to be as high as 168.98, whitrongly signifies the model significance. Furthermore, determination coefficient (R^2) and adjusted determination coefficient (adj. R^2) value were found close to unity ($R^2 = 0.995$ and adj. $R^2 = 0.9891$) which satisfies pre-set 95% confidence level. The model developed for hardness is statistically adequate which are proven from various tests (model F-values, significance of terms and coefficient of determination) conducted.

`

Table 5.33: ANOVA test results for response - Hardness

Source	DF	Seq SS	Contribution	Adj SS	Adj MS	F-Value	P-Value
Model	14	500.351	99.48%	500.351	35.739	164.36	0.000
Linear	4	225.930	44.92%	212.271	53.068	244.06	0.000
FD	1	16.100	3.20%	1.445	1.445	6.65	0.024
MT	1	0.009	0.00%	0.015	0.015	0.07	0.798
GP	1	2.420	0.48%	2.428	2.428	11.16	0.006
ZR	1	207.401	41.24%	208.384	208.384	958.35	0.000
Square	4	265.677	52.82%	265.677	66.419	305.46	0.000
FD*FD	1	111.387	22.15%	0.124	0.124	0.57	0.464
MT*MT	1	35.425	7.04%	1.468	1.468	6.75	0.023
GP*GP	1	6.665	1.33%	0.305	0.305	1.40	0.259
ZR*ZR	1	112.200	22.31%	112.200	112.200	516.00	0.000
2-Way Interaction	6	8.744	1.74%	8.744	1.457	6.70	0.003
FD*MT	1	0.277	0.06%	0.277	0.277	1.27	0.281
FD*GP	1	0.008	0.00%	0.008	0.008	0.03	0.855
FD*ZR	1	1.052	0.21%	1.052	1.052	4.84	0.048
MT*GP	1	4.202	0.84%	4.202	4.202	19.33	0.001
MT*ZR	1	1.103	0.22%	1.103	1.103	5.07	0.044
GP*ZR	1	2.103	0.42%	2.103	2.103	9.67	0.009
Error	12	2.609	0.52%	2.609	0.217		
Lack-of-Fit	10	2.443	0.49%	2.443	0.244	2.93	0.281
Pure Error	2	0.167	0.03%	0.167	0.083		
Total	26	502.960	100.00%				
Model adequacy: $R^2 = 0.9948$ and R^2-adj = 0.9888							
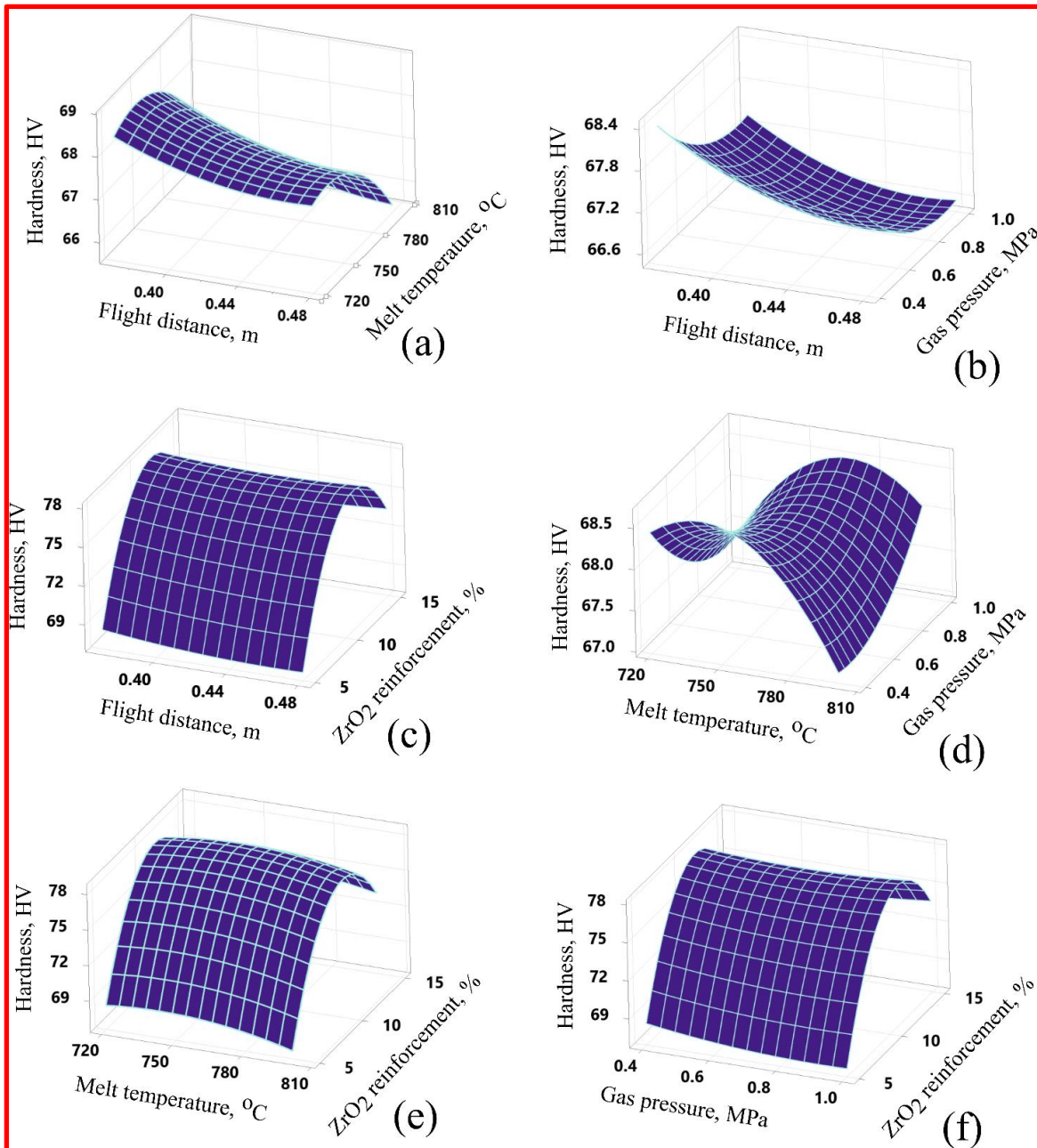
Figure 5.53: Surface plots for hardness: a) Flight distance and melt temperature, b) Flight distance and gas pressure, c) Flight distance and ZrO₂ reinforcement, d) melt temperature and gas pressure, e) melt temperature and ZrO₂ reinforcement and f) gas pressure and ZrO₂ reinforcement

5.5.3 Response: Ultimate Tensile Strength

Here, the factors (individual, square and interaction) are analysed subjected to maximizing the UTS. Table 5.18 present the details of F-statistics and P-values < 0.05, which determines the significance of factors for UTS. The individual terms such as flight distance and melt temperature were found insignificant for UTS. ZrO_2 reinforcement contributions are more followed by gas pressure on UTS. The square terms of flight distance melt temperature and gas pressure were insignificant which indicates linear relationship with UTS. Although individual terms (flight distance and melt temperature) were found insignificant, but also their interaction among themselves were found insignificant as their P-values < 0.05. Furthermore, gas pressure interaction with flight distance and ZrO_2 reinforcements were insignificant for UTS. Insignificant terms signifies that those terms do not contribute towards UTS. However, model derived insignificant terms expulsion in regression equation, results in imprecise input-output relationship and reduces prediction accuracy. Higher model F-values of 206.4 with better R^2 value of 0.995 indicates the model is statistically significant for making effective predictions, as shown in Figure 5.54. The model developed for UTS shows the lack-of-fit term of p-values greater than 0.05 and is statistically insignificant. Note that, expulsion of insignificant terms in regression equation and in models make the lack-of-fit term significant. However, this results in imprecise regression equations and reduce prediction precisions.
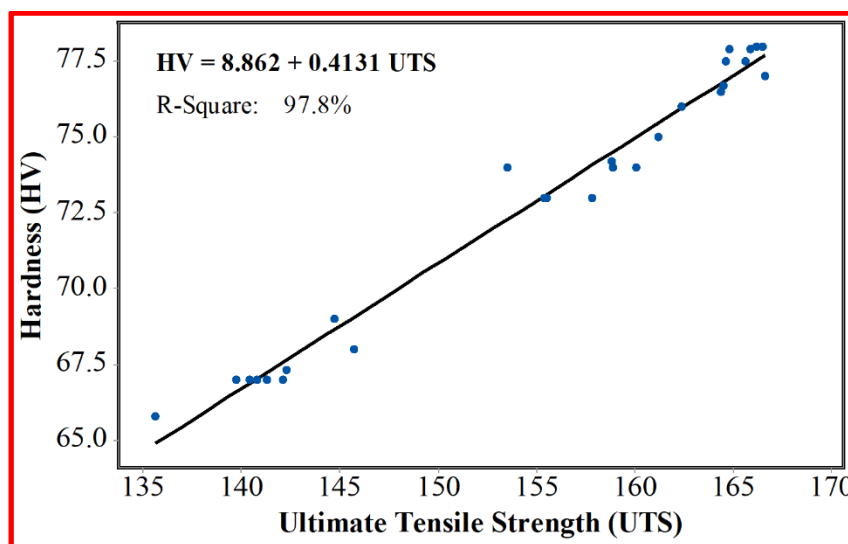
Figure 5.54: Relationship between hardness and ultimate tensile strength

`

Spray forming composites are fabricated for each experimental condition according to Table 5.34. Hardness and ultimate tensile strengths are measured for each condition. From analysis of variance, the effects of factors (i.e. ZrO_2 reinforcement as dominating effect followed by gas pressure, and negligible influence of melt temperature and flight distance) were found almost identical for both hardness and UTS. Therefore, relative dependency among the hardness and ultimate tensile strengths of composites are determined with those experimental data presented in Table 5.34. Best-fit curve and correlation coefficient value estimate the dependency among the outputs. From Figure 5.54 it was confirmed that the ultimate tensile strength increases with the increased values of hardness. Furthermore, best-fit curve for hardness was established with the linear function of ultimate tensile strength. The correlation coefficient established for responses (hardness and ultimate tensile strength) was found equal to 0.978. The better correlation coefficient value ensures the developed linear relationship (HV = 8.862 + 0.4131 UTS) can help to predict hardness for known values of ultimate tensile strengths.

Table 5.34: ANOVA test results for response - UTS

Source	DF	Seq SS	Contribution	Adj SS	Adj MS	F-Value	P-Value
Model	14	2869.70	99.55%	2869.70	204.98	187.67	0.000
Linear	4	1315.03	45.62%	1291.53	322.88	295.62	0.000
FD	1	40.91	1.42%	0.01	0.01	0.01	0.930
MT	1	1.50	0.05%	1.02	1.02	0.94	0.352
GP	1	5.89	0.20%	6.02	6.02	5.51	0.037
ZR	1	1266.72	43.94%	1284.48	1284.48	1176.04	0.000
Square	4	1436.72	49.84%	1436.72	359.18	328.86	0.000
FD*FD	1	612.23	21.24%	1.01	1.01	0.92	0.356
MT*MT	1	179.59	6.23%	3.43	3.43	3.14	0.102
GP*GP	1	62.04	2.15%	0.42	0.42	0.39	0.545
ZR*ZR	1	582.87	20.22%	582.87	582.87	533.66	0.000
2-Way Interaction	6	117.96	4.09%	117.96	19.66	18.00	0.000
FD*MT	1	16.02	0.56%	16.02	16.02	14.67	0.002
FD*GP	1	0.29	0.01%	0.29	0.29	0.27	0.615

`

FD*ZR	1	31.83	1.10%	31.83	31.83	29.15	0.000
MT*GP	1	59.68	2.07%	59.68	59.68	54.64	0.000
MT*ZR	1	9.46	0.33%	9.46	9.46	8.66	0.012
GP*ZR	1	0.68	0.02%	0.68	0.68	0.62	0.445
Error	12	13.11	0.45%	13.11	1.09		
Lack-of-Fit	10	11.02	0.38%	11.02	1.10	1.06	0.580
Pure Error	2	2.09	0.07%	2.09	1.04		
Total	26	2882.81	100.00%				
Model adequacy: R2 = 0.9955 and R2-adj = 0.9901							

5.5.4 Model Prediction Accuracy

RSM model derived empirical regression (output expressed as function of input variables) equations based on experimental data. Note that, hardness and strength are well-known mechanical properties expressed in terms of durability and serviceability of spray formed parts. Ten sets of different values of input variables selected for experimentation and output values (hardness and ultimate tensile strength) predicted by the models are compared to test their practical utility in industries. The input-output data of ten random experiments are presented in Table 5.35. The experimental and predicted data of hardness and ultimate tensile strength are found close to one another (refer Figure 5.55(b), (d). Further, model predicted hardness and ultimate tensile strength fall within the ranges of -2.47 to +1.75%, and -9.54 to +10.81%, respectively, when tested for ten experimental data (refer Figure 5.55(b), (d)). The derived mathematical equation ensures the model predicted in both the positive and negative directions (refer Figure 5.55(b), (d)). Good consistency was witnessed between experimental and predicted data resulted with the average absolute percent deviation in prediction being equal to 1.21% for hardness, and 6.09% for ultimate tensile strength. Therefore, RSM model derived response equations for hardness and ultimate tensile strength, could help in the future applications and studies where experimental data is lacking.

Table 5.35: Validation results for Spray forming process

Input variables				Experimental Values		Prediction Values		Percent prediction	
A, m	B, ºC	C, MPa	D, %	HV	UTS	HV	UTS	HV	UTS
0.43	775.0	0.85	8.5	78.2	166.7	75.9	162.1	-1.42	-5.75
0.39	780.0	0.45	6.0	72.3	156.4	70.6	149.7	-1.00	-9.54
0.41	790.0	0.90	9.5	81.5	169.9	77.2	165.8	-2.47	-5.03
0.40	760.0	1.00	10.0	76.9	162.2	78.3	165.4	0.96	5.20
0.39	760.5	0.75	12.0	80.3	172.1	78.2	166.9	-1.26	-6.48
0.47	725.0	0.80	10.5	77.5	168.4	77.3	167.3	-0.18	-2.71
0.38	735.5	0.70	7.5	72.5	153.7	74.2	158.2	1.26	6.34
0.38	795.5	0.85	5.5	66.8	144.5	69.1	147.6	1.75	6.14
0.42	770.0	0.90	13.0	78.9	168.7	77.7	166.7	-0.66	-2.92
0.39	730.5	0.85	14.5	73.1	150.5	74.9	158.4	1.14	10.81
Minimum percent deviation								**-2.47**	**-9.54**
Maximum percent deviation								**1.75**	**10.81**
Average absolute percent deviation								**1.21**	**6.09**
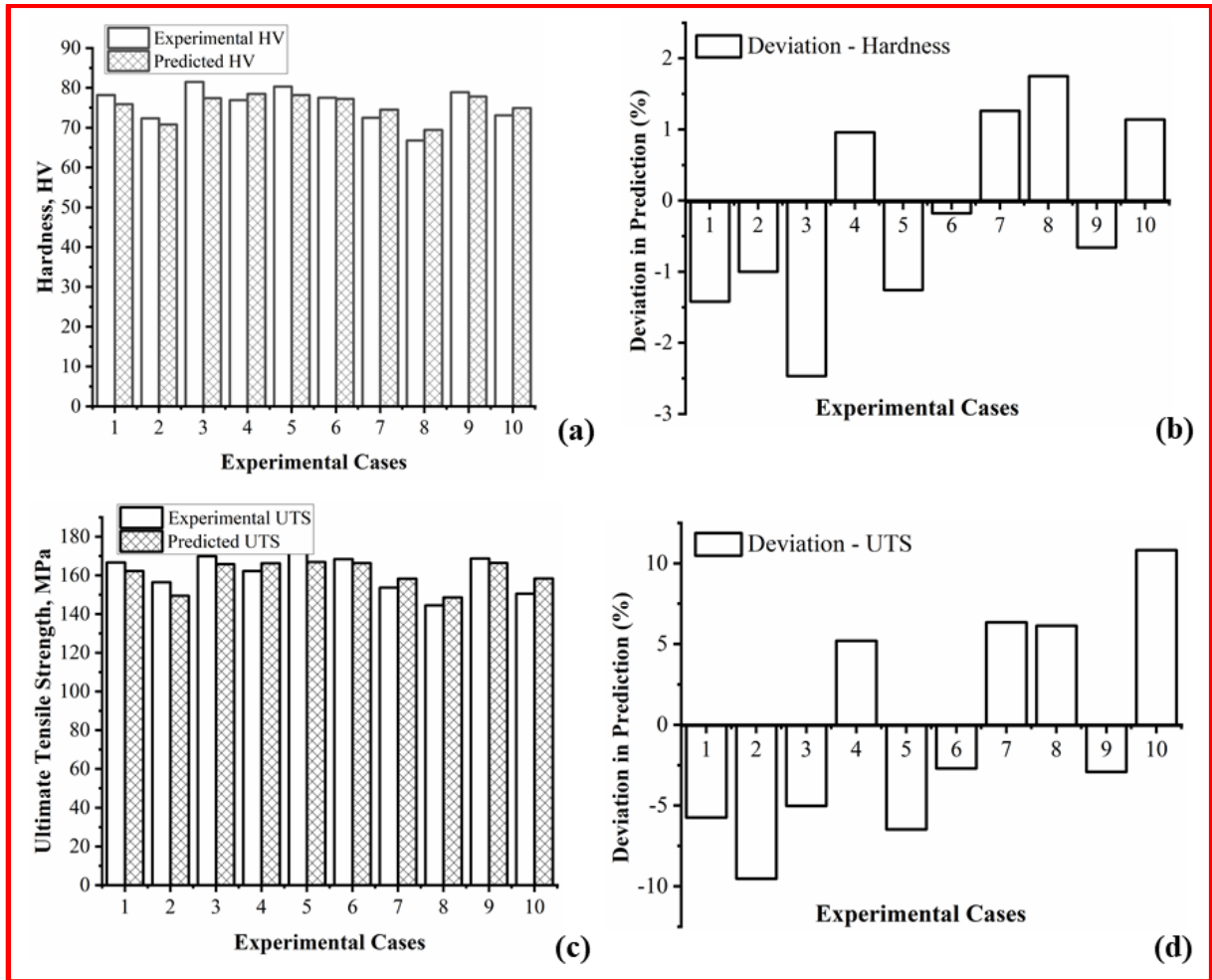
Figure 5.55: Model validation results: a) & c) experimental and model predicted hardness and UTS values, b) & d) percent deviation in prediction for hardness and UTS

5.5.5 Multi-objective optimization: MOPSO-CD

The present work aims at optimizing the bi-objective functions (hardness and ultimate tensile strength) by determining set of decision variables (melt temperature, ZrO_2 reinforcements, gas pressure and flight distance) subjected to input variable constraints as discussed below,

$0.37 \leq$ flight distance ≥ 0.480; $720 \leq$ melt temperature ≥ 800; $0.40 \leq$ gas pressure ≥ 1.0; $5.0 \leq ZrO_2$ reinforcements ≥ 15.0.

There are many solutions (hardness and ultimate tensile strength) in determining the optimal spray forming conditions. The complexity of this research work in determining an approximate method is probably infeasible due to lack of polynomial algorithms and no universal standard rule defined yet for this problem. Traditional weighted approaches

`

(principal component analysis, critic, entropy, user preference) are practiced by distinguished researchers to solve the multi-objective optimization problems. Pareto based optimization methods (MOPSO-CD, NSGA-II and so on) are excellent tools offering optimal solutions. Indeed, selecting the best among the potential solutions is being considered as a tedious task for researchers. To resolve this problem, weights was assigned for each output parameter and the corresponding desirability value was determined. Note that, composite desirability value (D$_o$) was estimated taking by taking in to the account of individual desirability functions (hardness and ultimate tensile strength), which are varied in the ranges between 0 and 1. The computation of overall desirability value (D$_o$) for multi-objective optimization is done by applying Equation 5.3.

$$D_O = \sqrt[2]{\left(d_{HV}^{W_1} \times d_{UTS}^{W_2}\right)} \tag{5.3}$$

The desirability (d_{HV} and d_{UTS} represents desirability index associated to hardness and UTS) values close to a zero value represents completely undesirable and one signifies totally desirable. The computation of individual desirability value for hardness and ultimate tensile strength is presented Equation 5.4,

$$d_{HV} = \frac{HV - HV_{min}}{HV_{max} - HV_{min}}, d_{UTS} = \frac{UTS - UTS_{min}}{UTS - UTS_{min}} \tag{5.4}$$

In Equation 8, W$_1$, and W$_2$ represents the weight fraction corresponding to hardness and UTS. The different sets of weights assigned to each output are presented in Table 5.20. HV$_{max}$, HV$_{min}$, UTS$_{max}$ and UTS$_{min}$ are the maximum and minimum values of hardness and UTS, respectively. MOPSO-CD determined optimal spray forming input-output conditions with corresponding desirability value presented in Table 5.36. It was noted that, highest desirability value equal to 0.9958 was obtained for the weight fractions (0.05 for hardness and 0.95 for ultimate tensile strength) and the corresponding spray forming input-output data was presented in Table 5.36 and Figure 5.56.

Table 5.36. Multi-objective optimization results for spray forming process

Exp. No.	Weights of responses		Input variables				Output values		Desirability Value (D_o)
	HV	UTS	A, m	B, ºC	C, MPa	D, %	HV	UTS	
1	0.05	0.95	0.38	797.98	0.97	11.61	78.96	169.45	0.9958
2	0.10	0.90	0.38	795.15	0.96	11.68	78.95	169.28	0.9931
3	0.15	0.85	0.37	797.86	0.88	11.19	78.53	168.97	0.9863
4	0.20	0.80	0.36	787.17	0.99	11.13	79.06	168.91	0.9890
5	0.25	0.75	0.36	788.01	0.95	11.71	78.90	168.71	0.9852
6	0.30	0.70	0.48	778.59	0.93	11.79	78.44	168.69	0.9797
7	0.35	0.65	0.36	792.49	0.96	12.04	78.81	168.69	0.9837
8	0.40	0.60	0.36	792.54	0.9	11.15	78.62	168.67	0.9806
9	0.45	0.55	0.36	791.24	0.93	11.9	78.72	168.61	0.9813
10	0.50	0.50	0.36	796.04	0.95	10.48	78.57	168.58	0.9781
11	0.55	0.45	0.37	784.91	0.98	10.77	78.89	168.38	0.9829
12	0.60	0.40	0.37	770.39	0.97	11.77	78.94	167.77	0.9803
13	0.65	0.35	0.37	770.39	0.97	11.77	78.94	167.77	0.9808
14	0.70	0.30	0.35	795.15	0.96	11.68	78.95	169.28	0.9895
15	0.75	0.25	0.35	797.98	0.97	11.61	78.96	169.45	0.9898
16	0.80	0.20	0.36	771.74	0.98	12.03	78.98	167.78	0.9850
17	0.85	0.15	0.37	764.32	1.0	11.82	78.99	167.36	0.9851
18	0.90	0.10	0.36	769.89	0.97	11.55	79.04	167.95	0.9889
19	0.95	0.05	0.36	787.17	0.99	11.13	79.10	168.91	0.9927
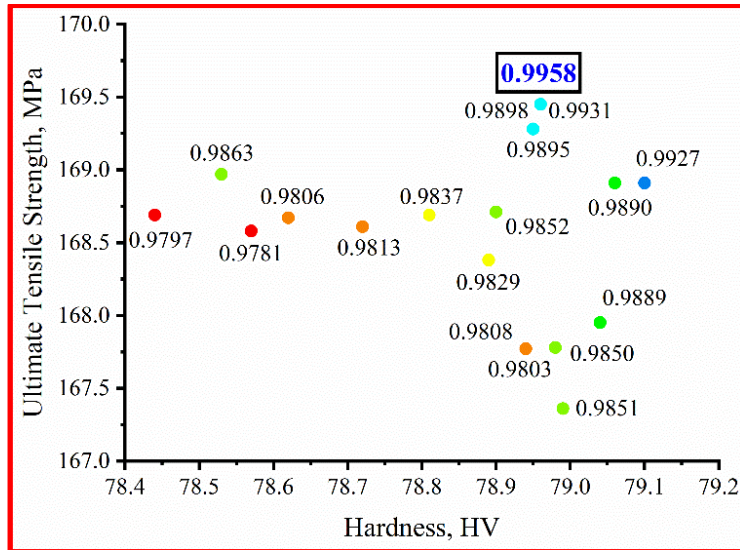
Figure 5.56: Desirability value of hardness vs ultimate tensile strength

5.5.6 Evaluation of the Hardness of Al-12Si+ ZrO$_2$ composite

From the analysis above, it is fair to conclude that the optimum flight distance is 420 mm. Therefore, the hardness is tested under 40 N load at a sliding velocity of 1.5 m/s. The variation of hardness with respect or reinforced composition of ZrO$_2$ is shown in Figure 5.57. The study found that the developed metal matrix composite increases in hardness value with increasing the composition of the reinforced ZrO$_2$ particle. The maximum percentage of improvement for 15% ZrO$_2$ is 10.8%. The contribution of work-hardening caused by deformation of solid grains during the spray forming process could be the reason. The other reasons are homogenous distribution of ZrO$_2$ particles in aluminium silicon metal matrix (Arif et al., 2017). These findings suggest that the materials with higher hardness have enhanced abrasive resistance and wear properties and similar trend was observed by (Mazahery et al., 2012).

191

`
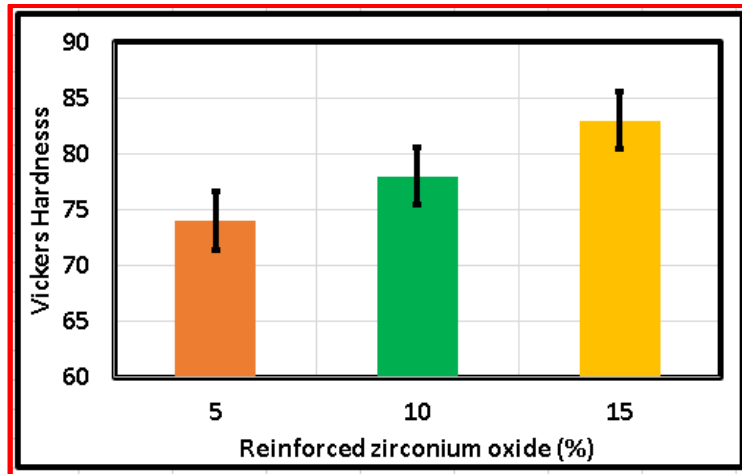
Figure 5.57: Vickers hardness with respect to weight fraction of ZrO₂

5.5.7 Metallographic study

The mode of fracture in the developed matrix that has changed from ductile to cleavage nature is dominated by voids and micro-crack nucleation and propagation, as depicted in Figure 5.58. The lower wt. % of zirconium oxide as a reinforcement material, the fracture indicates the breakage of the particulates. It can be observed that the fracture morphology of Al-12.5Si+5% ZrO₂ is a typical plastic fracture morphology as shown in Figure 5.58(a), while the Figure 5.58(b) shows the fracture image of Al-12.5Si+10% ZrO₂. Higher addition of zirconium oxide as a reinforcement material makes the dimple size and depth of the Al-12.5Si alloy changed. Because of the presence of zirconium oxide, a layered structure emerged in the middle of the micrograph. The amount of zirconium oxide distributed at the edge of the dimple is mainly due to the propagation of the crack in the developed metal matrix composites along the interface during the fracture process. Figure 5.58(c) shows the fracture morphology of Al-12.5Si+15% ZrO₂ composite. The higher concentration of ZrO₂ in Al-12.5Si alloy results in a brittle fracture due to higher percentage of ZrO₂ particles content in the matrix.

(a)

(b)

(c)
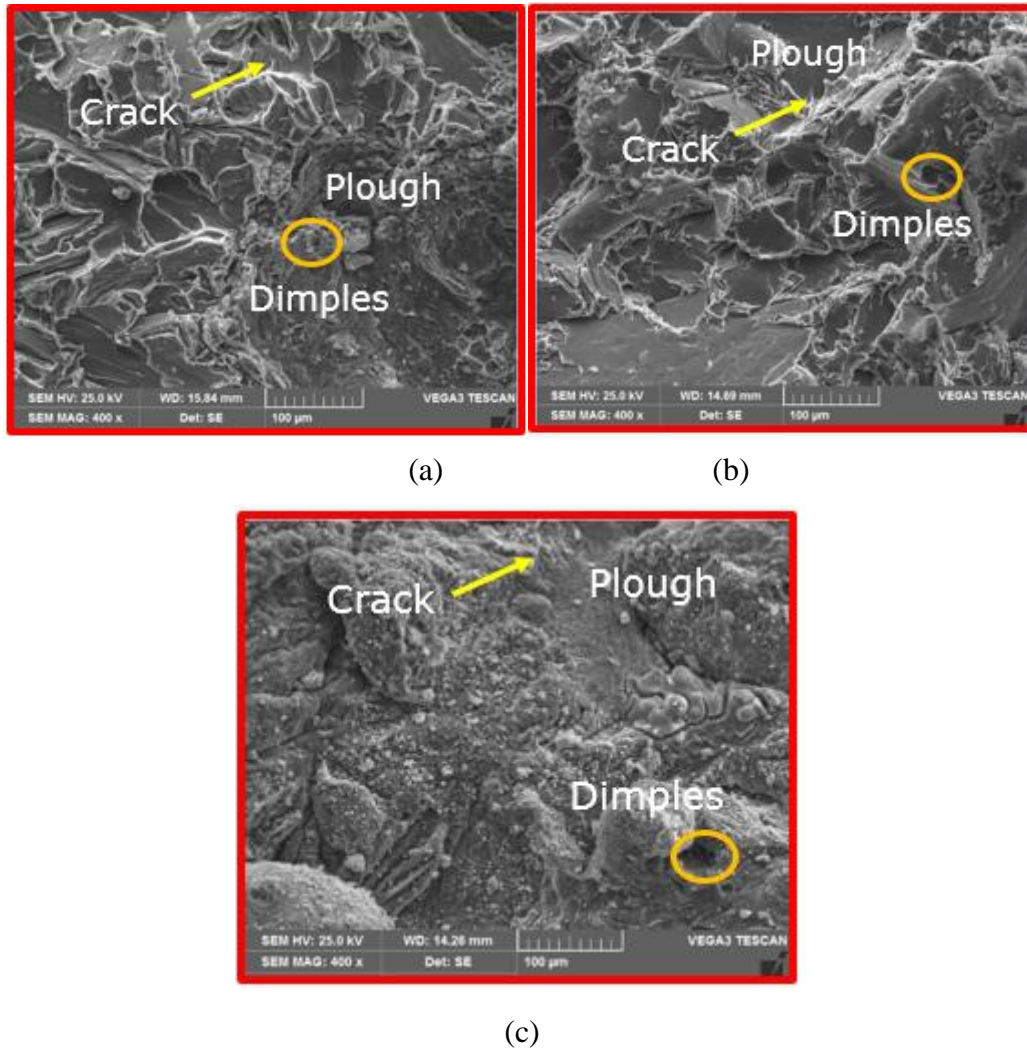
Figure 5.58: Fracture images of tensile specimens of   Al+12.5Si+ZrO$_2$ composite with(a) 5 wt. % (b) 10 wt.% (c) 15 wt.% reinforcements

Summary

Dry sliding wear behaviour of AlSi-ZrO$_2$ alloy with varying percentage of reinforcement composite material has been studied on a pin-on-disc testing machine with varying flight distance from 380 mm to 480 mm using the applied loads of 10, 20, 30 and 40 N, up to a sliding distance of 4200 m. Further, ANN and ANN-GA models has been successfully validated with experimental data for various operating conditions. The following are the major outcomes of the work are described below:

- The wear properties of the fabricated composites were investigated as a function sliding distance, applied nominal load for all the three compositions of metal matrix composites Al-12.5Si with 5%, 10% and 15% varying ZrO2 compositions. Response

parameter such as coefficient of friction, wear loss, wear rate and specific wear rate are measured during the tests.

- Combining the aluminum silicon alloy with reinforced zirconium oxide will yield a material with higher mechanical properties and wear behavior. The wear resistance of the fabricated hybrid composite was found to be considerably higher for lesser composition of reinforced zirconium oxide in aluminum silicon alloy.

- The microstructure of the spray deposited AlSi-ZrO_2 alloy showed the presence of zirconium oxides and silicon in a fabricated hybrid composite. Further, SEM image showed uniform distribution of zirconium oxide in the aluminum silicon matrix.

- SEM investigations of wear debris and worn surfaces showed that the abrasion and delamination were the main source to increase the wear mechanism.

- The coefficient of friction decreases with increasing the applied load during the initial stages as expected. The higher load with plastic deformation of asperities increases both coefficients of friction and area of contact increase.

- The specific wear rate decreases with increasing applied load. This is due to the work hardening and deformation of plastic state which occurs at higher loads. It was observed that there was an increase in hardness near the surface layers when compared with the interior region.

- ANN and optimized ANN-GA models were developed using MATLAB R2018 software for the estimation of wear loss as a function of effect of flight distance, nominal load and zirconium oxide concentration. Empirical regression equations tested for ten random experimental trials resulted with an average absolute percent deviation in prediction of 1.21% for hardness, and 6.09% for ultimate tensile strength, respectively.

- Hardness was found to have direct linear relationship with ultimate tensile strength and found to have good correlation coefficient value equal to 0.978. Furthermore, hardness can be predicted from the known values of UTS, with the derived mathematical linear expression.

- MOPSO-CD integrated with DFA ensures accurate prediction of optimal spray forming conditions (ZrO_2 reinforcements: 11.6%, melt temperature: 798 ^{o}C, gas pressure: 0.97 MPa, flight distance: 0.35 m) with highest desirability value equal to 0.9958. The optimal spray forming condition ensures highest hardness and ultimate tensile strength values equal to 80.4 HV and 173.2 MPa, respectively.

- Fracture surface morphology associated with optimal spray forming conditions showed uniform structure with strong intermetallic bonding and absence of internal defects (pores, cracks etc.) ensuring highest bonding strength.

- Eventually, it is suggested that the use of zirconium dioxide as reinforcement material has good possibility to enhance the wear properties for the aluminum alloys and developed RBFNN and RBFNN-GA model can effectively predict optimal result based on the experimental data.

5.6 Wear behaviour of Al-12.5Si composite reinforced with 15% ZrO_2 particles using stir casting and spray deposition

5.6.1 Microstructural investigation of stir casting and spray deposition for Al-12.5Si with 15% ZrO_2 as reinforced material

The microstructural images of the developed metal matrix composite for spray deposition and stir casting methods is shown in Figure 5.59. It can be observed that very clear grain boundaries were observed with the presence of precipitates uniformly distributed along the grain boundaries. For the test specimen, in both cases (spray deposition and stir casting), the Figure 5.59 clearly indicates the mark of an adhesive wear with plastic deformation. The edge cracking and metallic fracture of ridges were seen on the surface of the stir cast composite material. The primary silicon particles are easily detached from the Al matrix and the debris of silicon particles is embedded in the matrix. This results in non-uniform and deep grooves. Interestingly, the worn surface of spray deposited composite (refer Figure 5.59(b)) shows smooth appearance and marks with smaller grooves and few small dimples. This can be explained by the fact of oxidation of asperities and plastic deformation on the surface indicating the abrasive wear and existence of mixed metallic. In general, the wear decreases with increase in the hardness of the material. The lesser wear rate of the spray formed metal matrix composite as compared with stir cast composite material is attributed to the refinement of microstructure. This is due to the uniform distribution Si particles of α-Al matrix and large number of fine particles. In both the cases, the deep interior of the tested specimens shows grains elongated in the rolling direction (same as the sliding wear direction). This shows the reinforcement of zirconium oxide particles aligning themselves in the sliding direction during the process of the wear. Most of the contents in this section is published (**Lecture Notes in Mechanical Engineering: Springer**)

It is noted that the during the wear process, the sliding between the two surfaces exerts a tangential force on the particles. This will be in contact with the counter-face material. This leads to localized shear stress which results in particle pull out or fracture, as defined by Rosenfield, 1987.

<table>
<tr><td>(a)</td><td>(b)</td></tr>
</table>
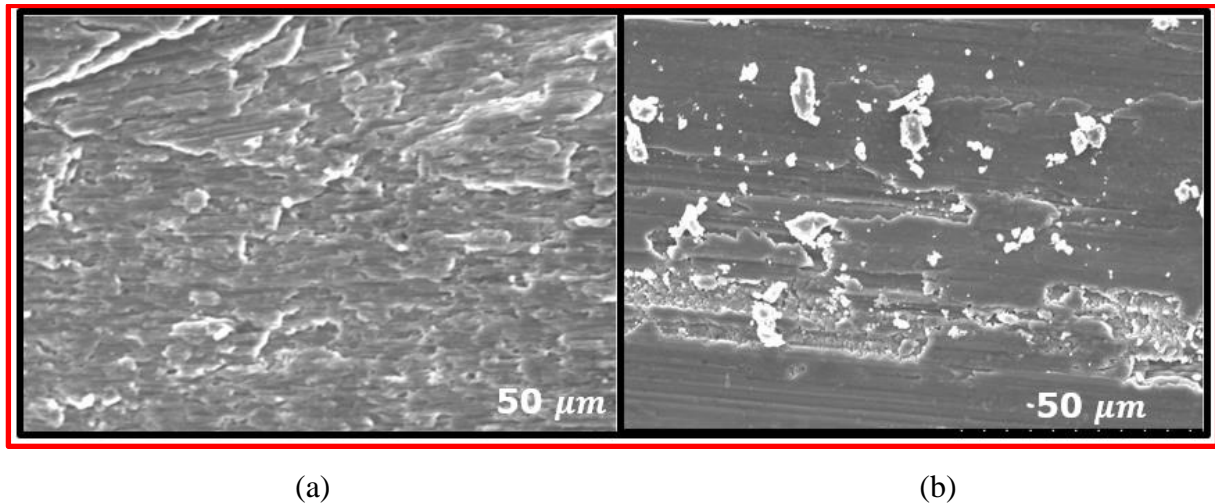
Figure 5.59: SEM microstructure images of worn surfaces of the Al 12.5Si-15(wt%) ZrO$_2$ composite tested under 40 N for (a) Stir cast (b) Spray formed process

5.5.2 Wear and hardness characteristics for stir casting and spray forming of Al12.5Si-ZrO$_2$ composites

The wear loss pattern of the developed metal matrix composites with increasing applied nominal load is shown in Figure 5.60. From the plot, it can be noticed that the wear loss is significant at higher loads for both the methods. However, the wear loss is small in spray formed composite compared to stir casting composite. The reason is the uniform distribution of reinforcing zirconium oxide material in aluminium silicon matrix which is released during sliding condition and formed a protecting tribo-layer between counter disc surface and pin (Akhlaghi et al., 2011; Ravindran et al., 2013). It can be observed that the slope of the wear loss rises in stir casting composites at the load of 25 N. This is due to the delamination and higher amount of deformation of the plastic occurred on the mating surface.

`
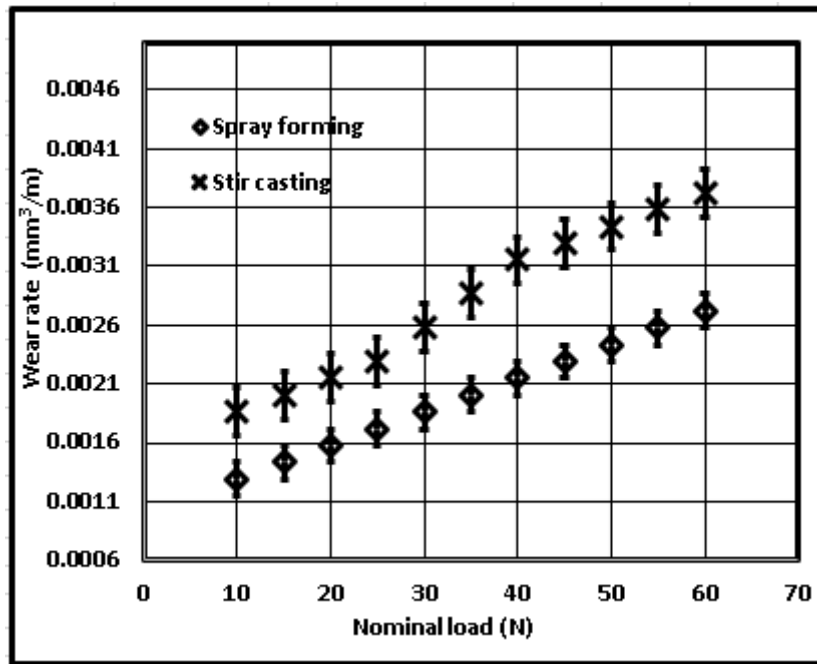
Figure 5.60: Influence of nominal applied load on wear rate of metal matrix composites

Figure 5.61 shows the variation of the wear characteristics with applied nominal load for developed metal matrix composite at a sliding distance of 2300 mm and sliding velocity of 1.9 m/s. It can be inferred from the Figure 5.60, for both the methods, that the wear rate is directly proportional to the applied loads. Comparative study on these two methods revealed that spray formed composite has got better wear resistance than the stir casting composite under identical sliding conditions. The wear resistance is larger in stir casting and lower for spray formed composite. At larger applied loads, the difference between wear rates of stir casting and spray formed is more significant, which implies that much of the larger loads is utilized in wear rather than in plastic deformation of the samples. It was noted that there was decrease in wear rate of 18% using spray deposition technique.

`
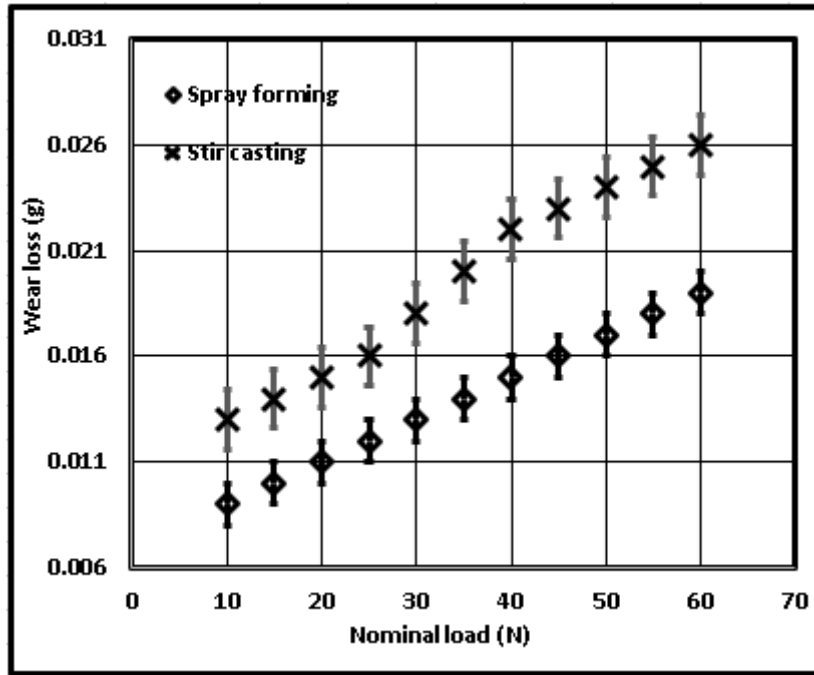
Figure 5.61: Influence of nominal applied load on wear rate of metal matrix composites

Figure 5.62 depicts the variation of the coefficient of friction (COF) with applied nominal load for the wear of the composite subjected to stir casting and spray forming process. It can be observed in both the cases (stir casting and spray forming) that the COF decreases in the entire range of nominal load applied. One may expect the coefficient of friction is inversely proportional to the applied load. The asperities deformation does not occur and the actual area of contact remains unchanged. For both the cases, the COF decreases till 40 N. It is worthy to note that decreasing the hardness on the surface or increasing nominal load, the actual area of contact increases. This leads to increase in COF. The microstructural structure of the metal matrix composites also influences the friction and wear properties.
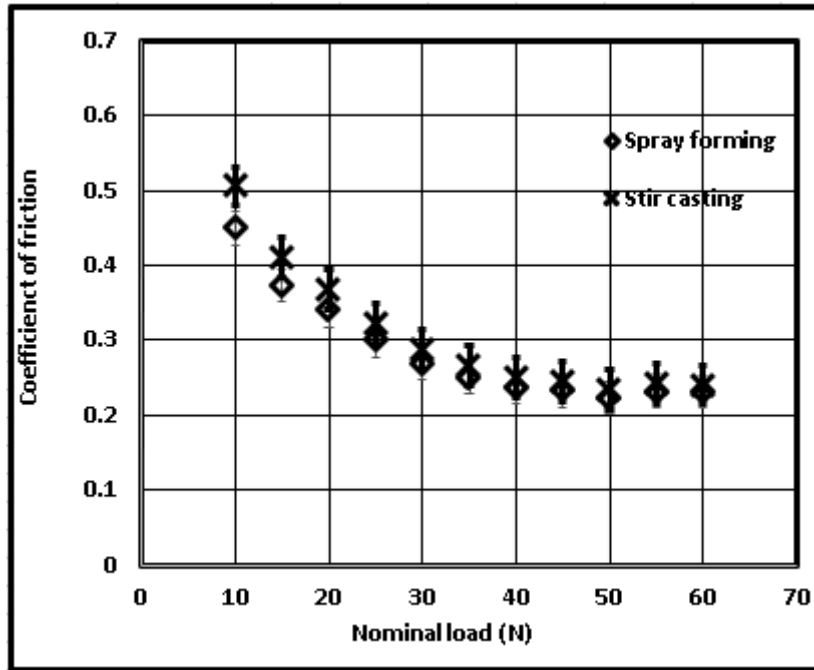
Figure 5.62: Influence of nominal applied load on coefficient of friction of metal matrix composites

The hardness of Al+12.5Si+15%ZrO$_2$ metal matrix composites for stir casting and spray forming composite is shown in Figure 5.63. It can be inferred from the Figure 5.59 that the hardness value of the Al+12.5Si+15% ZrO$_2$ hybrid composite is increased in spray forming method because of considerable uniform distribution of zirconium oxide in the aluminium silicon alloy which can be also observed in the microstructure (refer Figure 5.59). The increase in hardness value is due to addition of zirconium oxide powder that is normally harder.It is worth noting that the surface layers are much denser than the inner core. However, in wear testing. It is found that the surface hardness layer is much higher than after the stir casting process. Another possibility is that the deformation of the plastic at surface layers during wear tests is accompanied by work hardening. In spray forming process, the average hardness of 79 HV which is 14.5% larger than the average hardness of stir casting composite.

`
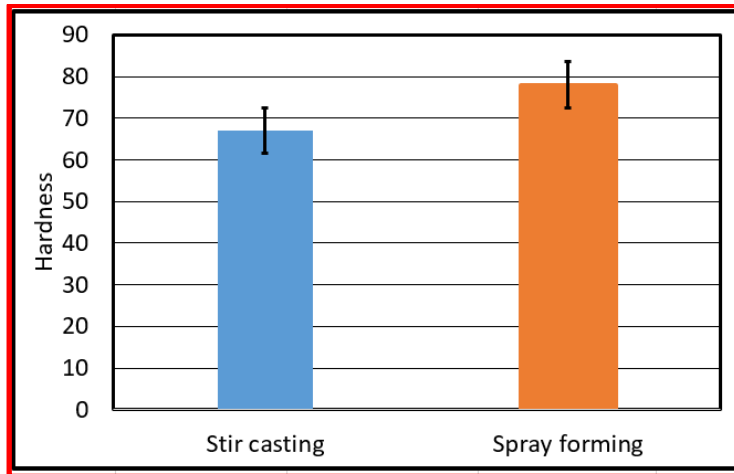
Figure 5.63: Variation of hardness of Al-12.5Si+ZrO₂ composite fabricated with spray forming and stir casting method

Summary

Aluminium silicon composite reinforced with ZrO_2 was developed using spray deposition and stir casting method. The experiments were performed using pin on disc wear machine on the developed metal matrix composite. The following conclusion are drawn from this study:

1) The increase in weight loss was observed at higher applied load for all the composite samples.

2) Maximum friction coefficient was observed in spray deposition composite of 0.45, when compared with stir casting composite of 0.52.

3) As the abrasive particle size expanded, weight reduction increased at a quicker rate until a certain particle size was reached, after which it increased at a slower rate.

4) In both spray deposition and stir casting methods, microstructural images revealed that ZrO_2 particles were evenly distributed along grain boundaries. The microstructure refinement resulted in improved properties in the spray formed metal matrix composite. It was found that the nominal average size of formed ZrO_2 particles was observed to be less than $5\mu m$.

5) The wear properties and friction factor are lower in stir casting composite compared with spray formed composite.

`

CHAPTER 6
CONCLUSION AND SCOPE FOR FUTURE WORK

6.1 Conclusions

This research has highlighted the successful adoption of zirconium oxide as reinforced material in aluminium silicon. The effect of flight distance on the mechanical, microstructural properties and wear properties of AlSi-ZrO$_2$ alloy were investigated. Single object optimization is studied based on the Taguchi technique and ANOVA was used to find the most influencing parameter on each response. Artificial neural network and genetic algorithm have been used as a predictive modelling tool to analyse the responses.

- Stir casting is an ideal processing route employed to prepare Al-12.5%Si composites reinforced with varying wt. percent of ZrO$_2$ particles. ZrO$_2$ reinforcements showed maximum impact followed by stir speed, stir time and casting temperature on casting properties (ultimate tensile strength, hardness, and wear loss).

- Super ranking concept based optimal stir casting conditions resulted in 37.68% reduction in wear loss (13.8 g to 8.4 g), 5.6% and 25.1% increase in UTS (162.7 to 203.4 MPa) and hardness (63.8 to 67.4 HV) values compared to initial stir casting conditions. Pareto ANOVA determined optimal stir casting conditions, which are not one among the set of L$_9$ experiments and corresponding experimental results justify their effectiveness.

- The samples prepared as per stir cast optimized conditions are subjected to hot pressing technique to heal or reduce the pores, resulting in enhanced properties. The influence of Hot-pressing variables (i.e., temperature, pressure, and dwell time) on properties, namely wear loss, UTS and hardness were studied experimentally. Pressure contributes more, followed by temperature and dwell time, on the properties.

- Micro hardness increases as the percentage of ZrO$_2$ particles increases, due to consequent rise in barriers and dislocation density. In Aluminum-matrix, fine equiaxed grain morphology with a uniform distribution of ZrO$_2$ and Silicon Phase was observed.

- As opposed to stir casting processing, spray deposition results in a more uniform distribution and homogeneous dispersion of ZrO$_2$ particles, resulting in higher micro hardness values.

- In both spray deposition and stir casting, an increase in ZrO_2 particle prevents a decrease in the distance between the ZrO_2 particles, resulting in dislocation movement in Al-Si alloy, lowering compressive strength through the dispersion strengthening process.

- The tensile strength of the composite increases as the percentage of ZrO_2 particles in the composite increases. The tensile strength of spray deposition treated composites with 15 wt. percent ZrO_2 particles, on the other hand, reached a limit of 139.87 MPa. This is due to a faster work hardening rate, the configuration of dislocation tangles around the particles, uniform reinforcement distribution, and plastic incongruity between the reinforcement and the matrix.

- The microstructure of the spray deposited AlSi-ZrO_2 alloy is significantly affected by deposit substrate and the nozzle distance. For the lesser flight distance (320 mm), needle and α-Al like constituent of eutectic Si phase are observed and this is due to higher undercooling experienced by the liquid pool. Interestingly, at the optimized flight distance of 420 mm, well-defined pre-solidified particles were noticed.

- Evaluation of hardness and mechanical properties of spray formed alloys exhibits higher tensile, compressive and yield strength. The combination of AlSi-ZrO_2 precipitation and strengthening results in the improved mechanical properties.

- The wear properties of the fabricated composites were investigated as a function of sliding distance, applied nominal load for all the three compositions of metal matrix.

- In summary, the smaller flight distance leads to a large scale of compositional inhomogeneity in the preform. The thickness of the deposit increases with the increase in incoming fraction of liquid at the deposition surface. In addition, a refined and uniform microstructure is evolved at intermediate distances. Also, the liquid pool has a thickness that is comparable to the interaction domain created during spray deposition.

`

REFERENCES

Akbari, M., Shojaeefard, M.H., Asadi, P., Khalkhali, A., 2017b. Wear Performance of A356 Matrix Composites Reinforced with Different Types of Reinforcing Particles. Journal of Materials Engineering and Performance, 26, 4297-4310. https://doi.org/10.1007/s11665-017-2901-6

Akbari, M., Asadi, P., Zolghadr, P., Khalkhali, A., 2017b. Mutlicriteria optimization of mechanical properties of aluminium composites reinforced with different reinforcing particles type. Proceedings of the Institution of Mechanical Engineers, Part E: Journal of Process Mechanical Engineering, 232(3), 323-337. https://doi.org/10.1177/0954408917704994

Altinkok, N., Koker. R., 2004. Neural network approach to prediction of bending strength and hardening behaviour of particulate reinforced (Al-Si-Mg)-aluminium matrix composites. Material & Designs, 25(7), 595-602. https://doi.org/10.1016/j.matdes.2004.02.014

Annavarapu, S., Apelian, D., Lawley, A., 1988. Processing effects in spray casting of steel strip. Metallurgy Materials Transactions, 19, 3077-3086. https://doi.org/10.1007/BF02647735

Anand, S., Srivatsan, T. S., Wu, Y., Lavernia, E.J., 1997. Processing, microstructure and fracture behaviour of a spray atomized and deposited aluminium–silicon alloy. Journal of Materials Science, 32(11), 2835-2848. https://doi.org/10.1023/A:1018668332318

Anil, M., Srivastava, V. C., Ghosh, M. K., Ojha, S. N. 2010. Influence of tin content on tribological characteristics of spray formed Al–Si alloys. Wear, 268(11-12), 1250-1256. https://doi.org/10.1016/j.wear.2010.01.018

Anil, M., 2007. Spray forming of aluminium alloy and their tribological characteristics. PhD Thesis, BHU Varanasi.

Arunachalam, R., Piya, S., Krishnan, P. K., Muraliraja, R., Christy, J. V., Mourad, A. H. I., Al-Maharbi, M., 2020. Optimization of stir–squeeze casting parameters for production of

`

metal matrix composites using a hybrid analytical hierarchy process–Taguchi-Grey approach. Engineering Optimization, 52(7), 1166-1183. https://doi.org/10.1080/0305215X.2019.1639693

Arif, S., Tanwir, M., Ansari, A.H., Siddiqui, M.A., Mohsin, M., 2017. Study of mechanical and tribological behaviour of Al/SiC/ZrO2 hybrid composites fabricated through powder metallurgy technique. Material Research Express, 4, 076511. https://doi.org/10.1088/2053-1591/aa7b5f

Arif, S., Jamil, B., Shaikh, M.B., Aziz, T., Ansari, A.H., Khan, M., 2020. Characterization of surface morphology, wear performance and modelling of graphite reinforced aluminium hybrid composites. Engineering Science and Technology an International Journal, 23(3), 67-690. https://doi.org/10.1016/j.jestch.2019.07.001

Akhlaghi, F., Mahdavi, S., 2011. Effect of the SiC content on the tribological properties of hybrid Al/Gr/SiC composites processed by in-situ powder metallurgy (IPM) method. Advanced Material Research, 264–265 (2011) 1878–1886. https://doi.org/10.4028/www.scientific.net/AMR.264-265.1878

Asl, M. S., Kakroudi, M. G., Rezvani, M., Golestani-Fard, F., 2015a. Significance of hot pressing parameters on the microstructure and densification behavior of zirconium diboride. International Journal of Refractory Metals and Hard Materials, 50, 140-145. https://doi.org/10.1016/j.ijrmhm.2015.01.004

Asl, M. S., Kakroudi, M. G., Nayebi, B., Nasiri, H., 2015b. Taguchi analysis on the effect of hot pressing parameters on density and hardness of zirconium diboride. International Journal of Refractory Metals and Hard Materials, 50, 313-320. https://doi.org/10.1016/j.ijrmhm.2014.09.006

Avinash, L., Ram Prabhu, T., Parthasarathy, A., Varun Kumar, K. N., Sajjan, B., 2016a. Wear and mechanical behaviour of Hypo-eutectic Al-7% Si-0.5% Mg alloy (A357) reinforced with Al2O3 particles. In Applied Mechanics and Materials, 829, 66-72. https://doi.org/10.4028/www.scientific.net/AMM.829.66

`

Avinash, L., Ram Prabhu, T., Bontha, S., 2016b. The Effect on the dry sliding wear behavior of gravity cast A357 reinforced with dual size silicon carbide particles. In Applied Mechanics and Materials, 829, 83-89. https://doi.org/10.4028/www.scientific.net/AMM.829.83

Azimi, A., Shokuhfar, A., Nejadseyfi, O., Fallahdoost, H., Salehi, S., 2015. Optimizing consolidation behavior of Al 7068–TiC nanocomposites using Taguchi statistical analysis. Transactions of Nonferrous Metals Society of China, 25(8), 2499-2508. https://doi.org/10.1016/S1003-6326(15)63868-7

Benzerga, A.A., Hong, S.S., Kim, K.S., Needleman, A., Van der Giessen, E., 2001. Smaller is softer: an inverse size effect in a cast aluminium alloy. ActaMaterialia, 49(15), 3071-3083. https://doi.org/10.1016/S1359-6454(01)00195-1

Baiqing, X., Yongan, Z., Qiang, W., Likai, S., Changan, X., Chengjia, S., Xinlai, H., 2003. The study of primary Si phase in spray forming hypereutectic Al–Si alloy. Journal of materials processing technology, 137(1), 183-186. https://doi.org/10.1016/S0924-0136(02)01092-0

Bao, Y., Gawne, D.T., Gao, J., Zhang, T., Cuenca, B.D., Alberdi, A., 2013. Thermal-spray deposition of enamel on aluminium alloys. Surface and Coatings Technology, 232, 150-158. https://doi.org/10.1016/j.surfcoat.2013.04.065

Brown, J. R., 1999. Foseco Non-Ferrous Foundryman's Handbook. Oxford: Butterworth Heinemann. https://doi.org/10.1016/B978-075064286-6/50003-6.

Campbell, J., 2011. Complete Casting Handbook. Oxford: Butterworth-Heinemann. https://doi.org/10.1016/B978-0-444-63509-9.00001-7.

Ceschini, L., Morri, A., Morri, A., Toschi, S., Johansson, S., Seifeddine, S., 2015. Effect of microstructure and overaging on the tensile behavior at room and elevated temperature of C355-T6 cast aluminum alloy. Materials & Design, 83, 626-634. https://doi.org/10.1016/j.matdes.2015.06.031

`

Crepeau, P.N., 1995. Effect of iron in Al-Si casting alloys: a critical review, AFS Transactions, 103, 361-366.

Coello, C.A., Pulido, G.T., Lechuga, M.S., 2004. Handling multiple objectives with particle swarm optimization. IEEE Trans Evol Comput, 8(3), 256–79.
DOI: 10.1109/TEVC.2004.826067

Dann, P.C., Hogan, L.M., Eady, J.A., 1979. Mechanisms of coarsening of secondary dendrite arm spacings in Al–Cu alloys and an organic analogue. Met. Forum 2, 212–19

Daoud, A., Elkhar, M.O., 2002. Influence of Al2O3 or ZrO2 particulate addition on the microstructure aspects of AlNi and AlSi alloys. Journal of Material Processing and Technology, 120(1-3), 296-302. https://doi.org/10.1016/S0924-0136(01)01067-6

Ding, S., Chen, C., Xin, B., Pardalos, P.M., 2018. A bi-objective load balancing model in a distributed simulation system using NSGA-II and MOPSO approaches. Applied Soft Computing, 63, 249-267. https://doi.org/10.1016/j.asoc.2017.09.012

Das, S.K., Green, J.A.S., Kaufman, J.G., 2007. The development of recycle-friendly automotive aluminum alloys. JOM, 59, 47-51. https://doi.org/10.1007/s11837-007-0140-2

Dai, X., Yang, X., Campbell, J., Wood, J., 2003. Effects of runner system design on the mechanical strength of Al–7Si–Mg alloy castings. Materials Science and Engineering: A, 354(1-2), 315-325. https://doi.org/10.1016/S0921-5093(03)00021-2

Dirisenapu, G., Dumpala, L., Seelam, P. R. 2019. Experimental optimization of mechanical properties of Al7010/B4C/BN hybrid metal matrix nanocomposites using Taguchi technique. Materials Research Express, 6(10), 105068.
https://doi.org/10.1680/jemmr.19.00080

Dwivedi, D.K., Arjun, T.S., Thakur, P., Vaidya, H., Singh, K., 2004. Sliding wear and friction behaviour of Al-18%Si-0.5%Mg alloy. Journal of Material Processing Technology, 152, 323-328. https://doi.org/10.1016/j.jmatprotec.2004.04.379

Dwivedi, D.K., 2006. Wear behaviour of cast hypereutectic aluminium silicon alloys. Materials and Design, 27, 610-616. https://doi.org/10.1016/j.matdes.2004.11.029

Du Plessis, A., & Rossouw, P. (2015). Investigation of porosity changes in cast Ti6Al4V rods after hot isostatic pressing. Journal of Materials Engineering and Performance, 24(8), 3137-3141. https://doi.org/10.1007/s11665-015-1580-4

Eisaabadi, B.G., Varahram, N., Davami, P., Kim, S.K., 2012. Effect of oxide bifilms on the mechanical properties of cast Al–7Si–0.3Mg alloy and the roll of runner height after filter on their formation. Materials Science and Engineering: A, 548, 99-105. https://doi.org/10.1016/j.msea.2012.03.097

Elias, C. N., Duailibi, J., Oliveira, L.G.D., 2004. Mechanical properties of alumina-zirconia composites for ceramic abutments. Materials Research, 7(4), 643-649. https://doi.org/10.1590/S1516-14392004000400021

Greer, A.L., Bunn, A.M., Tronche, A., Evans, P., Bristow, D.J., 2000. Modelling of inoculation of metallic melts: application to grain refinement of aluminium by Al+Ti+b. Acta metallurgic actmaterialia, 48(8), 2823-2835. https://doi.org/10.1016/S1359-6454(00)00094-X

Grant, P.S., Cantor, B., Rogers, S., Katgerman, L., 1991. A computer model for droplet and particle trajectories and thermal profiles in spray forming. Cast Metals, 3, 227-293. https://doi.org/10.1080/09534962.1990.11819044

Grant, P.S., Cantor, B., Katgerman, L., 1993. Modelling of droplet dynamic and thermal histories during spray forming—II. Effect of process parameters. Acta metallurgica materialia, 41(11), 3109-3118. https://doi.org/10.1016/0956-7151(93)90040-Y

Grigoris, E., Skolianos, S.M., 2002, Wear behaviour of artificially aged AA2024/40 lm SiCp composites in comparison with conventionally wear resistant ferrous materials. Wear, 253(9-10), 946–56. https://doi.org/10.1016/S0043-1648(02)00216-8

Goudar, D.M., Raju, K., Srivastava, V.C., Rudrakshi, G.B., 2013a. Effect of copper and iron on the wear properties of spray formed Al–28Si alloy. Materials & Design, 51, 383-390.

`

https://doi.org/10.1016/j.matdes.2013.04.018

Goudar, D. M., Raju, K., Srivastava, V.C., Rudrakshi, G. B., 2013b. Effect of secondary processing on the microstructure and wear behaviour of spray formed Al–30Mg 2 Si–2Cu alloy. Materials & Design, 47, 489-496. https://doi.org/10.1016/j.matdes.2012.11.010

Goudar, D.M., Srivastava, V.C., Rudrakshi, G.B., Raju, K., Ojha, S.N. 2015. Effect of Tin on the Wear Properties of Spray Formed Al–17Si Alloy. Transactions of the Indian Institute of Metals, 68(1), 3-7. https://doi.org/10.1007/s12666-015-0573-1

Feng, W., Jishan, Z., Baiqing, X., Yongan, Z., 2011. Microstructure, Mechanical Properties, and Age-Hardening Behavior of an Al-Si-Fe-Mn-Cu-Mg Alloy Produced by Spray Deposition. Journal of Materials Engineering and Performance, 20(1), 155-159. https://doi.org/10.1007/s11665-010-9654-9

Fei, N. C., Mehat, N. M., Kamaruddin, S., 2013. Practical applications of Taguchi method for optimization of processing parameters for plastic injection moulding: a retrospective review. ISRN Industrial engineering, 1-8. https://doi.org/10.1155/2013/462174

Hassan, AM., Alrashdan, A., Hayajneh, M.T., Mayyas, A.T., 2009. Prediction of density, porosity and gardness in aluminium-copper-based composite materials using aritificial neural network. Journal of Material Processing Technology, 209(2), 894-899. https://doi.org/10.1016/j.jmatprotec.2008.02.066

Hashim, J., Looney, L., Hashmi, M. S. J. 2002. Particle distribution in cast metal matrix composites—Part I. Journal of Materials Processing Technology, 123(2), 251-257. https://doi.org/10.1016/S0924-0136(02)00098-5

Hendronursito, Y., Ojahan Rajagukguk, T., Safii, R. N., Sofii, A., Isnugroho, K., Candra Birawidha, D., Al Muttaqii, M., 2020. Analysis of Aluminium Basalt Particulate Composite Using Stirring Casting Method through Taguchi Method Approach. International Conference on Engineering Science and Technology Indonesia, 807(1), 012003. doi:10.1088/1757-899X/807/1/012003

`

Herbert, M.A., Maiti, R., Mitra, R., Chakraborty, M., 2006. Microstructural evolution and wear properties of in-situ Al–4.5Cu–5TiB2 composite processed in mushy state. Solid State Phenomenon, 116–117, 217–220.

https://doi.org/10.4028/www.scientific.net/SSP.116-117.217

Herbert, M.A., Maiti, R., Mitra, R., Chakraborty, M., 2007a. Microstructural evolution, hardness and alligatoring in the mushy state rolled cast Al–4.5Cu alloy and in-situ Al4.5Cu–5TiB2 composite. Metallurgy and Material and Transaction A, 38 (9), 2110–2126.

https://doi.org/10.1007/s11661-007-9264-9

Herbert, M.A., 2007b. Some studies on the mushy state rolling of Al–4.5Cu alloy based in-situ composites reinforced with TiB2 or TiC particles, Ph.D. Dissertation, Indian Institute of Technology, Kharagpur,West Bengal, India, July 2007.

Herbert, M.A., Maiti, R., Mitra, R., Chakraborty, M., 2008. Wear behaviour of cast and mushy stated rolled Al-4.5Cu alloy and in-situ Al4.5Cu-5TiB2 composite. Wear, X, 1606-1618. https://doi.org/10.1016/j.wear.2008.03.010

Hernandez, F. C. R., Ramírez, J. M. H., Mackay, R., 2017. Applications in the Automotive and Aerospace Industries. In Al-Si Alloys (pp. 163-171). Springer, Cham.

Hogan L.M., 2001. Crystals, Dendritic Solidification of, Encyclopedia of Materials: Science and Technology (Second Edition), 1913-1918.

Hunsicker, H.Y., Mondolfo, L.F., Tombin, P.A., 1990. Properties of Pure Metals, Properties and Selection. in ASM Handbook. Nonferrous Alloys and Special Purpose Materials, 2, ed: ASM International, 1990. https://doi.org/10.31399/asm.hb.v02.9781627081627

Joseph, R.D., 1993. Aluminium and Aluminium alloys. ASM International Technology.

Jokhio, M. H., Panhwer, M. I., Unar, M. A., 2016. Manufacturing of aluminum composite material using stir casting process. arXiv preprint arXiv:1604.01251.

`

Jiang, W., Fan., Dai., Y., Li, C., 2014. Effects of rare earth elements addition on microstructures, tensile structures, tensile properties and fractography of A357 alloy. Material Science Engineering, 597, 237-244. https://doi.org/10.1016/j.msea.2014.01.009

Jung, H., Mangelinck-Noël, N., Bergman, C., Billia, B., 2009. Determination of the average nucleation undercooling of primary Al-phase on refining particles from Al–5.0 wt% Ti–1.0 wt% B in Al-based alloys using DSC. Journal of Alloys and Compounds, 477, 622–627. https://doi.org/10.1016/j.jallcom.2008.10.109

Karimzadeh, F., Ebnonnasir, A., Foroughi, A., 2006. Artificial neural network modelling evaluationg of epitaxial growth of Ti6A14V weldment. Material Science and Engineering: A, 432(1-2), 184-190. https://doi.org/10.1016/j.msea.2006.05.141

Kaushik, N., Rao R., 2016. Effect of grit size on two body abrasive wear of Al 6082 hybrid composites produced by stir casting method. Tribology International. 102, 52–60. https ://doi.org/10.1016/j.tribo int.2016.05.015

Kavimani, V., Prakash, K.S., Thankachan, T., 2017. Surface characterization and specific wear rate prediction of r-GO / AZ31 composite under dry sliding wear condition. Surfaces and Interfaces, 6, 143–153. https://doi.org/10.1016/j.surfin.2017.01.004

Kennedy, J., Eberhart, R., 1995. Particle swarm optimization. In Proceedings of ICNN'95-international conference on neural networks, 4, 1942-1948. https ://doi.org/10.1109/ICNN.1995.488968

Kumari, R., Mishra, A. R., 2020. Multi-criteria COPRAS Method Based on Parametric Measures for Intuitionistic Fuzzy Sets: Application of Green Supplier Selection. Iranian Journal of Science and Technology, Transactions of Electrical Engineering, 1-18. Society. https://doi.org/10.1007/s40998-020-00312-w

Kumaraswamy, H.S., Bharat, V., Rao, T.K., 2018. Influence of Mechanical &tribological BehaviourOf Al 2024 MMC Fabricated by Stir Casting Technique-A Review. Material Today Proceedings, 5(5), 11962-11970. https://doi.org/10.1016/j.matpr.2018.02.170

`

Kori, S.A., Chandrashekharaih, T.M., 2007. Studies on the dry sliding wear behaviour of hypoeutectic and eutectic Al-Si alloys. Wear, 263(1-6), 745-755. https://doi.org/10.1016/j.wear.2006.11.026

Kaufman, J. G., Rooy, E. L., 2004. Aluminum Alloy Castings: Properties, Processes, and Applications. ASM International.

Kumar, D., Kumar, V., 2020. Impact of controlling parameters on the performance of MOPSO algorithm. Procedia Computer Science, 167, 2132-2139. https://doi.org/10.1016/j.procs.2020.03.261

Lakshmikanthan, A., Bontha, S., Krishna, M., Koppad, P.G., Ramprabhu, T., 2019. Microstructure, mechanical and wear properties of the A357 composites reinforced with dual sized SiC particles. Journal of Alloys and Compounds, 786, 570-580. https://doi.org/10.1016/j.jallcom.2019.01.382

Lakshmikanthan, A., Udayagiri, S. B., Koppad, P.G., Gupta, M., Munishamaiah, K., Bontha, S., 2020. The effect of heat treatment on the mechanical and tribological properties of dual size SiC reinforced A357 matrix composites. Journal of Materials Research and Technology, 9(3), 6434-6452. https://doi.org/10.1016/j.jmrt.2020.04.027

Lavernia, E., 1989. The evolution of microstructure during spray atomization and deposition. International Journal of Rapid Solidification, 5(1), 47.

Lavernia, E., Ayers, J.D., Srivatsan, T.S., 1992. Rapid solidifaction processing with specific application of aluminium alloys. International Material reviews, 37(1), 1-44. https://doi.org/10.1179/imr.1992.37.1.1

Lisboa, P.J., Taktak, A.F.Z., 2006. The use of artificial neural networks in decision support in Cancer: A systematic review. Neural Networks, 19(4), 408-415. https://doi.org/10.1016/j.neunet.2005.10.007

`

Liu, L., Samuel, F.H., 1988. Effect of inclusions on the tensile properties of Al-7% Si0.35% Mg (A356.2) aluminium casting alloy. Journal of Materials Science, 33, 2269-2281. https://doi.org/10.1023/A:1004331219406

Liu, L., Li, W., Tang, Y., Shen, B., Hu, W., 2009. Friction and wear properties of short carbon fiber reinforced aluminium matrix composites. Wear, 266(7-8), 733–8. https://doi.org/10.1016/j.wear.2008.08.009

Liu, B., Lei, Q., Xie, L., Wang, M., Li, Z., 2016. Microstructure and mechanical properties of high product of strength and elongation Al-Zn-Mg-Cu-Zr alloys fabricated by spray deposition. Materials & Design, 96, 217-223. https://doi.org/10.1016/j.matdes.2016.02.011

Ludema, K.C., 1984. A review of scuffing and running in of lubricated surfaces with asperities and oxides in perspective. Wear, 100(1-3), 315-331. https://doi.org/10.1016/0043-1648(84)90019-X

Marigoudar, R., Sadashivappa, K., 2011. Dry sliding wear behaviour of SiC Particles reinforced zinc-aluminium (ZA43) alloy metal matrix composites. Journal of Minerals Material and Characterization Engineering, 10(5), 419–425. https ://doi.org/10.4236/jmmce .2011.10503 1

Mazahery, A., Shabani, M.O., 2012. Study on microstructure and abrasive wear behaviour of sintered Al matrix composites. Ceramics International, 38(5), 4263-4269. https://doi.org/10.1016/j.ceramint.2012.02.008

Major, F.J., 2008. Aluminium and Aluminium Alloy Castings. in ASM Handbook. Castings, 15, ed: ASM International.

Moazami-Goudarzi, M., Akhlaghi, F., 2016. Wear behaviour of Al 5252 alloy reinforced with micrometric and nanometric SiC particles. Tribology International, 102, 28–37. https://doi.org/10.1016/j.triboint.2016.05.013

`

Muthaiah, V.S., Mula, S., 2016. Effect of zirconium on thermal stability of nano crystalline aluminium alloy prepared by mechanical alloying. Journal of Alloys and Compounds, 688, 571-580. https://doi.org/10.1016/j.jallcom.2016.07.038

Mukherjee, I., Ray, P. K., 2006. A review of optimization techniques in metal cutting processes. Computers & Industrial Engineering, 50(1-2), 15-34. https://doi.org/10.1016/j.cie.2005.10.001

Murthy, A., Harshith, D.N., Nitish, R., Nagaraj, S.N., Gurumurthy, B.M., Abhishek, V.N., Patil, I.S., 2018. Thrust and torque force analysis in the drilling of aramid fibre-reinforced composite laminates using RSM and MLPNN-GA. Heliyon, 4(7), 1-39. https://doi.org/10.1016/j.heliyon.2018.e00703

Nagarkar, M.P., Patil, G.J.V., Patil, R.N.Z., 2016. Optimization of nonlinear quarter car suspension–seat–driver model. Journal of advanced research, 7(6), 991-1007. https://doi.org/10.1016/j.jare.2016.04.003

Ojha, S.N., Jha, J.N., Singh, S.N., 1991. Microstructural modifications in AlSi eutectic alloy produced by spray deposition. Scripta Materila, 25(2), 443-447.

Pariona, M.M., Bolfarini ,C., Dos Santos, R.J., Kiminami, C.S., 2000. Application of mathematical simulation and the factorial design method to the optimization of the atomization stage in the spray forming of a Cu–6% Zn alloy. Journal of Materials Processing Technology, 102(1-3), 221-229. https://doi.org/10.1016/S0924-0136(00)00482-9

Parthasarathy, A., Avinash, L., Varun Kumar, K.N., Sajjan, B., Varun, S., 2017. Fabrication and Characterization of Al-0.4% Si-0.5% Mg-SiCp Using Permanent Mould Casting Technique. In Applied Mechanics and Materials, 867, 34-40. https://doi.org/10.4028/www.scientific.net/AMM.867.34

Patel, G.C.M., Krishna, P., Parappagoudar, M.B., Vundavilli, P.R., 2016. Multi-objective optimization of squeeze casting process using evolutionary algorithms. International Journal of Swarm Intelligence Research (IJSIR), 7(1), 55-74. DOI:10.1515/afe-2016-0073

`

Patel, G.C.M., Krishna, P., Parappagoudar, M.B., Vundavilli ,P.R., Bhushan, S.B., 2018. Squeeze casting parameter optimization using swarm intelligence and evolutionary algorithms. In Critical developments and applications of swarm intelligence, 245-270.

Patel, G. M., Chate, G. R., Parappagoudar, M. B., 2020a. Modelling and Optimization of Alpha-set Sand Moulding System Using Statistical Design of Experiments and Evolutionary Algorithms. In Optimization of Manufacturing Processes (pp. 1-28). Springer, Cham.

Patel, G. M., Jagadish, Kumar, R. S., Naidu, N. S., 2020b. Optimization of Abrasive Water Jet Machining for Green Composites Using Multi-variant Hybrid Techniques. In Optimization of Manufacturing Processes (pp. 129-162). Springer, Cham.

Prabaharan, T., 2020. Mechanical and Tribological Characterization of Stir Cast AA6061 T6–SiC Composite. Silicon, 1-8. https://doi.org/10.1007/s12633-020-00781-y

Prasad, S.V., Asthana, R., 2004. Aluminum metal-matrix composites for automotive applications: tribological considerations. Tribology Letters, 17, 445-453. https://doi.org/10.1023/B:TRIL.0000044492.91991.f3

Prabaharan, T. 2020. Mechanical and Tribological Characterization of Stir Cast AA6061 T6–SiC Composite. Silicon, 1-8. https://doi.org/10.1007/s12633-020-00781-y

Prabu, S. B., Karunamoorthy, L., Kathiresan, S., Mohan, B., 2006. Influence of stirring speed and stirring time on distribution of particles in cast metal matrix composite. Journal of materials processing technology, 171(2), 268-273. https://doi.org/10.1016/j.jmatprotec.2005.06.071

OICAs statistics of worldwide vehicles sales. 2013. Available: http://www.oica.net/category/sales-statistics/ 2015-03-23

Polmear, I., John, D.S., 2005. Light Alloys: From Traditional Alloys to Nanocrystals: Elsevier Science, 2005. https://doi.org/10.1016/B978-075066371-7/50005-0.

`

Qingping, W., Fanfei, M., Jinbo, Z., 2014. Microstructural characterization and mechanical property of fly Ash/Al-25Mg composites, Journal of Wuhan University of Technology Material Science Edition. 1, 1019-1022. DOI 10.1007/s11595-014-1036-y

Ravindran, P., Manisekar, K., Rathika, P., Narayanasamy, P., 2013. Tribological properties of powder metallurgy – processed aluminium self-lubricating hybrid composites with SiC additions. Material Science and Design, 45, 561–570.
https://doi.org/10.1016/j.matdes.2012.09.015

Raju, K., Harsha, A.P., Ojha, S.N., 2013. Evolution of Microstructure and its Effects on wear and mechanical properties of spray cast Al-12Si alloy. Material Science and Engineering, 528-7728-7728. https://doi.org/10.1016/j.msea.2011.06.078

Rosenfield, A.R., 1987. A shear instability model of sliding wear. Wear, 116(3), 317–328.
https://doi.org/10.1016/0043-1648(87)90180-3

Ramesh, C.S., Pramod, S., Keshavamurthy, R.A., 2011. Study on microstructure and mechanical properties of Al 6061–TiB2 in situ composites. Material Science Engineering A. 528, 4125–32. https://doi.org/10.1016/j.msea.2011.02.024

Raju, K., Harsha, A.P., Ojha, S.N., 2011. Evolution of microstructure and its effect on wear and mechanical properties of spray cast Al-12Si alloy. Material Science and Engineering A, 528, 7723-7728. https://doi.org/10.1016/j.msea.2011.06.078

Ramanathan, A., Krishnan, P. K., Muraliraja, R., 2019. A review on the production of metal matrix composites through stir casting–Furnace design, properties, challenges, and research opportunities. Journal of Manufacturing Processes, 42, 213-245.
https://doi.org/10.1016/j.jmapro.2019.04.017

Rao, R.S., Das, S., 2010. Effect of matrix alloy and influence of SiC particle on the sliding wear characteristics of aluminium alloy composites. Material Science and Design, 31, 1200–1207. https://doi.org/10.1016/j.matdes.2009.09.032

`

Rao, R.S., Das, S., 2011a. Effect of sliding distance on the wear and friction behavior of as cast and heat-treated Al–SiCp composites. Material Science and Design. 32, 3051– 3058. https://doi.org/10.1016/j.matdes.2011.01.033

Rao, R.S., Das, S., 2011b. Effect of SiC content and sliding speed on the wear behaviour of aluminium matrix composites. Material Science and Design, 32, 1066–1071. https://doi.org/10.1016/j.matdes.2011.01.033

Rao, R.S., Das, S., 2011c. Effect of applied pressure on the tribological behaviour of SiCp reinforced AA2024 alloy. Tribology International, 44(4), 454–462. https://doi.org/10.1016/j.triboint.2010.11.018

Ray, K., Patra, H., Swain, A.P., Parida, B., Mahapatra, S., Sahu, A., Rana, S., 2020. Glass/jue/sisal fibre reinforced hybrid polypropylene polymer composites: Fabrication and analysis of mechanical and water absorption properties. Material Today Proceedings, 1-8. https://doi.org/10.1016/j.matpr.2020.02.964

Riahi, A.R., Alpas, A.T., 2001. The role of tribo-layers on the sliding wear behavior of graphitic aluminum matrix composites. Wear, 251, 1396-1407. https://doi.org/10.1016/S0043-1648(01)00796-7

Rudrakshi G.B., Srivastava, V.C., Pratak, J.P., Ojha, S.N., 2004. Spray forming of Al-Si-Pb alloys and their wear characteristics. Journal of Material Science and Engineering, 383, 34-38. https://doi.org/10.1016/j.msea.2004.02.033

Rashmimittal*, Devendra, S., 2011. Dry sliding wear behaviour of spray formed ZrSio4 reinforced Al-Si-Sn alloy. Advanced Materials Letters, 3(1), 38-43. https://doi.org/10.5185/amlett.2011.5258

Rovira, M.M., Lancini, B.C., Robert, M.H., 1999. Thixo-forming of Al–Cu alloys. Journal of Material Processing and Technology, 92–93, 42–49. https://doi.org/10.1016/S0924-0136(99)00220-4

`

Sahin, Y., 2003. Wear behaviour of aluminium alloy and its composites reinforced by SiC particles using statistical analysis. Material Science and Design, 24, 95–103. https://doi.org/10.1016/S0261-3069(02)00143-7

Sajjan, B., Avinash, L., Varun, S., Varun Kumar, K.N., Parthasarathy, A., 2017. Investigation of Mechanical Properties and Dry Sliding Wear Behaviour of Graphite Reinforced Al7068 Alloy. In Applied Mechanics and Materials, 867, 10-18. https://doi.org/10.4028/www.scientific.net/AMM.867.10

Sabatino, M.D., Arnberg, L., 2009. Castability of aluminium alloys. Transactions of the Indian Institute of Metals, 62, 321-325. https://doi.org/10.1007/s12666-009-0049-2

Seifeddine, S., 2006. Characteristics of cast aluminium-silicon alloys - microstructures and mechanical properties. Ph.D. Thesis - Dissertation No. 1058 Ph.D. Thesis. Linköping: Linköping Studies in Science and Technology, Sweeden.

Sigworth, G., 2011. Understanding quality in aluminium castings. International Journal of Metal casting, 5, 7-22. https://doi.org/10.1007/BF03355504

Shabani, M.O., Mazahery, A., 2011a. Modelling of the wear properties in A356 matrix composite reinforced with B4C particulates. Synthetic Metals, 161(13-14), 1226-1231. https://doi.org/10.1016/j.synthmet.2011.04.009

Shabani, M.O., Mazahery, A., 2011b. The ANN application in FEM modelling of mechanical properties of Al-Si alloy. Applied Mathematical Modelling, 35(12), 5707-5713. https://doi.org/10.1016/j.apm.2011.05.008

Shankar, S., Apelian, D., 2002. Die soldering: Mechanism of the interface reaction between molten aluminum alloy and tool steel. Metallurgical and Materials Transactions B, 33, 465-476, 2002. https://doi.org/10.1007/s11663-002-0057-7

Sheibani, S., Najafabadi, M.F., 2007. In situ fabrication of Al–TiC metal matrix composites by reactive slag process. Material Science and Design, 28, 2373–2378. https://doi.org/10.1016/j.matdes.2006.08.004

`

Shen, Y.L., Chawla, N., 2001. On the correlation between hardness and tensile strength in particle reinforced metal matrix composites. Material Science and Engineering:A, 297(1-2), 44-47. https://doi.org/10.1016/S0921-5093(00)01256-9

Srivastava, A.K., Anandani, R.C., Dhar, A., Gupta, A. K., 2001. Effect of thermal conditions on microstructural features during spray forming. Materials Science and Engineering: A, 304, 587-591. https://doi.org/10.1016/S0921-5093(00)01540-9

Srivastava, S., Mandal, R.K., Ojha, S.N., 2004. Evolution of microstructure in spray formed Al-18%Si alloy. Materials Science and Engineering: A, 383(1), 14-20. https://doi.org/10.1016/j.msea.2004.02.031

Singh, S.K., Gupta, A.K., Mahesh, K., 2010. Prediction of mechanical properties of extra deep drawn steel in blue brittle region using artificial neural network. Materials & Design, 31(5), 2288-2295. https://doi.org/10.1016/j.matdes.2009.12.012

Singh, M., Pant, M., Godiyal, R. D., Kumar Sharma, A., 2020a. MCDM approach for selection of raw material in pulp and papermaking industry. Materials and Manufacturing Processes, 35(3), 241-249. https://doi.org/10.1080/10426914.2020.1711917

Singh, M., Pant, M., 2020b. A review of selected weighing methods in MCDM with a case study. International Journal of System Assurance Engineering and Management, 1-19. https://doi.org/10.1007/s13198-020-01033-3

Stadler, F., Antrekowitsch, H., Fragner, W., Kaufmann, H., Uggowitzer, P.J., 2011. The effect of Ni on the high-temperature strength of Al-Si cast alloys. Materials Science Forum, 274-277. https://doi.org/10.4028/www.scientific.net/MSF.690.274

Stadler, F., Antrekowitsch, H., Fragner, W., Kaufmann, H., Uggowitzer, P.J., 2012. Effect of main alloying elements on strength of Al–Si foundry alloys at elevated temperatures. International Journal of Cast Metals Research, 25(4), 215-224. https://doi.org/10.1179/1743133612Y.0000000004

`

Stojčić, M., Zavadskas, E. K., Pamučar, D., Stević, Ž., Mardani, A., 2019. Application of MCDM methods in sustainability engineering: A literature review 2008–2018. Symmetry, 11(3), 350. https://doi.org/10.3390/sym11030350

Svensson, I.L., 2003. Component casting with simulation. School of Enginering, Jönköping University, Sweden.

Tian, C., Law, J., van der Touw, J., Murray, M., Yao, J., Graham, D., 2012. Effect of melt cleanliness on the formation of porosity defects in automotive aluminium high pressure die castings. Journal of Materials Processing Technology, 122(1), 82- 93. https://doi.org/10.1016/S0924-0136(01)01229-8

Timelli, G., Ferraro, S., Fabrizi, A., 2013. Effects of chromium and bismuth on secondary aluminium foundry alloy. International Journal of Cast Metals Research, 26, 239-246, 2013. https://doi.org/10.1179/1743133613Y.0000000061

Tjong S.C., Ma, Z.Y., 2000. Microstructural and mechanical characteristics of in situ metal matrix composites. Material Science and Engineering, 29(3-4), 49–113. https://doi.org/10.1016/S0927-796X(00)00024-3

Tuti, Y., Asad A., Khalid, S., Haque, M.M., 2004. Tribological wear properties of aluminium-silicon eutectic base alloy under dry sliding condition. Journal of Material Processing Technology, (153-154), 833-838. https://doi.org/10.1016/j.jmatprotec.2004.04.147

Vencl A., Rac, A., Bobić, I., 2004. Tribological behaviour of Al-based MMCs and their application in automotive industry. Tribology in Industry, 26, 31-38.

Wallace, J.F., Schwam, D., Hong, W., 2001. Mold materials for permanent mold casting of aluminum alloys. Washington D.C.

`

Wang, L., Makhlouf, M., Apelian, D., 1995. Aluminium die casting alloys: alloy composite, microstructure and performance relationship. International Material Reviews, 40(6), 221-238. https://doi.org/10.1179/imr.1995.40.6.221

Wang, F., Ma, Y., Zhang, Z., Cui, X., Jin, Y., 2004. A comparison of the sliding wear behavior of a hypereutectic Al–Si alloy prepared by spray-deposition and conventional casting methods. Wear, 256(3), 342-345. https://doi.org/10.1016/S0043-1648(03)00412-5

Xu, Q., Lavernia, E., 1999. Microstructural evolution during the initial stages of spray atomization and deposition. Scripta Materila, 41(5), 535-540.

Yang, Y., Hannula, S.P., 2008. Development of precision spray forming for rapid tooling. Materials Science and Engineering: A, 477(1), 63-68. https://doi.org/10.1016/j.msea.2007.09.080

Yadav, S.P.S., Ranganath, S., Sharieff, S., Suresh, R., Avinash, L., 2020. Investigations on the change in state of stress with respect to the sliding direction in dry sliding wear of hard elastic material with different geometry and orientation on ductile flat surface. FME Transactions, 48(3), 716-723. https://doi.org/10.5937/fme2003716S

Yasmin, T., Khalid, A., Haque, M.M., 2004. Tribological (wear) properties of aluminium silicon eutectic base alloy under dry sliding condition. Journal of Material Processing Technology, 153-154, 833-838. https://doi.org/10.1016/j.jmatprotec.2004.04.147

Yigezu, B. S., Jha, P. K., Mahapatra, M.M., 2013. The key attributes of synthesizing ceramic particulate reinforced Al-based matrix composites through stir casting process: a review. Materials and Manufacturing Processes, 28(9), 969-979. https://doi.org/10.1080/10426914.2012.677909

Zalensas, D.L., 1993. Aluminum casting technology, 201. Des Plaines: American Foundrymen's

`

Zhao, H. D., Wang, F., Li, Y. Y., Xia, W., 2009. Experimental and numerical analysis of gas entrapment defects in plate ADC12 die castings. Journal of materials processing technology, 209(9), 4537-4542. https://doi.org/10.1016/j.jmatprotec.2008.10.028

Zheng, X. G., Shi, Y. N., & Lou, L. H., 2015. Healing process of casting pores in a Ni-based superalloy by hot isostatic pressing. Journal of Materials Science & Technology, 31(11), 1151-1157. https://doi.org/10.1016/j.jmst.2015.07.004

`

BIO DATA

Name :	Ishwaragouda S Patil
Fathers Name	Shekaragouda t patil
BE	Completed in the year 1994
College	B V Bomaraddi College of Engineering, Hubli
MTech	Completed in the year 2000
	Gogte Institute of Technology ,Belagavi
Experience	26 years of Experience both in the Industry and Teaching
	Worked as a Export Quality manager in the Fine Blanking Pvt Ltd, Hubli
	At Present Working as a Assistant Professor in the Department Of Tontadarya College Of Engineering, Gadag

The above-mentioned information is true and best of knowledge

ISWARAGOUDA S PATIL

`